Západočeská univerzita v Plzni

Fakulta aplikovaných věd

PRVKOVÉ SLOŽENÍ A STRUKTURA TENKOVRSTVÝCH MATERIÁLŮ A JEJICH KORELACE S MATERIÁLOVÝMI VLASTNOSTMI

Ing. Radomír Čerstvý

Dizertační práce k získání akademického titulu doktor
v oboru Fyzika plazmatu a tenkých vrstev

Školitel: prof. RNDr. Jaroslav Vlček, CSc.

Katedra fyziky

Plzeň 2019

University of West Bohemia
Faculty of Applied Sciences

ELEMENTAL COMPOSITION AND STRUCTURE OF THIN FILM MATERIALS AND THEIR CORRELATION WITH MATERIAL PROPERTIES

Ing. Radomír Čerstvý

A thesis submitted for the degree of Doctor of Philosophy
in the field of Plasma Physics and Physics of Thin Films

Supervisor: prof. RNDr. Jaroslav Vlček, CSc.
Department of Physics

Pilsen 2019

Předmluva

Předkládám k posouzení a obhajobě dizertační práci zpracovanou na katedře fyziky Fakulty aplikovaných věd Západočeské univerzity v Plzni. Prohlašuji, že jsem předloženou práci vypracoval samostatně na základě výsledků dosažených během doktorského studia a s využitím citované odborné literatury. Dizertační práce je předložena ve formě 12 vědeckých článků publikovaných v impaktovaných vědeckých časopisech.

Vědecký výzkum, jehož výsledky jsou použity v předkládané dizertační práci, probíhal pod vedením prof. RNDr. Jaroslava Vlčka, CSc. na katedře fyziky Západočeské univerzity v Plzni od září 2008 do srpna 2012, a to v rámci projektu MSM4977751302 (2005 – 2011): Procesy ve výbojovém plazmatu a nové tenkovrstvé materiály s unikátními vlastnostmi a projektu GAP108/12/0393 (2012 – 2015): Tvrdé nanokompozitní vrstvy se zvýšenou houževnatostí a unikátními vlastnostmi.

V Plzni dne 20. 8. 2019 ……………………………………

Ing. Radomír Čerstvý

Poděkování

Při této příležitosti bych rád poděkoval svému školiteli prof. RNDr. Jaroslavu Vlčkovi, CSc. za cenné rady, trpělivost a pečlivé vedení během mého doktorského studia i při zpracování této dizertační práce. Děkuji také všem kolegům z katedry fyziky ZČU za vytvoření přátelského prostředí a přínosnou spolupráci. V neposlední řadě bych chtěl také poděkovat své rodině a přátelům za všestrannou podporu během celého mého doktorského studia.

Obsah

1. Úvod

Makroskopické vlastnosti materiálu (mechanické, chemické, optické, tepelné, …) silně závisí, kromě jeho prvkového složení, zejména na jeho struktuře. V případě objemových materiálů, připravovaných klasickými metalurgickými technologiemi za rovnovážných podmínek (vysoká teplota, atmosférický tlak a pomalé ochlazování), lze jejich strukturu stanovit z příslušných rovnovážných fázových diagramů, zobrazujících vztahy mezi strukturou (fázovým složením), prvkovým složením a teplotou. Problém však nastává u materiálů vytvářených ve formě tenkých vrstev, neboť ty jsou obvykle připravovány daleko od rovnovážných podmínek (relativně nízký tlak i teplota a rychlé ochlazování), takže ve většině případů obsahují mnohem více mřížkových poruch, jako jsou vakance, dislokace, hranice zrn, precipitáty sekundárních fází či metastabilní fáze, než stejné, konvenčně připravené, objemové materiály. V důsledku složitosti povahy depozičního procesu a velkého množství parametrů určujících kinetická omezení růstového procesu tenkých vrstev je poměrně obtížné předvídat mikrostrukturu a fyzikální vlastnosti takto deponovaných tenkých vrstev pouze ze znalosti použitých depozičních podmínek. Je proto nesmírně důležité studovat souvislosti mezi parametry depozičního procesu, prvkovým složením, strukturou a vlastnostmi připravených tenkovrstvých materiálů.

Navzdory rostoucímu komerčnímu významu materiálů připravených ve formě tenkých vrstev na různých substrátech a velkému objemu dostupné vědecké literatury je porozumění vztahům mezi depozičními parametry, mikrochemií a mikrostrukturou tenkých vrstev stále velmi malé. Je to částečně v důsledku složitosti depozičního procesu, ale také v důsledku faktu, že tenké vrstvy jsou v mnoha případech jen málo nebo neadekvátně charakterizovány. Provádění kvantitativní chemické a strukturní analýzy tenkých vrstev, zvláště komplexních sloučenin, je totiž často dosti obtížné a působí nemalé nesnáze. Například mnoho dobře zvládnutých analyzačních technik používaných pro objemové materiály nemůže být použito pro chemickou analýzu tenkých vrstev kvůli omezenému množství dostupného materiálu tenké vrstvy o tloušťce často pouze několik stovek nm či jednotek μm. Také analýzy struktury tenkých vrstev mohou být problematické. Malé velikosti zrn, růstová textura a velké množství defektů komplikují fázovou identifikaci, přesné stanovení mřížkových parametrů, kvalitativní stanovení typu a charakteru defektů, nemluvě o jejich případné kvantifikaci. Přesto však existují 2 analyzační techniky, využívající k analýze pevných látek jejich interakci s rentgenovým zářením, které lze používat jak pro objemové, tak i pro tenkovrstvé materiály. Jedná se o rentgenovou fluorescenci (XRF), užívanou ke stanovení prvkového složení materiálu, a rentgenovou difrakci (XRD), užívanou ke stanovení struktury materiálu.

1.1 Rentgenové záření

Rentgenové záření, objevené v roce 1895 W. C. Röntgenem, je krátkovlnné elektromagnetické vlnění o vlnových délkách λ v rozsahu 0,01 nm – 10 nm, respektive o energiích E v rozsahu 125 keV – 0,125 keV. Obecně je rentgenové záření generováno buď při změnách pohybového stavu rychle se pohybujících elektricky nabitých částic (elektronů, protonů), nebo při ozařování látek dostatečně energetickým rentgenovým zářením z rentgenové lampy či radioaktivním zářením γ z vhodného radioizotopu.

Spektrum rentgenového záření se skládá ze dvou složek, spojitého (brzdného) rentgenového záření a charakteristického rentgenového záření.

1.1.1 Spojité rentgenové záření (Bremsstrahlung)

Spojité (brzdné) rentgenové záření je emitováno v případě, kdy jsou volné elektrony prudce brzděny např. při jejich interakci s elektronovými obaly atomů látky. V tomto případě mohou tyto elektrony ztratit libovolné množství své kinetické energie pružným či nepružným rozptylem při interakci s atomy látky, což vede ke vzniku spojitého (brzdného) spektra rentgenového záření látky (tzv. Bremsstrahlung). Každá jednotlivá interakce elektron-atom vede ke zpomalení elektronu a vygenerování příslušného fotonu rentgenového záření, jehož vlnová délka λ závisí na konkrétní energetické ztrátě elektronu. Zprůměrování mnoha interakcí elektron-atom tak vede ke vzniku spojitého spektra, které je na straně krátkých vlnových délek omezeno minimální vlnovou délkou λ_{min}, jež odpovídá maximální kinetické energii E_{max} elektronu, urychlenému napětím U, a pro niž platí

$$\lambda_{min} = \frac{hc}{eU},$$

kde e je náboj elektronu, h je Planckova konstanta a c je rychlost světla.

1.1.2 Charakteristické rentgenové záření

V případě vázaných elektronů, např. v atomu, je proces vzniku rentgenového záření o něco komplikovanější. K jeho vysvětlení však můžeme využít Bohrův model atomu, ve kterém jsou elektrony, jejichž počet je dán příslušným protonovým číslem Z, charakterizovány 4 kvantovými čísly, s jejichž pomocí můžeme stanovit a zároveň i označit všechny možné energetické stavy elektronu v atomu. Hlavní kvantové číslo n udává relativní energii elektronu, respektive příslušné energetické hladiny v atomu a nabývá celočíselných hodnot 1, 2, 3, 4, … (ve spektroskopii se používá k označení energetických hladin písmen K, L, M, N, …). Vedlejší kvantové číslo l charakterizuje orbitální moment hybnosti elektronu a tvar orbitalu. Nabývá celočíselných hodnot 0, 1, 2, 3, …, $n-1$ (ve spektroskopii se používá k označení orbitalů písmen *s*, *p*, *d*, *f*, …). Magnetické kvantové číslo m udává orientaci atomového orbitalu v prostoru a nabývá celočíselných hodnot v rozmezí $\langle -l, +l \rangle$ včetně 0. Spinové kvantové číslo s udává spin (smysl rotace) elektronu a nabývá pouze 2 hodnot ± ½. Pro popis rentgenových spekter se ještě zavádí kvantové číslo pro celkový moment hybnosti elektronu $j = l \pm ½$.

Jestliže na látku dopadají vysoce urychlené elektrony, resp. fotony, s energií větší než je ionizační potenciál příslušné vnitřní energetické hladiny atomu, dojde k ionizaci atomu, tj. emisi elektronu z této vnitřní energetické hladiny a vzniku iontu daného stavu atomu. Přechod z nestabilního excitovaného stavu do základního stavu se děje přeskokem elektronu z vyšší energetické hladiny na uvolněnou nižší energetickou hladinu a je doprovázen vyzářením fotonu charakteristického rentgenového záření, jehož energie je rovna právě rozdílu vazebných energií počátečního a konečného stavu elektronu. Tyto přeskoky mezi energetickými hladinami se však nemohou dít zcela libovolně, ale platí pro ně tzv. výběrová pravidla, jenž charakterizují dovolené přechody. Pro velmi intenzivní dipólové přechody platí, že změna hlavního kvantového čísla $\Delta n \geq 1$, změna vedlejšího kvantového čísla $\Delta l = \pm 1$ a změna kvantového čísla pro celkový moment hybnosti elektronu $\Delta j = 0$ nebo 1. Pro mnohem méně intenzivní kvadrupólové přechody platí $\Delta l = 0$ nebo 1 a $\Delta j = 0$, 1 nebo 2. To tedy znamená, že spektrum charakteristického rentgenového záření je čárové (diskrétní) a závisí na druhu atomu, tj. je pro danou látku (materiál) charakteristické.

1.1.2.1 Značení čar charakteristického rentgenového spektra

Podle zažité konvence se nejčastěji série spektrálních čar označují tak, že se velkým písmenem označí konečná hladina přeskoku. K–série tedy odpovídá elektronovým přeskokům, které končí na nejnižší energetické hladině K, L–série přeskokům, jenž končí na hladině L, respektive jejich podhladinách L_I, L_{II}, L_{III}. Jednotlivé spektrální čáry se pak označují řeckými písmeny, např. α_1, α_2, β_1, γ_3 apod. Tyto symboly obvykle označují relativní intenzitu spektrálních čar, přičemž α je v dané sérii nejintenzivnější.

1.1.3 Interakce rentgenového záření s látkou

Vzájemné působení rentgenového záření na látku a naopak je mnohostranný děj, při kterém dochází k vzájemnému ovlivňování vlastností jak rentgenového záření, tak látky, přes kterou rentgenové záření prochází. Z toho důvodu se omezíme pouze na procesy, jenž jsou důležité pro uvažované analyzační techniky XRF a XRD.

1.1.3.1 Absorpce rentgenového záření

Prochází-li rentgenové záření látkou, dochází k jeho zeslabení (absorpci), a to v důsledku procesů, které lze podle mechanismu vzniku kvalitativně rozdělit na vlastní absorpci (fotoelektrickou absorpci), koherentní (Rayleighův) a nekoherentní (Comptonův) rozptyl. Kvalitativně lze absorpci monochromatického rentgenového záření o vlnové délce λ vrstvou látky o tloušťce d a hustotě ρ popsat vztahem

$$I = I_0 e^{-\mu\rho d} \ ,$$

kde I_0 je intenzita rentgenového záření před dopadem na látku, I je intenzita rentgenového záření po průchodu látkou a μ je hmotnostní absorpční koeficient látky.

Hmotnostní absorpční koeficient μ nezávisí na fyzikálním ani chemickém stavu látky, tj. nezávisí na skupenství ani krystalické formě látky a je dán pouze jednotlivými druhy atomů látky. V případě chemických sloučenin nebo směsí je výsledný hmotnostní absorpční koeficient μ_{ABC} pouhým součtem hmotnostních absorpčních koeficientů atomů prvků A, B a C, ze kterých se látka skládá, a lze jej vyjádřit jako

$$\mu_{\mathrm{ABC}} = X_{\mathrm{A}}\mu_{\mathrm{A}} + X_{\mathrm{B}}\mu_{\mathrm{B}} + X_{\mathrm{C}}\mu_{\mathrm{C}} \ ,$$

kde X_A, X_B, X_C jsou hmotnostní zlomky prvků A, B, C v dané sloučenině nebo směsi a μ_A, μ_B, μ_C jejich hmotnostní absorpční koeficienty. Určitá hodnota hmotnostního absorpčního koeficientu platí vždy pouze pro jedinou vlnovou délku rentgenového záření, přičemž pro jinou, byť velice blízkou vlnovou délku, může být jeho hodnota velmi odlišná.

1.1.3.1.1 Vlastní absorpce (fotoelektrická absorpce)

Při vlastní absorpci fotonu rentgenového záření dochází k vytržení vnitřního elektronu z atomu, tj. k fotoionizaci atomu. Jedná se tak vlastně o vytvoření počátečního stavu pro následnou emisi fotonu charakteristického rentgenového záření.

1.1.3.1.2 Koherentní (Rayleighův) rozptyl

O koherentním rozptylu hovoříme v případě, kdy foton rentgenového záření po průchodu látkou mění svoji dráhu nikoliv však svoji energii. Vysvětluje se pružnou srážkou fotonu rentgenového záření s elektronem, který se rozkmitá se stejnou frekvencí, jako má dopadající foton rentgenového záření a stane se tak zdrojem elektromagnetického vlnění se stejnou vlnovou délkou. Liší se pouze amplituda tohoto elektromagnetického vlnění.

1.1.3.1.3 Nekoherentní (Comptonův) rozptyl

O nekoherentním rozptylu hovoříme v případě, kdy foton rentgenového záření po průchodu látkou mění svoji dráhu a zároveň i svoji energii. Vysvětluje se pružnou srážkou fotonu rentgenového záření s elektronem, kterému předá část své energie, takže energie rentgenového fotonu je po srážce menší. Tuto ztrátu energie můžeme vyjádřit rozdílem vlnových délek $\Delta\lambda$ fotonu rentgenového záření po srážce (λ') a před srážkou (λ), pro který platí

$$\Delta\lambda = \lambda' - \lambda = \frac{h}{m_e c}(1 - \cos\theta),$$

kde h je Planckova konstanta, c je rychlost světla, m_e je hmotnost elektronu a 2θ je úhel mezi směry dopadajícího a rozptýleného fotonu rentgenového záření. V praxi se nejčastěji setkáváme s Comptonovým rozptylem při měření v oblasti vlnových délek odpovídajících charakteristickému rentgenovému záření anody rentgenové lampy. Čára odpovídající charakteristickému záření rentgenové lampy je ve spektru přítomná vždy a často bývá doprovázená další čarou, posunutou k delším vlnovým délkám, která vznikla právě Comptonovým efektem z charakteristické čáry anody rentgenové lampy.

Zda při interakci rentgenového záření převažuje koherentní či nekoherentní rozptyl je dáno energií rentgenového fotonu v porovnání s vazebnou energií elektronů v látce. Jsou-li tyto energie porovnatelné, převažuje koherentní rozptyl. Pokud je energie rentgenového fotonu podstatně vyšší, pak převládá nekoherentní rozptyl.

1.1.3.2 Meziprvkové ovlivnění v reálných látkách

Při interakci rentgenového záření s reálnými látkami, které jsou ve většině případů sloučeninami nebo směsmi atomů různých prvků, dochází ke všem dosud popsaným jevům. Dochází k nim však současně pro atomy všech prvků a jednotlivé děje se tak vzájemně prolínají a ovlivňují. Rovněž rentgenové záření nemá v reálném vzorku nebo prostoru spektrometru jen jednu vlnovou délku, ale vyskytují se zde vlnové délky charakteristických rentgenových záření všech prvků přítomných ve vzorku a případně i prvků, používaných při konstrukci přístroje.

Kromě již diskutovaných jevů se jako výsledek jejich vzájemného působení při rentgenové spektrální analýze uplatňují zejména spektrální interference, vzájemné přibuzování a vzájemná absorpce.

O spektrální interferenci mluvíme tehdy, když stejnou vlnovou délku (v rámci rozlišovací schopnosti přístroje), jako má námi měřený prvek, má některý z dalších prvků, přítomných ve vzorku. U moderních spektrometrů se jedná vždy o čáru jiné série nebo jiného řádu spektra. Rentgenové záření rušícího prvku se přičte k námi měřenému rentgenovému záření, které se tak jeví jako zesílené. Zesílení nezávisí na koncentraci stanovovaného prvku, ale je závislé pouze na koncentraci rušivého prvku.

Přibuzováním máme na mysli případ, kdy je přítomen prvek, jehož charakteristické rentgenové záření má větší energii než absorpční hrana stanovovaného prvku. Námi stanovovaný prvek je pak buzen nejen primárním rentgenovým zářením rentgenové lampy, ale též charakteristickým rentgenovým zářením rušivého prvku. Dochází tak k nárůstu intenzity charakteristického rentgenového záření měřeného prvku, přičemž jeho intenzita je větší, než by odpovídalo koncentračnímu obsahu měřeného prvku. Zesílení intenzity je závislé jak na obsahu měřeného prvku, tak i na obsahu rušícího prvku. Nejsilněji přibuzuje prvek, jehož charakteristické rentgenové záření leží nejblíže na krátkovlnné straně absorpční hrany stanovovaného prvku.

Na absorpci charakteristického rentgenového záření stanovovaného prvku se podílejí všechny prvky obsažené ve vzorku, jejichž absorpční hrana je delší než vlnová délka analytické čáry měřeného prvku. Nejsilněji absorbuje prvek, jehož absorpční hrana leží nejblíže na dlouhovlnné straně analytické čáry. Absorpční vlivy jsou úměrné koncentraci ovlivňovaného i rušivého prvku.

1.1.3.3 Difrakce rentgenového záření

V případě, že rentgenové záření dopadá na krystalickou látku, kterou lze charakterizovat jako pravidelné prostorové uspořádání atomů látky na dlouhou vzdálenost, dochází vedle zmíněných interakcí rentgenového záření s látkou i k jevu, známému jako difrakce. Tento jev má nesmírný význam jak pro studium vlastností rentgenového záření, tak pro analýzu krystalických látek samotných.

Difrakce rentgenové záření na krystalické látce je vlastně výsledkem dvou fyzikálních jevů. Jedním z nich je pružný (Rayleighův) rozptyl dopadajícího rentgenového záření na atomech látky, při němž se každý atom látky stává zdrojem elektromagnetického vlnění se stejnou vlnovou délkou, jakou má dopadající rentgenové záření. Při pružném rozptylu tedy mají elektromagnetické vlny rozptýlené (vyzařované) jednotlivými atomy neměnný fázový rozdíl, neboť atomy tvoří množinu koherentních zdrojů. Kromě toho, v krystalických látkách, kde jsou meziatomové vzdálenosti srovnatelné s vlnovou délkou rozptýleného rentgenového záření, pak může nastat mezi rozptýlenými elektromagnetickými vlnami pozorovatelný interferenční jev, projevující se koncentrací rozptýlené elektromagnetické energie (rentgenového záření) v určitém směru, tedy vznikem difrakčního maxima.

Difrakci rentgenového záření (vlnění) na krystalech lze interpretovat také jako odraz těchto elektromagnetických vln od rovnoběžných atomových rovin krystalu charakterizovaných Millerovými indexy (hkl). Difrakce pak nastává pouze tehdy, je-li dráhový rozdíl vln odražených od sousedních rovnoběžných krystalových rovin roven celistvému počtu vlnových délek λ dopadajícího rentgenového záření. Výše uvedené skutečnosti popisuje známá Braggova rovnice

$$2d_{(\mathrm{hkl})} \sin\theta = n\lambda,$$

kde n je řád difrakce ($n = 1, 2, 3, \ldots$), θ je Braggův úhel dopadu rentgenového vlnění na systém rovnoběžných krystalových rovin (hkl), $d_{(\mathrm{hkl})}$ je mezirovinná vzdálenost rovin (hkl) a λ je vlnová délka dopadajícího rentgenového záření. Není-li splněna podmínka daná Braggovou rovnicí, nedojde ke vzniku difrakcí, neboť při odrazu vln budou vznikat různé dráhové rozdíly odražených vln, tj. nenastane jejich konstruktivní interference.

Podrobnější informace o charakteru rentgenového záření, jeho interakcích s látkou a meziprvkovém ovlivnění lze nalézt v monografiích [1], [2], [3], [4].

1.2 Zdroje rentgenového záření pro XRF a XRD analýzy

Jako zdroje rentgenového záření pro techniky XRF a XRD nejčastěji slouží rentgenové lampy. Jsou to v podstatě vakuové trubice se dvěma elektrodami, katodou a anodou, mezi kterými je vysoké napětí až 60 kV. Katoda je tvořena přímo žhaveným wolframovým vláknem, jež termoemisí emituje elektrony, které jsou vysokým napětím urychlovány směrem k anodě vyrobené z materiálu, jehož rentgenové záření chceme vybudit. Po dopadu elektronů na anodu se malá část (~ 5%) jejich energie přemění na spojité a charakteristické rentgenové záření materiálu anody, které z rentgenky vychází skrze beryliové okénko. Podstatná část energie urychlených elektronů je však absorbována a přeměněna na teplo, které je nutné z rentgenové lampy odvádět chladicí vodou, aby nedošlo k jejímu poškození.

1.3 Detekce rentgenového záření

K detekci rentgenového záření, tj. určení intenzity (počtu fotonů) detekovaného rentgenového záření pro zvolenou vlnovou délku, která projde do detektoru, lze použít plynové detektory, scintilační detektory nebo polovodičové detektory. Rozhodujícími parametry detektorů jsou účinnost v oblasti měřených vlnových délek a množství detekovaných fotonů za jednotku času (nebo obráceně, doba mezi dvěma po sobě jdoucími detekovanými fotony, tzv. mrtvá doba detektoru), případně jejich proporcionalita a rozlišení. Detektory tedy slouží k převedení detekovaného rentgenového záření na elektrické impulzy, jež mohou být zaznamenávány, počítány a dále elektronicky zpracovávány.

1.3.1 Plynový (proporcionální) detektor

Jeho konstrukce je tvořena kovovým válcem zapojeným jako katoda elektrického obvodu, v jehož ose je napnuté tenké kovové vlákno zapojené jako anoda. Prostor mezi elektrodami je vyplněn směsí dvou plynů, detekčního (obvykle Ar, Kr nebo Xe) a zhášecího (CH_4 nebo CO_2). Ve stěně válce je vstupní okénko, jímž do detektoru vstupují fotony detekovaného rentgenového záření. Pro krátkovlnná rentgenová záření bývá vyrobeno z Al nebo Be, pro dlouhovlnná pak z pokovené mylarové nebo teflonové fólie o tloušťkách v jednotkách μm. Základním procesem v plynovém detektoru je ionizace plynu fotonem rentgenového záření, při níž vzniká pár nabitých částic, elektron a iont, s určitými počátečními kinetickými energiemi. Dopadem nabitých částic (zejména elektronu) na elektrody dojde ke vzniku elektrického pulzu, jenž je zaregistrován v elektrických obvodech měřicí elektroniky. Dále je nutné, aby ionizovaný plyn co nejrychleji rekombinoval zpět na neutrální atomy, čemuž napomáhá zhášecí plyn, neboť pokud by byl plyn ionizován při dopadu dalšího rentgenového fotonu, tak ten by nebyl zaregistrován.

V případě vhodně zvoleného vysokého napětí mezi anodou a katodou plynového detektoru jsou elektrony vzniklé ionizací urychlovány tímto napětím tak, že dosáhnou kinetické energie dostatečné pro sekundární ionizaci dalších atomů plynu. Velikost sekundární ionizace, a tím i výstupního elektrického pulzu, je pak úměrná energii absorbovaného fotonu rentgenového záření, čímž dostáváme proporcionální plynový detektor. Plynové detektory bývají buď v provedení zataveném (trvalá plynová náplň) nebo průtokovém (plynová náplň se neustále obnovuje).

1.3.2 Scintilační detektor

Scintilační detektor se skládá ze dvou částí, zapouzdřeného scintilačního krystalu a fotonásobiče. Scintilační krystal jodidu sodného aktivovaného thaliem, NaI(Tl), převádí rentgenové záření na záření ve viditelné oblasti spektra (410 – 420 nm), jež je přivedeno do fotonásobiče, kde vzniká elektrický impulz. Detektor se chová proporcionálně, to znamená, že intenzita výstupních elektrických pulzů z fotonásobiče je úměrná energii absorbovaného rentgenového záření. Celková účinnost detekce rentgenového záření scintilačním detektorem je menší než u plynových detektorů a scintilační detektory jsou vhodné pro detekci krátkovlnného rentgenového záření.

1.3.3 Polovodičový detektor

Polovodičový detektor je vyroben z křemíku, germania nebo jiného polovodičového materiálu tak, že na jeho přední straně je tenká (~ 20 nm) Au vrstvička, která je zapojena jako katoda a na opačném konci je sběrná elektroda zapojená jako anoda. Mezi obě elektrody je přiloženo vysoké napětí 1500 V. Foton detekovaného rentgenového záření projde vstupním beryliovým okénkem, pronikne do těla detektoru a vytvoří v něm páry elektron-díra, přičemž počet elektronů závisí na energii absorbovaného fotonu rentgenového záření. Čím je jeho energie větší, tím více elektronů vznikne. V důsledku přiloženého napětí jsou vzniklé elektrony přitahovány k anodě, a když ji dosáhnou, dojde k poklesu napětí a vzniku negativního elektrického pulzu, jehož velikost je úměrná počtu elektronů a tím i energii absorbovaného fotonu rentgenového záření. Takto vzniklé elektrické pulzy jsou následně registrovány měřicí elektronikou.

Podrobnější informace o zdrojích rentgenového záření a jeho detekci lze nalézt v monografiích [1], [2], [3], [4].

1.4 Rentgenová fluorescenční spektrometrie (XRF)

Základy rentgenové spektrální analýzy byly položeny v roce 1913, když H. G. J. Moseley nalezl vztah mezi vlnovou délkou rentgenového záření λ a protonovým číslem prvku Z, který jej vyzařuje, a souvislost mezi intenzitou rentgenového záření prvku a jeho obsahem ve vzorku.

Rentgenová spektrální analýza využívá tzv. sekundární buzení, tj. charakteristické rentgenové záření prvků obsažených v analyzované látce vzniká v důsledku ozařování vzorku analyzované látky energetickým rentgenovým zářením generovaném nejčastěji rentgenovou lampou. Jedná se tedy o rentgenovou fluorescenci, neboť vznik charakteristického rentgenového záření látky vzorku je časově totožný s absorpcí budícího rentgenového záření z rentgenové lampy. Metoda slouží ke kvalitativní i kvantitativní analýze pevných i kapalných látek v širokém koncentračním rozsahu od ~ 1 ppm do 100 %, a lze ji principiálně použít pro všechny prvky počínaje Be.

1.4.1 Rentgenový fluorescenční spektrometr

Rentgenový fluorescenční spektrometr je zařízení, které je schopno vytvářet a registrovat čárové spektrum fluorescenčního rentgenového záření látek. Každý rentgenový fluorescenční spektrometr musí obsahovat zdroj budicího (primárního) rentgenového záření, např. rentgenovou lampu, detektor rentgenového záření, kolimátory sekundárního (fluorescenčního) svazku rentgenového záření, vakuový čerpací systém a odpovídající řídicí a měřicí elektroniku.

Klasický rentgenový fluorescenční spektrometr funguje tak, že na vzorek dopadá energie ve formě primárního rentgenového záření z rentgenové lampy a její absorpcí ve vzorku dochází k vybuzení charakteristického rentgenového záření atomů prvků obsažených ve vzorku analyzované látky. Vzniklé charakteristické fluorescenční rentgenové záření v sobě nese informaci o kvalitativním (vlnové délky, resp. energie spektrálních čar) a kvantitativním (četnost fotonů, resp. intenzity spektrálních čar) prvkovém složení vzorku analyzované látky. Podle toho, jak je fluorescenční rentgenové záření dále zpracováváno, dělíme spektrometry na:

- Energiově disperzní (EDXRF) – fluorescenční rentgenové záření vycházející ze vzorku dopadá jako celek na detektor o vysoké proporcionalitě odezvy, který registruje absorbované fotony charakteristického rentgenového záření. Signál detektoru je pak v multikanálovém analyzátoru rozdělen podle amplitudy pulzů, jež odpovídá energii registrovaného fotonu rentgenového záření, do diskrétních energetických intervalů. Četnost fotonů rentgenového záření příslušející určité amplitudě pulzu pak odpovídá intenzitě rentgenového záření dané spektrální čáry.

- Vlnově disperzní (WDXRF) – fluorescenční rentgenové záření vycházející ze vzorku dopadá na analyzační monokrystal o známé mezirovinné vzdálenosti $d_{(hkl)}$, kde je difrakcí rozkládáno na jednotlivé vlnové délky pod příslušnými úhly θ. Fotony difraktovaného charakteristického rentgenového záření o zvolené vlnové délce λ pak dopadají do detektoru, který je registruje ve formě pulzů, jejichž četnost odpovídá intenzitě charakteristického rentgenového záření o dané vlnové délce.

1.4.3 Kvalitativní a kvantitativní analýza prvkového složení látek

Výsledkem měření vzorku látky na rentgenovém fluorescenčním spektrometru je závislost intenzit spektrálních čar fluorescenčního rentgenového záření vzorku analyzované látky na vlnové délce, respektive energii, tedy charakteristické rentgenové spektrum. Jelikož každá látka je složena z atomů prvků a každý prvek má jedinečné spektrum charakteristického rentgenového záření, je možné provést kvalitativní analýzu prvkového složení daného vzorku látky tím, že porovnáme naměřené vlnové délky, respektive energie spektrálních čar fluorescenčního rentgenového záření vzorku analyzované látky s databází vlnových délek, respektive energií spektrálních čar charakteristického rentgenového záření jednotlivých prvků.

Rentgenová fluorescenční spektrometrie je povrchově citlivá technika, neboť informační hloubka je dána únikovou hloubkou fluorescenčního rentgenového záření měřeného prvku ze vzorku analyzované látky. Informační hloubka tak silně závisí nejen na energii vybuzeného fluorescenčního rentgenového záření měřeného prvku, ale také na složení látky, skrze kterou toto rentgenové záření musí projít, než je detekováno. Obecně tato úniková hloubka leží mezi ~ 100 nm (pro měkké rentgenové záření) a ~ 1000 μm (pro tvrdé rentgenové záření). Takže pro správnou interpretaci XRF analýz objemových materiálů je nezbytné, aby prvkové složení objemu materiálu bylo stejné jako prvkové složení analyzované povrchové vrstvy, tj. analyzovaný vzorek látky musí být vysoce homogenní.

Rentgenová fluorescenční spektrometrie je tradičně používána jako relativní analyzační technika. To znamená, že pro převedení naměřených intenzit charakteristických spektrálních čar na koncentrace prvků ve vzorku analyzované látky jsou potřeba kalibrační standardy s vhodným koncentračním rozsahem prvkového složení a stejnými povrchovými parametry a mikrostrukturou jako má vzorek analyzované látky. V prvním kroku jsou nejprve změřeny intenzity fluorescenčního rentgenového záření těchto standardů, vyrobených z referenčních materiálů, jejichž složení známe s dostatečnou přesností, a získaná závislost intenzity fluorescenčního záření daného prvku na jeho koncentraci v použitých standardech je tzv. kalibrační křivka daného prvku. Pro jednoduché aplikace, např. analýzu objemových vzorků látek s malými změnami v prvkovém složení postačují většinou lineární aproximace kalibrační křivky. V druhém kroku je pak možné ze získané kalibrační křivky interpolací stanovit koncentraci analyzovaného prvku v neznámém vzorku s podobným složením, stejnými povrchovými parametry a mikrostrukturou, změřeném za stejných podmínek jako použité standardy. Pro velké rozsahy prvkového složení musíme zahrnout efekty meziprvkového ovlivnění (vzájemná absorpce fluorescenčního rentgenového záření a přibuzování), které pak vedou ke koncentračně závislé směrnici analyzační křivky.

Kdykoli jsou však (certifikované) referenční materiály nedostupné, nebo se charakter vzorků analyzované látky liší od referenčních standardů, jako např. v případě tenkých vrstev či nových nanomateriálů, je nezbytné použít metody kvantifikace založené na metodě fundamentálních parametrů, vyvinuté Crissem a Birkssem v roce 1968. Cílem této metody je matematické stanovení meziprvkového ovlivnění při kvantitativní rentgenové fluorescenční analýze. Kvantitativní prvková analýza metodou fundamentálních parametrů umožňuje, aby za předpokladu, že jsou známy přístrojové faktory jako propustnost a detekční účinnost rentgenového spektrometru pro daný prvek, mohla být rentgenová fluorescenční spektrometrie používána jako absolutní technika. Zmíněné přístrojové faktory přitom mohou být relativně snadno získány měřením vzorků čistých látek, a jakmile jsou známy, lze matematicky spočítat intenzitu kterékoliv spektrální čáry charakteristického fluorescenčního rentgenového záření látky o daném kvantitativním prvkovém složení pomocí fundamentálních parametrů (fluorescenčního výtěžku, absorpčních koeficientů a spektra rentgenové lampy). Tento přístup může být rovněž použit v opačném směru, tedy k výpočtu kvantitativního prvkového složení vzorku látky z naměřených intenzit jeho charakteristického fluorescenčního rentgenového spektra. V tomto případě spočívá aplikace metody fundamentálních parametrů v teoretickém výpočtu intenzit fluorescenčního rentgenového záření pro modelový vzorek o předpokládaném koncentračním složení a srovnáním vypočtených intenzit s intenzitami naměřenými. V dalších krocích pak postupně korigujeme složení modelového vzorku, než získáme blízkou shodu mezi vypočtenými a naměřenými intenzitami spektrálních čar charakteristického rentgenového záření analyzovaného vzorku látky. Poslední použité koncentrace ve výpočtu je pak možno považovat za skutečné složení vzorku.

Při analýze tenkých vrstev je používání metody fundamentálních parametrů vlastně jediným vhodným způsobem jak stanovit jejich kvantitativní prvkové složení, neboť kalibrační standardy s podobným kvantitativním prvkovým složením a tloušťkou nejsou většinou dostupné. Ve srovnání s tradiční kalibrační procedurou je používání metody fundamentálních parametrů navíc rychlé a laciné. Metoda fundamentálních parametrů používaná v software FP-Multi od firmy PANalytical počítá rentgenovou fluorescenci spektrálních čar K- a L-série na základě excitace primárním a sekundárním rentgenovým zářením, a to včetně započtení vlivu multivrstev. Rentgenová fluorescence pro spektrální čáry M-série, excitace fotoelektrony a terciální rentgenová fluorescence v ní nejsou zohledněny [5].

Podrobnější informace o rentgenové fluorescenční spektrometrii a analýze prvkového složení látek lze nalézt v monografiích [1], [2], [3], [4].

1.5 Rentgenová difraktometrie (XRD)

Rentgenová difraktometrie (XRD) je univerzální, nedestruktivní analytická metoda, která umožňuje kvalitativně i kvantitativně analyzovat pevnou látku z hlediska její struktury, a to na základě jejího difrakčního projevu, získaného při působení monochromatického rentgenového záření na vzorek dané pevné látky.

1.5.1 Rentgenový difraktometr

Rentgenový difraktometr je zařízení, které je schopno vytvářet a registrovat difrakční projev různých krystalických forem látek, tzv. fází, obsažených v analyzovaném vzorku pevné látky. Každý rentgenový difraktometr musí obsahovat zdroj vhodného monochromatického rentgenového záření (rentgenovou lampu), detektor rentgenového záření a mechanismus, zajišťující pohyb detektoru, nebo vzorku a detektoru, vzhledem k primárnímu svazku rentgenového záření, tzv. goniometr. Dále musí obsahovat clony primárního a difraktovaného svazku, zabezpečující definované měřicí podmínky, filtr k odfiltrování β složky charakteristického rentgenového záření a odpovídající řídicí a měřicí elektroniku.

Aby mohla být doba k registraci jednoho bodu difrakčního záznamu co nejvíce zkrácena, používá se buďto fokusační (Seemannovo-Bohlinovo) nebo semifokusační (Braggovo-Brentanovo) uspořádání zdroje rentgenového záření, analyzovaného vzorku a detektoru. Díky fokusaci se tak dosahuje vysoké intenzity difraktovaného rentgenového záření dopadajícího do detektoru a vysoké rozlišovací schopnosti přístroje.

- Difraktometr s Braggovým-Brentanovým uspořádáním patří k nejběžnějším typům difraktometrů pro strukturní analýzu polykrystalických látek. Vzorek látky je umístěn v ose goniometru tak, že jeho povrch je tečný k fokusační kružnici, jejíž poloměr se mění v závislosti na natočení vzorku kolem osy goniometru, přičemž vzdálenost detektoru od vzorku se nemění. Difraktované paprsky se pak fokusují na kružnici, jejíž poloměr je roven vzdálenosti osy goniometru od ohniska rentgenové lampy. Detektor difraktovaného záření se pohybuje podél této kružnice dvojnásobnou úhlovou rychlostí než vzorek. To tedy znamená, že dopadající svazek i svazek difraktovaného záření svírají s povrchem vzorku stejný úhel rovný Braggovu úhlu θ pro určitou osnovu rovin. Při této konfiguraci se tedy na dané difrakci s Braggovým úhlem θ_{hkl} podílejí pouze ty krystality, jejichž roviny {hkl} jsou rovnoběžné s povrchem vzorku.

- V případě Seemannovy-Bohlinovy geometrie dopadá monochromatizovaný svazek rentgenového záření z rentgenové trubice na vzorek pod pevně nastaveným úhlem ψ, jehož velikost se může měnit v intervalu $\langle 0°, 10° \rangle$. Difraktované svazky jsou fokusovány na fokusační kružnici, podél níž se pohybuje detektor, přičemž se jeho vzdálenost od vzorku mění. Malý úhel ψ natočení vzorku vůči dopadajícímu svazku záření má za následek jednak malou hloubku pronikání dopadajícího rentgenového záření pod povrch vzorku a jednak ozáření velké plochy povrchu vzorku. Oba tyto efekty jsou příhodné pro studium struktury povrchových vrstev nebo struktury tenkých vrstev nanesených na různých substrátech. Změnou úhlu ψ můžeme vybírat různé skupiny krystalitů podílejících se na difrakci, neboť při daném Braggově úhlu θ_{hkl} difraktují pouze ty krystality, jejichž roviny {hkl} svírají s povrchem úhel o velikosti $\theta_{\mathrm{hkl}} - \psi$. Tím je možné sledovat rozdělení orientací krystalitů v tenkých vrstvách, případně závislost mezirovinných vzdáleností na orientaci krystalitů u povrchových vrstev podrobených makroskopickému napětí.

- U moderních difraktometrů je pak možné pro analýzu tenkých vrstev modifikovat klasické Braggovo-Brentanovo uspořádáním na tzv. difrakci pod malým úhlem či metodu paralelního svazku, kdy kvůli menší hloubce průniku rentgenového záření do vzorku a většímu efektivnímu signálu od tenké vrstvy necháme na vzorek dopadat rentgenové záření pod malým úhlem v intervalu $\langle 0{,}5°, 10° \rangle$, podobně jako v případě Seemannovy-Bohlinovy geometrie. Na rozdíl od ní se však při záznamu intenzity difraktovaného záření pohybuje pouze detektor a vzorek i rentgenová lampa zůstávají v klidu. Jelikož tak dochází k silné defokusaci svazku difraktovaného záření (k udržení fokusace by se musel detektor od vzorku vzdalovat a zase přibližovat), a tím i výraznému poklesu intenzity difraktovaného záření, je do difraktovaného svazku umístěn kolimátor tvořený sadou dlouhých rovnoběžných desek kolmých k difrakční rovině. Tak se vlastně vytvoří paralelní svazek difraktovaného záření, jenž je následně snímán detektorem. Pokles intenzity difraktovaného záření je částečně kompenzován větší ozářenou plochou vzorku a delší drahou dopadajícího rentgenového záření v tenké vrstvě.

1.5.2 Kvalitativní a kvantitativní analýza struktury látek

Výsledkem měření vzorku pevné látky na rentgenovém difraktometru je tzv. difrakční záznam (difraktogram) představující závislost intenzity difraktovaného záření I na Braggově úhlu θ. Jeho vyhodnocením získáme parametry, jež se přímo vztahují k reálné struktuře analyzované polykrystalické pevné látky. Jsou to:

- polohy difrakčních linií 2θ → mezirovinné vzdálenosti d → mřížkové konstanty (a, b, c, α, β, γ),
- intenzity difrakčních linií → odchylky od pravidelného uspořádání, přednostní orientace (textura),
- šířky difrakčních linií → velikost koherentně difraktujících oblastí a mikrodeformace,
- tvar difrakčních linií.

Srovnáním naměřeného difraktogramu (z hlediska mezirovinných vzdáleností difrakčních linií d a jejich intenzit I) se standardy známých krystalických látek obsažených např. v mezinárodní databázi PDF-4+, vydávané organizací International Centre for Diffraction Data (Pennsylvania, USA) [6], můžeme provést kvalitativní fázovou analýzu změřeného vzorku pevné látky, tj. stanovit jeho fázové složení. Základem této rentgenové databáze PDF-4+ je mnohatisícový soubor karet, z nichž každá popisuje jednu konkrétní krystalickou látku z hlediska mezirovinných vzdáleností, relativních intenzit, Millerových indexů, typu krystalické mřížky a jejich mřížkových konstant a podobně.

Po stanovení fázového složení analyzované látky je také možno využít vhodné difrakční linie identifikovaných fází ve změřeném difrakčním záznamu ke kvantifikaci těchto fází. Množství fáze v analyzovaném vzorku je úměrné integrální intenzitě její difrakční linie (ploše pod difrakční linií). Pro stanovení množství dané fáze v analyzovaném vzorku však musí být nejprve provedena kalibrace rentgenového difraktometru a použitých měřicích parametrů s pomocí standardů obsahujících známá množství dané fáze.

Následnou hlubší analýzou získaných parametrů změřeného difrakčního záznamu můžeme stanovit i další charakteristiky analyzované polykrystalické pevné látky jako např. parametry krystalické mřížky, velikost koherentně difraktujících oblastí („velikost zrn“), přednostní orientaci (texturu), mikrodeformaci a případně i stanovit typ a charakter defektů (např. dislokace, vakance, intersticiální atomy, vrstevnaté chyby).

V případě aplikace XRD pro strukturní analýzu tenkovrstvých vzorků je však důležité si uvědomit, že XRD dává integrovanou informaci z celé tloušťky vrstvy a často také substrátu, je-li tloušťka vrstvy < 5—10 μm. Přesnost XRD analýzy je však obvykle dostačující pro obecné určení fázového složení, růstové textury, mřížkových parametrů či makropnutí analyzovaných tenkovrstvých vzorků. Samotné rozšíření difrakčních linií, korigované na přístrojové rozšíření, pak může být použito k odhadnutí „velikosti zrna“ a hustoty defektů, které způsobují nerovnoměrné rozdělení deformací často pozorované ve vrstvách deponovaných PVD technikou.

Podrobnější informace o rentgenové difraktometrii a analýze struktury pevných látek lze nalézt v monografiích [7], [8], [9], [10].

1.6 Použité analyzační přístroje a software

Pro stanovení prvkového složení a struktury čtyř typů nových tenkovrstvých materiálů (viz kapitola 2) vytvářených různými metodami magnetronové depozice byly využívány následující analyzační přístroje:

- Vlnově disperzní rentgenový fluorescenční spektrometr MagiX PRO od firmy PANalytical vybavený 4 kW rentgenovou lampou s Rh anodou, scintilačním detektorem a proporcionálním průtokovým plynovým detektorem, sadou analyzačních monokrystalů (LIF 200, PE 002, PX1, PX3, PX4, PX5) a kolimátorů 150 µm, 550 µm a 400 µm. Po softwarové stránce byl přístroj vybaven softwarem SuperQ 4.0 pro řízení spektrometru, sběr dat a kalibraci, softwarem IQ+ pro bezstandardovou analýzu objemových materiálů a softwarem FP-Multi pro analýzu tenkých vrstev pomocí metody fundamentálních parametrů. Uvedená konfigurace přístroje umožňovala analyzovat prvkové složení pevných látek počínaje B.

- Rentgenový difraktometr X'Pert PRO MPD od firmy PANalytical vybavený 2 kW rentgenovou lampou s Cu anodou, rychlým polovodičovým detektorem X'Celerator, proporcionálním detektorem, sadou divergenčních clon, grafitovým monochromátorem difraktovaného rentgenového záření a kolimátorem difraktovaného záření pro metodu difrakce pod malým úhlem. Po softwarové stránce byl přístroj vybaven softwarem X'Pert Data Collector pro řízení difraktometru a sběr dat, softwarem X'Pert HighScore Plus pro analýzu difrakčních záznamů a vyhodnocení struktury analyzovaných vzorků a databází difrakčních standardů PDF-4+.

1.7 Použitá literatura

[1] E. P. Bertin, Principles and Practice of X-Ray Spectrometric Analysis, 2nd ed., Plenum Press, New York, 1975

[2] Handbook of X-Ray Spectrometry, 2nd ed., Revised and Expanded, edited by R. E. Van Grieken and A. A. Markowicz, Dekker, New York, 2002

[3] R. Jenkins, X-Ray Fluorescence Spectrometry, 2nd ed., A Wiley-Interscience Publication, New York, 1999

[4] V. Helán, Rentgenová spektrometrie Sborník přednášek z kurzu 2 (upravené a doplněné vydání), 2 THETA, Český Těšín, 2005

[5] P. Van De Weijer, D. K. G. Boer, Elemental Analysis of Thin Layers, Philips J. Res. 47 (1993) 247-262

[6] PDF-4+ 2019 (Database), edited by Dr. Soorya Kabekkodu, International Centre for Diffraction Data, Newtown Square, PA, USA, 2019

[7] H. P. Klug, L. E. Alexander, X-ray diffraction Procedures for Polycrystalline and Amorphous Materials, 2nd ed., Wiley-Interscience, New York, 1974

[8] Mario Birkholz, Thin Film Analysis by X-Ray Scattering, Wiley-VCH Verlag GmbH & Co. KGaA, Weinheim, 2006

[9] Defect and Microstructure Analysis by Diffraction, edited by R. L. Snyder, J. Fiala, H. J. Bunge, IUCr series, Oxford University Press, New York, 1999

[10] V. Valvoda, M. Polcarová, P. Lukáč, Základy strukturní analýzy, Karolinum, Praha, 1991

2. Cíle dizertační práce

Předkládaná dizertační práce je zaměřena na analýzu prvkového složení (pomocí metody rentgenové fluorescence) a struktury (pomocí metody rentgenové difrakce) čtyř typů nových tenkovrstvých materiálů vytvářených různými metodami magnetronové depozice.

Jde o následující materiály:

A. Ochranné povlaky Al-Si-N, Al-Ti-O, Si-Zr-O, Si-B-C-N a Al_2O_3 s dostatečnou tvrdostí a vysokou teplotní stabilitou ve vzduchu za velmi vysokých teplot.

B. Otěruvzdorné ochranné povlaky nc-TiC/*a*-C a Mo-C s dostatečnou tvrdostí a nízkým koeficientem tření.

C. Multifunkční vrstvy Al-Cu-O, Zr-Al-O, Al-O-N se zvýšenou odolností proti vzniku trhlin při namáhání.

D. Fotokatalytické vrstvy TiO_2.

Cílem dizertační práce je přispět k objasnění složitých vzájemných vztahů mezi parametry depozičních procesů, prvkovým složením a strukturou vytvořených tenkovrstvých materiálů a jejich vlastnostmi.

3. Výsledky

Z hlediska výsledků je dizertační práce rozdělena do 4 částí (A – D), které obsahují nejdůležitější výsledky získané během mého řádného doktorského studia na katedře fyziky Západočeské univerzity v Plzni v letech 2008 až 2012, a to ve formě 12 vědeckých článků v impaktovaných mezinárodních časopisech.

Část A – Ochranné povlaky Al-Si-N, Al-Ti-O, Si-Zr-O, Si-B-C-N a Al_2O_3 s dostatečnou tvrdostí a vysokou teplotní stabilitou ve vzduchu za velmi vysokých teplot – obsahuje práce:

A-I: J. Musil, M. Šašek, P. Zeman, R. Čerstvý, D. Heřman, J. Han, V. Šatava: Properties of magnetron sputtered Al-Si-N thin films with a low and high Si content.
Surface and Coatings Technology, 2008, roč. 202, č. 15, s. 3485-3493
ISSN: 0257-8972

A-II: J. Musil, V. Šatava, R. Čerstvý, P. Zeman, T. Tölg: Formation of crystalline Al-Ti-O thin films and their properties.
Surface and Coatings Technology, 2008, roč. 202, č. 24, s. 6064-6069
ISSN: 0257-8972

A-III: J. Musil, V. Šatava, P. Zeman, R. Čerstvý: Protective Zr-containing SiO_2 coatings resistant to thermal cycling in air up to 1400 °C.
Surface and Coatings Technology, 2009, roč. 203, č. 10-11, s. 1502-1507
ISSN: 0257-8972

A-IV: P. Zeman, J. Čapek, R. Čerstvý, J. Vlček: Thermal stability of magnetron sputtered Si-B-C-N materials at temperatures up to 1700 °C.
Thin Solid Films, 2010, roč. 519, č. 1, s. 306-311
ISSN: 0040-6090

A-V: J. Musil, J. Blažek, P. Zeman, Š. Prokšová, M. Šašek, R. Čerstvý: Thermal stability of alumina thin films containing γ-Al_2O_3 phase prepared by reactive magnetron sputtering.
Applied Surface Science, 2010, roč. 257, č. 5, s. 1058-1062
ISSN: 0169-4332

Část B – Otěruvzdorné ochranné povlaky nc-TiC/*a*-C a Mo-C s dostatečnou tvrdostí a nízkým koeficientem tření – obsahuje práce:

B-I: J. Musil, P. Novák, R. Čerstvý, Z. Soukup: Tribological and mechanical properties of nanocrystalline-TiC/*a*-C nanocomposite thin films.
Journal of Vacuum Science and Technology A, 2010, roč. 28, č. 2, s. 244-249
ISSN: 0734-2101

B-II: P. Novák, J. Musil, R. Čerstvý, A. Jäger: Coefficient of friction and wear of sputtered a-C thin coatings containing Mo.
Surface and Coatings Technology, 2010, roč. 205, č. 5, s. 1486-1490
ISSN: 0257-8972

Část C – Multifunkční vrstvy Al-Cu-O, Zr-Al-O, Al-O-N se zvýšenou odolností proti vzniku trhlin při namáhání – obsahuje práce:

C-I: J. Blažek, J. Musil, P. Stupka, R. Čerstvý, J. Houška: Properties of nanocrystalline Al–Cu–O films reactively sputtered by DC pulse dual magnetron.
APPLIED SURFACE SCIENCE, 2011, roč. 2011, č. 258, s. 1762-1767

ISSN: 0169-4332

C-II: J. Musil, J. Sklenka, R. Čerstvý: Transparent Zr-Al-O oxide coatings with enhanced resistance to cracking.
Surface and Coatings Technology, 2012, roč. 206, č. 8-9, s. 2105-2109
ISSN: 0257-8972

C-III: J. Musil, R. Jílek, M. Meissner, T. Tölg, R. Čerstvý: Two-phase single layer Al-O-N nanocomposite films with enhanced resistance to cracking.
Surface and Coatings Technology, 2012, roč. 206, č. 19-20, s. 4230-4234
ISSN: 0257-8972

C-IV: J. Musil, J. Sklenka, R. Čerstvý, T. Suzuki, T. Mori, M. Takahashi: The effect of addition of Al in ZrO_2 thin film on its resistance to cracking.
Surface and Coatings Technology, 2012, roč. 2012, č. 207, s. 355-360
ISSN: 0257-8972

Část D – Fotokatalytické vrstvy TiO_2 – obsahuje práci:

D-I: J. Šícha, J. Musil, M. Meissner, R. Čerstvý: Nanostructure of photocatalytic TiO_2 films sputtered at temperatures below 200 °C.
Applied Surface Science, 2008, roč. 254, č. 13, s. 3793-3800
ISSN: 0169-4332

Provedl jsem všechna měření prvkového složení vytvořených tenkovrstvých materiálů, kterými se zabývají práce A-I, A-II, A-III, A-V, B-I, B-II, C-I, C-II a C-IV. Použil jsem metodu rentgenové fluorescence na vlnově disperzním rentgenovém spektrometru MagiX PRO, a to včetně navržení vhodných kalibračních standardů a stanovení příslušných kalibračních závislostí intenzity fluorescenčního rentgenového záření na množství analyzovaného prvku. Provedl jsem také všechna měření struktury vytvořených tenkovrstvých materiálů, kterými se zabývají práce A-I, A-II, A-III, A-IV, A-V, B-I, B-II, C-I, C-II, C-III, C-IV a D-I. Použil jsem metodu rentgenové difrakce na rentgenovém difraktometru X’Pert PRO MPD včetně stanovení strukturních parametrů analyzovaných tenkovrstvých materiálů. Podílel jsem se na objasnění složitých vzájemných vztahů mezi parametry depozičních procesů, prvkovým složením a strukturou vytvořených tenkovrstvých materiálů a jejich vlastnostmi. Podílel jsem se také na přípravě všech uvedených vědeckých publikací.

3.1 Část A

Ochranné povlaky Al-Si-N, Al-Ti-O, Si-Zr-O, Si-B-C-N a Al_2O_3 s dostatečnou tvrdostí a vysokou teplotní stabilitou ve vzduchu za velmi vysokých teplot

3.1.1 A-I: Properties of magnetron sputtered Al-Si-N thin films with a low and high Si content

Available online at www.sciencedirect.com

ScienceDirect

Surface & Coatings Technology 202 (2008) 3485 – 3493

www.elsevier.com/locate/surfcoat

Properties of magnetron sputtered Al–Si–N thin films with a low and high Si content

J. Musil [a,*], M. Šašek [a], P. Zeman [a], R. Čerstvý [a], D. Heřman [a], J.G. Han [b], V. Šatava [a]

[a] *Department of Physics, Faculty of Applied Sciences, University of West Bohemia, Univerzitní 22, 306 14 Plzeň, Czech Republic*
[b] *Center for Advanced Plasma Surface Technology, SungKyunKwan University, Suwon, Republic of Korea*

Received 26 September 2007; accepted in revised form 17 December 2007
Available online 23 December 2007

Abstract

The article reports on properties of Al–Si–N films with a low ($\leq$10 at.%) and high ($\geq$25 at.%) Si content reactively sputtered using a closed magnetic field dual magnetron system operated in ac pulse mode. The films were sputtered from a composed target (a Si plate fixed by an Al ring with inner diameter $\O_i$=15 or 26 mm). Main attention was devoted to the investigation of a relationship between the structure of the films and their mechanical properties, thermal stability of hardness, and oxidation resistance. It was found that (1) while the films with a low ($\leq$10 at.%) Si content are crystalline (c-(Al–Si–N)), those with a high ($\geq$25 at.%) Si content are amorphous (a-(Al–Si–N)) when sputtered at the substrate temperature T_s=500 °C, (2) both groups of the films exhibit (i) a high hardness H=21 and 25 GPa, respectively, and high values of the oxidation resistance exceeding 1000 °C; 1100 °C (Δm=0 mg/cm^2) and 1300 °C ($\Delta m\approx$0.003 mg/cm^2), respectively, (3) the hardness of a-(Al–Si–N) does not vary with increasing annealing temperature T_a up to 1100 °C even after 4 h, and (4) a high oxidation resistance of c-(Al–Si–N) film with a low (<10 at.%) Si content is due to the formation of a dense, nearly amorphous Al_2O_3 surface layer which is formed in reaction of free Al atoms with ambient oxygen and prevents the fast penetration of oxygen into bulk of the film. Obtained results contribute to understand the effect of Al and Si in the Al–Si–N thin film on its mechanical properties, thermal stability and oxidation resistance.

Keywords: Al–Si–N films; Structure; Mechanical properties; Thermal annealing; Oxidation resistance; Reactive magnetron sputtering

1. Introduction

Recently, it has been recognized and experimentally demonstrated that properties of nanocomposite coatings are determined not only by their structure, elemental and phase composition but also by their nano-morphology, i.e. by the size of grains and the shape of crystallites and volume fraction of the matrix [1–7]. Besides, it has been found that the nano-morphology of a film can affect not only its enhanced properties but also can result in new unique properties. These facts have stimulated a very intensive investigation of hard nc-^{T}MeN/a-Si_3N_4 nanocomposite coatings in the last decade; here ^{T}Me=Ti, V, Cr, Zr, Nb, Mo, Hf, Ta, W, ^{T}MeN is the transition metal nitride, nc- and a- denotes the nanocrystalline and amorphous phase, respectively. Main attention in the field of hard nanocomposite coatings has been concentrated on three problems: (1) the finding of the relationship between the mechanical properties (hardness H, Young's modulus E and elastic recovery W_e), the structure, the phase composition and the nano-morphology, (2) the explanation of the origin of enhanced hardness and (3) the preparation of nanocomposites with maximum hardness H_{max} approaching or even exceeding that of the diamond. The development in this field has been established mainly by the investigation of the third problem. It has been found that the maximum hardness H_{max} is achieved in films with a low ($\leq$10 at.%) Si content when ^{T}MeN grains are surrounded by a-Si_3N_4 tissue phase with thickness of approximately of ~1 to 2 monolayers [8]. The nitride-based nanocomposites of the type nc-^{T}MeN/a-Si_3N_4 with a low ($\leq$10 at.%) Si content are, however, a specific group of nanocomposites exhibiting only some enhanced properties, for instance, the enhanced hardness.

---

[*] Corresponding author. Tel.: +420 377 63 22 00; fax: +420 377 63 22 02.
E-mail address: musil@kfy.zcu.cz (J. Musil).

0257-8972/$ - see front matter © 2008 Published by Elsevier B.V.
doi:10.1016/j.surfcoat.2007.12.024

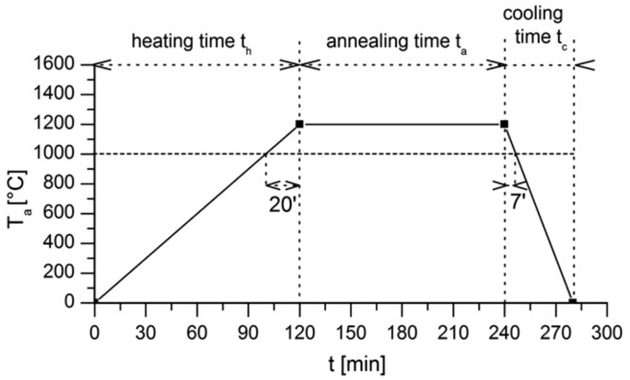

Fig. 1. Schematic diagram of three-step thermal treatment cycle. The cycle without annealing at T_a is called two-step thermal treatment cycle.

However, not only high hardness but also the thermal stability and oxidation resistance of nanocomposites at temperatures above 1000 °C is very important for new advanced applications. The nc-^{T}MeN/a-Si_3N_4 nanocomposites do not meet this requirement due to a low content of the amorphous a-Si_3N_4 phase. Therefore, the nanocomposites have been started to be doped with selected elements such as Al, Y, etc with aim to increase their thermal stability. It has been found that, for instance, the doping of TiN with Al significantly improves its oxidation resistance from ~600 to 850 °C [9]. The thermal stability and oxidation resistance of nc-^{T}MeN/a-Si_3N_4 nanocomposites with a low (≤10 at.%) Si content is limited by a low (<1000 °C) crystallization temperature of the dominating ^{T}MeN phase. Recently, it has been found that the thermal stability and oxidation resistance of the nc-^{T}MeN/a-Si_3N_4 nanocomposites can be easily increased above 1000 °C if these nanocomposites contain a high (≥25 at.%) amount of Si [10–19]. This improvement in thermal stability and oxidation resistance of nc-^{T}MeN/a-Si_3N_4 nanocomposites with a high (>20 at.%) Si content is due to their X-ray amorphous structure which remains stable during thermal annealing up to ~1400 to 1500 °C.

It is expected that similar properties should be achieved also for Al–Si–N thin films. No detailed investigation of the Al–Si–N system has been carried out so far. To our knowledge, only Ti–Si–Al–N [20–22], Ti–Al–V–Si–N [21], Ti–Cr–Al–Si–N [23] nitride thin films with a low (≤10 at.%) Si content have been investigated so far. These systems, however, also do not exhibit the thermal stability and oxidation resistance above 1000 °C because a low amount of Si prevents the formation of amorphous Al–Si based materials [24]. This fact clearly indicates that to understand the role of Al in the film, a simple Al–Si–N system with a high (≥25 at.%) Si content should be investigated at first. Recently, Patscheider et al. [25] has also reported on the investigation of the microstructure and mechanical properties of Al–Si–N coatings with Si ranging in a wide interval from 0 to 23 at.%. The aim of their study was to prepare hard, optically transparent coatings with a hardness exceeding that of Al_2O_3. No thermal stability of mechanical properties and oxidation resistance has been reported.

This article reports on a systematic investigation of the structure, mechanical properties, thermal stability and oxidation resistance of Al–Si–N films with a low (~5 at.%) and high (~40 at.%) Si content with aim to develop new hard coatings with a hardness above 20 GPa and oxidation resistance above 1000 °C.

2. Experimental

Al–Si–N films were reactively sputtered in an $Ar+N_2$ mixture using a closed magnetic field dual magnetron system operated in ac pulse mode generated by a pulse power supply DORA MSS-10 with output power 10 kW (produced in Poland). The repetition frequency f_r of pulses was 2 kHz and the ac frequency inside pulses was 56 kHz. The constant magnetron discharge current I_d was controlled by the duty cycle of 2 kHz pulses which ranged between 15–25% depending on the plasma impedance. Both magnetrons were equipped with the same targets (Ø 50 mm) composed of a Si plate (Ø 28 mm) fixed by an Al ring with inner diameter $Ø_i=15$ or 26 mm. The inner diameter $Ø_i$ controlled the amount of Si in the film: ~5 at.% Si at $Ø_i=15$ mm and ~40 at.% Si at $Ø_i=26$ mm. The Al–Si–N films were prepared under the following conditions: discharge current $I_d=1$ A, substrate bias $U_s=U_{fl}$, substrate temperature $T_s=500$ °C, substrate-to-target distance $d_{s\text{-}t}=100$ mm, partial pressure of nitrogen p_{N2} ranging from 0 to 0.5 Pa and total pressure $p_T=p_{Ar}+p_{N2}=0.7$ Pa; here U_{fl} is the floating potential.

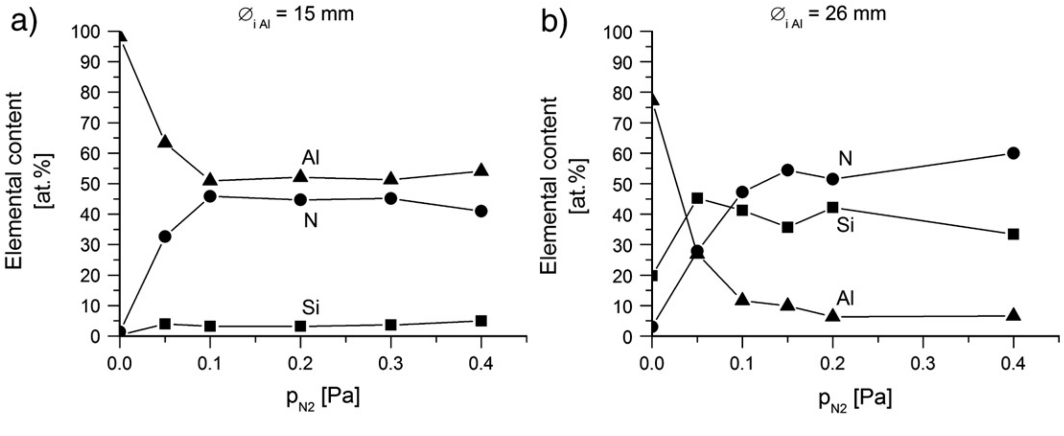

Fig. 2. Elemental composition of the Al–Si–N film with (a) a low (<10 at.%) and (b) high (~40 at.%) Si content as a function of p_{N_2}.

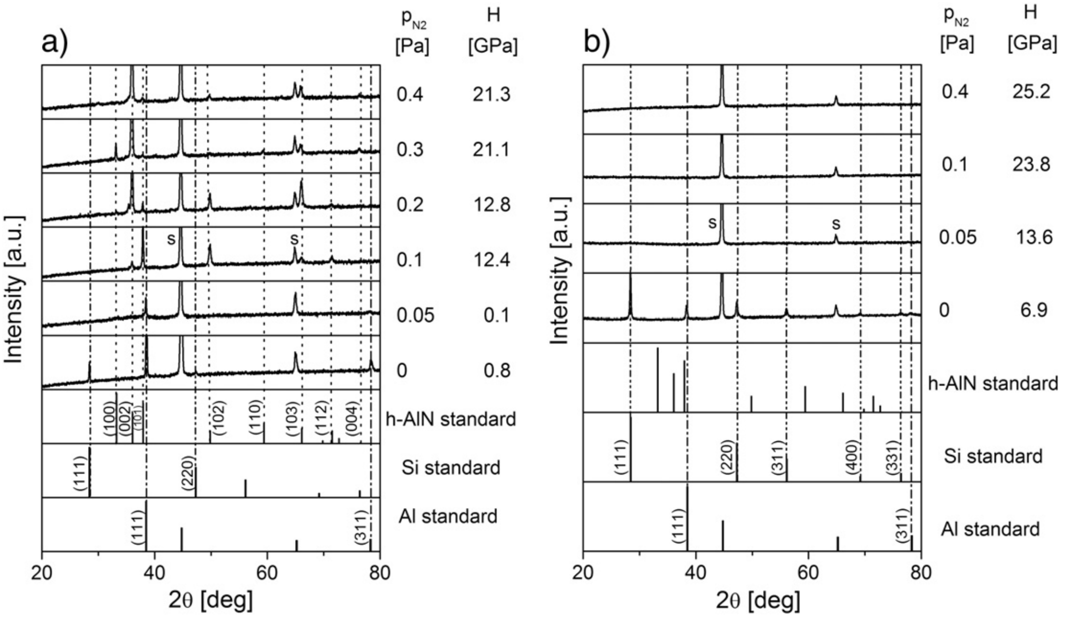

Fig. 3. Evolution of the structure of the Al–Si–N films with (a) a low (<10 at.%) and (b) high (~40 at.%) Si content sputtered on the 15330 steel with increasing p_{N_2} at $T_s = 500$ °C, $U_s = U_{fl}$ and $p_T = 0.7$ Pa.

The Al–Si–N films were deposited onto CSN 15330 steel discs (Ø 25 mm, 5 mm thick), Si(111) wafers ($30 \times 5 \times 0.4$ mm^3) and sintered polycrystalline Al_2O_3 (corundum, $10 \times 10 \times 0.5$ mm^3). The thickness h of the sputtered films ranged from ~2000 to ~5000 nm.

The film thickness and the macrostress σ were measured on films deposited on Si(111) substrates using a stylus profilometer DEKTAK 8. The macrostress σ was determined from the difference in the Si plate curvature before and after the film deposition using a Stoney's formula [26]. The film structure was characterized using an XRD spectrometer PANalytical X'Pert PRO in Bragg–Brentano configuration with CuKα radiation. The elemental composition was determined by X-Ray Fluorescence (XRF) spectroscopy with a PANalytical XRF Spectrometer MagiX PRO with the accuracy of 10% and by Rutherford back-scattering spectrometry (RBS) with the accuracy of 5%. The microstructure was characterized by a high-resolution transmission electron microscope (HRTEM) JEOL JEM-3010. Mechanical properties were determined from load vs. displacement curves measured by a microhardness tester Fischerscope H100 with a Vicker's diamond indenter at load $L = 50$ mN. The oxidation resistance was measured in flowing air (1 l/h) using a symmetrical high-resolution Setaram thermogravimetric system TAG 2400. An annealing cycle consists generally of three steps: (1) heating from RT to a predetermined annealing temperature T_a, sometimes called the heating ramp, (2) annealing at a selected value of T_a and (3) cooling from T_a down to RT, sometimes called the cooling

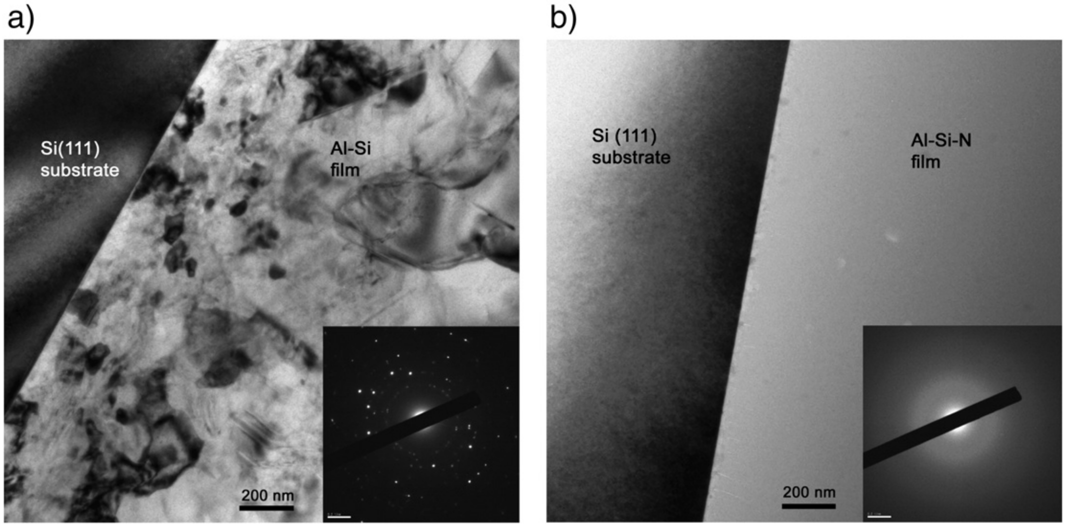

Fig. 4. Cross-section bright-field TEM images of (a) Al–Si and (b) Al–Si–N film sputtered at $I_d = 1$ A, $T_s = 500$ °C, $p_{N_2} = 0$ and 0.1 Pa, respectively, on the Si(111) substrate. The electron diffraction patterns are inserted.

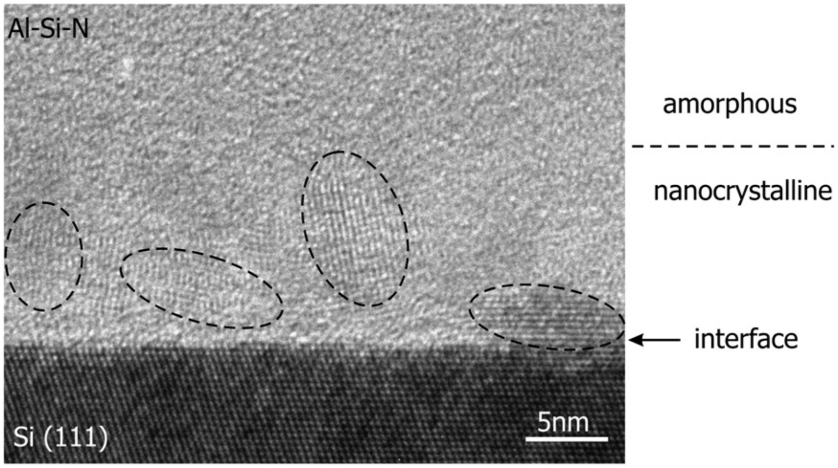

Fig. 5. Bright-field image of the interface region in the cross-section of a Al–Si–N film sputtered at $I_d = 1$ A, $T_s = 500$ °C, $p_{N_2} = 0.1$ Pa and $p_T = 0.7$ Pa (Fig. 4b).

ramp, see Fig. 1. In some experiments, annealing at T_a is omitted, i.e. the temperature is increased to T_a and immediately decreased down to RT. Such thermal annealing is called *two-step thermal treatment cycle*. Thermal annealing experiments were carried out at 10 °C/min heating and 30 °C/min cooling rate, respectively, on substrates coated only on one side. Thermogravimetric curves corresponding to oxidation of the bare substrates were subsequently subtracted and the resulting curves then characterized the oxidation resistance of pure films only, without any substrate effects. The measurements of all the parameters of sputtered Al–Si–N films were performed with an accuracy better than 10%.

3. Results and discussion

3.1. Elemental composition

The elemental composition of the Al–Si–N films is strongly influenced by the partial pressure of nitrogen p_{N2} and the inner diameter $Ø_i$ of the Al fixing ring, see Fig. 2. The amount of Si in the film is low (~5 at.%) when Al ring with $Ø_i = 15$ mm is used (Fig. 2a). From this figure it is clearly seen that (i) in the Al–Si–N films with a low Si content Al dominates over Si for all p_{N2} used and (ii) the Al–Si–N films sputtered at $p_{N_2} \geq 0.1$ Pa exhibit almost the same elemental composition. Based on known values of the formation enthalpies, $\Delta H_{Si_3N4} = -745.1$ kJ/mol and $\Delta H_{AlN} = -318.6$ kJ/mol [27], we assume that N has a higher affinity to Si than to Al and thus the Si_3N_4 phase is formed at first. Because the amount of N is lower than that necessary for the formation of stoichiometric Si_3N_4 and AlN the films should be composed of a mixture of $Si_3N_4 + AlN + Al$. It means that all the sputtered Al–Si–N films with a low Si content contain free Al atoms. Free Al atoms can be easily oxidized resulting in an enhancement of the oxidation resistance; details are given in Section 3.6.2. The amount of Si in the film is high (~40 at.%) when the Al ring with $Ø_i = 26$ mm is used (Fig. 2b). In this case the amount of N is higher than that of Si and Al at $p_{N_2} > 0.1$ Pa and no free Al is expected to be in Al–Si–N films produced at $p_{N_2} > 0.1$ Pa.

3.2. Structure

The developments of the structure of the Al–Si–N films with a low (<10 at.%) and high (~40 at.%) Si content with increasing p_{N2} are shown in Fig. 3.

3.2.1. Al–Si–N films with a low (<10 at.%) Si content

All the films are crystalline. The Al–Si film sputtered at $p_{N_2} = 0$ Pa is polycrystalline with strong Al(111) and weak Al (311), Si(111) and Si(220) X-ray reflections. The low-intensity Si reflections correspond to a low amount of Si in the film. Already a small addition of N_2 to Ar gas leads to a considerable increase (~30 at.%) of N in the film resulting in a strong suppression of Si and Al reflections and in the formation of hexagonal AlN grains, which change the preferred crystallographic orientation from (101) to (002) with increasing p_{N_2}. The Al–Si–N films with no Al(111) reflection produced at $p_{N_2} \geq 0.3$ Pa exhibit the highest hardness $H \approx 21$ GPa.

3.2.2. Al–Si–N films with a high (~40 at.%) Si content

The films are characterized with a polycrystalline Al–Si structure for $p_{N_2} = 0$ Pa and an X-ray amorphous Al–Si–N structure for $p_{N_2} > 0$ Pa on polycrystalline 15330 steel. From Fig. 3 it is clearly seen that already a very small addition of

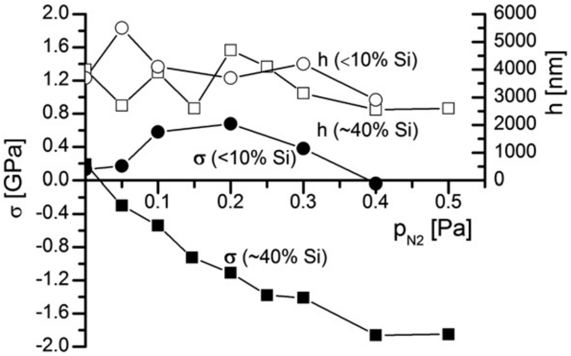

Fig. 6. Macrostress σ in the Al–Si–N films and their thickness *h* as a function of p_{N_2}.

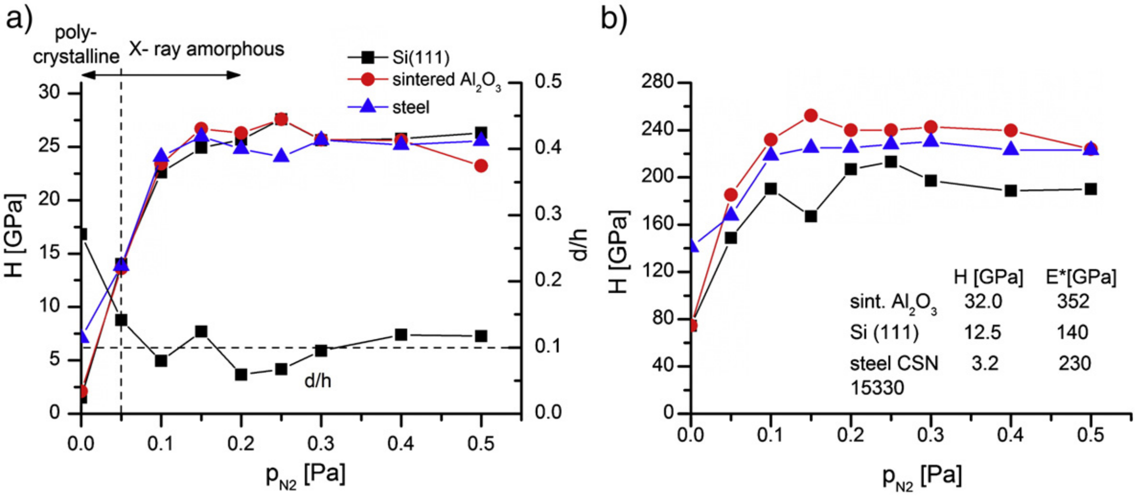

Fig. 7. Developments of (a) hardness H and (b) effective Young's modulus E^* of the Al–Si–N films with a high (~40 at.%) Si content, sputtered on Si(111), steel and sintered Al_2O_3 substrates, with increasing partial pressure of nitrogen p_{N_2}. The ratio d/h in Fig. 7a shows a correctness of the H measurement; d is the indentation depth of diamond indenter and h is the film thickness.

nitrogen ($p_{N_2}=0.05$ Pa) is sufficient to create the X-ray amorphous Al–Si–N film in spite of the fact that the substrate temperature $T_s=500$ °C, used in sputtering, is relatively high.

3.3. Microstructure

The microstructure of Al–Si and Al–Si–N films with a high (~40 at.%) Si content was characterized using bright-field TEM images. The images of cross-section of the Al–Si and Al–Si–N films are displayed in Fig. 4. From these images it is clearly seen that while the Al–Si film exhibits a polycrystalline structure, the Al–Si–N film is completely amorphous. This fact is confirmed by the electron diffraction patterns which are inserted in Figs. 4a and b and also by XRD patterns displayed in Fig. 3b.

In spite of the amorphous structure of the Al–Si–N film sputtered at $p_{N_2}=0.1$ Pa, the film is nanocrystalline near the interface, see Fig. 5. The nanocrystalline region is very thin ~12 nm. The origin of nanocrystallization at the interface is probably due to the substrate; this phenomenon is a subject of experiments being now carried out in our labs.

3.4. Macrostress

The macrostress σ generated in the Al–Si–N films during sputtering strongly depends on both (i) the Si content in the film and (ii) the partial pressure of nitrogen p_{N_2}. This fact is shown in Fig. 6 where the dependence $\sigma=f(p_{N_2})$ in thick (~2500 nm to ~5000 nm) Al–Si–N films with a low (<10 at.%) and high (~40 at.%) Si content is displayed.

The Al–Si–N films with a low (<10 at.%) Si content exhibit a tensile stress $\sigma>0$. On the contrary, the Al–Si–N films with a high (~40 at.%) Si content is in compression stress ($\sigma<0$). The measurement of the elemental composition of the Al–Si–N films produced at different values of p_{N_2} indicates that the increase in compressive stress σ correlates well with the increase of the amount N in the films. Because the formation enthalpy ΔH_f of Si_3N_4 (−745.1 kJ/mol [27]) is higher than that of AlN (−318.6 kJ/mol [27]), the Si_3N_4 phase, which is amorphous (a-Si_3N_4) due to a low deposition temperature ($T_s=500$ °C), is formed at first. The aluminum nitride AlN starts to form at p_{N_2} when all Si is converted into a-Si_3N_4. We believe

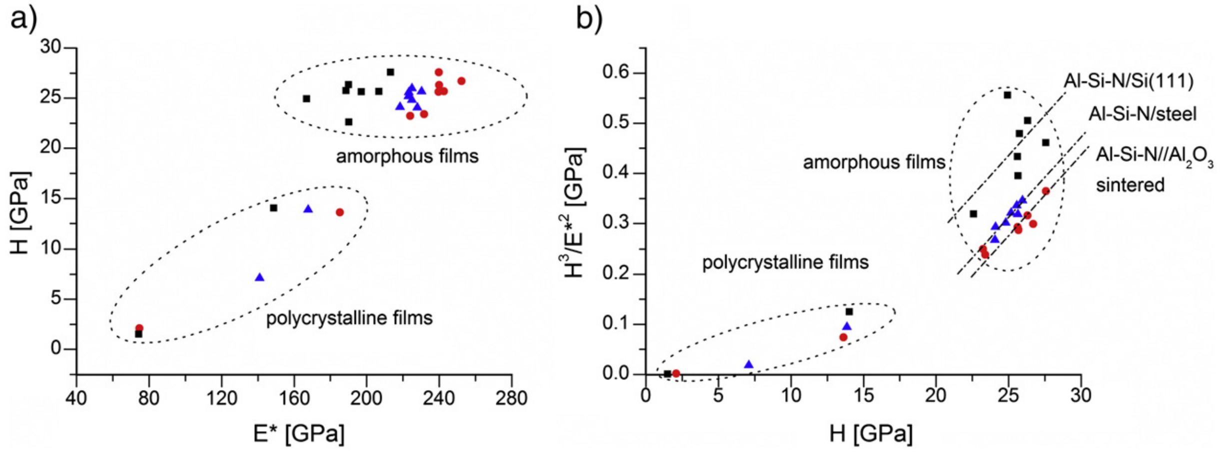

Fig. 8. $H=f(E^*)$ and $H^3/E^{*2}=f(H)$ for the Al–Si–N films with a high (~40 at.%) Si content sputtered on Si(111), steel and sintered Al_2O_3 substrates.

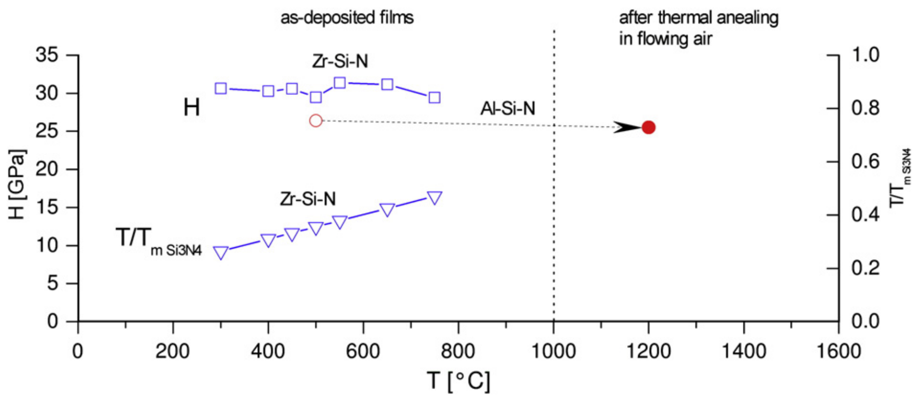

Fig. 9. Hardness H of as-deposited Zr–Si–N films with a high (>20 at.%) Si content sputtered at $I_d = 1$ A, $p_{N_2} = 0.4$ Pa and different values of T_s on the Si(100) substrate and the Al–Si–N film with a high (~40 at.%) Si content sputtered at $p_{N_2} = 0.4$ Pa and $T_s = 500$ °C after its thermal annealing in two-step cycle in flowing air.

that the increase in compressive stress σ is connected with the formation of nitride phases in the Al–Si–N composite films, particularly with an incorporation of AlN grains into an amorphous a-Si_3N_4 matrix. In spite of the increase of the compressive stress σ with increasing p_{N_2}, its saturation value is relatively low, of about −1.8 GPa in the ~3000 nm thick Al–Si–N film. A similar value $\sigma_{max} \approx -1.5$ GPa has been recently measured also for Ti–Si–N films with a high Si content [17].

3.5. Mechanical properties

Basic mechanical properties of materials are (i) hardness H, (ii) effective Young's modulus $E^* = E/(1-\nu^2)$, and (iii) resistance to plastic deformation directly proportional to the ratio H^3/E^{*2} [28]; here E is the Young's modulus and ν is the Poisson's ratio.

In this paper, the mechanical properties of the Al–Si–N films with a high (~40 at.%) Si content are discussed only; for the mechanical properties of the films with a low Si content see, for instance, Ref. [25]. The films were sputtered on Si (111), 15330 steel and sintered Al_2O_3 substrates. The hardness H and effective Young's modulus E^* as a function of p_{N_2} are displayed in Fig. 7. Both H and E^* strongly increase with increasing p_{N_2} up to ~0.1 Pa. The Al–Si–N films sputtered at $p_{N_2} > 0.1$ Pa exhibit almost the same value of $H \approx 25$ GPa. This is a maximum value of H_{max} of the Al–Si–N films sputtered under conditions given in Section 2. It is also necessary to note that the maximum value of H_{max} practically does not depend on the substrate. On the contrary, maximum values of the Young's modulus E^*_f of the Al–Si–N films strongly depend on the substrate. The higher the effective Young's modulus E^*_s of the substrate is, the higher the maximum value of $E^*_{f\,max}$ of the Al–Si–N film is.

The mechanical behavior of materials is determined by a combined action of hardness H and Young's modulus E^* [29–31]. Therefore, it is important to know the interrelationship between H and E^* and the relation between the ratio H^3/E^{*2} and H, see Fig. 8. Three issues can be drawn from Fig. 8a: (1) H approximately increases with increasing E^*, (2) the polycrystalline c-(Al–Si–N) films exhibit a lower hardness ($H \leq 15$ GPa) and (3) the amorphous a-(Al–Si–N) films with almost the same hardness exhibit the lower value of Young's modulus E^*_f in the case when the Young's modulus of the substrate E^*_s is lower; the last fact is also seen in Fig. 7b. Fig. 8b clearly shows that a-

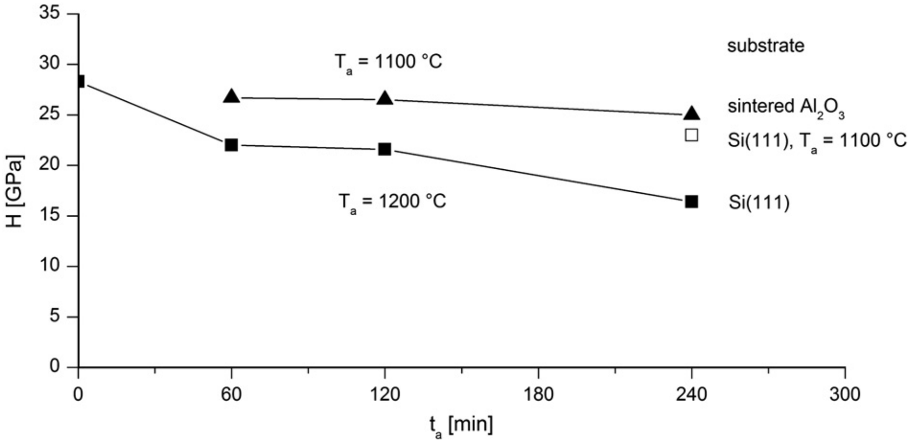

Fig. 10. Variation of hardness H of a 2500 nm thick $Si_{33}Al_7N_{60}$ film sputtered on the Si (111) and sintered Al_2O_3 substrates with increasing annealing time t_a in three-step thermal treatment process at two values of $T_a = 1100$ °C and 1200 °C.

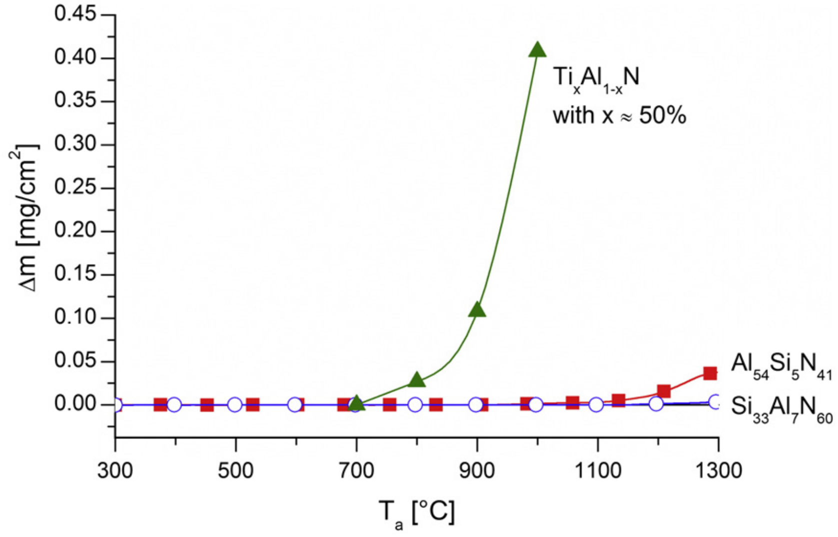

Fig. 11. Mass increase Δm of ~2500 nm thick (a) polycrystalline $Al_{54}Si_5N_{41}$ and (b) amorphous $Si_{33}Al_7N_{60}$ films, sputtered on the Si(111) and Al_2O_3 substrates, as a function of annealing temperature T_a in two-step thermal treatment process with 10 °C/min heating and 30 °C/min cooling rate, respectively.

(Al–Si–N) films exhibit a higher resistance to plastic deformation (a higher ratio H^3/E^{*2}).

3.6. Thermal stability

The thermal stability of mechanical and physical properties is of a key importance for every thin film and coating. The thermal stability is defined as a temperature T_{stab} at which the mechanical properties of the coating start to change. The temperature T_{ox} at which the coating starts to oxidize is called the oxidation resistance of the coating. Experiments performed so far indicate that $T_{ox} \approx T_{stab}$.

3.6.1. Thermal stability of hardness

The measurement of the thermal stability of hardness H of sputtered films can be realized by two methods: (1) by increasing of the substrate temperature T_s, and (2) by thermal annealing of as-deposited films in air. As an example of the first method, the hardness H of amorphous Zr–Si–N films with a high (≥50 vol.%) content of the Si_3N_4 phase deposited at different values of T_s is displayed in Fig. 9; for more details see Refs. [13,16]. From this figure it is seen that H almost does not depend on T_s. It indicates that H is determined by the amorphous structure of the film and not by the macrostress σ generated in the film during its growth. Namely, if H is determined by σ, its value should decrease with increasing value of T_s because the ratio $T_s/T_m > 0.2$ increases with increasing T_s and already the ratio $T_s/T_m \approx 0.25$ should be sufficient to relax the macrostress σ in nitride films [32]. The amorphous a-(Al–Si–N) films with a high (~40 at.%) Si content sputtered at $T_s = 500$ °C also exhibit a high (>0.3) ratio T_s/T_m; $T_{m\ Si_3N_4} = 2173$ K, $T_{m\ AlN} = 2523$ K [33] and $T_s/T_m > 0.3$ for both the Si_3N_4 and AlN phases under the assumption that exist separately in the Al–Si–N thin film. Therefore, no dependence $H = f(T_s)$ was investigated for the amorphous a-(Al–Si–N) films with a high Si content.

The effect of the post-deposition annealing on the film hardness H was tested on the a-(Al–Si–N) film with a high (~40 at.%) Si content. The post-deposition annealing of the Al–Si–N film sputtered at $T_s = 500$ °C in two-step thermal treatment cycle with a maximum annealing temperature 1200 °C (the temperature in this process was above 1000 °C for 27 min) does not influence its hardness H because of a perfect thermal stability of the amorphous structure of the film at $T_a \leq 1200$ °C. Practically no decrease in H was measured after the thermal treatment process, see Fig. 9. Also, no change in the X-ray amorphous structure was found. It means that the thermal stability of the amorphous structure also results in the thermal stability of the mechanical properties.

3.6.1.1. Effect of annealing time. The film properties can be influenced not only by the value of T_a but also by the annealing time t_a at a given temperature T_a. The dependence of H of the Al–Si–N film, sputtered on Si(111) and Al_2O_3 substrate, as a function t_a at two values of $T_a = 1100$ °C and 1200 °C (three-step thermal treatment cycle) is displayed in Fig. 10. The hardness H of the Al–Si–N film on both Si(111) and Al_2O_3

Table 1
Mechanical properties of the Al–Si–N films with a low and high Si content used in the oxidation experiments

Film	h	Al	Si	N	H	E^*	H^3/E^{*2}	σ	a_D	Structure
	[nm]		[at. %]		[GPa]	[GPa]	[GPa]	[GPa]	[nm/min]	
$Al_{54}Si_5N_{41}$	2600	54	5	41	21.3	230	0.18	−0.04	6.2	Crystalline
$Si_{33}Al_7N_{60}$	2500	7	33	60	25.6	240	0.29	−1.8	10.6	Amorphous

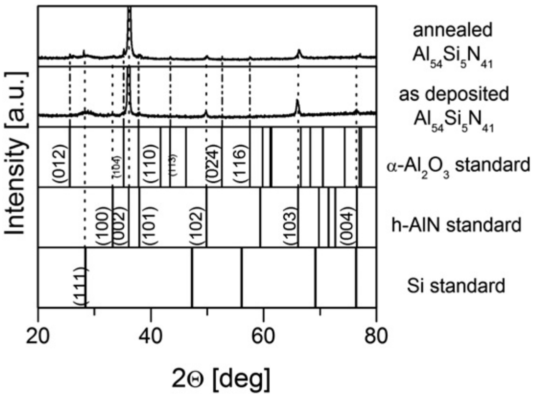

Fig. 12. XRD patterns from c-$Al_{54}Si_5N_{41}$/Si(111) in the as-deposited state and after thermal annealing in two-step cycle up to 1300 °C in flowing air at a 10 °C/min heating and 30 °C/min cooling rate, respectively.

substrates remains almost constant during annealing at $T_a = 1100$ °C for $t_a = 4$ h. When T_a is increased to 1200 °C, the hardness H of the film deposited on the Si(111) substrate continuously decreases with increasing annealing time from ~27 GPa to ~17 GPa. That is probably caused by a slight oxidation of the film which results in the formation of a surface oxide layer growing in the thickness with the annealing time t_a and having a lower hardness than the Al–Si–N film bulk; for more details see Ref. [14] where a similar phenomenon has been investigated. The dependence $H = f(t_a)$ of Al–Si–N films sputtered on the Al_2O_3 substrate has not been investigated so far.

3.6.2. Oxidation resistance

Generally, the oxidation resistance of a film strongly depends on its structure. Recently, it has been found that hard amorphous ^{T}Me–Si–N films with a high (>20 at.%) Si content exhibit better oxidation resistance compared to polycrystalline ones [6,7,18,19]. Experiments described in this paper, however, show that the Al–Si–N films, in which ^{T}Me was replaced with Al, also exhibit a high oxidation resistance, see Fig. 11. In this figure the oxidation resistance of the Al–Si–N films with a low (5 at.%) and high (33 at.%) Si content, i.e. $Al_{54}Si_5N_{41}$ and $Si_{33}Al_7N_{60}$ films, is compared. The mechanical properties of the as-deposited Al–Si–N films used in the oxidation experiment are summarized in Table 1. The crystalline c-(Al–Si–N) film exhibits a high oxidation resistance up to ~1000 °C (an increase in mass $\Delta m < 0.005$ mg/cm^2 in two-step thermal treatment process when the film is deposited on the Si(111) substrate) and the amorphous a-(Al–Si–N) film exhibits even higher oxidation resistance, up to ~1150 °C ($\Delta m = 0$ in two-step thermal treatment process when the film is deposited on the Al_2O_3 substrate).

This experiment clearly shows that the crystalline Al–Si–N films containing a large amount of Al also exhibit a good oxidation resistance. That is due to the existence of free Al atoms in the film, their easy oxidation and the formation of a dense Al_2O_3 surface layer preventing the fast penetration of oxygen into the bulk of the film.

3.6.2.1. Structure of thermally annealed Al–Si–N films. The structure of the Al–Si–N films with both a low (5 at.%) and high (33 at.%) Si content practically does not change during thermal annealing in two-step treatment process up to 1300 °C. The amorphous structure of the as-deposited $Si_{33}Al_7N_{60}$ film remains amorphous and the as-deposited $Al_{54}Si_5N_{41}$ film with hexagonal AlN(002) preferred crystallographic orientation remains crystalline with the same preferred orientation, see Fig. 12. After the annealing the $Al_{54}Si_5N_{41}$ film also exhibits low-intensity Al_2O_3(012), (104), (110) and (116) reflections.

3.6.2.2. Comparison of oxidation resistance of Al–Si–N film with ^{T}Me–Si–N films. Recently, an excellent oxidation resistance of amorphous ^{T}Me–Si–N films considerably exceeding 1000 °C has been reported [5–7,10–19]. Experiments described in this paper show that the replacement of ^{T}Me with Al in ^{T}Me–Si–N films with a high (>20 at.%) Si content also results in an excellent oxidation resistance of Al–Si–N films, see Fig. 13. A low (~800 °C) oxidation of the $Si_{24}W_{17}N_{59}$ film is due to the formation of volatile oxides [13]. In Fig. 13 the oxidation resistance of a polycrystalline TiAlN film [9] is also given for a comparison.

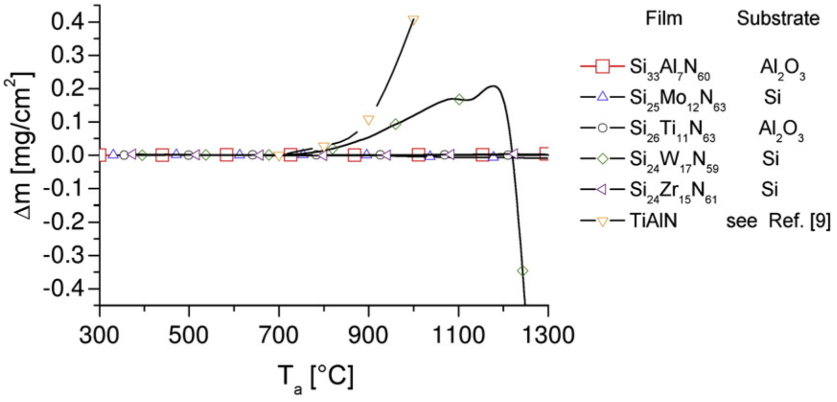

Fig. 13. Comparison of the oxidation resistance of a ~2600 nm thick amorphous $Si_{33}Al_7N_{60}$ film with selected (i) ^{T}Me–Si–N films with a high (>20 at.%) Si content and (ii) TiAlN film [9], represented by an increase in the film mass Δm as a function of T_a.

4. Conclusions

Main results of the investigation of the sputtered Al–Si–N films are the following:

1. The Al–Si–N films with a low (<10 at.%) Si content are polycrystalline. On the contrary, the Al–Si–N films with a high (≥20 at.%) Si content are amorphous in spite of the fact that they are sputtered at relatively high values of the substrate temperature $T_s = 500$ °C.
2. The amorphous a-(Al–Si–N) films are (i) harder and (ii) more resistant to plastic deformation compared to the polycrystalline c-(Al–Si–N) films.
3. The thermal stability of hardness H of the a-(Al–Si–N) film is high and does not vary with increasing annealing temperature T_a up to 1100 °C even after 4 h.
4. The oxidation resistance of both the crystalline c-(Al–Si–N) film with a low (<10 at.%) Si content and the amorphous a-(Al–Si–N) film with a high (≥20 at.%) Si content is also high. The c-(Al–Si–N) film exhibits a high oxidation resistance up to ~1000 °C and the a-(Al–Si–N) film up to ~1150 °C.
5. A high oxidation resistance of the c-(Al–Si–N) film with a low (<10 at.%) Si content is due to the existence of free Al atoms in the film, their easy oxidation and the formation of a dense Al_2O_3 surface layer which prevents a fast penetration of the oxygen into bulk of the film.

Obtained results indicate that the substitution of ^{T}Me with Al in ^{T}Me–Si–N films results in the formation of hard Al–Si–N films with good and thermally stable mechanical properties and excellent oxidation resistance exceeding 1000 °C.

Acknowledgements

This work was supported in part by the Ministry of Education of the Czech Republic under Project Nos. MSM 4977751302 and ME 673, and the Grant Agency of the Czech Republic under project No. 106/06/0327.

References

[1] H. Gleiter, Prog. Mater. Sci. 33 (1989) 223.
[2] S. Veprek, J. Vac. Sci. Technol. A17 (1999) 2401.
[3] J. Musil, Surf. Coat. Technol. 125 (2000) 322.
[4] J. Patscheider, MRS Bull. 28 (3) (2003) 180.
[5] J. Musil, in: J.Th.M. De Hosson, A. Cavaleiro (Eds.), Nanostructured Hard Coatings, Kluwer Academic/Plenum Publishers, New York, USA, 2006, p. 407.
[6] J. Musil, in: S. Zhang, N. Ali (Eds.), Nanocomposite films and coatings, Imperial College Press, London, UK, 2007, p. 281.
[7] J. Musil, P. Baroch, P. Zeman: in R. Wei (Ed.), Plasma Surface Engineering and its Practical Applications, Research Signpost Publisher, USA, in press.
[8] S. Veprek, S. Reiprich, Thin Solid Films 268 (1995) 64.
[9] W.-D. Münz, J. Vac. Sci. Technol. A4 (1986) 2717.
[10] H. Zeman, J. Musil, P. Zeman, J. Vac. Sci. Technol. A22 (2004) 646.
[11] J. Musil, R. Daniel, P. Zeman, O. Takai, Thin Solid Films 478 (2005) 238.
[12] J. Musil, P. Dohnal, P. Zeman, J. Vac. Sci. Technol. B23 (2005) 1568.
[13] J. Musil, R. Daniel, J. Soldan, P. Zeman, Surf. Coat. Technol. 200 (2006) 3886.
[14] P. Zeman, J. Musil, R. Daniel, Surf. Coat. Technol. 200 (2006) 4091.
[15] P. Zeman, J. Musil, Appl. Surf. Sci. 252 (2006) 8319.
[16] R. Daniel, J. Musil, P. Zeman, C. Mitterer, Surf. Coat. Technol. 201 (2006) 3368.
[17] J. Musil, P. Zeman, P. Dohnal, R. Čerstvý, Plasma Process. Polym. 4 (2007) S574.
[18] J. Musil, P. Zeman, Solid State Phenomena 127 (2007) 31.
[19] J. Musil, J. Vlcek, P. Zeman, Advanced amorphous non-oxide coatings with oxidation resistance above 1000 °C, Advances in Applied Ceramics, Special Issue on NANOCERAMICS, submitted for publication.
[20] S. Carvalho, L. Rebouta, A. Cavaleiro, L.A. Rocha, J. Gomes, E. Alves, Thin Solid Films 398-399 (2001) 391.
[21] P.J. Martin, A. Bendavid, J.M. Cairney, M. Hoffman, Surf. Coat. Technol. 200 (2005) 2228.
[22] S. Carvalho, E. Ribeiro, L. Rebouta, C. Tavares, J.P. Mendoca, A.C. Monteiro, N.J.M. Carvalho, J.Th.M. De Hosson, A. Cavaleiro, Surf. Coat. Technol. 177-178 (2004) 459.
[23] K. Yamamoto, S. Kujime, K. Takahara, Surf. Coat. Technol. 200 (2005) 1383.
[24] M. Naka, T. Shibayanagi, M. Maeda, S. Zhao, H. Mori, Vacuum 59 (2000) 252.
[25] A. Pelisson, M. Parlinska-Wojtan, H.J. Hug, J. Patscheider, Surf. Coat. Technol. 202 (2007) 884.
[26] J.D. Wilcock, D.S. Cambell, Thin Solid Films 3 (1969) 3.
[27] E.A. Brandes (Ed.), Smithells Metals Reference Book, 7th Edition, Butterworth Heinemann, 1992, pp. 8–23.
[28] T.Y. Tsui, G.M. Pharr, W.C. Oliver, et al., Mater. Res. Soc. Symp. Proc. 383 (1995) 447.
[29] J. Musil, F. Kunc, H. Zeman, H. Poláková, Surf. Coat. Technol. 154 (2002) 304.
[30] M. Jirout, J. Musil, Surf. Coat. Technol. 200 (2006) 6792.
[31] J. Musil, M. Jirout, Surf. Coat. Technol. 201 (2007) 5148.
[32] J.A. Thornton, D.W. Hoffman, Thin Solid Films 171 (1989) 5.
[33] H. Holleck, J. Vac. Sci. Technol. A4 (1986) 2662.

3.1.2 A-II: Formation of crystalline Al-Ti-O thin films and their properties

Surface & Coatings Technology 202 (2008) 6064–6069

Contents lists available at ScienceDirect

Surface & Coatings Technology

journal homepage: www.elsevier.com/locate/surfcoat

Formation of crystalline Al–Ti–O thin films and their properties

J. Musil *, V. Šatava, R. Čerstvý, P. Zeman, T. Tölg

Department of Physics, University of West Bohemia, Univerzitní 22, 306 14 Plzeň, Czech Republic

ARTICLE INFO

Article history:
Received 14 March 2008
Accepted in revised form 10 July 2008
Available online 22 July 2008

Keywords:
Al–Ti–O thin film
Structure
Crystallization
Mechanical properties
Oxidation resistance
Reactive magnetron sputtering

ABSTRACT

The article reports on the effect of addition of Ti into Al_2O_3 films with Ti on their structure, mechanical properties and oxidation resistance. The main aim of the investigation was to prepare crystalline Al–Ti–O films at substrate temperatures $T_s \leq 500$ °C. The films with three different compositions (41, 43 and 67 mol% Al_2O_3) were reactively sputtered from a composed Al/Ti target and their properties were characterized using X-ray diffraction (XRD), X-ray fluorescent spectroscopy (XRF), microhardness testing, and thermogravimetric analysis (TGA). It was found that (1) the addition of Ti stimulates crystallization of Al–Ti–O films at lower substrate temperatures, (2) Al–Ti–O films with a nanocrystalline cubic γ-Al_2O_3 structure, hardness of 25 GPa and zero oxidation in a flowing air up to ~1050 °C can be prepared already at low substrate temperature of 200 °C, and (3) the crystallinity of Al–Ti–O films produced at a given temperature improves with the increasing amount of Ti. The last finding is in a good agreement with the binary phase diagram of the TiO_2–Al_2O_3 system.

1. Introduction

At present, there is an urgent need to prepare crystalline α-Al_2O_3 thin films at substrate temperatures T_s of about 500 °C or less for high-speed cutting tools. That is a very difficult task because α-Al_2O_3 is a high-temperature phase creating at $T_s \approx 1000$ °C. The alumina is a polymorphous material with γ-, κ-, δ-, χ-, θ-metastable phases and only one thermodynamically stable rhombohedral α-Al_2O_3 phase. For the creation of α-Al_2O_3 thin films the highest substrate temperature T_s of about 1000 °C is necessary to be used. This fact strongly limits the deposition of α-Al_2O_3 thin films only onto substrates with a high thermal stability, e.g. cemented carbides. Therefore, a great effort has been devoted to the search of a process or method which allows the crystallization temperature T_{cr} of the α-Al_2O_3 phase to be decreased [1–12].

An usual method used to form crystalline alumina thin films at $T_s \leq 500$ °C is the ion plating process used in magnetron sputtering. It has been found that T_{cr} of the film decreases and its crystallinity increases when high fluxes of ions ν_i are incident at the surface of the growing film. Therefore, reactive ionized magnetron sputtering [13] or reactive high-power pulsed magnetron sputtering [1–3,5,9–12] has been used in many experiments. Also, a low-temperature formation of α-Al_2O_3 thin films on a crystalline Cr_2O_3 template has been reported [4–6]. This method requires, however, a low-temperature formation of a crystalline Cr_2O_3 based layer to be mastered. However, in many cases a low-temperature metastable γ-Al_2O_3 phase is formed only [14–20].

Besides these methods, the addition of selected elements into Al_2O_3 film with selected elements seems to be also beneficial for the decrease of T_{cr} of the α-Al_2O_3 phase. For instance, it has been already found that the addition of Zr into HfO_2 oxide with Zr decreases T_{cr} of HfO_2 due to strong crystallization tendency of ZrO_2 [21]. The decrease in T_{cr} can be expected also when Ti is added into Al_2O_3 oxide, see a phase diagram of the TiO_2–Al_2O_3 system displayed in Fig. 1. From this figure it is clearly seen that the temperature separating amorphous and crystalline materials, which is denoted as T_{cr}, decreases with the increasing amount of the TiO_2 phase in the mixture $Al_2O_3+TiO_2$.

The main aim of our study was to stimulate crystallization of Al_2O_3-based thin films by the addition of Ti as predicted by the phase diagram for the bulk TiO_2–Al_2O_3 system. To fulfil this goal a detailed investigation of the structure, mechanical properties, and oxidation resistance of reactively sputtered Al–Ti–O thin films with low and high content of Ti was carried out.

2. Experimental

Al–Ti–O thin films were sputtered in an $Ar+O_2$ mixture using an unbalanced magnetron equipped with a composed target of 116 mm in diameter and consisting of an Al (99.5%) plate of 100 mm in diameter fixed with a Ti (99.99%) ring of inner diameter $Ø_{\mathrm{in\ Ti}}$, see Fig. 2.

The amount of Ti incorporated into the sputtered film was controlled by the diameter $Ø_{\mathrm{in\ Ti}}$ of the hole in the Ti target. The magnetron was supplied by a dc pulse asymmetric bipolar IAP 1010 power supply operated at the repetition frequency $f_r = 50$ kHz, The average magnetron current I_{da} was controlled by the pulse length τ. The following parameters – $\tau = 7.5$ µs, $\tau/T = 0.375$, $t_2 = 2.5$ µs with $U_d = +100$ V, $t_1 = t_3 = 5$ µs – were used in our experiments, see Fig. 3a; T is the period of pulses. Real

---

* Corresponding author. Tel.: +420 377 63 2200; fax: +420 377 63 2202.
E-mail address: musil@kfy.zcu.cz (J. Musil).

0257-8972/$ – see front matter
doi:10.1016/j.surfcoat.2008.07.012

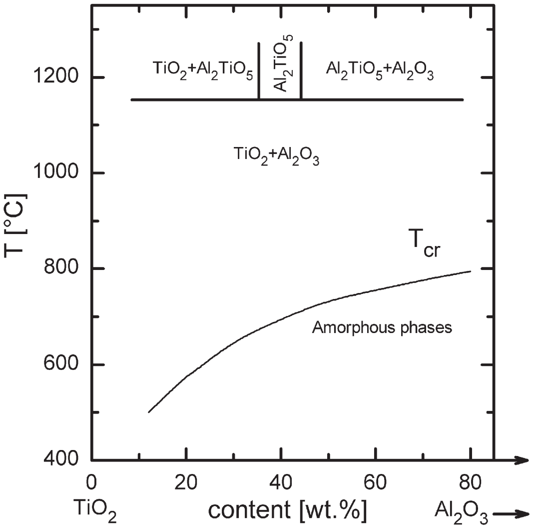

Fig. 1. Binary phase diagram of the TiO_2–Al_2O_3 system [22].

shapes of the discharge voltage U_d and current I_d in the pulsed operation as functions of time t are displayed in Fig. 3b and c. The difference in U_d adjusted on the pulsed power supply (Fig. 3a) and the real time development of $U_d(t)$ in presence of discharge is due to a change of the plasma impedance with time t.

The films were sputtered under the following conditions: I_{da} = 1–1.5 A, substrate-to-target distance d_{s-t} = 60 mm, substrate bias $U_s = U_{fl}$, substrate temperature T_s ranging from 200 °C to 800 °C and the total pressure $p_T = p_{Ar} + p_{O2}$ = 1 Pa; here U_{fl} is the floating potential. The films were deposited onto polished and ultrasonically precleaned Si(100) (35×5×0.4 mm^3 and 15×15×0.4 mm^3) and sintered polycrystalline corundum Al_2O_3 substrates (10×10×0.5 mm^3). Long stripes (35×5×0.4 mm^3) of Si(100) were used to measure the macrostress σ generated in the film during its growth from bending of the Si(100) stripe using the Stoney's formula [23].

The film thickness h and the substrate bending due to macrostress were measured by a stylus profilometer Dektak 8 with a resolution of 1 nm. The structure was determined by X-ray diffraction (XRD) analysis using a PANalytical X'Pert PRO diffractometer working in the Bragg–Brentano configuration using Cu Kα radiation (λ = 0.1540562 nm). Some XRD measurements were performed also in the glancing angle configuration at an incidence angle of 1°. The elemental composition was determined by X-ray fluorescent spectroscopy (XRF) using a PANalytical XRF spectrometer MagiX PRO. The mechanical properties, i.e. the microhardness H, effective Young's modulus $E^* = E/(1-\nu^2)$, and elastic recovery $W_e = A_e/A_t$, were evaluated from load vs. displacement curves measured by a computer controlled microhardness tester Fischerscope H 100 with a Vicker's diamond indenter at load L = 10 mN; here E and ν are the Young's modulus and the Poisson's ratio, respectively, A_e is the work necessary for the elastic deformation of the film and A_t is the total work done by the load applied to the film. The oxidation resistance was measured in a synthetic air with a flow rate of 1 l/h using a symmetrical high-resolution Setaram thermogravimetric system TAG 2400. The oxidation tests were carried out at 10 °C/min heating and 30 °C/min cooling rate, respectively, on substrates coated only on one side. Thermogravimetric curves corresponding to oxidation of the bare substrates were subsequently subtracted and the resulting curves then

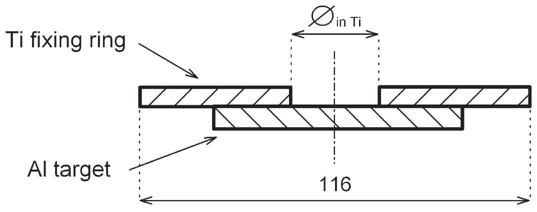

Fig. 2. Schema of the composed target used in sputtering of thin Al–Ti–O films.

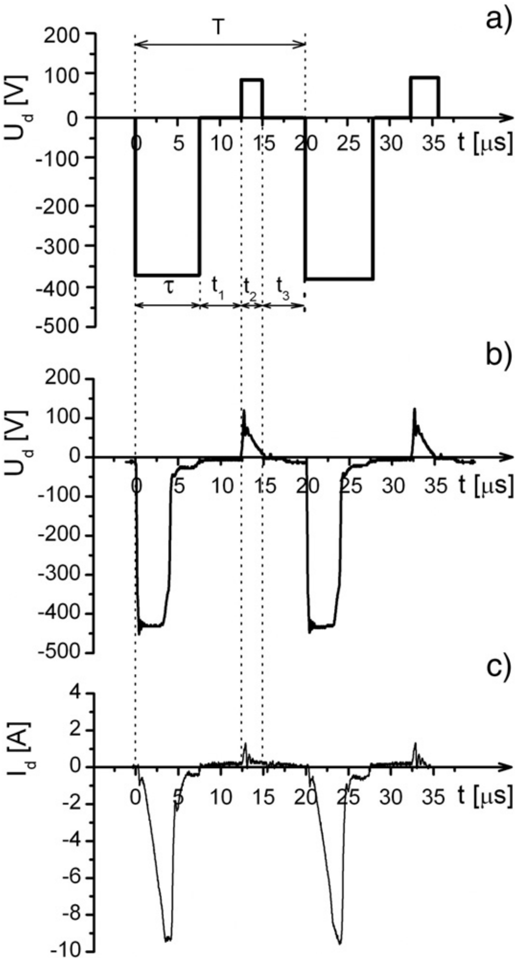

Fig. 3. Time evolution of voltage U_d without (a) and with (b) magnetron discharge and current I_d with magnetron discharge (c).

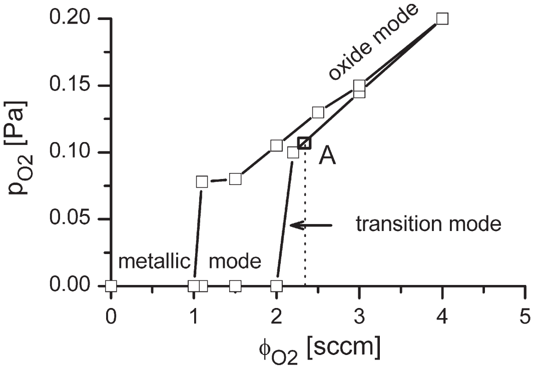

Fig. 4. Dependence of the oxygen partial pressure p_{O2} on the oxygen flow rate ϕ_{O2} showing operation point A used in sputtering of the Al–Ti–O films and the hysteresis effect in the reactive sputtering process. Sputtering conditions: I_{da} = 1.5 A, P_{da} = 600 W, $U_s = U_{fl}$, p_{O2} = 0.1 Pa, p_T = 1 Pa and d_{s-t} = 60 mm.

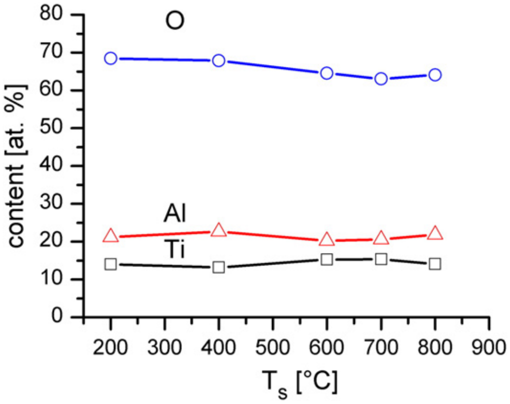

Fig. 5. Elemental composition of the thin Al–Ti–O films, sputtered at I_{da} = 1.5 A, U_s = U_{fl}, p_{O2} = 0.1 Pa, p_T = 1 Pa from the composed target with $Ø_{in\ Ti}$ = 35 mm, as a function of the substrate temperature T_s.

characterized the oxidation resistance of pure films only, without any substrate effects.

3. Results and discussion

Al–Ti–O films were reactively sputtered on the Si(100) substrates held on floating potential in the oxide mode of sputtering, see Fig. 4. The deposition rate a_D of the Al–Ti–O films sputtered in the oxide mode was quite low; a_D ≈ 4 nm/min.

3.1. Elemental composition

The elemental composition of Al–Ti–O films depends on four basic parameters: (i) the geometry of a composed target and sputtering yields of individual elements (γ_{Al} = 1, γ_{Ti} = 0.57 [24]), (ii) the ion bombardment of the growing film, (iii) the total pressure p_T of the sputtering gas, and (iv) the substrate temperature T_s. In our case, when no substrate bias is applied, i.e. U_s = U_{fl}, and a relatively high total pressure p_T = 1 Pa is used, the elemental composition of a film is not influenced by the ion and neutral particle bombardment. Therefore, it should be influenced by the substrate temperature T_s only. However, Fig. 5 shows that also T_s has a small effect on the elemental composition. Consequently, the ratio Al/(Al+Ti), which is important for the characterization of properties of the Al–Ti–O films, is controlled only by the inner diameter $Ø_{in\ Ti}$ of the Ti ring, see Table 1. A strong decrease in the Ti content occurs when $Ø_{in\ Ti}$ ≥ 50 mm.

The results displayed in Fig. 5 show that the Al–Ti–O films sputtered at $Ø_{in\ Ti}$ = 35 mm have an average elemental composition: 20 at.% Al, 12 at.% Ti and 68 at.% O. This elemental composition corresponds to ~41 mol% Al_2O_3. Due to problems with an exact determination of oxygen the mol% of Al_2O_3 in the TiO_2–Al_2O_3 system was determined based on the measured ratio Al/(Al+Ti) only. According to the phase diagram of the TiO_2–Al_2O_3 system (Fig. 6), we can expect that an Al_2TiO_5 intermetallic oxide should be formed, preferentially at high temperatures T ≥ 1200 °C.

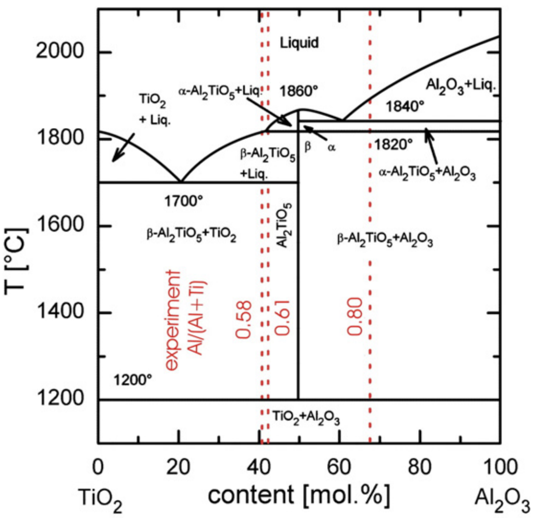

Fig. 6. Phase diagram of the TiO_2–Al_2O_3 system showing a variation of the phase composition with the increasing amount of Al_2O_3 and increasing temperature T [25].

Table 1
The ratio Al/(Al+Ti) and content of Al_2O_3 in the Al–Ti–O films sputtered from the composed Al/Ti target with a different diameter $Ø_{in\ Ti}$

$Ø_{in\ Ti}$ [mm]	35	50	60
Al/(Al+Ti)	0.58	0.61	0.80
Al_2O_3 [wt.%]	47	49	71
Al_2O_3 [mol%]	41	43	67

3.2. Structure

The evolution of the structure of Al–Ti–O films, characterized with XRD patterns, as a function of the substrate temperature T_s and the amount of Ti in the films is displayed in Fig. 7. As can be seen, both of these parameters strongly influence the film structure. The crystallinity of the Al–Ti–O film improves with the increasing amount of Ti incorporated in the film. The Al–Ti–O films produced at lower values of T_s are X-ray amorphous/nanocrystalline having a structure corresponding to metastable cubic γ-Al_2O_3 (PDF-2, 4–880). The existence of this structure was confirmed by glancing angle XRD measurements at an incidence angle of 1°, see Fig. 8. Also, it is worthwhile to note that a strong discontinuity at the vicinity of the Si reflection (around 68°) seen in XRD patterns displayed in Fig. 7 is a general feature for single crystals depending on the equipment settings.

On the contrary, the well-crystalline Al–Ti–O films with an orthorhombic Al_2TiO_5 structure are deposited at higher values of T_s. The Al_2TiO_5 aluminum titanate is formed, however, at temperatures T_s considerably lower than 1200 °C as predicted by the phase diagram. The temperature corresponding to the structural transformation increases with the decreasing amount of Ti in the film. The Al–Ti–O films with the amorphous/nanocrystalline γ-Al_2O_3 structure exhibit almost two times higher microhardness, H = 25–27 GPa, compared to those with the Al_2TiO_5 one, see Fig. 7.

The crystalline structure of the Al–Ti–O films with the ratio Al/(Al+Ti) = 0.80 is demonstrated by XRD patterns measured from the films on the substrate tilted at angle 2° compared to standard X-ray methodology, see Fig. 9. The substrate tilting resulted in an elimination of a strong reflection from the single-crystalline Si(100) substrate. However, this experiment clearly shows that only the films sputtered at T_s ≥ 600 °C are crystalline with a γ-Al_2O_3(441) orientation. The films sputtered at T_s < 600 °C are X-ray amorphous. The temperature T_s necessary to form the amorphous Al–Ti–O films decreases from 400 °C to 200 °C with the increasing Ti content, see Fig. 7. This decrease in T_s is in a good qualitative agreement with the phase diagram of the TiO_2–Al_2O_3 system given in Fig. 1. However, it is worthwhile to note that values of T_s corresponding to the transition from amorphous to crystalline Al–Ti–O films found in our experiment are lower than those predicted by the phase diagram. We believe that is due to a non-equilibrium film growth in reactive magnetron sputtering.

3.3. Mechanical properties

The microhardness H of Al–Ti–O films strongly depends on their structure. Therefore, H strongly varies with increasing T_s and content of Ti in the films. The hardness of the films with the Al_2TiO_5 structure

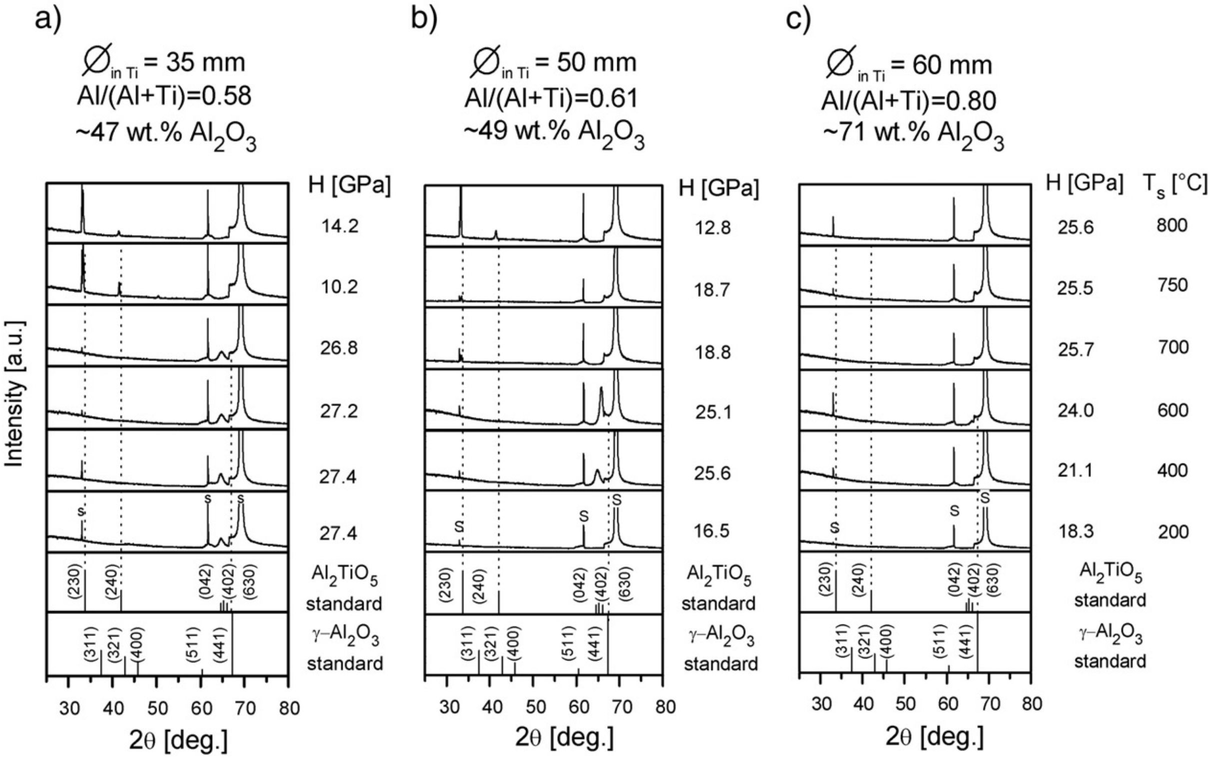

Fig. 7. Evolution of the structure and microhardness *H* of the Al–Ti–O thin films with the increasing substrate temperature T_s and Al_2O_3 content. Deposition conditions: $I_{da}=1.5$ A, $U_s=U_{fl}$, $p_{O2}=0.1–0.15$ Pa and $p_T=1$ Pa.

is considerably lower than those with the amorphous/nanocrystalline γ-Al_2O_3 structure and achieves of about 10 GPa only, see Fig. 7. In some cases the hardness of sputtered films can be affected by the macrostress σ generated in the film during its growth. Therefore, a correlation between *H* and σ was also investigated, see Fig. 10. The interrelationship between *H* and σ shows that *H* is not determined by σ; *H* does not vary with increasing T_s up to ~700 °C while σ continuously decreases in the same interval. The decrease in σ with increasing T_s is due to the thermal relaxation of σ which dominates with the increasing ratio T_s/T_m (0.41 and 0.46 for Al_2O_3 and TiO_2, respectively, at $T_s=973$ K; $T_{m\ Al2O3}=2323$ K, $T_{m\ TiO2}=2113$ K). From Fig. 10 it is seen that a ~1000 nm thick nanocrystalline Al–Ti–O thin film with the γ-Al_2O_3 structure produced at $T_s=700$ °C exhibits a high hardness $H\approx25$ GPa and a quite low macrostress $\sigma\approx-2$ GPa.

The decrease in σ correlates well with the increase in a_D with the increasing T_s, see Fig. 10b. Because the energy delivered to a growing film by bombarding ions decreases with increasing a_D ($E=(U_p-U_s)i_s/a_D$) [26] a reduced ion bombardment also contributes to decrease of σ.

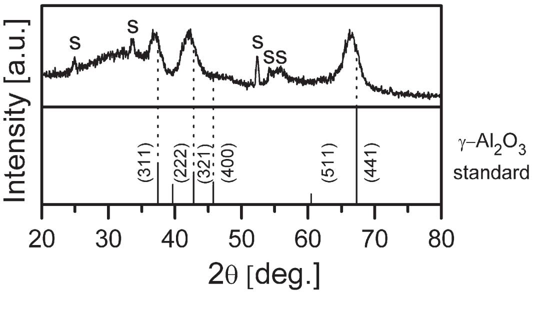

Fig. 8. GA-XRD pattern of an Al–Ti–O film with the ratio Al/(Al+Ti)=0.80 sputtered at $Ø_{in\ Ti}=60$ mm and at $T_s=400$ °C.

3.4. Oxidation resistance

A 745 nm thick $Al_{31}Ti_7O_{62}$ film sputtered at $Ø_{in\ Ti}=60$ mm, $I_{da}=1.5$ A, $U_d=400$ V, $P_{da}=600$ W, $U_s=U_{fl}$, $T_s=700$ °C, $d_{s-t}=60$ mm, $p_{O2}=0.15$ Pa, $p_T=1$ Pa and $a_D=3.5$ nm/min was selected for the investigation of the oxidation resistance. According to X-ray diffraction measurements the as-deposited Al–Ti–O film is nanocrystalline with the γ-Al_2O_3

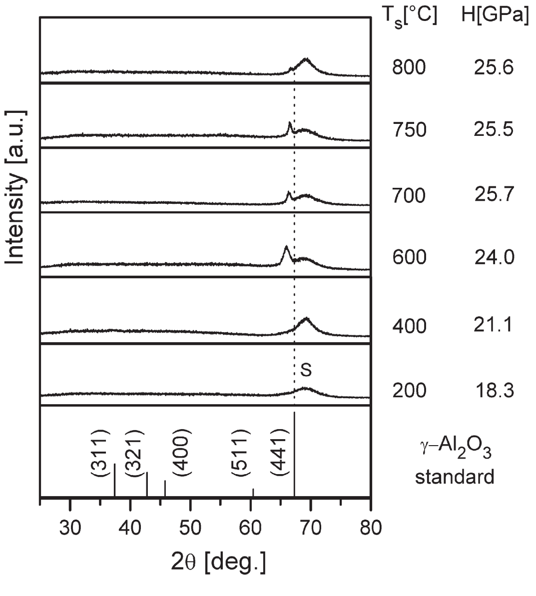

Fig. 9. XRD patterns from the Al–Ti–O thin films with the ratio Al/(Al+Ti)=0.80 measured on the Si(100) substrate tilted at 2° as a function of the substrate temperature T_s. Compare with the XRD patterns in Fig. 6c measured on the same films by the standard X-ray methodology.

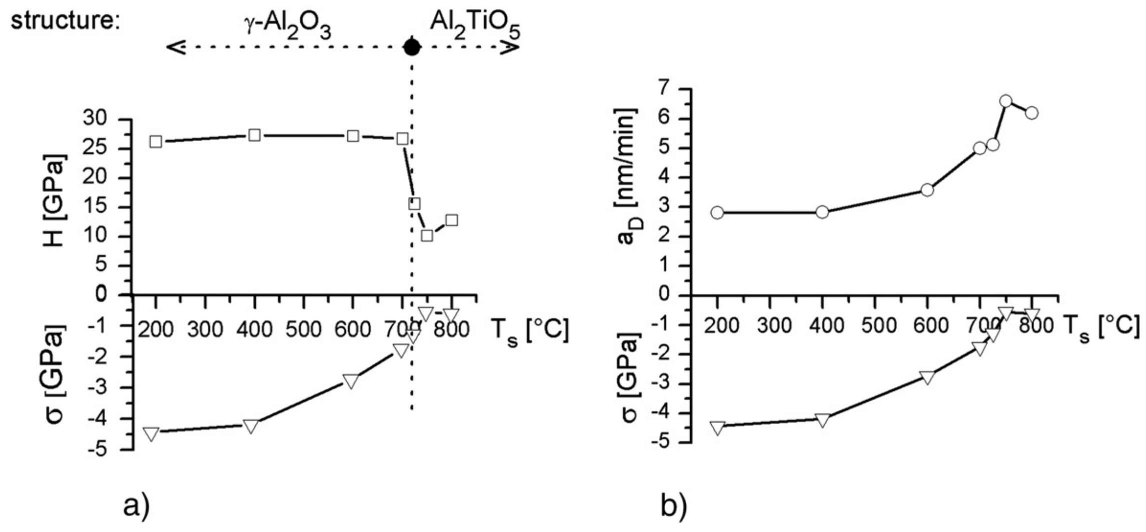

Fig. 10. Evolution of (a) microhardness H vs. compressive macrostress σ (≤0), and (b) deposition rate a_D vs. σ in the Al–Ti–O films with the increasing substrate temperature T_s. Deposition conditions are the same as those given in the caption to Fig. 5.

structure. The structure of the film changes during thermal annealing in a flowing air and consists of a mixture of rutile TiO_2 and α-Al_2O_3 grains after increasing of the annealing temperature T_a up to 1300 °C, see Fig. 11. The thermal annealing of the film results in almost no change of the elemental composition but in a strong drop of microhardness H, see Table 2.

The $Al_{31}Ti_7O_{62}$ film sputtered on the Si(100) substrate exhibits almost no increase in the mass $\Delta m = 0$ mg/cm^2 up to $T_a \approx 1050$ °C, see Fig. 12. A negligible mass gain $\Delta m \approx 0.002$ mg/cm^2 observed at $T_a = 1100$ °C rises with the increasing temperature up to $T_a = 1300$ °C, which is the temperature limit of the Si substrate. In order to investigate the oxidation resistance above 1300 °C, the film was deposited onto a more heat-resistant substrate, the sintered corundum Al_2O_3 substrate. As can be seen from Fig. 12, in this case no mass change is observed up to $T_a = 1700$ °C, which is the temperature limit of our TG system operating in a flowing air. This result indicates that the Al–Ti–O film was already fully saturated with oxygen after the deposition.

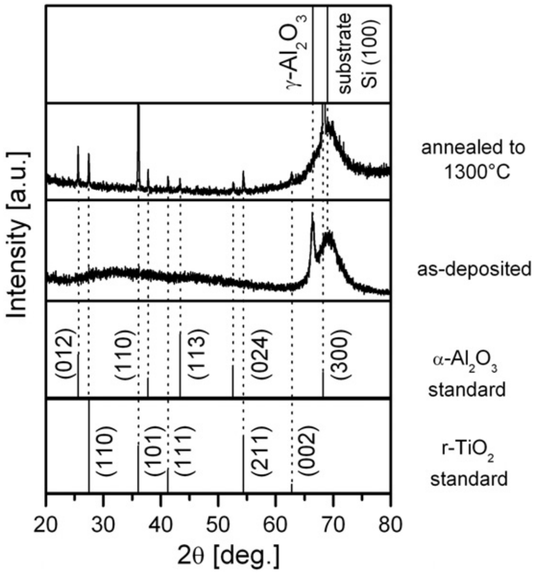

Fig. 11. XRD pattern of an as-deposited 745 nm thick $Al_{31}Ti_7O_{62}$ film on the Si(100) substrate and that of the same film after thermal annealing in a flowing air to $T_a = 1300$ °C.

It is important to emphasize that the oxidation of the backside of substrates was always subtracted. Therefore, the increase of Δm of the $Al_{31}Ti_7O_{62}$ film deposited on the Si(100) substrate at $T_a > 1050$ °C, which is similar to that of an uncoated Si(100) substrate (compare in Fig. 13), indicates that the external atmosphere freely penetrates through the film to the Si(100) surface and oxidizes it. This fact is also supported by the zero mass gain of the $Al_{31}Ti_7O_{62}$ film deposited on the corundum substrate with a high oxidation resistance up to $T_a = 1700$ °C. The penetration of oxygen through the Al–Ti–O film can be connected with the structural transformation from the cubic γ-Al_2O_3 phase to a mixture of rutile $TiO_2 + \alpha$-Al_2O_3 phases. We believe that this phase transformation contributes to a formation of voids along grain boundaries allowing the external atmosphere (oxygen) to penetrate along them to the surface of a substrate. The same oxidation behavior was also found for an $Al_{19}Ti_{14}O_{67}$ film deposited at $T_s = 200$ °C and $Ø_{in\ Ti} = 35$ mm, see Fig. 13.

This experiment indicates that the protection ability of the nanocrystalline Al–Ti–O film with the γ-Al_2O_3 structure is limited by the transformation of the γ-Al_2O_3 phase into a mixture of rutile $TiO_2 + \alpha$-Al_2O_3 phases. Further study is, however, necessary to fully understand the effect of the structure of the as-deposited Al–Ti–O film on its protection ability.

4. Conclusions

Main results of the study can be summarized as follows.

1. Alloying of an Al_2O_3 film with Ti strongly influences its crystallization temperature T_{cr} which decreases with increasing Ti content in the Al–Ti–O film. This decrease in T_{cr} is in a good qualitative agreement with the phase diagram of the TiO_2–Al_2O_3 system.
2. The Al–Ti–O films have either an amorphous/nanocrystalline cubic γ-Al_2O_3 structure when produced at lower values of T_s or a crystalline Al_2TiO_5 structure when produced at higher values of T_s. The amorphous/nanocrystalline Al–Ti–O films exhibit more than

Table 2
Elemental composition and microhardness of as-deposited ($T_s = 700$ °C) and thermally annealed ($T_a = 1300$ °C) 745 nm thick Al–Ti–O films in a flowing air

Film	Ti [at.%]	Al [at.%]	O [at.%]	H [GPa]
As-deposited	7	31	62	25.5
Annealed	7	30	63	11.5

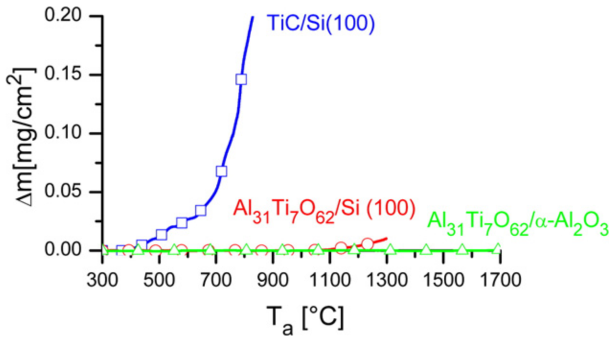

Fig. 12. Mass gain Δm of a 745 nm thick $Al_{31}Ti_7O_{62}$ film on the Si(100) and Al_2O_3 substrates after thermal annealing in a flowing air as a function of the annealing temperature T_a. Heating time $t_h = 170$ min up to $T_a = 1700$ °C, cooling time $t_c = 56$ min to *RT*, annealing time $t_a = 70$ min at $T_a \geq 1000$ °C. For comparison Δm of a TiC film on the Si(100) substrate after thermal annealing is also given [27].

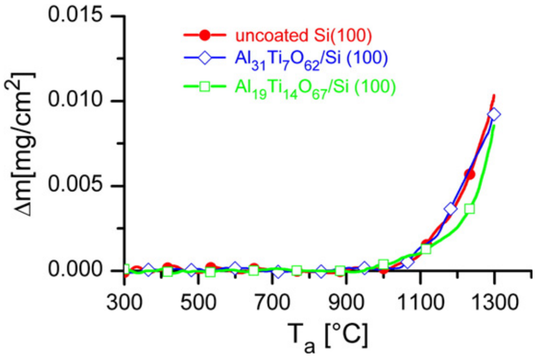

Fig. 13. Comparison of $\Delta m = f(T_a)$ for nanocrystalline $Al_{31}Ti_7O_{62}$ and $Al_{19}Ti_{14}O_{67}$ films with the γ-Al_2O_3 structure on the Si(100) substrate with that for an uncoated Si (100) substrate.

two times higher microhardness ($H = 25$–27 GPa) compared to those with the Al_2TiO_5 structure ($H \approx 10$–14 GPa).

3. The nanocrystalline Al–Ti–O film with the γ-Al_2O_3 structure and high hardness $H \approx 25$ GPa can be sputtered already at $T_s \approx 200$ °C if $Al/(Al+Ti) \geq 0.58$. The temperature T_s is necessary for the production of the Al–Ti–O film with $H \approx 25$ GPa, however, increases when the amount of Ti in the film decreases.
4. The cubic γ-Al_2O_3 phase transforms into a mixture of rutile TiO_2 + α-Al_2O_3 phases during thermal annealing above 1000 °C. This transformation determines the thermal stability of as-deposited crystalline Al–Ti–O films with the γ-Al_2O_3 structure and results in a formation of voids along grain boundaries and a connection between the substrate surface and external atmosphere.
5. The oxidation resistance of the as-deposited crystalline Al–Ti–O film with a cubic γ-Al_2O_3 phase investigated on corrundum (sintered Al_2O_3) substrate in flowing air is considerably higher than 1700 °C.

In summary, we can conclude that the *alloying* of Al_2O_3 films with Ti is a simple way to produce the crystalline-Al_2O_3 based coatings thermally stable above 1000 °C. The excellent oxidation resistance of hard Al–Ti–O films opens new application areas.

Acknowledgments

This work was supported in part by the Ministry of Education of the Czech Republic under Project MSM 4977751302 and in part by the Grant Agency of the Czech Republic under the Project No. 106/06/0327.

References

[1] O. Zywitzki, G. Hoetzsch, F. Fietzke, K. Goedicke, Surf. Coat. Technol. 82 (1996) 169.
[2] O. Zywitzki, G. Hoetzsch, Surf. Coat. Technol. 94–95 (1997) 303.
[3] J.M. Schneider, W.D. Sproul, Reactive pulsed dc magnetron sputtering and control, in: D.A. Glocker, S.I. Shah (Eds.), Handbook of Thin Film Process Technology, IOP Publishing Ltd, 1998, p. A5.1:1.
[4] P. Jin, S. Nakao, S.X. Wang, L.M. Wang, Appl. Phys. Lett. 32 (2003) 1024.
[5] A. Schutze, D.T. Quinto, Surf. Coat. Technol. 162 (2003) 174.
[6] J.M. Andersson, Z.s. Czikany, P. Jin, U. Helmerson, J. Vac. Sci. Technol. A22 (2004) 117.
[7] M.A. Omari, R.S. Sorbello, C.R. Aita, J. Vac. Sci. Technol. A24 (2006) 317.
[8] A. Khanna, D.K. Bhat, J. Vac. Sci. Technol. A25 (2007) L5.
[9] D. Mercs, C. Petitot, A. Duranteau, V. Demange, C. Coddet, Plasma Process. Polym. 4 (2007) S175.
[10] G. Erkens, Surf. Coat. Technol. 201 (2007) 4806.
[11] R. Chistyakov, B. Abraham, W.D. Sproul, Proc. of 49 th Annual Technical Conference, USA, Society of Vacuum Coaters, 2006, p. 88.
[12] M. Sridharan, M. Sillassen, J. Bottiger, J. Chevalier, H. Birkedal, Surf. Coat. Technol. 202 (2007) 920.
[13] S. Rossnagel, J. Hopwood, Appl. Phys. Lett. 63 (1993) 3285.
[14] R. Cremer, M. Witthaut, D. Neuschutz, G. Erken, T. Leyendecker, M. Feldhege, Surf. Coat. Technol. 120–121 (1999) 213.
[15] A. Larsson, S. Ruppi, Int. J. Refract. Met. Hard Mater. 19 (2001) 515.
[16] A. Schutze, D.T. Quinto, Surf. Coat. Technol. 162 (2003) 174.
[17] A. Khanna, D.G. Bhat, Surf. Coat. Technol. 201 (2006) 168.
[18] K. Bobzin, E. Lugscheider, M. Maes, C. Pinero, Thin Solid Films 494 (2006) 255.
[19] M. Sridharan, M. Sillassen, J. Bottiger, J. Chevalier, H. Birkedal, Surf. Coat. Technol., doi:10.1016/j.surfcoat.2007.05.061.
[20] E. Wallin, J.M. Andersson, M. Lattemann, U. Helmersson, Thin Solid Films, doi:10.1016/j.tsf.2007.07.135.
[21] Y.E. Hong, Y.S. Kim, K. Do, D. Lee, D.H. Ko, J. Vac. Sci. Technol. A23 (2005) 1413.
[22] V.D. Kushkov, A.M. Zaslavskii, I.S. Kozlov, A.V. Melnikov, A.E. Slivinskaya, Prob. Spets. Elektrometall. 1 (1991) 56.
[23] J.D. Wilcock, D.S. Campbell, Thin Solid Films 3 (1969) 3.
[24] Periodic Table of the Elements, Materials Research Corporation (MRS), MRC Advanced Materials Division, 542 State Route 303, Orangeburg, New York 10962, 1989.
[25] P. Pena, S. De Aza, Ceramica (Florence) 33 (1980) 23.
[26] J. Musil, Physical and mechanical properties of hard nanocomposite films prepared by reactive magnetron sputtering, in: A. Cavaleiro, J.T. De Hosson (Eds.), Nanostructured Hard Coatings, New York, Springer, 2006, p. 407.
[27] J. Soldan, J. Musil, P. Zeman, Plasma Process. Polym. 4 (2007) S6.

3.1.3 A-III: Protective Zr-containing SiO_2 coatings resistant to thermal cycling in air up to 1400 °C

Surface & Coatings Technology 203 (2009) 1502–1507

Contents lists available at ScienceDirect

Surface & Coatings Technology

journal homepage: www.elsevier.com/locate/surfcoat

Protective Zr-containing SiO_2 coatings resistant to thermal cycling in air up to 1400 °C

J. Musil *, V. Šatava, P. Zeman, R. Čerstvý

Department of Physics, Faculty of Applied Sciences, University of West Bohemia, Univerzitní 22, 306 14 Plzeň, Czech Republic

ARTICLE INFO

Article history:
Received 8 October 2008
Accepted in revised form 26 November 2008
Available online 3 December 2008

Keywords:
Oxide nanocomposite
Mechanical properties
Thermal cycling
Substrate oxidation
Magnetron sputtering

ABSTRACT

The article reports on the evolution of the structure, mechanical properties and protection ability of 7 µm thick Zr-containing SiO_2 coatings during thermal cycling in air. The films were reactively sputtered from a composed target (a Si plate fixed by a Zr ring with inner diameter $Ø_{inZr}=20$ mm) using a closed magnetic field dual magnetron system operated in AC pulse mode. Main attention is devoted to the investigation of the effect of the film structure on the thermal stability of the mechanical properties and the protection of the substrate. Only the SiO_2 film with a low content of Zr was investigated in detail. It was found that (1) the $Si_{31}Zr_5O_{64}$ film sputtered at the substrate temperature $T_s=500$ °C is amorphous, (2) the structure of the $Si_{31}Zr_5O_{64}$ film gradually changes during thermal annealing in air from the amorphous to that containing a crystalline t-ZrO_2 phase, (3) the t-ZrO_2 phase is stable in wide range of T_a up to 1500 °C and no conversion of the t-ZrO_2 phase into the m-ZrO_2 phase is observed during subsequent cooling to room temperature (RT), (4) the hardness H and effective Young's modulus E^* of the $Si_{31}Zr_5O_{64}$ film are thermally stable during heating at temperatures ranging from the RT up to 1400 °C and (5) the $Si_{31}Zr_5O_{64}$ film interacts with the Al_2O_3 substrate forming a mixture of t-ZrO_2+m-ZrO_2+SiO_2+$Al_6Si_2O_{13}$ on the substrate surface at annealing temperatures $T_a \geq 1500$ °C. Main issue of this investigation is the finding that the properties of a protective coating do not change during thermal cycling as far the structure of a coating is unchanged during the increase and decrease of the annealing temperature T_a.

1. Introduction

In recent years a great attention has been devoted to the investigation of thermal stability of hard protective and functional nanocomposite coatings with the aim to develop new advanced coatings thermally stable at temperatures above 1000 °C [1–12]. Three fundamental issues can be drawn from these investigations:

1. Properties of the coating vary in concert with the variation of its elemental and phase composition. For instance, in the TM-Si–N coating the amount of N strongly influences not only its phase composition but also the stoichiometry x of TMN_x transition metal nitride; here x=N/TM. The amorphous TM-Si–N nanocomposite coating with overstoichiometric $TMN_{x>1}$ phase is thermally stable to higher temperatures compared to that with substoichiometric $TMN_{x<1}$ phase. More details are given in references [9,12].
2. High-temperature protection function (HTPF) of best polycrystalline coatings does not exceed 1000 °C due to accelerated diffusion of oxygen along grain boundaries. A small improvement in HTPF can be achieved if grains are separated by a thin amorphous tissue phase which prevents a penetration of external atmosphere along grains.
3. Two new groups of amorphous coatings–(i) a-Si_3N_4/MeN silicon nitride-based composites and (ii) Si–B–C–N composites–thermally stable up to ~1500 and ~1700 °C, respectively, have been developed. These amorphous coatings due to absence of grains (no diffusion of oxygen from an external atmosphere to a substrate) ensure an excellent protection of a substrate against oxidation up to a temperature of ~1500 °C, at which the coating material starts to crystallize. The hardness H of these amorphous coatings exceeds 20 GPa, which is sufficiently high for many applications being realized.

However, every amorphous structure converts first to the nanocrystalline and later to crystalline when the operation temperature T achieves or exceeds the crystallization temperature T_{cr} of the coating material. The crystallization process results in the formation of coatings with new properties. Very important is also the fact that the structure of a coating changes at temperatures $T \geq T_{cr}$. The conversion of one type of structure to another one is most dangerous for the thermal stability of a coating because the change in the structure is accompanied with the change of the volume of grains resulting in cracking of a coating. That is a reason why it is of a vital importance to develop new material systems which ensure no transformation of the coating structure in a wide temperature range, especially at $T>1000$ °C.

Recent trends in the development of coatings which protect substrates against oxidation at temperatures above 1000 °C are summarized in Fig. 1. Crystalline coatings (Fig. 1a) enable the

---

* Corresponding author. Tel.: +420 377 63 2200; fax: +420 377 63 2202.
E-mail address: musil@kfy.zcu.cz (J. Musil).

0257-8972/$ – see front matter © 2008 Elsevier B.V. All rights reserved.
doi:10.1016/j.surfcoat.2008.11.026

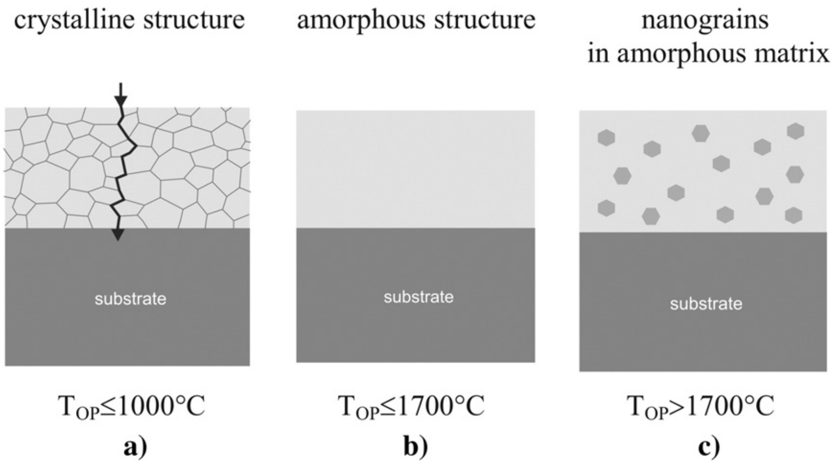

Fig. 1. Improvement of the oxidation protection (OP) of a substrate by changing of nanostructure of coating [9–13]. To our knowledge, Si–B–C–N coatings exhibit an amorphous structure up to 1700 °C [12].

connection of an external atmosphere with a substrate along grain boundaries and thus their protection ability is low. On the contrary, amorphous coatings (Fig. 1b) exhibit the best protection of a substrate against oxidation. The protection ability of an amorphous coating is, however, limited by its complete crystallization. Therefore, nanocomposite coatings composed of a small amount of nanograins embedded in an amorphous matrix offer still a great potential in the protection of substrates against oxidation. The nanograins are not in a mutual contact, there is no direct connection between an external atmosphere and a substrate (Fig. 1c), and still a good protection of a substrate against oxidation is ensured above the crystallization temperature of amorphous coatings. Moreover, the hardness of these nanocomposite coatings is expected to be increased due to an incorporation of nanograins.

The aim of this article is to demonstrate that (1) a coating with nanocrystalline structure can also protect a substrate against oxidation if there is no contact of an external atmosphere with a substrate as shown in Fig. 1c and (2) it is possible to create a protective coating thermally stable at annealing temperatures T_a above 1000 °C (no change in its properties) as far as the crystalline structure of a coating will not be changed to another one. The Si–Zr–O system was selected for this experiment due to (i) chemical stability of SiO_2 at high temperatures and low price of Si and (ii) easy crystallization of amorphous ZrO_2 at around 500 °C. There are several papers which have dealt with on the Si–Zr–O films [14–21]. However, no paper has reported on the thermal stability of mechanical properties of the Si–Zr–O coatings and an efficient protection of a substrate against oxidation using this coating so far.

2. Experimental

The Si–Zr–O thin films were reactively sputtered in an $Ar+O_2$ mixture using a closed dual magnetron equipped with a composed Si–Zr target (Ø=50 mm) consisting of a Si plate (Ø=28 mm, 4 mm thick) fixed with a Zr (99.9%) ring of inner diameter $Ø_{\text{in Zr}}=20$ mm. The magnetron was operated in AC pulse mode generated by a pulse power supply DORA MSS-10 with maximum output power 10 kW. The repetition frequency f_r of the pulses was 2 kHz and the AC frequency inside pulses was 56 kHz. The magnetron discharge current I_d was controlled by the duty cycle of 2 kHz pulses. More details are given in reference [22]. The Si–Zr–O films were sputtered under the following conditions: averaged discharge current $I_{da}=1$ A, averaged discharge power $P=1$ kW, substrate bias voltage $U_s=U_{fl}$, substrate temperature $T_s=500$ °C, substrate-to-target distance $d_{s-t}=80$ mm, partial pressure of oxygen $p_{O2}=0.1$ Pa and total pressure $p_T=p_{Ar}+p_{O2}=1$ Pa; here U_{fl} is the floating potential. The films sputtered under these deposition conditions have the following elemental composition: 31 at.% Si, 5 at.% Zr and 64 at.% O. The 7 μm thick $Si_{31}Zr_5O_{64}$ films were deposited on Si(100) ($30\times5\times0.4$ mm^3 and $10\times10\times0.4$ mm^3) and sapphire ($10\times10\times0.5$ mm^3) substrates with the deposition rate $a_D=100$ nm/min.

The film thickness h was measured using a stylus profilometer DEKTAK 8. The film structure was characterized using an XRD spectrometer PANalytical X Pert PRO in Bragg–Brentano configuration with CuKα radiation. The elemental composition was determined by X-ray Fluorescence (XRF) spectroscopy with a PANalytical XRF Spectrometer MagiX PRO. Mechanical properties were determined from load vs. displacement curves measured by a microhardness tester Fischerscope H100 with a Vicker´s diamond indenter at a load $L=20$ mN. The oxidation resistance was measured in flowing air (1 l/h) using a symmetrical high-resolution Setaram thermogravimetric system TAG 2400. The thermal annealing cycle consisted of two or three steps, i.e. the heating from RT to a predetermined annealing temperature $T_{a\ max}$ and immediate cooling down RT or the heating from RT to a predetermined annealing temperature $T_{a\ max}$, annealing at of $T_{a\ max}$ for selected annealing time t_a and cooling down from $T_{a\ max}$ down to RT. The thermal cycles used in the oxidation tests of the Si–Zr–O coatings/sapphire substrate couples are defined in Fig. 2 and are denoted as “heating I”, “heating II” and “heating III”. The heating and cooling rates were 10 and 30 °C/min, respectively. The repetition of thermal annealing is called the thermal cycling. The measurements of all parameters of as-sputtered and annealed Si–Zr–O films were performed with accuracy better than 10%.

3. Results and discussion

3.1. Crystallization induced by thermal annealing

The as-sputtered $Si_{31}Zr_5O_{64}$ films were thermally annealed (with the temperature cycle “heating I”) to annealing temperatures $T_{a\ max}$

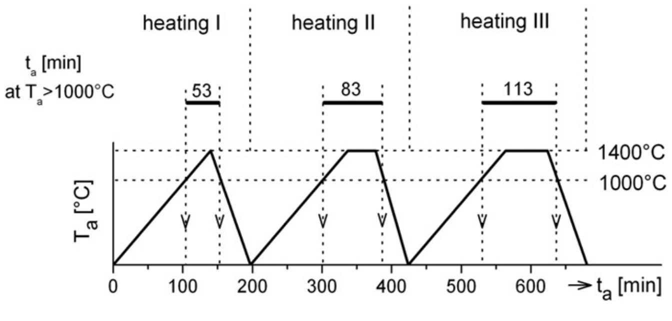

Fig. 2. Evolution of annealing temperature T_a with annealing time t_a used in thermal cycling of $Si_{31}Zr_5O_{64}$ film/substrate couples.

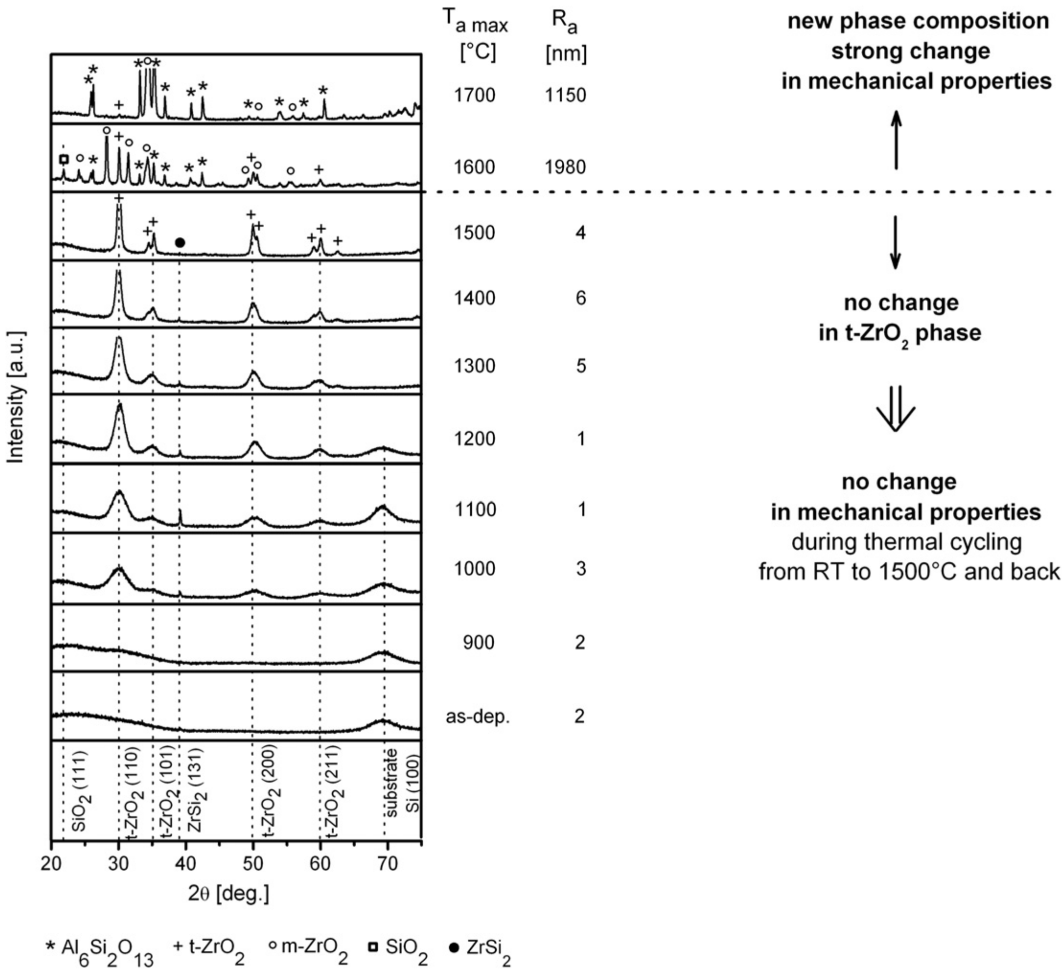

Fig. 3. Evolution of structure and roughness R_a of $Si_{31}Zr_5O_{64}$ film with increasing maximum annealing temperature $T_{a\ max}$.

ranging from 900 up to 1700 °C. The $Si_{31}Zr_5O_{64}$ films sputtered on the Si(100) substrate were annealed to $T_a = 1300$ °C only to avoid melting of silicon ($T_{m\ Si} = 1420$ °C). The $Si_{31}Zr_5O_{64}$ films sputtered on the sapphire substrate were annealed with maximum temperatures between 1300 °C and 1700 °C. Fig. 3 displays the evolution of the film structure, characterized with X-ray diffraction patterns measured at room temperature (RT) after thermal annealing to a given $T_{a\ max}$. Note that a new as-deposited $Si_{31}Zr_5O_{64}$ film of the same (i) elemental composition and (ii) thickness h was used for each annealing experiment. Main results of these experiments can be summarized as follows.

1. Nanocrystallization from amorphous phase starts above 900 °C, when the $t\text{-}ZrO_2$ phase crystallizes.
2. Small $t\text{-}ZrO_2$ grains are detected at $T_{a\ max} \approx 1000$ °C. Intensities of X-ray reflections from these grains are superposed on an X-ray amorphous background and increase with increasing annealing temperature $T_{a\ max}$. Low roughness of thermally annealed $Si_{31}Zr_5O_{64}$ films may indicate that ZrO_2 grains are embedded in an $a\text{-}SiO_{2-x}$ matrix.
3. After crystallization the $Si_{31}Zr_5O_{64}$ film with the $t\text{-}ZrO_2$ structure is thermally stable (no conversion to $m\text{-}ZrO_2$) in a wide range of temperatures $T_{a\ max}$ from RT up to 1500 °C.
4. The increase of intensity and the decrease of width of X-ray reflections from the $t\text{-}ZrO_2$ grains with increasing annealing temperature $T_{a\ max}$ indicate their growth. Also, a formation of new $t\text{-}ZrO_2$ grains after the decomposition of $ZrSi_2$ grains very probably contributes to the increase of X-ray reflections from the $t\text{-}ZrO_2$ grains. However, a separation of both effects on the increase of the intensities of X-ray reflections, i.e. the growth of the $t\text{-}ZrO_2$ grains and the rise of new ones, requires a more detailed investigation which is out of scope of this paper and which will be carried out in the near future. The growth of the intensities of X-ray reflections from $t\text{-}ZrO_2$ stops at ~1500 °C due to an interaction between SiO_2 from the film and the Al_2O_3 substrate which results in (i) a formation of $Al_5Si_2O_{13}$ ($3Al_2O_3 \cdot 2\ SiO_2$) mullite phase and (ii) a strong increase of the surface roughness R_a at $T_a \approx 1500$ °C.
5. A mixture of $t\text{-}ZrO_2 + m\text{-}ZrO_2 + Al_6Si_2O_{13} + SiO_2$ phases is created on the substrate surface at $T_a > 1500$ °C.

Obtained results indicate that no dramatic changes in properties of the $Si_{31}Zr_5O_{64}$ film should take place up to ~1500 °C because the film exhibits no change in the $t\text{-}ZrO_2$ structure up to ~1500 °C. The correctness of this hypothesis was confirmed by measurements of mechanical properties of the $Si_{31}Zr_5O_{64}$ film after its thermal cycling.

3.2. Effect of annealing time on film structure

The time of thermal annealing t_a can also influence the film structure. Therefore, the $Si_{31}Zr_5O_{64}$ film was thermally annealed with 1 cycle ("heating I"), 2 cycles ("heating I" + "heating II") and 3 cycles ("heating I" + "heating II" + "heating III") as a function of the annealing time t_a at (i) $T_{a\ max} = 1400$ °C (isothermal annealing) and (ii) $T_a > 1000$ °C (the increase of T_a from 1000 °C to 1400 °C + isothermal annealing at 1400 °C + the decrease of T_a from 1400 °C to 1000 °C as defined in Fig. 2). The same test piece was used for each annealing experiment. XRD patterns from the thermally annealed $Si_{31}Zr_5O_{64}$ film measured at RT are displayed in Fig. 4.

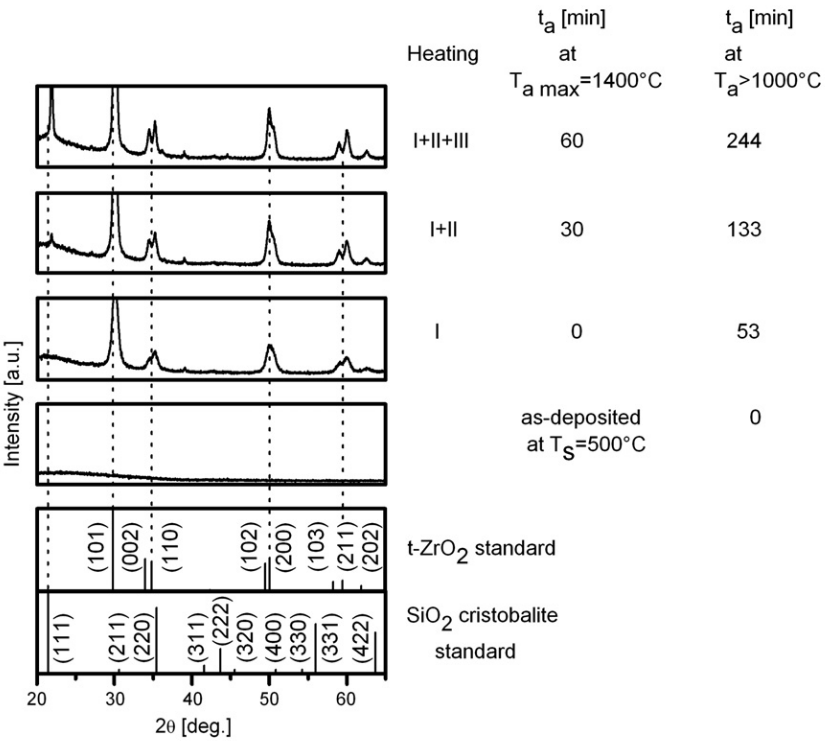

Fig. 4. Evolution of the structure of the $Si_{31}Zr_5O_{64}$ film on the sapphire substrate with increasing annealing time t_a at (i) maximum temperature $T_{a\ max}=1400$ °C (isothermal annealing) and (ii) $T_a>1000$ °C (the increase of T_a from 1000 °C to 1400 °C + isothermal annealing at 1400 °C + the decrease of T_a from 1400 °C to 1000 °C.

Experimental data displayed in Fig. 4 show that thermal annealing during thermal cycling up to the maximum temperature $T_{a\ max}=1400$ °C results in a fast crystallization of the as-deposited $Si_{31}Zr_5O_{64}$ film, when the t-ZrO_2 phase crystallizes initially and just after longer exposure of the film to temperatures $T_a \geq 1000$ °C, in our case at $t_a \geq 133$ min, crystalline SiO_2(111) grains are formed and their amount in the film increases with increasing t_a as indicated by an increasing intensity of the SiO_2(111) reflection.

3.3. Mechanical properties of $Si_{31}Zr_5O_{64}$ film

The hardness H and effective Young´s modulus $E^*=E/(1-\nu^2)$ of the $Si_{31}Zr_5O_{64}$ film sputtered on the sapphire substrate after annealing up to $T_{a\ max}=1400$ °C as a function of the annealing time t_a at $T_a>1000$ °C is displayed in Fig. 5; here E is the Young´s modulus and ν is the Poisson´s ratio. The annealing time t_a was increased by using 1 cycle ("heating I", $t_a=53$ min), 2 cycles ("heating I" + "heating II", $t_a=136$ min) and 3 cycles ("heating I" + "heating II" + "heating III", $t_a=249$ min). The thermally annealed $Si_{31}Zr_5O_{64}$ film exhibits a higher hardness ($H \approx 10$–11 GPa) compared to that of the as-deposited amorphous $Si_{31}Zr_5O_{64}$ film ($H \approx 8$ GPa). This is due to a thermally induced conversion of the amorphous structure to the crystalline one.

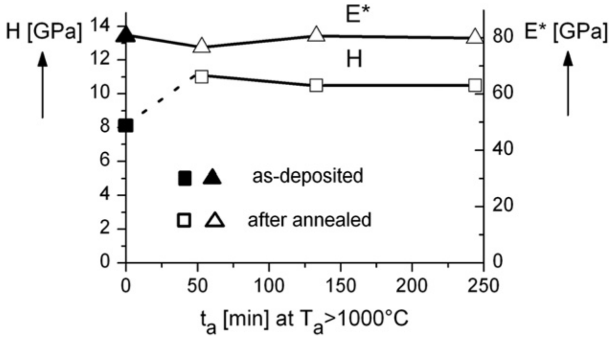

Fig. 5. Hardness H and effective Young's modulus E^* of the $Si_{31}Zr_5O_{64}$ film on the sapphire substrate after thermal cycling from RT to $T_{a\ max}=1400$ °C and back to RT in flowing air as a function of annealing time t_a at $T_a>1000$ °C.

A main result of this experiment is the fact that the values of H and E^* of the film thermally annealed at $T_{a\ max}=1400$ °C do not change significantly with increasing annealing time t_a as soon as the nanocrystallization has taken place during heating to temperatures above 900 °C. This is possible because $T_{a\ max}=1400$ °C is sufficiently far away from the temperature T_{sc} at which one structure of the film changes to another one. In our case the temperature T_{sc} at which the structure conversion takes place is ~1500 °C. The nearness of T_a to T_{sc} is very important for the thermal stability of the film properties because the thermal stability of film properties decreases with approaching temperature T_a to T_{sc}. This behaviour of the thermal stability has been already demonstrated for the Al–Si–N films [22] and is of great practical importance.

The measured values of H, E^* and the resistance to plastic deformation characterized by the ratio H^3/E^{*2} are summarized in Table 1. The values of the ratio H^3/E^{*2} of thermally annealed (with the temperature cycle "heating I") crystalline $Si_{31}Zr_5O_{64}$ films are more than two times greater than those of the as-deposited amorphous

Table 1
Comparison of mechanical properties of as-deposited ($T_s=500$ °C) and thermally annealed (with the temperature cycle "heating I") 7 µm thick $Si_{31}Zr_5O_{64}$ films sputtered on the Si(100) and sapphire substrates

$T_{a\ max}$ [°C]	Substrate	H [GPa]	E^* [GPa]	W_e [%]	H^3/E^{*2} [GPa]
As-deposited	Si(100)	7.8	80	57	0.075
900	Si(100)	8.7	78	62	0.109
1000	Si(100)	9.8	77	68	0.160
1150	Si(100)	10.2	79	70	0.172
1200	Si(100)	10.2	77	71	0.178
1300	Si(100)	10.1	78	70	0.172
As-deposited	Sapphire	8.1	81	58	0.081
1400	Sapphire	11.0	77	77	0.227

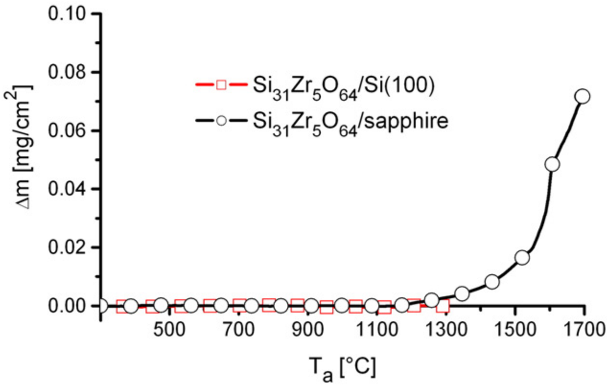

Fig. 6. Increase of mass Δm of (i) 7 µm thick $Si_{31}Zr_5O_{64}$ film/Si(100) substrate and (ii) 7 µm thick $Si_{31}Zr_5O_{64}$ film/sapphire substrate couples after thermal annealing (with the temperature cycle "heating I") in flowing air as a function of annealing temperature T_a.

$Si_{31}Zr_5O_{64}$ films. A higher value of the ratio H^3/E^{*2} indicates that the conversion of the amorphous structure to the nanocrystalline or crystalline one during heating to temperatures above 900 °C improves the toughness of the film [23]. Now, it remains to show if the oxidation resistance of the $Si_{31}Zr_5O_{64}$ film/substrate couple is also influenced by the conversion of the t-ZrO_2 phase of the $Si_{31}Zr_5O_{64}$ film to a mixture of t-ZrO_2 + m-ZrO_2 + $Al_6Si_2O_{13}$ + SiO_2 phases created on the substrate surface at $T_a > 1500$ °C.

3.4. Oxidation resistance of $Si_{31}Zr_5O_{64}$ film/substrate couple

The oxidation resistance of the $Si_{31}Zr_5O_{64}$ film/substrate couple was tested for two systems: (1) the $Si_{31}Zr_5O_{64}$ film/Si(100) substrate and (2) the $Si_{31}Zr_5O_{64}$ film/sapphire substrate. Both substrates were coated only on one side and oxidation of the uncoated backside of the substrate was subtracted. The oxidation resistance is represented by the change of mass Δm of the $Si_{31}Zr_5O_{64}$ film/substrate couple after thermal annealing to a maximum annealing temperature $T_{a\ max}$. The system (1) was annealed to $T_{a\ max} = 1300$ °C (a thermal limit of the Si substrate) and the system (2) to $T_{a\ max} = 1700$ °C (a thermal limit of the Setaram thermogravimeter operated in air). Results of the measurements of the oxidation resistance of these two systems in flowing air are displayed in Fig. 6.

From Fig. 6 it is seen that the $Si_{31}Zr_5O_{64}$ film/Si(100) substrate couple exhibits no increase in mass ($\Delta m = 0$ mg/cm^2), i.e. neither the film nor the Si(100) substrate side underneath the film are oxidized in flowing air up to $T_a \approx 1300$ °C (a thermal limit of the Si substrate). The $Si_{31}Zr_5O_{64}$ film sufficiently protects the Si(100) substrate against oxidation. The $Si_{31}Zr_5O_{64}$ film/sapphire substrate couple also exhibits no increase in mass ($\Delta m = 0$ mg/cm^2) up to $T_a \approx 1250$ °C. The oxidation of the film/sapphire substrate couple starts at around 1250 °C. A slow increase in Δm with increasing T_a is observed in the range from ~1250 to ~1550 °C and a more rapid increase in Δm is observed at $T_a > 1550$ °C.

The $Si_{31}Zr_5O_{64}$ films were sputtered at a high deposition rate ($a_D = 100$ nm/min) in the transition mode of sputtering, i.e. at relatively low values of partial pressure of oxygen when there is a deficiency of atomic oxygen to form stoichiometric SiO_2 oxide. This is well known fact in reactive sputtering of oxides. This means that the as-deposited $Si_{31}Zr_5O_{64}$ films are composed of the stoichiometric ZrO_2 and sub-stoichiometric SiO_{2-x} due to preferential bonding of oxygen to Zr. The stoichiometric ZrO_2 phase is formed because of a higher negative value of the heat of formation compared to that of the SiO_2 phase: $\Delta H_{ZrO2} = -1101.3$ kJ/mol and $\Delta H_{SiO2} = -910.9$ kJ/mol. Based on these facts it can be concluded that the increase in Δm of the $Si_{31}Zr_5O_{64}$ film/sapphire substrate couple is due to oxidation of substoichiometric SiO_{2-x} oxide.

Also, it is worthwhile to note that the increase in mass at $T_a \approx 1550$ °C is very low ($\Delta m \approx 0.02$ mg/cm^2) and decreases with decreasing T_a.

4. Conclusions

The thermal stability of the structure and mechanical properties and oxidation resistance of a reactively sputtered $Si_{31}Zr_5O_{64}$ coating was investigated in detail. The main attention was concentrated on the effect of high-temperature annealing on the interrelationship between the structure and phase composition of the coating and its (i) mechanical properties and (ii) ability to protect the substrate against oxidation. Obtained results can be summarized as follows:

The 7 µm thick $Si_{31}Zr_5O_{64}$ coating reactively sputtered at the substrate temperature $T_s = 500$ °C with a high deposition rate $a_D = 100$ nm/min at the substrate-to-target distance $d_{s-t} = 80$ mm is amorphous. During annealing in air, its amorphous structure starts to nanocrystallize at approximately 900 °C and the t-ZrO_2 phase forms. The t-ZrO_2 phase is stable in a wide range of T_a up to 1500 °C. The $Si_{31}Zr_5O_{64}$ coating/sapphire substrate couple is resistant to the thermal cycling ("heating I" + "heating II" + "heating III") up to $T_{a\ max} \approx 1400$ °C. No significant change in mechanical properties of this coating was observed during annealing at $T_a > 1000$ °C for up to 4 h as soon as a nanocrystalline structure formed during initial heating above 900 °C. The $Si_{31}Zr_5O_{64}$ coating/sapphire substrate couple exhibits (1) almost zero oxidation ($\Delta m \leq 0.02$ mg/cm^2) up to 1500 °C due to the stability of the t-ZrO_2 phase in a wide range of T_a from ~900 to ~1500 °C and a small amount of Zr in the coating, and (2) hardness $H = 10.5$ GPa, effective Young's modulus $E^* = 80$ GPa and the ratio $H^3/E^{*2} = 0.18$ GPa.

The protection of a substrate against oxidation with the Zr-containing SiO_2 coating is fully comparable with that of amorphous a-Si_3N_4/MeN coatings with a high (>50 vol.%) content of the Si_3N_4 phase. However, a higher crystallization temperature T_{cr} of some oxides compared to that of the Si_3N_4 nitride indicates that new nanocomposite coatings based on oxides with an efficient protection of the substrate against oxidation in flowing air at temperatures above 1500 °C could be developed in the near future.

Based on the obtained results it can be expected that (1) the properties of the hard protective coating will not change during thermal cycling in air as far its structure is unchanged during increasing and decreasing the annealing temperature T_a and (2) new material systems exhibiting no change in the phase composition will be developed if their elemental composition is correctly selected.

Acknowledgements

This work was supported in part by the Ministry of Education of the Czech Republic under Project MSM No. 4977751302 and in part by the Grant Agency of the Czech Republic under the Project No. 106/06/0327.

References

[1] I. Wadsworth, I.J. Smith, L.A. Donohue, W.-D. Munz, Surf. Coat. Technol. 94-95 (1997) 315.
[2] L. Hultman, Vacuum 57 (1) (2000) 1.
[3] R.A. Andrievski, Russ. Chem. Rev. 71 (10) (2002) 853.
[4] A. Niederhofer, T. Bolom, P. Nesladek, K. Moto, C. Eggs, D.S. Patil, S. Veprek, Surf. Coat. Technol. 146–147 (2001) 183.
[5] S. Veprek, M.G.J. Veprek-Hejman, P. Karvankova, J. Prochazka, Thin Solid Films 476 (2005) 1.
[6] R.A. Andrievski, Russ. Chem. Rev. 74 (12) (2005) 1061.
[7] A. Raveh, I. Zukerman, R. Shneck, R. Avni, I. Fried, Surf. Coat. Technol. 201 (2007) 6136.
[8] J. Vlcek, S. Potocky, J. Cizek, J. Houska, V. Perina, J. Zemek, Y. Setsuhara, S. Konuma, J. Vac. Sci. Technol. A23 (6) (2005) 1513.
[9] J. Musil, P. Zeman, Solid State Phenom. 127 (2007) 31.
[10] J. Musil, Properties of hard nanocomposite thin films, Invited Chapter 5 in the book "Nanocomposite films and coatings", S.Zhang and N.Ali (Eds.), 2007, Imperial College Press, Coven Garden London WC2 9HE, London, UK, 281.
[11] J. Musil, P. Baroch, P. Zeman, Hard nanocomposite coatings. Present status and trends, Chapter 1, in: R. Wei (Ed.), Plasma Surface Engineering Research and its Practical Applications, Research Signpost Publisher, India, 2008, p. 1.
[12] J. Musil, J. Vlcek, P. Zeman, Adv. Appl. Ceram. 107 (3) (2008) 148.

[13] J. Musil: X-ray amorphous coatings with thermal stability above 1000 °C, Invited lecture at the 5th High power impulse magnetron sputtering (HIPIMS) Conference 2008, 8–9 July 2008, Venlo, the Netherlands.
[14] W.C. Butterman, W.R. Foster, Am. Mineral. 52 (1967) 880.
[15] T. Wakasugi, A. Wannagon, R. Ota, T. Horai, T. Itakura, J. Fukunaga, Mater. Sci. Res. Int. 5 (1999) 38.
[16] T. Hanada, N. Soga, M. Ohkawa, Advance in Ceramics, Science and Technology of Zirconia III 24 (1988) 319.
[17] D.H. Kuo, C.H. Chien, C.H. Huang, Thin Solid Films 420–421 (2002) 47.
[18] S.B. Amor, B. Rogier, B. Baud, M. Jacquet, M. Nardin, Mater. Sci. Eng. B, Solid-State Mater. Adv. Technol. 57 (1998) 28.
[19] M. Houssa, M. Naili, C. Zhao, H. Bender, M.M. Heyns, A. Stesmans, Semicond. Sci. Technol. 16 (2001) 31.
[20] F.J. Ferrer, F. Yubero, J.A. Meji´as, F.J. Garci´a-Lopez, A.R. Gonza´lez-Elipe, J. Appl. Phys. 102 (2007) 8.
[21] A. Sawa, K. Nakanishi, T. Hanada, Thin Solid Films 516 (2008) 4665.
[22] J. Musil, M. Šašek, P. Zeman, R. Čerstvý, D. Heřman, J.G. Han, V. Šatava, Surf. Coat. Technol. 202 (2008) 3485.
[23] J. Musil, M. Jirout, Surf. Coat. Technol. 201 (2007) 5148.

3.1.4 A-IV: Thermal stability of magnetron sputtered Si-B-C-N materials at temperatures up to 1700 °C

Thin Solid Films 519 (2010) 306–311

Contents lists available at ScienceDirect

Thin Solid Films

journal homepage: www.elsevier.com/locate/tsf

Thermal stability of magnetron sputtered Si–B–C–N materials at temperatures up to 1700 °C

P. Zeman *, J. Čapek, R. Čerstvý, J. Vlček

Department of Physics, University of West Bohemia, Univerzitní 22, 306 14 Plzeň, Czech Republic

ARTICLE INFO

Article history:
Received 15 January 2010
Received in revised form 14 June 2010
Accepted 12 August 2010
Available online 20 August 2010

Keywords:
Si–B–C–N films
Thin films
Thermal stability
Differential scanning calorimetry
Thermogravimetry
X-ray diffraction
Reactive sputtering

ABSTRACT

Thermal stability of deposited Si–B–C–N materials (film fragments or powders without a substrate) in inert gases (He and Ar) up to 1700 °C was investigated using differential scanning calorimetry, high-resolution thermogravimetry and X-ray diffraction measurements. Amorphous Si–B–C–N films were fabricated by dc magnetron co-sputtering of a single B_4C–Si target in two nitrogen–argon gas mixtures (50% $N_2 + 50\%$ Ar or 25% $N_2 + 75\%$ Ar). It was found that the deposited Si–B–C–N materials can be more stable at high temperatures in the inert atmosphere than the usually used substrates (e.g. SiC or BN). The materials with the compositions (in at.%) $Si_{32-33}B_{10}C_2N_{50-51}$, for which $N/(Si+B+C) = 1.1$–1.2, retained their amorphous structure up to 1600 °C without any structural transformations and detectable mass changes.

1. Introduction

A crucial factor of many industrial sectors is the ability to operate at high temperatures. For that reason, advanced high-temperature materials with heat-resistant capabilities are being extensively developed. Recently, amorphous Si–B–C–N materials have been found to accomplish such demands due to their extraordinary high-temperature stability and oxidation resistance (see, for example, [1–5]). So far, the amorphous Si–B–C–N ceramics have been prepared by thermolysis of polymeric precursors as a powder material [1–5] or by coating technologies, including plasma-assisted chemical vapor deposition [6,7] and reactive magnetron sputtering [8–16], as a thin-film material.

Reactive magnetron sputtering allows one to operate at much lower substrate temperatures in the absence of hydrogen-containing precursors. Its further advantages are compatibility with semiconductor and other high technologies and ease of scaling up to larger substrate sizes.

In our previous papers, high oxidation resistance of Si–B–C–N films in flowing air up to 1300–1350 °C [8,16], and even at temperatures exceeding 1500 °C [13,14] has been reported. The Si–B–C–N films prepared using optimized process parameters (B_4C–Si target with a 75% Si fraction in an erosion area, 50% $N_2 + 50\%$ Ar gas mixture, rf induced negative substrate bias voltage of −100 V and substrate temperature of 350 °C) retained their amorphous structure during heat treatment in air up to 1700 °C. A relatively low mass gain (<0.05 mg/cm^2) measured at 1700 °C was caused by the growth of an oxide surface layer, being composed mainly of Si and O with a B content. The elemental composition of the Si–B–C–N bulk underneath the oxide layer remained, however, unchanged [13].

Based on these results, the present paper deals with thermal stability of Si–B–C–N films in inert gases. Our aim was to investigate, by means of differential scanning calorimetry, high-resolution thermogravimetry and X-ray diffraction measurements, the processes occurring in the Si–B–C–N materials during their controlled heating up to 1700 °C.

2. Experimental details

The Si–B–C–N films, selected for thermal stability investigations, were deposited using reactive dc magnetron co-sputtering of silicon, boron and carbon from a single B_4C–Si target in nitrogen–argon mixtures. The target was formed by a B_4C plate (thickness of 6 mm) overlapped by p-type Si stripes with fixed 25% $B_4C + 75\%$ Si fractions in the target erosion area. The total pressure of 0.5 Pa was kept constant during the depositions of all the films. Two different Ar fractions (50% and 75%) in the gas mixture were used at fixed values of the negative substrate bias voltage $V_b = -100$ V induced by an rf generator operating at a frequency of 13.56 MHz, and of the substrate temperature $T_s = 350$ °C adjusted by an Ohmic heater. Moreover, the films were prepared in a 50% $N_2 + 50\%$ Ar gas mixture with the substrate on a floating potential $V_f = -34$ V and T_s in the range from

---

* Corresponding author. Tel.: +420 377 63 22 11; fax: +420 377 63 22 02.
E-mail address: zemanp@kfy.zcu.cz (P. Zeman).

0040-6090/$ – see front matter © 2010 Elsevier B.V. All rights reserved.
doi:10.1016/j.tsf.2010.08.080

190 to 250 °C (without the heater). The values of the process parameters for all the films investigated are summarized in Table 1. For more details concerning the deposition process, see our previous papers [8,10,13].

The thermal analysis of the films was carried out independently using two devices. A Setaram Labsys DSC 1600 system was used for differential scanning calorimetry (DSC) in flowing argon up to 1600 °C and a symmetrical high-resolution Setaram TAG 2400 system for thermogravimetry (TG) in flowing helium up to 1700 °C. The flow of both inert gases was set to approximately 1 l/h. Dynamic heating was performed with a heating and cooling rate of 40 and 40 °C min^{-1}, respectively, for DSC and 10 and 30 °C min^{-1}, respectively, for TG.

To obtain a sufficient DSC signal and to exclude an influence of a substrate, approximately 4 µm thick films were deposited onto polished and ultrasonically pre-cleaned Cu substrates ($25 \times 40 \times 0.5$ mm^3), which were subsequently chemically removed using nitric acid with a concentration of 25%. After filtering, washing in water and drying, freestanding film fragments were mechanically ground in an agate mortar to provide a fine powder. An approximately 8 mg mass of the powder was charged into a 100 µl alumina crucible covered with a lid and used for each DSC measurement. The identical uncharged crucible was used as a reference. Each run was immediately followed by a second run under the same conditions to serve as a baseline.

To investigate mass changes during controlled heating in helium, the films were deposited onto polished and ultrasonically pre-cleaned single-crystalline SiC substrates, similarly as in case of our recent oxidation tests in air [13]. Unfortunately, the thermal stability of the SiC substrate during heating to 1700 °C in helium was insufficient due to a mass loss above 1400 °C. Similar behavior was revealed also for other (commercially available) pure non-oxide substrates, such as pyrolytic BN, graphite, CVD-diamond, WC, tungsten or Mo (see Fig. 1). The only substrate, which was resistant to the apparent degradation, was sapphire. However, a problem related to this substrate was connected with a mutual reaction between sapphire (Al_2O_3) and the Si–B–C–N film. It resulted in the formation of an $Al_2Si_8O_7N_8$ ceramic product at the substrate–film interface causing the film spallation. As a consequence of these findings, we decided to carry out TG measurements with only the freestanding film fragments (without their grinding) removed from the Cu substrates. This fact excluded to measure mechanical properties of the films after their cooling down. The total mass of the film fragments inside a 100 µl alumina crucible covered with a lid was about 1.5 mg for each TG measurement. The measured values of the mass changes were expressed per the total film surface area using known values of the film thickness and density. The TG values corresponding to the measurement with an empty alumina crucible under the same conditions, serving as a baseline, were subsequently subtracted from the TG values of each measured sample. The resulting curve represents the actual mass changes occurring in the film during its heating.

X-ray diffraction (XRD) measurements of as-deposited and annealed samples after their cooling down to a room temperature were carried out on a PANalytical X´Pert PRO diffractometer working in Bragg-Brentano configuration using Cu Kα radiation (λ = 0.154187 nm). Data were collected using an ultrafast detector X'Celerator with a scanning step size of 0.02° and a counting time of 50 s per step.

Table 1
The Ar fraction in the gas mixture, the substrate voltage, V_s, and the substrate temperature, T_s, used in depositions of the Si–B–C–N films investigated. V_b is the rf induced negative substrate bias voltage and V_f is the floating potential.

Si–B–C–N film	Ar fraction	V_s (V)	T_s (°C)
I	50%	$V_b = -100$ V	350
II	50%	$V_f = -34$ V	190–250
III	75%	$V_b = -100$ V	350

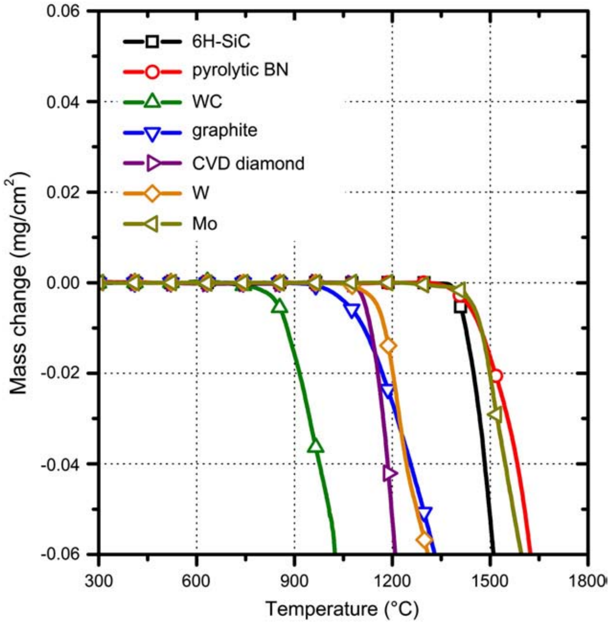

Fig. 1. Thermogravimetric curves for various pure non-oxide substrates annealed in helium up to 1700 °C at a heating rate of 10 °C min^{-1}.

The elemental composition of the films was determined by Rutherford backscattering spectrometry (RBS) and elastic recoil detection (ERD) methods. The Si, B, C, N, O and Ar contents were measured by RBS, and the H content was assessed by ERD. The accuracy of RBS is 1–2 at.% while that of ERD is approximately 0.1–0.2 at.% [13].

Film hardness, reduced Young's modulus, and elastic recovery were determined using an ultramicroindenter (Fischerscope H-100B) according to the ISO 14577-1:2002 E standard. The measurements were performed with a preset maximum load of 30 mN.

The film thickness and a bending of the silicon substrate after deposition of the film, from which a residual macrostress was determined using the modified Stoney's formula including the biaxial modulus of the substrate, were measured by profilometry (Dektak 8 Stylus Profiler, Veeco).

3. Results and discussion

The elemental composition of the as-deposited Si–B–C–N films investigated is presented in Table 2. As shown, the 50% Ar fraction in the gas mixture results in the concentration ratio of $N/(Si + B + C) = 1.1–1.2$ in films I and II with a low (≤5 at.%) total content of hydrogen and oxygen. The enlarged admixture (4 at.%) of hydrogen in the films produced at $V_s = V_f = -34$ V and $T_s = 190–250$ °C can be explained by a reduced ion-induced and thermal desorption of hydrogen from the surface of growing films. With the increased Ar fraction in the gas mixture from 50 to 75%, the Si content in the films raised from 32 to 40 at.% due to an enhanced physical sputtering of silicon from the composed B_4C–Si target [8]. A high affinity of nitrogen for silicon in

Table 2
The elemental composition (at.%) of the as-deposited Si–B–C–N films investigated.

Si–B–C–N film	Si	B	C	N	H	O	Ar	$\frac{N}{Si + B + C}$
I	32	10	2	51	2.4	2	0	1.16
II	33	10	2	50	4.0	1	0	1.11
III	40	11	2	43	1.4	2	1	0.81

the deposited material led to a relatively weak decrease (from 51 to 43 at.%) in the N content in the films in spite of the substantial decrease (2 times) in the N_2 partial pressure in the discharge gas. Taking into account practically constant contents of boron (10–11 at.%) and carbon (2 at.%) in all the films, we obtain a significantly different value of 0.8 for the N/(Si + B + C) concentration ratio in film III. The different values of the N/(Si + B + C) concentration ratio in the films produced under different experimental conditions (Table 1) do not cause substantial changes in the values of film hardness (22–24 GPa), reduced Young's modulus (164–191 GPa) and elastic recovery (72–74%) at a low compressive stress (0.6–1.0 GPa) in the films.

DSC analysis of the Si–B–C–N films provides information about changes occurring in the structure of the materials during their heating. Such changes are detected as exothermic or endothermic reaction peaks on the DSC curves due to crystallization, phase transformation, melting or other processes in materials. The measurements performed for three Si–B–C–N samples are displayed in Fig. 2 as two successive runs for each sample. As can be seen, there is no peak corresponding to any reactions occurring during the heating to 1600 °C for films I and II deposited in the 50% N_2 + 50% Ar gas mixture. The results indicate that the structure of these films retains its amorphous state without any pronounced changes. Such expectation was confirmed by the XRD measurements of the samples before and after annealing. The XRD patterns of the samples are given in Fig. 3. Both films I and II are characterized by very broad peaks with the corresponding values of 2θ between 20° and 40°, which indicate the amorphous state of the Si–B–C–N films before and after annealing. Two practically negligible XRD peaks, which can be recognized in the patterns at the positions of 26.65° and 28.41°, are assigned to silicon dioxide (quartz) and silicon [17], respectively. The Si (111) peak originates from a low-background substrate holder used in the X-ray diffractometer for the fixation of the sample, and the SiO_2 (101) peak is present as a consequence of a very low contamination, being introduced by grinding of the film fragments in an agate mortar. Although agate is a highly abrasive resistant and inert material minimizing the contamination during sample grinding in the mortar, an absolute elimination of the SiO_2 impurities is practically impossible. The presence of the SiO_2 crystallites, however, does not influence the behavior of the Si–B–C–N films during annealing at all.

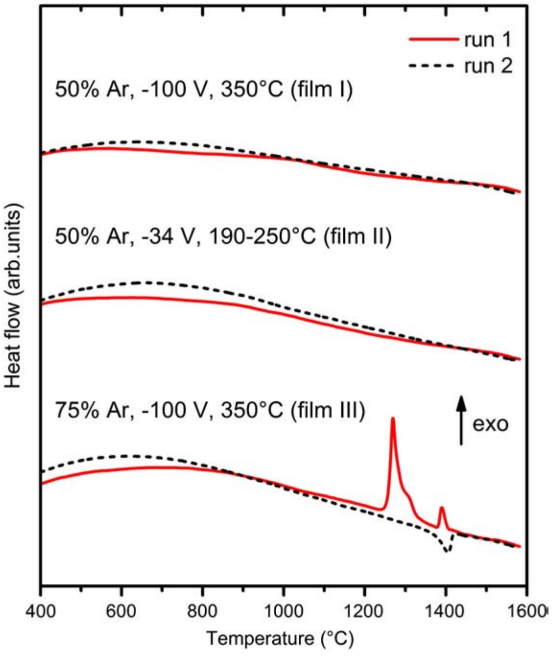

Fig. 2. DSC curves, including two successive runs, for the Si–B–C–N films in the form of powders (~8 mg) annealed in argon up to 1600 °C at a heating rate of 40 °C min^{-1}.

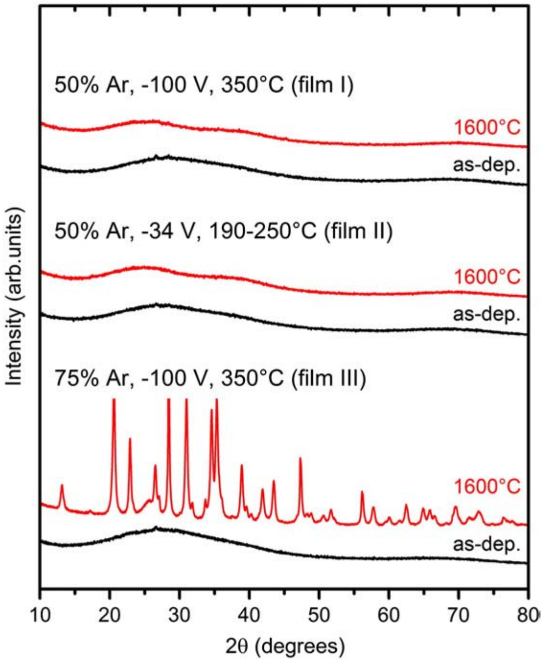

Fig. 3. XRD patterns taken from the Si–B–C–N film powders in as-deposited state and after the DSC measurements in argon up to 1600 °C.

The thermal stability of the Si–B–C–N film III deposited with the 75% Ar fraction in the gas mixture, $V_b = -100$ V and $T_s = 350$ °C is quite different from those of films I and II, as seen in Figs. 2 and 3. During the annealing, several exothermic reaction processes take place leading to a DSC signal with some overlapping peaks (run 1 in Fig. 2). These reactions, which are detected just above 1250 °C, result in crystallization of the amorphous structure of film III as evidenced from the XRD after the annealing to 1600 °C (see Fig. 3). Dominant X-ray diffraction peaks belong to the crystalline phases, identified as α-Si_3N_4, Si and β-Si_3N_4 according to the JCPDS database [17].

To relate the individual reactions in the film during annealing to evolution of its material structure, a more detailed investigation was carried out. The film was heated up to various characteristic temperatures in order to separate an effect of the individual reactions detected on the DSC curve in Fig. 4. Each DSC measurement was done with a new charge of the film material and after its cooling down the XRD was used to analyze changes in the material structure. As seen

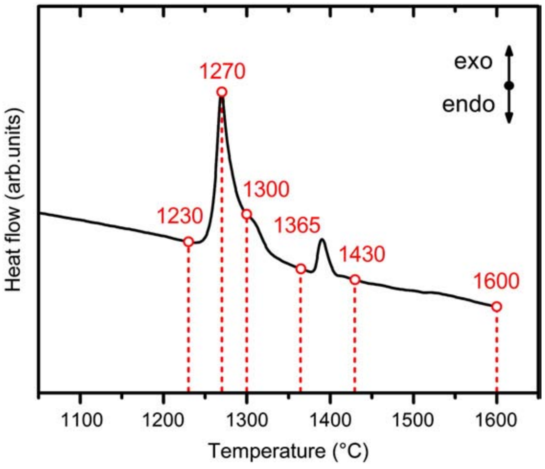

Fig. 4. A detail of the DSC curve for the Si–B–C–N film prepared at 75% Ar fraction in the gas mixture, substrate bias voltage of − 100 V and substrate temperature of 350 °C.

from the XRD patterns in Fig. 5, amorphous state of film III (deposited at the 75% Ar fraction in the gas mixture, $V_b = -100$ V and $T_s = 350$ °C) is retained up to 1230 °C when the heat flow signal starts to grow up, resulting in appearance of the first exothermic peak. This peak is assigned to crystallization of the α-Si_3N_4 phase, as evidenced in the pattern acquired after cooling down from the corresponding temperature of 1270 °C. The low reaction peak for 1300 °C in Fig. 4 is related to crystallization of pure Si (see Fig. 5). At least up to 1365 °C there are no other reaction peaks on the DSC curve, which would correspond to changes in the film structure. However, further increase in the temperature leads to structural changes in the Si–B–C–N material. The last exothermic peak in Fig. 4 corresponds to the formation of new phases in the film material. The narrower reflection lines in the pattern taken from the Si–B–C–N film powder after its cooling down from 1430 °C (see Fig. 5) have been identified as reflections of the β–Si_3N_4 phase, while the broader peak with the value of 2θ ranging from 24° to 27° is usually ascribed in the literature to semi-crystalline disordered turbostratic boron nitride (t-BN) [18–20] or carbonitride (t-BCN) [21,22], or graphite [23,24]. Due to the low content of carbon in our film, we believe that this peak is related to the presence of the t-B(C)N phase. As shown in Figs. 4 and 5, no further structural changes have been observed in this material during the heating up to 1600 °C.

Besides the DSC analysis, all of the Si–B–C–N films were subjected to TG measurement monitoring changes in their mass during annealing up to 1700 °C (see Fig. 6). The TG tests were carried out in helium having a lower atomic mass than argon and thus enabling one to reduce a TG signal noise. This results in a higher instrument accuracy. As shown in Fig. 6, no mass changes are observed up to approximately 1400 °C for all the films. Films I and II, deposited with the 50% Ar fraction in the gas mixture, exhibited a higher stability than film III prepared with the 75% Ar fraction. The onset of the corresponding mass losses, caused probably by a partial release of nitrogen from the films, started just above 1580 °C and 1500 °C, respectively. The mass changes in film III can be also related to evaporation of pure silicon ($T_{melt} = 1414$ °C) from the film material. The signal from Si was detected by the XRD (see Figs. 5 and 7) and also by DSC in the run 2 as the endothermic peak corresponding to the melting of silicon (see Fig. 2). Let us recall that the lower mass of 1.5 mg for each sample was used during the TG measurements to suppress a possible intensive evaporation of Si at the highest temperatures, leading to a reaction with the PtRh 6%–PtRh 30% thermocouple used, causing its destruction.

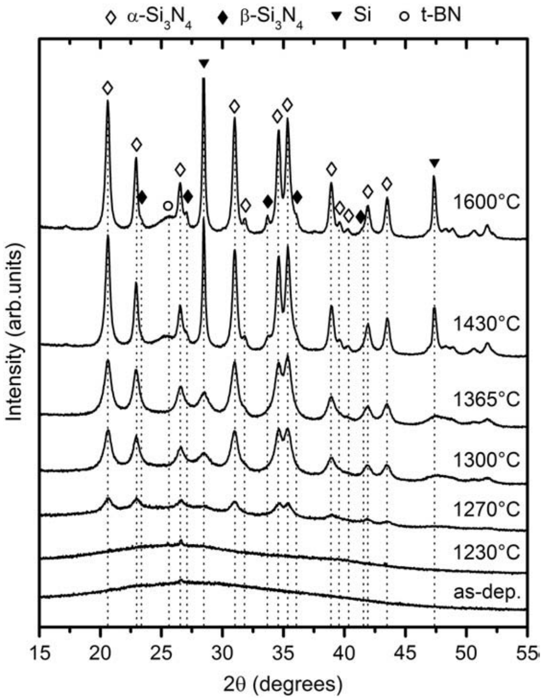

Fig. 5. XRD patterns taken from the Si–B–C–N films prepared at 75% Ar fraction in the gas mixture, substrate bias voltage of −100 V and substrate temperature of 350 °C, and annealed as powders in the DSC instrument to various temperatures being defined in Fig. 4.

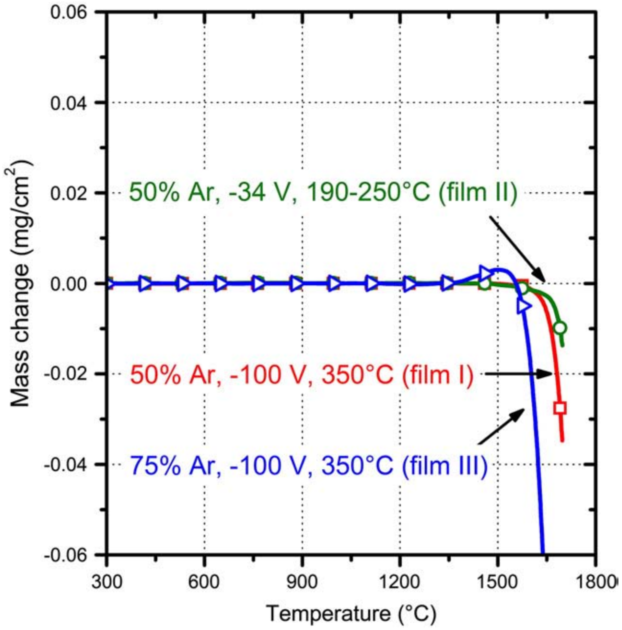

Fig. 6. Thermogravimetric curves for the Si–B–C–N films in the form of fragments annealed in helium up to 1700 °C at a heating rate of 10 °C min^{-1}.

Fig. 7 shows the XRD patterns taken from the samples after their TG analyses to 1600 °C and 1700 °C. Comparing Figs. 3 and 7, we can

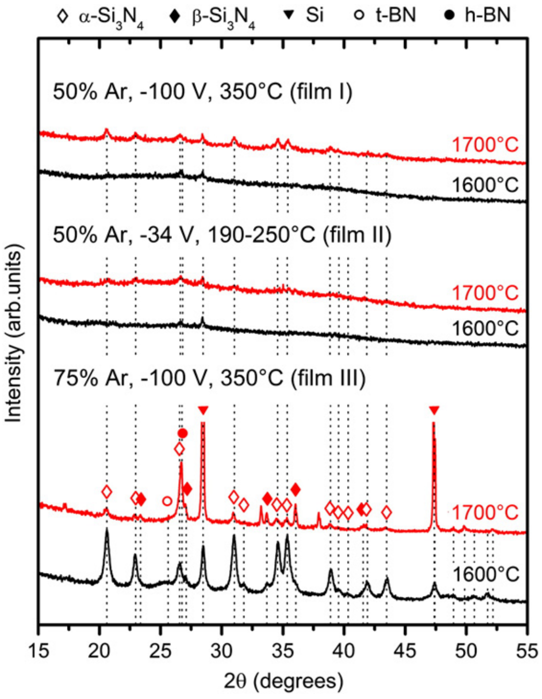

Fig. 7. XRD patterns taken from the Si–B–C–N film fragments after the TG measurements in helium to 1600 °C and 1700 °C.

conclude that there are no differences in the structures of the corresponding film materials after their annealing in argon and helium, respectively, to 1600 °C. Films I and II, deposited with the 50% Ar fraction in the gas mixture, remain amorphous without any XRD peaks (the existence of the peaks at the positions of 26.65° and 28.41° has been clarified earlier), whereas film III deposited with the 75% Ar fraction is crystalline with the same phase composition in both cases. The increase of the annealing temperature to 1700 °C (see Fig. 7) leads, however, to a change in the structure of films I and II. Both the films are characterized by crystallization of the α-Si_3N_4 phase which is the only phase detected. The crystallization is, however, very poor and most of the film volume remains still amorphous. This is clearly seen from comparison of the XRD patterns of films I and II after the annealing to 1700 °C with that of film III which unambiguously contains well-crystallized Si and β-Si_3N_4 in addition to the α-Si_3N_4 phase. The phase composition of film III is maintained almost unchanged with raising the annealing temperature from 1600 to 1700 °C, but the intensities of all XRD peaks coming from Si and α-Si_3N_4 change. The intensities of the Si reflections increase, whereas the intensities of the α-Si_3N_4 reflections drop. This fact indicates a break up of Si–N bonds in the α-Si_3N_4 phase (not in β-Si_3N_4) and a release of some nitrogen from the film. Another interesting fact is disappearance of the broad peak, located around 25° after the annealing to 1600 °C, with the increase in the temperature to 1700 °C. The peak is assigned to the disordered turbostratic t-B(C)N phase discussed earlier. It is well known that the disordered semi-crystalline structures are transformed to those of a higher order with increasing the annealing temperature. Hence, the disappearance of this broad peak is likely connected with an increase in the intensity of a peak located at 26.71°, being close to the position of the reflection (002) from the hexagonal boron nitride h-BN (26.76°) according to the JCPDS database [17]. Some of the XRD peaks remain still unidentified. We believe that they do not originate in the film but in a reaction of the released nitrogen with the corundum crucible used. Further investigations are being in progress.

Calculated bonding structures corresponding to the compositions of the Si–B–C–N films deposited with the 50% and 75% Ar fractions in the gas mixture are presented in Fig. 8 to understand significant differences in high-temperature behavior of the materials. Fundamentals of the ab initio molecular-dynamics simulations used are described in Ref. [25]. As shown in Fig. 8, a sufficiently high N/(Si + B + C) concentration ratio in films I and II deposited with the 50% Ar fraction in the gas mixture leads to a preferential bonding of Si, B and C atoms with N atoms and also to a substantial (more than 2.5 times) reduction in abundance of Si–Si bonds. Taking into account the simulated bonding statistics, crystallization of film III prepared with the 75% Ar fraction is probably caused by a relatively high population of the Si–Si bonds within the Si–B–C–N network. This is because the Si–Si bonds become unstable as temperature approaches the melting point of Si (1414 °C), favoring the diffusion of Si atoms in the volume which probably results in the formation of new, more stable bonds and in crystallization of the material. As a consequence, the stability of such material toward thermal decomposition is lower.

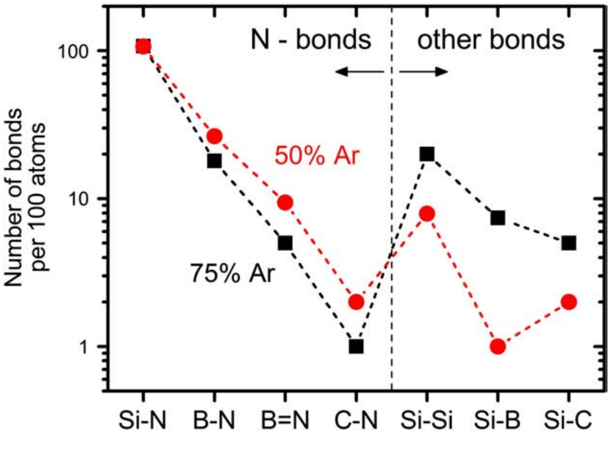

Fig. 8. Ab initio simulations of bonding statistics for the elemental compositions $Si_{32}B_{12}C_3N_{53}$ and $Si_{42}B_{11}C_2N_{45}$ related to the as-deposited Si–B–C–N films prepared with 50% and 75% Ar fraction in the gas mixture, respectively, substrate bias voltage of − 100 V and substrate temperature of 350 °C. Low contents of O, H and Ar in the films (see Table 2) were neglected here (adapted from [14]).

In addition to higher Si/C concentration ratios and incorporation of boron in the amorphous Si–B–C–N material [25], a sufficiently high value of the concentration ratio N/(Si + B + C) ≥ 1 in the material is needed to achieve its high stability at elevated temperatures.

4. Conclusions

Thermal stability of deposited Si–B–C–N materials (film fragments or powders without a substrate) was investigated using differential scanning calorimetry in argon up to 1600 °C, high-resolution thermogravimetry in helium up to 1700 °C and X-ray diffraction measurements. Amorphous Si–B–C–N films were fabricated by dc magnetron co-sputtering of a composed B_4C–Si target in two different nitrogen–argon gas mixtures (50% N_2 + 50% Ar or 25% N_2 + 75% Ar). It was shown that the deposited Si–B–C–N materials can be more stable at high temperatures in the inert atmosphere than the usually used substrates (e.g. SiC or BN). The films with the compositions (in at.%) $Si_{32-33}B_{10}C_2N_{50-51}$, for which N/(Si + B + C) = 1.1–1.2, retained their amorphous structure up to 1600 °C without any structural transformations and detectable mass changes. A slight crystallization started to develop just above this temperature. The films with the composition $Si_{40}B_{11}C_2N_{43}$, for which N/(Si + B + C) = 0.8, started to crystallize at about 1250 °C and the onset of its mass losses was observed at 1400 °C. In addition to higher Si/C concentration ratios and incorporation of boron in the amorphous Si–B–C–N material [25], the N/(Si + B + C) concentration ratio seems to be a key parameter in the preparation of Si–B–C–N films with an extraordinary thermal stability.

Acknowledgments

This work was supported by the Ministry of Education of the Czech Republic through project No. MSM 4977751302.

References

[1] R. Riedel, A. Kienzle, W. Dressler, L. Ruwisch, J. Bill, F. Aldinger, Nature (London) 382 (1996) 796.
[2] H.-P. Baldus, M. Jansen, Angew. Chem. Int. Ed Engl. 36 (1997) 328.
[3] M. Weinmann, J. Schuhmacher, H. Kummer, S. Prinz, J. Peng, H.J. Seifert, M. Christ, K. Müller, J. Bill, F. Aldinger, Chem. Mater. 12 (2000) 623.
[4] P. Gerstel, A. Müller, J. Bill, F. Aldinger, Chem. Mater. 15 (2003) 4980.
[5] J. Haug, P. Lamparter, M. Weinmann, F. Aldinger, Chem. Mater. 16 (2004) 83.
[6] M.A. Rooke, P.M.A. Sherwood, Chem. Mater. 9 (1997) 285.
[7] D. Hegemann, R. Riedel, C. Oehr, Chem. Vap. Deposition 5 (1999) 61.
[8] J. Vlček, Š. Potocký, J. Čížek, J. Houška, M. Kormunda, P. Zeman, V. Peřina, J. Zemek, Y. Setsuhara, S. Konuma, J. Vac. Sci. Technol., A 23 (2005) 1513.
[9] A. Vijayakumar, R.M. Todi, V.O. Todi, K.B. Sundaram, J. Electrochem. Soc. 154 (2007) H875.
[10] J. Houška, J. Vlček, Š. Potocký, V. Peřina, Diamond Relat. Mater. 16 (2007) 29.
[11] A. Vijayakumar, R.M. Todi, K.B. Sundaram, J. Electrochem. Soc. 154 (2007) H271.
[12] J. Čížek, J. Vlček, Š. Potocký, J. Houška, Z. Soukup, J. Kalaš, P. Jedrzejowski, J.E. Klemberg-Sapieha, L. Martinu, Thin Solid Films 516 (2008) 7286.
[13] J. Vlček, S. Hřeben, J. Kalaš, J. Čapek, P. Zeman, R. Čerstvý, V. Peřina, Y. Setsuhara, J. Vac. Sci. Technol., A 26 (2008) 1101.
[14] J. Čapek, S. Hřeben, P. Zeman, J. Vlček, R. Čerstvý, J. Houška, Surf. Coat. Technol. 203 (2008) 466.
[15] A. Vijayakumar, A.P. Warren, K.B. Sundaram, R.M. Todi, J. Mater. Sci. 20 (2009) 144.
[16] J. Kalaš, R. Vernhes, S. Hřeben, J. Vlček, J.E. Klemberg-Sapieha, L. Martinu, Thin Solid Films 518 (2009) 174.

[17] PDF-2 Database Sets 1–47, cards Si (5–565), SiO2 (46–1045), α-Si3N4 (41–360), β-Si3N4 (33–1160), BN (34–0421), JCPDS — International Centre for Diffraction Data, 1997.
[18] J. Thomas Jr., N.E. Weston, T.E. O'Connor, J. Am. Chem. Soc. 84 (1963) 4619.
[19] T. Goto, T. Tanaka, H. Masumoto, T. Hirai, J. Mater. Sci. 5 (1994) 324.
[20] S. Alkoy, C. Toy, T. Gönül, A. Tekin, J. Eur. Ceram. Soc. 17 (1997) 1415.
[21] J. Yu, E.G. Wang, J. Ahn, S.F. Yoon, Q. Zhang, J. Cui, M.B. Yu, J. Appl. Phys. 87 (2000) 4022.
[22] N. Janakiraman, M. Weinmann, J. Schuhmacher, K. Müller, J. Bill, F. Aldinger, J. Am. Ceram. Soc. 85 (2002) 1807.
[23] Y. Hishiyama, M. Nakamura, Carbon 33 (1995) 1399.
[24] L. Li, Z.H. Zhu, G.Q. Lu, Z.F. Yan, R. De Marco, Appl. Catal., A 309 (2006) 201.
[25] J. Houška, J. Vlček, S. Hřeben, M.M.M. Bilek, D.R. McKenzie, Europhys. Lett. 76 (2006) 512.

3.1.5 A-V: Thermal stability of alumina thin films containing γ-Al_2O_3 phase prepared by reactive magnetron sputtering

Applied Surface Science 257 (2010) 1058–1062

Contents lists available at ScienceDirect

Applied Surface Science

journal homepage: www.elsevier.com/locate/apsusc

Thermal stability of alumina thin films containing γ-Al_2O_3 phase prepared by reactive magnetron sputtering

J. Musil [a,b,*], J. Blažek [a], P. Zeman [a], Š. Prokšová [a], M. Šašek [a], R. Čerstvý [a]

[a] Department of Physics, Faculty of Applied Sciences, University of West Bohemia, Univerzitní 22, CZ-306 14 Plzeň, Czech Republic
[b] Institute of Physics, Academy of Sciences of the Czech Republic, Na Slovance 2, CZ-182 21 Praha 8, Czech Republic

ARTICLE INFO

Article history:
Received 15 July 2010
Received in revised form 30 July 2010
Accepted 30 July 2010
Available online 6 August 2010

Keywords:
Al_2O_3 (alumina)
Annealing
Thermal stability
Nanocrystalline material
Sputtering

ABSTRACT

The paper reports on thermal stability of alumina thin films containing γ-Al_2O_3 phase and its conversion to a thermodynamically stable α-Al_2O_3 phase during a post-deposition equilibrium thermal annealing. The films were prepared by reactive magnetron sputtering and subsequently post-deposition annealing was carried out in air at temperatures ranging from 700 °C to 1150 °C and annealing times up to 5 h using a thermogravimetric system. The evolution of the structure was investigated by means of X-ray diffraction after cooling down of the films. It was found that (1) the nanocrystalline γ-Al_2O_3 phase in the films is thermally stable up to 1000 °C even after 5 h of annealing, (2) the nanocrystalline θ-Al_2O_3 phase was observed in a narrow time and temperature region at ≥1050 °C, and (3) annealing at 1100 °C for 2 h resulted in a dominance of the α-Al_2O_3 phase only in the films with a sufficient thickness.

1. Introduction

Alumina (Al_2O_3) is an electrically and thermally insulating ceramic material which exhibits excellent chemical inertness, and high optical transparency. It occurs in several transient metastable (χ, κ, η, γ, δ, and θ) phases and one thermodynamically stable α phase with high melting point (2047 °C) [1] and relatively high hardness (21 GPa) [2]. The number of metastable phases occurring with increasing annealing temperature up to the formation of the stable α-Al_2O_3 phase and the temperature range of their existence depend on both the composition and the structure of the initial material (diaspore, gibbsite, tohdit, boehmite, bayerite) [3]. The lowest formation temperature of the α-Al_2O_3 phase (700–800 °C) is achieved for the diaspore which possesses almost perfect hcp structure as α-Al_2O_3.

In recent years, a great effort has been devoted to the deposition of thin ceramic films with the thermodynamically stable α-Al_2O_3 phase at low substrate temperatures $T_s < 700$ °C. The industry demands to deposit wear-resistant α-Al_2O_3 coatings on cutting tools made of high-speed steel which does not allow exceed 550 °C due to its thermal degradation. The deposition of α-Al_2O_3 thin films at low temperatures is also needed in other applications, e.g. in the depositions of coatings on heat-sensitive substrates.

Based on the processing of the bulk α-Al_2O_3 material three ways to produce thin ceramic films with the α-Al_2O_3 phase at reduced temperatures have been proposed and tested: (1) the formation of α-Al_2O_3 films at low substrate temperatures $T_s \leq 700$ °C under ion bombardment of the growing film [4], (2) the epitaxial growth of α-Al_2O_3 thin films on a Cr_2O_3 template which crystallizes isostructurally to the α-Al_2O_3 phase with less than 5% in the lattice mismatch [5–8], and (3) the formation of Al–Me–O systems in which selected metals Me are added, e.g. Cr forming $(Cr,Al)_2O_3$ solid solution [9–12].

For the fabrication of the α-Al_2O_3 thin ceramic films different deposition methods are used: (1) chemical vapor deposition (CVD) from gas phase [13–17], (2) evaporation from a melted Al material [4,18–20], and (3) sputtering of a solid Al target [5,21–34]. It was found that formation temperatures of individual Al_2O_3 phases depend not only on the substrate temperature T_s used in the deposition of the Al_2O_3 films but also on the energy delivered to the growing film by bombarding ions and condensing atoms. This energy is determined by many process parameters which decide on the Al_2O_3 crystallization. Therefore it is difficult to compare experimental data obtained in different experimental devices.

The γ-Al_2O_3 phase can be synthesized at a relatively low substrate temperature $T_s \leq 550$ °C. However, the formation of α-Al_2O_3 requires deliver a sufficient amount of energy to the growing alumina film or an additional energy during post-deposition thermal

---

* Corresponding author at: Department of Physics, Faculty of Applied Sciences, University of West Bohemia, Univerzitní 22, Plzeň 306 14, Czech Republic.
Tel.: +420 377632200; fax: +420 377632202.
E-mail address: musil@kfy.zcu.cz (J. Musil).

0169-4332/$ – see front matter © 2010 Elsevier B.V. All rights reserved.
doi:10.1016/j.apsusc.2010.07.107

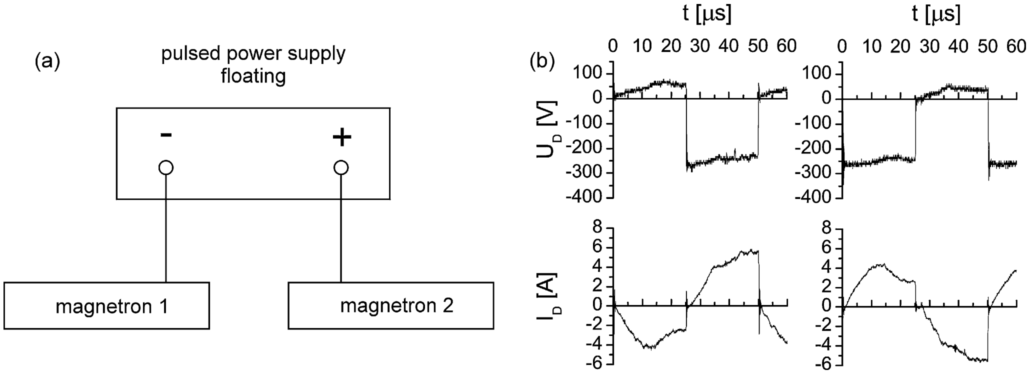

Fig. 1. (a) Electrical connection of dual magnetron system to the floating power supply and (b) characteristic waveforms of discharge voltage $U_d(t)$ and current $I_d(t)$ used in the deposition of Al_2O_3 thin films.

annealing. The ion bombardment (non-equilibrium process) is usually used to deliver the energy during the growth of the film and the heating (equilibrium process) is used to transform metastable Al_2O_3 phases to α-Al_2O_3 during the post-deposition annealing. To convert the γ-Al_2O_3 to α-Al_2O_3 phase an activation energy of 546 kJ/mol has been reported [35].

Although the deposition of the α-Al_2O_3 films at low substrate temperature has already been achieved there are still many open questions as to the formation and thermal stability of the metastable polymorphs of alumina. Thermal stability of metastable Al_2O_3 phases such as κ-Al_2O_3 [16,36], γ-Al_2O_3 [36–38] and an amorphous Al_2O_3 phase [37,38] has been investigated in detail. It was found that (1) the metastable Al_2O_3 phases convert to the stable α-Al_2O_3 phase during thermal annealing between 1000 °C and 1100 °C [16,36–40], (2) different metastable phases are formed during thermal annealing depending on the structure of the as-deposited film [37,38], and (3) the α-Al_2O_3 phase nucleates preferentially at film defects and crack network [16].

Despite a lot of information on the deposition process and properties of alumina films the isothermal aspect of thermal stability of the metastable phases is often missing. The aim of this article is to synthesize crystalline γ-Al_2O_3 films using dual magnetron sputtering and to investigate thermal stability of these films during post-deposition thermal annealing in air at various annealing temperatures and, especially, at various annealing times. The influence of the film thickness on the γ- to α-Al_2O_3 transformation is also discussed.

2. Experimental

The Al_2O_3 films were reactively sputtered in an $Ar + O_2$ mixture using a dual magnetron system (DMS) consisting of two magnetrons in the closed magnetic field configuration, each tilted to the vertical at an angle of 20° and equipped with Al targets (99.5% purity) of diameters of 50 mm. The dual magnetron system was supplied by a DC pulse power supply RMP-10 (Hüttinger Electronic) in the bipolar mode at a repetition frequency of 20 kHz. The power supply was floating (not grounded). The electrical connection of the DMS to the power supply and the characteristic voltage $U_d = f(t)$ and current $I_d = f(t)$ waveforms are given in Fig. 1.

The Al_2O_3 films were reactively deposited on Si(1 0 0) substrates (20 mm × 20 mm × 0.38 mm and 20 mm × 5 mm × 0.38 mm) in the oxide mode of sputtering. The following deposition conditions were used: the discharge current $I_{da} = 3$ A, the target power density $W_{ta} = 42$ W/cm^2 averaged over the negative voltage pulse, the substrate temperature $T_s = 500$ °C, substrate held at the floating potential U_{fl}, the substrate-to-target distance $d_{s-t} = 110$ mm, the oxygen partial pressure $p_{O_2} = 0.2$ Pa and the total pressure $p_T = 1.5$ Pa.

Measurements of thermal stability of the Al_2O_3 films during the post-deposition thermal annealing in air were carried out at temperatures ranging from 700 °C to 1150 °C and annealing times up to 5 h using a Setaram thermogravimetric system TAG 2400 with a heating rate of 10 °C/min and a cooling rate of 30 °C/min. The thickness of the films and the macrostress σ generated in them were measured by a stylus profilometer Dektak 8. The macrostress σ was evaluated from the bending of a thin Si plate (20 mm × 5 mm × 0.38 mm) using the Stoney's formula. The structure of the films was characterized by the glancing incidence X-ray diffraction (GIXRD) at an incident angle of 0.75° using a PANalytical X'Pert PRO diffractometer. The surface morphology of the films was observed by an optical microscope. The elemental composition of the films was measured by a PANalytical wavelength dispersive X-ray fluorescence (WDXRF) spectrometer MagiX PRO equipped with a 4 kW Rh-target X-ray tube, analytical software SuperQ v4.0 used for data collection and FP-MULTI software used for calibration and data analysis. A pure solid-state Al_2O_3 sample was used as a calibration standard. Analytical results for element concentrations were obtained with a relative accuracy of 10% compared to RBS analysis of selected samples. Mechanical properties of the Al_2O_3 films were determined from the load vs. displacement curves measured by a Fischerscope H100 microhardness tester with the Vicker's diamond indenter at a load of 10 mN.

3. Results and discussion

To investigate thermal stability of alumina films containing the γ-Al_2O_3 phase ~300 nm and ~1200 nm thick films were reactively deposited in the oxide mode of sputtering on the Si(1 0 0) substrates held at the floating potential and the substrate temperature $T_s = 500$ °C with the deposition rate $a_D \approx 5$ nm/min. The elemental composition of the films, characterized by the atomic ratio Al/O = 37.6/62.3 = 0.60, was found to be close to the stoichiometric composition within the accuracy of the WDXRF method applied. The GIXRD analysis revealed that the as-deposited films are characterized by three broad peaks with maxima located at $2\theta \approx 37.5°$, 46° and 67°, see Figs. 2 and 3. These maxima indicate that the films contain small γ-Al_2O_3 nanograins with the (3 1 1), (4 0 0) and (4 4 0) orientations. No other crystalline phases were detected in these films. This finding, however, does not exclude that some amount of an amorphous alumina phase can be present in the films besides nanocrystalline γ-Al_2O_3. Furthermore, both the ~300 nm thick and the ~1200 nm thick films are characterized by a relatively low compressive macrostress $\sigma \approx -1.0$ GPa and -0.5 GPa, respectively. Hardness $H = 13$ GPa, effective Young's modulus $E^* = 140$ GPa and elastic recovery $W_e = 65\%$ are typical values of these as-deposited alumina films with the thickness $h \approx 1200$ nm. The measured value of hardness is higher than that reported for completely amorphous

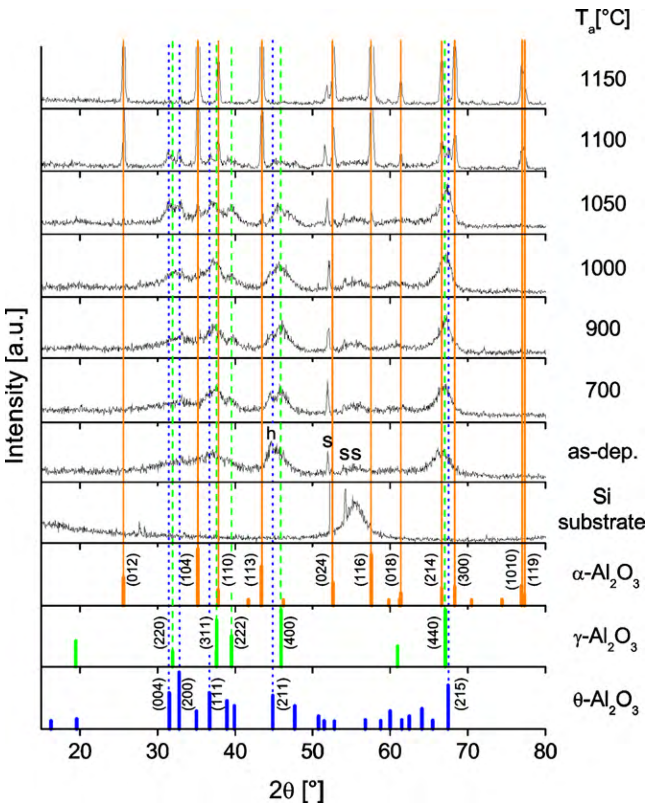

Fig. 2. GIXRD patterns of ~1200 nm thick Al_2O_3 films as a function of the annealing temperature T_a at a constant annealing time t_a = 5 h. Peaks denoted as 's' and 'h' are reflections from the substrate and substrate holder, respectively.

alumina films (7–9 GPa [41], 9–10 GPa [42], 10 GPa [37]) but is concurrently lower than that reported for highly crystalline or textured γ-Al_2O_3 films (17–20 GPa [41], 20 GPa [42]). This indication points out that our as-deposited films may contain amorphous alumina as well. Unfortunately, transmission electron microscopy, being able to identify an amorphous phase unambiguously, could not be carried out in this study.

3.1. Effect of annealing temperature on the structure evolution

Thermal stability of the alumina films containing the nanocrystalline γ-Al_2O_3 phase and the temperature, at which this metastable phase converts to the thermally stable α-Al_2O_3 phase, were studied in the ~1200 nm thick films. The as-deposited films were thermally annealed to different values of the annealing temperature T_a ranging from 700 °C to 1150 °C for a duration of 5 h to determine the evolution of the film structure with increasing T_a. Results of this experiment are summarized in Fig. 2.

From Fig. 2 it is seen that (i) with increasing T_a the number of nanograins with the (3 1 1), (4 0 0) and (4 4 0) crystallographic orientations slightly increases and new nanograins of the γ-Al_2O_3 phase with the (2 2 0) and (2 2 2) orientations appear, (ii) the first α-Al_2O_3 nanograins crystallize during annealing at $T_a \approx 1050$ °C and simultaneously the reflections of the metastable θ-Al_2O_3 phase are detected, (iii) the films annealed at $T_a \approx 1100$ °C are composed of a mixture of large α-Al_2O_3 grains and small θ-Al_2O_3 nanograins, and (iv) alumina films with a well-crystallized α-Al_2O_3 phase are formed at T_a = 1150 °C. The formation of alumina films with a pure α-Al_2O_3 phase at T_a = 1150 °C agrees well with data reported by other authors [35,38]. The formation of the θ-Al_2O_3 phase during thermal annealing has already been reported by Eklund et al. [38] for films which besides the γ-Al_2O_3 phase contained also an additional amorphous phase in the as-deposited state. Edlmayr et al. [37] observed the formation of the δ-Al_2O_3 phase during thermal annealing of the films with the similar as-deposited structure but they could not absolutely exclude also the formation of the θ-Al_2O_3 phase due to the similar JCPDS standard peak positions.

The most important finding of our experiment is the fact that the alumina films containing the nanocrystalline γ-Al_2O_3 phase can be reactively sputtered already at T_s = 500 °C and are thermally stable up to ~1000 °C for the 5 h annealing.

3.2. Effect of annealing time on the structure evolution

For the structure conversion not only the magnitude of T_a but also the annealing time t_a is of a key importance. Therefore, the evolution of the structure of the sputtered alumina films was investigated in detail as a function of the annealing time. The thermal annealing of the thicker (~1200 nm) and the thinner (~300 nm) alumina films with the γ-Al_2O_3 phase was performed at T_a = 1100 °C when a strong crystallization of the α-Al_2O_3 phase of the thicker films occurs (see Fig. 2). Obtained results are displayed in Fig. 3.

Fig. 3 clearly shows that the annealing time t_a strongly influences the structure of the alumina films at the temperature T_a = 1100 °C, which is close to that corresponding to the γ → α transition. The heating to 1100 °C and immediate cooling down to room temperature (t_a = 0 h) does not significantly affect the structure of both as-deposited films (Fig. 3a and b). On the other hand, the annealing for $t_a \geq 1$ h leads to a formation of the thermally stable α-Al_2O_3 phase. These changes are more pronounced for the thicker (~1200 nm) films in which the structure is α-Al_2O_3 dominant already after t_a = 2 h. In case of the thinner films (~300 nm) the intensities of the reflections assigned to α-, θ- and γ-Al_2O_3 phases are roughly comparable even after t_a = 5 h, which indicates that the crystallization rate of the thinner films is slower than that of the thicker ones but the lower intensities of the reflections due to a smaller irradiated film volume must also be taken into account.

Similar phenomenon has been observed in the investigation of the crystallization of TiO_2 films when the intensities of reflection peaks increased considerably slower in thinner films compared to thicker ones during thermal annealing [43]. Moreover, the evolution of the structure of the thicker alumina films with increasing t_a (Fig. 3a) shows that the nanocrystalline Al_2O_3 films can be composed of a mixture γ- and θ-Al_2O_3 nanograins in a narrow interval of t_a at a given value of T_a. The narrow interval of the co-existence of the nanocrystalline γ- and θ-Al_2O_3 phases in sputtered alumina films can be probably a reason for a different phase composition of Al_2O_3 films reported in literature.

3.3. Film cracking during thermal annealing

The surface morphology of the ~1200 nm thick alumina films in the as-deposited state and after the thermal annealing at T_a = 900 °C and T_a = 1100 °C for t_a = 5 h is shown in Fig. 4. As can be seen from Fig. 4a the surface of the as-deposited films exhibits no visible defects. The annealing at 900 °C (Fig. 4b) results, however, in the occurrence of parallel cracks in the films. Since no phase transformations are observed at this value of the annealing temperature (see Fig. 2) these cracks arise most likely as a consequence of increasing thermal stresses due to different thermal expansion coefficients of the film α_f and the substrate α_s. The annealing at 1100 °C leads to the formation of a denser crack network which can be attributed to the conversion of the γ-Al_2O_3 phase into the α-Al_2O_3 phase having a different mass density ($\rho_{\gamma\text{-}Al_2O_3}$ = 3.62 g/cm^3 vs. $\rho_{\alpha\text{-}Al_2O_3}$ = 3.99 g/cm^3) [44]. These cracks are of random directions in contrast to those in Fig. 4b. The film

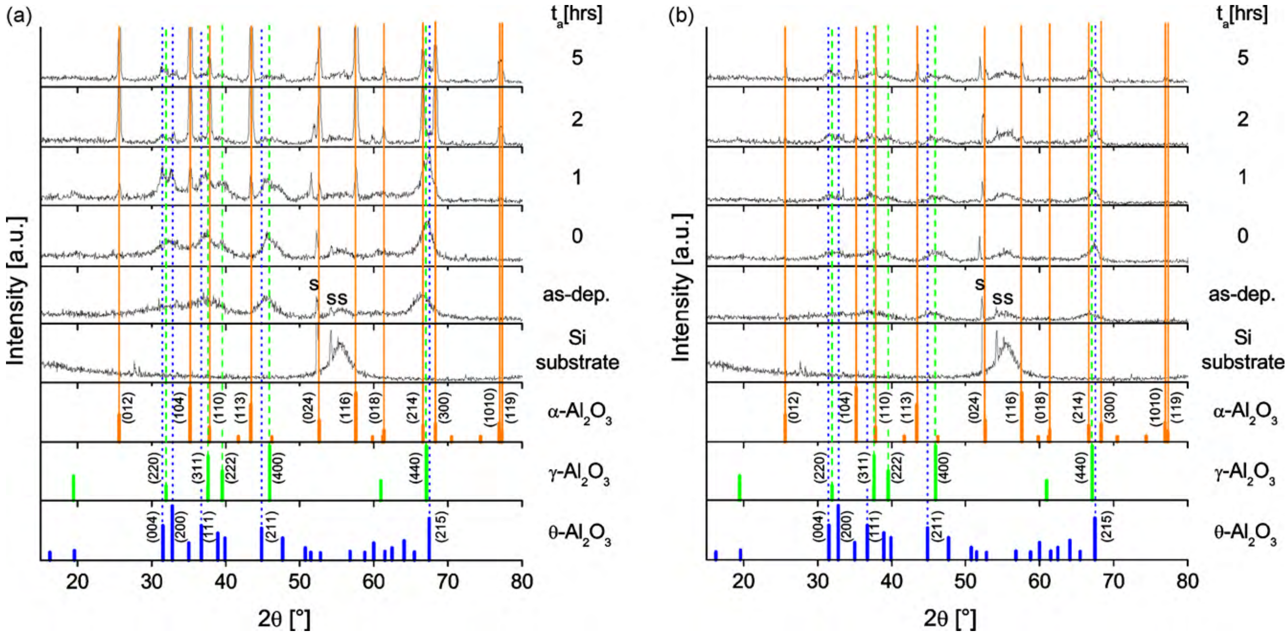

Fig. 3. GIXRD patterns of (a) thicker (~1200 nm) and (b) thinner (~300 nm) Al_2O_3 films as a function of the annealing time t_a at a constant annealing temperature $T_a = 1100\,^{\circ}C$ ($t_a = 0$ h denotes the increase of the annealing temperature to 1100 °C and immediate cooling down to RT).

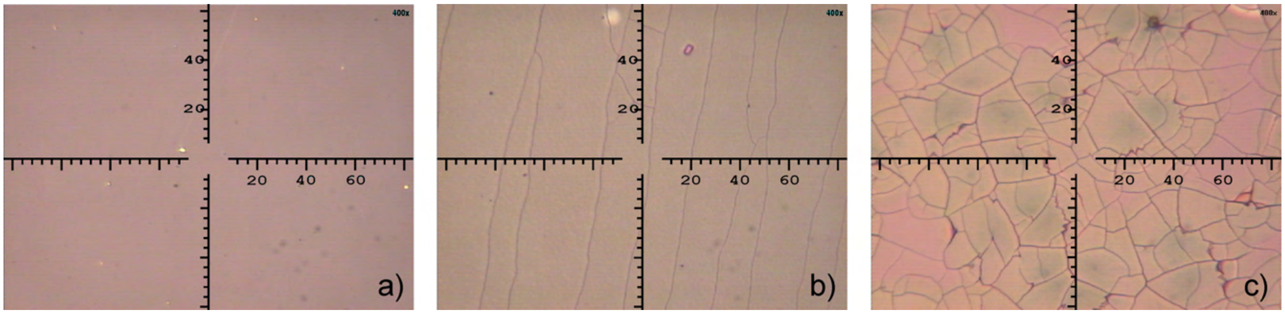

Fig. 4. Photographs of the surface morphology of ~1200 nm thick Al_2O_3 films (a) in the as-deposited state and after thermal annealing at (b) 900 °C and (c) 1100 °C for 5 h. Scales are given in μm units.

cracking caused by the phase conversion occurs just at temperatures exceeding 1000 °C due to a high thermal stability of the γ-Al_2O_3 phase. These observations are consistent with the results reported by other authors [36,37,39].

The film cracking during thermal annealing is a serious problem for potential industrial applications. To avoid cracking it is necessary to form nanocrystalline γ-Al_2O_3 already during its growth. The formation of the nanocrystalline film by a thermal annealing of the amorphous as-deposited Al_2O_3 film is not a correct approach for applications. No change of the film structure is necessary in whole range of operating temperatures. Recently, it has been shown that nanocrystalline films with the γ-Al_2O_3 structure can be prepared in Al–Ti–O system at substrate temperatures $T_s < 500\,^{\circ}C$ [45]. In this case no cracking should be expected due to a good thermal stability of the nanocrystalline γ-Al_2O_3 phase up to ~1000 °C. Moreover, the Al–Ti–O films with the γ-Al_2O_3 structure exhibit a high hardness $H \approx 25$ GPa.

4. Conclusions

Thermal stability of magnetron sputtered alumina thin films containing the γ-Al_2O_3 phase during post-deposition thermal annealing in air at various temperatures and annealing times was systematically investigated. Main results of the structure evolution of the Al_2O_3 films can be summarized as follows:

1. As-deposited films contain a nanocrystalline γ-Al_2O_3 phase. Even very thin films with a thickness of about 300 nm are of the same structure. No thermodynamically stable α-Al_2O_3 phase was found in these films.
2. The nanocrystalline γ-Al_2O_3 phase is thermally stable up to ~1000 °C even after 5 h of the annealing.
3. The α-Al_2O_3 phase starts to crystallize at $T_a \approx 1050\,^{\circ}C$. The crystallization of α-Al_2O_3 phase significantly improves with increasing the annealing time t_a.
4. A nanocrystalline θ-Al_2O_3 phase forms at $T_a \geq 1050\,^{\circ}C$ but the time and temperature region of its existence is very narrow.
5. The ~1200 nm thick alumina films are dominantly composed of the α-Al_2O_3 phase after annealing at $T_a = 1100\,^{\circ}C$ for 2 h; the thinner (~300 nm) films contain γ-, θ- and α-Al_2O_3 phases of a comparable amount even after 5 h of annealing.
6. The film annealing at $T_a = 1100\,^{\circ}C$, which is close to the $\gamma \rightarrow \alpha$ phase transition, results in the film cracking due to a different density of γ and α phases.

Acknowledgement

This work was supported in part by the Ministry of Education of the Czech Republic under Project No. MSM 4977751302.

References

[1] W.H. Gitzen, Alumina as a Ceramic Material, The American Ceramic Society, Westerville, 1970.

[2] H. Holleck, Material selection for hard coatings, J. Vac. Sci. Technol. A 4 (1986) 2661–2669.

[3] K. Wefers, Ch. Misra, Oxides and Hydrides of Aluminum, Aluminium Company of America, Alcoa Research Laboratories, 1987.

[4] R. Brill, F. Koch, J. Mazurelle, D. Levchuk, M. Balden, Y. Yamada-Takamura, H. Maier, H. Bolt, Crystal structure characterization of filtered arc deposition alumina coatings: temperature and bias voltage, Surf. Coat. Technol. 174–175 (2003) 606–610.

[5] J.M. Andersson, E. Wallin, U. Helmersson, U. Kreissig, E.P. Munger, Phase control of Al_2O_3 thin films grown at low temperatures, Thin Solid Films 513 (2006) 57–59.

[6] J.M. Andersson, Z. Czigany, P. Jin, U. Helmersson, Microstructure of α-alumina thin films deposited at low temperatures on chromia template layers, J. Vac. Sci. Technol. A 22 (2004) 117–121.

[7] P. Eklund, M. Sridharan, M. Sillassen, J. Bottiger, α-Cr_2O_3 template-texture effect on α-Al_2O_3 thin film growth, Thin Solid Films 516 (2008) 7447–7450.

[8] P. Jin, S. Nakao, S.X. Wang, L.M. Wang, Localized epitaxial growth of α-Al_2O_3 thin films on Cr_2O_3 template by sputter deposition at low substrate temperature, Appl. Phys. Lett. 82 (2003) 1024–1026.

[9] J. Ramm, M. Ante, T. Bachmann, B. Widrig, H. Brandle, M. Dobeli, Pulse enhanced electron emission (P3e^{TM}) arc evaporation and the synthesis of wear resistant Al–Cr–O coatings in corundum structure, Surf. Coat. Technol. 202 (2007) 876–883.

[10] J. Ramm, M. Ante, H. Brandle, A. Neels, A. Dommann, M. Dobeli, Thermal stability of thin film corundum-type solid solutions of $(Al_{1-x}Cr_x)_2O_3$ synthesized under low-temperature non-equilibrium conditions, Adv. Eng. Mater. 9 (7) (2007) 604–608.

[11] K. Pedersen, J. Bottiger, M. Sridharan, M. Sillassen, P. Eklund, Texture and microstructure of Cr_2O_3 and $(Cr, Al)_2O_3$ thin films deposited by reactive inductively coupled plasma magnetron sputtering, Thin Solid Films 518 (2010) 4294–4298.

[12] D. Diechle, M. Stueber, H. Leiste, S. Ulrich, V. Schier, Combinatorial approach to the growth of α-$(Al_{1-x},Cr_x)_2O_3$ solid solution strengthened thin films by reactive r.f. magnetron sputtering, Surf. Coat. Technol. 204 (2010) 3258–3264.

[13] D. Kyrylov, D. Kurapov, J.M. Schneider, Effect of ion irradiation during deposition on the structure of alumina thin films grown by PACVD, Appl. Phys. A 80 (2005) 1657–1660.

[14] S. Ruppi, A. Larsson, A. Flink, Nanoindentation hardness, texture and microstructure of α-Al_2O_3 and κ-Al_2O_3 coatings, Thin Solid Films 516 (2008) 5959–5966.

[15] J Skogsmo, M. Halvarsson, S. Vuorinnen, Microstructural study of the κ-$Al_2O_3 \rightarrow \alpha$-$Al_2O_3$ transformation in CVD κ-Al_2O_3, Surf. Coat. Technol. 54–55 (1992) 186–192.

[16] S. Vuorinen, L. Karlsson, Phase transformation in chemically vapour-deposited κ-alumina, Thin Solid Films 214 (1992) 132–143.

[17] S. Ruppi, Deposition, microstructure and properties of texture-controlled CVD α-Al_2O_3 coatings, Int. J. Refract. Met. Hard Mater. 23 (2005) 306–316.

[18] R.F. Bunshah, R.J. Schramm, Alumina deposition by activated reactive evaporation, Thin Solid Films 40 (1977) 211–216.

[19] J.E. Sundgren, H.T.G. Hentzell, A review of the present state of art in hard coatings grown from the vapor phase, J. Vac. Sci. Technol. A 4 (1986) 2259–2279.

[20] J. Rosen, S. Mraz, U. Kreissig, D. Music, J. Schneider, Effect of ion energy on structure and composition of cathodic arc deposited alumina thin films, Plasma Chem. Plasma Process. 25 (2005) 303–317.

[21] O. Zywitzki, G. Hoetzsch, F. Fietzke, K. Goedicke, Effect of the substrate temperature on the structure and properties of Al_2O_3 layers reactively deposited by pulsed magnetron sputtering, Surf. Coat. Technol. 82 (1996) 169–175.

[22] O. Zywitzki, G. Hoetzsch, Influence of coating parameters on the structure and properties of Al_2O_3 layers reactively deposited by means of pulsed magnetron sputtering, Surf. Coat. Technol. 86–87 (1996) 640–647.

[23] J.M. Schneider, W.D. Sproul, A.A. Voevodin, A. Matthews, Crystalline alumina deposited at low temperatures by ionized magnetron sputtering, J. Vac. Sci. Technol. A 15 (1997) 1084–1088.

[24] J.M. Schneider, W.D. Sproul, R.W.J. Chia, M.S. Wong, A. Matthews, Very-high-rate reactive sputtering of alumina hard coatings, Surf. Coat. Technol. 96 (1997) 262–266.

[25] D. Depla, J. Haemers, G. Buyle, R. De Gryse, Hysteresis behaviour during reactive magnetron sputtering of Al_2O_3 using a rotating cylindrical magnetron, J. Vac. Sci. Technol. A 4 (2006) 934–938.

[26] A. Khanna, D.G. Bhat, Nanocrystalline gamma alumina coatings by inverted cylindrical magnetron sputtering, Surf. Coat. Technol. 201 (2006) 168–173.

[27] A. Khanna, D.G. Bhat, A. Harris, B.D. Beake, Structure–property correlations in aluminium oxide thin films grown by reactive AC magnetron sputtering, Surf. Coat. Technol. 201 (2006) 1109–1116.

[28] A. Khanna, D.G. Bhat, Crystalline alumina coatings by reactive ac magnetron sputtering, J. Vac. Sci. Technol. A 25 (2007) L5–L8.

[29] J.M. Andersson, E. Wallin, E.P. Munger, U. Helmersson, Energy distributions of positive and negative ions during magnetron sputtering of an Al target in Ar/O_2 mixtures, J. Appl. Phys. 100 (2006) 57–59.

[30] E. Wallin, J.M. Andersson, M. Lattemann, U. Helmersson, Influence of residual water on magnetron sputter deposited crystalline Al_2O_3 thin films, Thin Solid Films 516 (2008) 3877–3883.

[31] Y. Chiba, Y. Abe, M. Kawamura, K. Sasaki, Formation process of Al_2O_3 thin film by reactive sputtering, Vacuum 83 (2009) 483–485.

[32] S. Fricke, A. Friedberger, U. Schmid, The influence of plasma power on the temperature-dependant conductivity and on the wet chemical etch rate of sputter-deposited alumina thin films, Surf. Coat. Technol. 203 (2009) 2830–2834.

[33] J.A. Thornton, J. Chin, Structure and heat treatment characteristics of sputter-deposited alumina, Ceram. Bull. 56 (1977) 504–508.

[34] R. Chistyakov, B. Abraham, W.D. Sproul, Proceedings of the 48th Annual Technical Meeting, Society of Vacuum Coaters, 2006.

[35] C.S. Nordahl, G.L. Messing, Thermal analysis of phase transformation kinetics in α-Al_2O_3 seeded boehmite and γ-Al_2O_3, Thermochim. Acta 318 (1998) 187–199.

[36] D.H. Trinh, K. Back, G. Pozina, H. Blomqvist, T. Selinder, M. Collin, I. Reineck, L. Hultman, H. Högberg, Phase transformation in κ- and γ-Al_2O_3 coatings on cutting tool inserts, Surf. Coat. Technol. 203 (2009) 1682–1688.

[37] V. Edlmayr, M. Moser, C. Walter, C. Mitterer, Stability of sputtered Al_2O_3 coatings, Surf. Coat. Technol. 204 (2010) 1576–1581.

[38] P. Eklund, M. Sridharan, G. Singh, J. Bottiger, Thermal stability and phase transformations of γ-/amorphous/Al_2O_3 thin films, Plasma Processes Polym. 6 (2009) S907–S911.

[39] O. Zywitzki, G. Hoetzsch, Effect of plasma activation on the phase transformations of aluminum oxide, Surf. Coat. Technol. 76–77 (1995) 754–762.

[40] O. Kyrylov, R. Cremer, D. Neuschütz, Deposition of alumina hard coatings by bipolar pulsed PECVD, Surf. Coat. Technol. 163–164 (2003) 203–207.

[41] M. Sridharan, M. Sillassen, J. Bøttiger, J. Chevallier, H. Birkedal, Pulsed DC magnetron sputtered Al_2O_3 and their hardness, Surf. Coat. Technol. 202 (2007) 920–924.

[42] F. Fietzke, K. Goedicke, W. Hempel, The deposition of hard crystalline Al_2O_3, layers by means of bipolar pulsed magnetron sputtering, Surf. Coat. Technol. 86–87 (1996) 657–663.

[43] L. Nichtova, R. Kuzel, Z. Matej, J. Sicha, J. Musil, Time and thickness dependence of crystallization of amorphous magnetron deposited TiO_2 thin films, Z. Kristallogr. Suppl. 30 (2009) 235–240.

[44] K.H. Hellwege, in: W. Pies, A. Weiss (Eds.), Crystal Structure Data of Inorganic Compounds, Landott-Börnstein, Springer, Berlin, 1975, pp. 46–59.

[45] J. Musil, V. Satava, R. Cerstvy, P. Zeman, T. Tolg, Formation of crystalline Al–Ti–O thin films and their properties, Surf. Coat. Technol. 202 (2008) 6064–6069.

3.2 Část B

Otěruvzdorné ochranné povlaky nc-TiC/*a*-C a Mo-C s dostatečnou tvrdostí a nízkým koeficientem tření

3.2.1 B-I: Tribological and mechanical properties of nanocrystalline-TiC/*a*-C nanocomposite thin films

Tribological and mechanical properties of nanocrystalline-TiC/*a*-C nanocomposite thin films

J. Musil[a)]
Department of Physics, Faculty of Applied Sciences, University of West Bohemia, Univerzitní 22, CZ-30614 Plzeň, Czech Republic and Institute of Physics, Academy of Sciences of the Czech Republic, Na Slovance 2, Cz-182 21 Praha 8, Czech Republic

P. Novák, R. Čerstvý, and Z. Soukup
Department of Physics, Faculty of Applied Sciences, University of West Bohemia, Univerzitní 22, CZ-30614 Plzeñ, Czech Republic

(Received 14 September 2009; accepted 28 December 2009; published 27 January 2010)

This article reports on interrelationships between x-ray structure, mechanical properties, coefficient of friction μ, and wear coefficient k of $\sim$3000 m thick nc-TiC/*a*-C nanocomposite films sputtered using unbalanced magnetron from a composed C/Ti target ($\varnothing = 100$ mm); here nc and *a* denotes the nanocrystalline and amorphous phase, respectively. It is shown that (1) μ and k of the nc-TiC/*a*-C nanocomposite film strongly depend not only on its hardness H but also on its effective Young's modulus $E^* = E/(1-\nu^2)$; here ν is the Poisson *s* ratio, (2) the nc-TiC/*a*-C nanocomposite films with C/Ti $>$ 1.5 and the ratio H^3/E^{*2} (characterizing the resistance of film to plastic deformation) ranging from $\sim$0.2 to $\sim$0.3 exhibit the lowest values of μ and k, and (3) μ increases with increasing load L of the testing ball. The main result of this investigation is the finding that the achievement of the lowest value E^* at a given value of H is of key importance in the formation of films with the lowest values of coefficient of friction μ and wear coefficient k. *© 2010 American Vacuum Society.*
[DOI: 10.1116/1.3294717]

I. INTRODUCTION

Recently, it was found that the addition of selected metal (Me) atoms into amorphous carbon (*a*-C) and amorphous carbon containing hydrogen (*a*-C:H) films not only reduces the macrostress σ generated in the Me/*a*-C and MeC/*a*-C composite films during growth but also (i) results in an increase in the film hardness H in the case if Me atoms form hard MeC grains, (ii) improves the film toughness, and (iii) enables to produce thicker films with thickness h greater than 1000 nm. These findings stimulated an intensive development of new group of thick ($\geq$1000 nm) Me/*a*-C and MeC/*a*-C composite coatings with (i) relatively high ($>$10 GPa) hardness H, (ii) low ($\leq$1 GPa) compressive macrostress σ, and (iii) low values of coefficient of friction μ ($\leq$0.1) and wear coefficient k ($\leq 1\times10^{-7}$ mm^3/N m).[1–27] Different Me atoms were incorporated in the *a*-C film and the following composite systems were investigated: (i) nc-MeC/*a*-C composite films with Me=Ti,[1–4,6,8,10,11,16,18,19,21–23,25,28–44] W,[5,6,8,12,14,19,20,26,28] Mo,[18,19] and Nb;[8,18,19] (ii) Me/*a*-C composite films with Me=Cu,[17,39] Si,[9,13,27] and Al;[45] (iii) MeC/Ag with Me=Ti, W,[12] (iv) nc-compound/*a*-C, e.g., WS$_2$/*a*-C and MoS$_2$/*a*-C.[20]

As expected, it was found that low values of μ ($\leq$0.1) and k ($\leq 1\times10^{-7}$ mm^3/N m) of the film depends not only on the kind and the amount of metal Me atoms added to *a*-C film but also on the process conditions used in its preparation. Therefore, the following correlations were investigated in detail: (i) the mechanical properties versus the process parameters;[28] (ii) the coating microstructure, the mechanical properties versus tribological properties;[29,31–35,38,39,45–47] (iii) the tribological properties versus the electrical properties;[29] (iv) chemical bonding versus tribological properties;[42,45] (v) the mechanical properties versus the tribological properties.[48] The results of these investigations disclose many interesting relationships between the physical properties of the film and its mechanical properties and tribological behavior but are still insufficient to define the condition under which the MeC/*a*-C film will exhibit the lowest values of μ and k.

Up until now, little attention was devoted to the effect of plastic/elastic properties of the film on its tribological properties.[3,4] The plastic/elastic properties depend on both the hardness H and the effective Young's modulus E^* and can be easily determined using nanoindentation measurements. Measured values of H and E^* permit to calculate the ratio H^3/E^{*2}, which gives an information on the resistance of the material to plastic deformation; for more details, see Ref. 49. The ratio H^3/E^{*2} is an important parameter in the investigation of correlations between the mechanical and tribological behaviors of coatings. The plastic deformation is reduced in materials with high hardness H and low modulus E^* because low modulus E^* allows the given load to be distributed over a wider area. Therefore, it is reasonable to expect that μ and k of the coatings could be improved when its effective Young's modulus E^* is reduced.

Correlations between mechanical and tribological properties of the film are very important for an assessment of its quality. Recently, the relation between mechanical and tribo-

---

[a)] Electronic mail: musil@kfy.zcu.cz

logical properties was investigated for the Cu/*a*-C composite film.[48] It was found that (i) μ of the Cu/*a*-C film decreases with increasing ratio H^3/E^{*2}, (ii) the Cu/*a*-C films with $H > 10$ GPa and $H^3/E^{*2} \geq 0.2$ GPa exhibit the lowest values (≤ 0.1) of μ and the lowest values ($\leq 2 \times 10^{-7}$ mm^3/N m) of k (measured using WC ball at the load $L = 2$ N), and (iii) high values of H and H^3/E^{*2} do not ensure that the lowest values of μ and k can be achieved. The last finding indicates that there is an optimum value of the ratio H^3/E^{*2} which results in the lowest values of μ and k of the film. Therefore, in the formation of film with lowest values μ and k, not only the optimum value of the ratio H^3/E^{*2} is important but also the film structure, elemental, and phase composition which must result in such values of H and E^*, which give the optimum ratio H^3/E^{*2}. Besides, the high ratio $H^3/E^{*2} \geq 0.2$ GPa, necessary to reach the lowest values of μ and k, indicates that the well lubricating and wear-resistant films should exhibit the lowest value of E^* at a given H. Such films are well resilient because they exhibit the high resistance to plastic deformation ($H^3/E^{*2} \geq 0.2$ GPa). This conclusion is in full agreement with the prediction of (i) Matthews and co-workers[49–53] who claimed that the nanocomposite coatings with a large H/E^* ratio (the value of this ratio is not defined), i.e., the nanocomposites with a sufficiently high hardness H (to resist to plastic deformation), but with a low elastic modulus E^*, can exhibit improved toughness and reduced wear and (ii) Lewin *et al.*[42] who claimed that the wear properties of coatings are optimized when the H/E^* ratio is highest (again, the value of this ratio is not defined). In summary, it can be concluded that *the tribological behavior of solid lubricant coatings is determined by a combined action of H* and E^*.

Up until now, values of μ and k are correlated with contents of individual phases in the nanocomposite coating, its structure (amorphous, nanocrystalline), carbon bond coordination (sp^2, sp^3), and its hardness H. All papers published until now, with exclusion of a few papers,[41,45,47,48,50–55] devote no attention to the role of the effective Young's modulus E^*, and the ratios H/E^* and H^3/E^{*2} on the tribological properties of wear-resistant and self-lubricating coatings. No trends between μ and k of the coating and its H, E^*, and the ratios H/E^* and H^3/E^{*2} were reported so far. Martinez-Martinez *et al.*[47] even said that the wear resistance of the nanocomposite TiC/*a*-C coatings is controlled by the friction of the tribological system rather than mechanical properties of the coating such as hardness, toughness, or resilience. On the contrary, Leyland and Mathews[50,51] reported on the significance of H/E ratio and optimization of hardness H and elastic modulus E^* in wear control of hard carbon and related coatings and claim that often wear properties are optimized when the ratio H/E^* is highest[52,53] but gives no information on the magnitude of E^*. Lindquist *et al.*[45] investigated tribological properties of TiC and TiAlC nanocomposite coatings and found that a higher friction coefficient (0.22) of the TiC coating is achieved at the higher ratio $H^3/E^{*2} = 0.54$ and a lower $\mu = 0.1$ of the TiAlC coating which contradicts with the prediction of Mathews and co-workers.[50–54]

At present, no clear information on the effect of E^*, and ratios H/E^* and H^3/E^{*2} on μ and k of the TiC/*a*-C coating is available. The paper in Ref. 48 clearly showed that μ and k of the *a*-C/Cu composite film decrease with increasing ratio H^3/E^{*2}. This result is in an excellent agreement with the prediction of Matthews and co-workers.[50–54] However, the paper[48] did not show what should be H and E^* of the film which results in an optimum ratio H^3/E^{*2} ensuring the lowest values of μ and k. This is an open problem which is the subject of the investigation reported in this article.

This article is devoted to a detailed investigation of physical, mechanical, and tribological properties of the TiC/*a*-C composite film. The attention is concentrated on the effect of the effective Young's modulus E^* on the coefficient of friction μ and wear coefficient k of the TiC/*a*-C composite film. The main aim of this study is to demonstrate that (1) μ and k of the TiC/*a*-C self-lubricating film correlates well with its mechanical properties, namely, with H and E^*; (2) there is an optimum H^3/E^{*2} ratio which ensures that the *a*-C/TiC nanocomposite film exhibits the lowest values of μ and k; (3) *a*-C/TiC nanocomposite film composed of nanograins embedded in the *a*-C matrix can exhibit a low value of E^* ensuring high values of the ratio $H/E^* > 0.1$.

II. EXPERIMENT

The TiC/*a*-C films were prepared by dc magnetron sputtering of C (99.99 at. %) target of 100 mm in diameter in Ar using a round unbalanced planar magnetron. The target was fixed to the magnetron by the titanium rings with seven inner diameters $\varnothing_{\text{in}} = 52$, 57, 60, 63, 66, 72, and 80 mm. Different diameters $\varnothing_{\text{in}}$ were used to control the amount of Ti in the film. The films were sputtered onto unheated Si (100) plate substrates ($20 \times 20 \times 0.381$ mm^3 for H, E^*, and μ measurements and $35 \times 5 \times 0.381$ mm^3 for the macrostress measurements) under the following conditions: discharge current I_d ranging from 0.5 to 2.5 A, substrate-to-target distance $d_{\text{s-t}} = 60$ mm, argon pressure $p = 1$ Pa, and deposition rate a_D ranging from ~17 to ~150 nm/min. The thickness h of the TiC$_x$ film was varied from 2700 to 3200 nm. More details on the experimental device are given in Ref. 48.

The structure of films was determined by x-ray diffraction using a Dron 4.07 diffractometer in the Bragg–Brentano configuration with Cu $K\alpha$ ($\lambda = 0.154\,187\,4$ nm) radiation. To avoid a strong reflection from Si substrate the slightly asymmetrical diffraction geometry was used. The mechanical properties of films, i.e., the microhardness H and the effective Young's modulus E^* were evaluated from the load versus displacement curves determined by a computer controlled microhardness tester Fisherscope H 100 equipped with the Vicker's diamond indenter. The mechanical properties of films were measured at low values of the indenter load $L = 30$ mN to ensure that the ratio $d/h \leq 0.1$ what is necessary condition to eliminate the effect of the substrate in indentation measurements; here d is the depth of diamond tip impression and h is the thickness of film. The values of H and E^* of the film are measured with accuracy of ±10%. The film thickness and macrostress σ generated in the film during

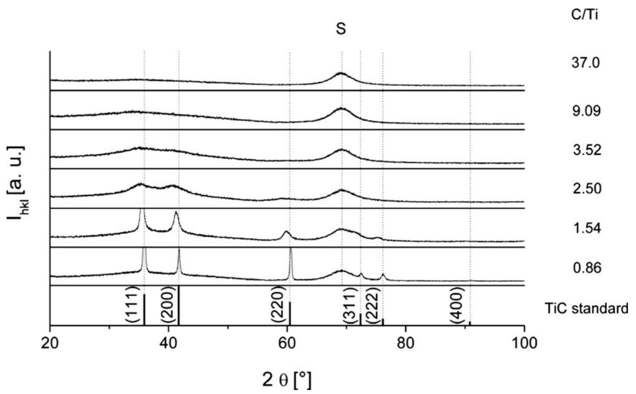

FIG. 1. Evolution of structure of TiC/*a*-C film with increasing C/Ti ratio. The dotted lines show positions of x-ray reflections from a powder TiC standard.

its growth were determined from the electromechanical Dektak 8 Profilometer analysis. The elemental composition of films was determined by x-ray fluorescence (XRF) measurements with accuracy of ±10%. The coefficient of friction μ of all TiC/*a*-C films was measured on a ball on disk tribometer (CSM Instruments) in ambient air with a WC ball (∅ =6 mm) under the load $L=2$ N load at velocity $v=0.05$ m/s and sliding distance $l=1000$ m. The wear coefficient k of TiC/*a*-C films was measured under the same conditions as those used in the friction tests. The wear loss, defined as volume loss per sliding distance, was measured using the Dektak 8 Profilometer. To show the effect of L on friction, μ of *a*-C film containing 0.3 at. % Ti was measured under different loads L ranging from 0.5 to 5 N.

III. RESULTS AND DISCUSSION

A. Structure of films

The structure of the TiC/*a*-C film strongly depends on C/Ti ratio, see Fig. 1. The TiC/*a*-C films with $\mathrm{C/Ti} \leq 1.54$ are polycrystalline films characterized with (111), (200) and (220) x-ray reflections. The polycrystalline TiC/*a*-C films gradually change with increasing C/Ti ratio, first to nanocrystalline films and later at high C/Ti ratios to amorphous films. The doted vertical lines in Fig. 1 show no change in the angle 2 theta of x-ray reflection from TiC grains with increasing C/Ti. It means that the sputtered films are not single phase TiC_x films but they are TiC/*a*-C composite films. The nanocrystalline nc-TiC/*a*-C films are composed of the TiC nanocrystals embedded in the *a*-C matrix. The intensities of x-ray reflections from the nanocrystalline films decrease and broaden with increasing C/Ti ratio up to their full disappearance in a broad x-ray amorphous peak of the *a*-C phase. The broadening of x-ray TiC reflection lines is a result of reducing the size d of TiC grains with increasing C/Ti ratio, see Table I.

The size d of the TiC grains and the C/Ti ratio, i.e., the amount of TiC phase and *a*-C phase in the film, determine its microhardness H and effective Young's modulus E^*. Therefore, H and E^* can be easily controlled by x-ray structure of film, see Fig. 1. Besides, it is well known that changes in the x-ray structure of film results not only in changes in its physical properties but also in changes in its functional properties. Therefore, it is reasonable to expect that also μ and k of the TiC/*a*-C film will strongly depend on its structure.

B. Friction and wear

Basic mechanical properties of thin films are the microhardness, H, and the effective Young's modulus, $E^*=E/(1-\nu^2)$. The ratio H^3/E^{*2} characterizes the resistance of film to plastic deformation. The resistance of the film to plastic deformation is higher, the higher is the H^3/E^{*2} ratio. It means that the likelihood of plastic deformation is reduced in materials with high hardness H and low modulus E^*. Usually, a low E^* becomes desirable as it allows the given load to be distributed over a larger area.[49,55,56]

Recently, it was shown that well lubricating and wear-resistant coatings, i.e., the coatings with low values of μ and k should be more resistant to plastic deformation. It was found that μ and k increase with increasing H^3/E^{*2} ratio.[48] However, it is not clear whether the H^3/E^{*2} ratio can be increased unlimited or if there is an optimum ratio H^3/E^{*2} at which the lubricating and wear-resistant coatings exhibit minimum values of μ and k? The answer to this question is a task of this investigation. The values H and E^* of sputtered films are controlled by the film structure as determined by x rays, see Fig. 1 and Table I.

TABLE I. Thickness l, mechanical and tribological properties of TiC/*a*-C composite films with x-ray structure displayed in Fig. 1. (The asterisk denotes the film relative to which the increase in H^3/E^{*2} and H/E^* is calculated. These two films are compared in the text.)

											Increase in	
C/Ti	h (nm)	σ (GPa)	D (nm)	μ	k (10^{-7} mm^3/N m)	H (GPa)	E^* (GPa)	W_e (%)	H^3/E^{*2} (GPa)	H/E	H^3/E^{*2} (GPa)	H/E
37.7	3100	−0.8	⋯	0.12	0.9	15.4	124.1	69.8	0.24	0.124	2.9×	1.8×
9.1	3200	−1.2	⋯	0.08	1.2	15.5	138.2	66.1	0.195	0.112	2.3×	1.6×
3.5	3000	−1.5	1	0.08	3.1	18.2	150.8	69.6	0.27	0.121		
2.5	3100	−1.9	2	0.16	4.2	21.8	162.8	76.6	0.39	0.134		
1.5	2700	−1.4	12	0.27	31.9	25.6	191.0	76.3	0.34	0.134		
0.86	2700	−0.3	35	0.25	9	16.4	230.6	51.7	0.083	0.71	1*	1*

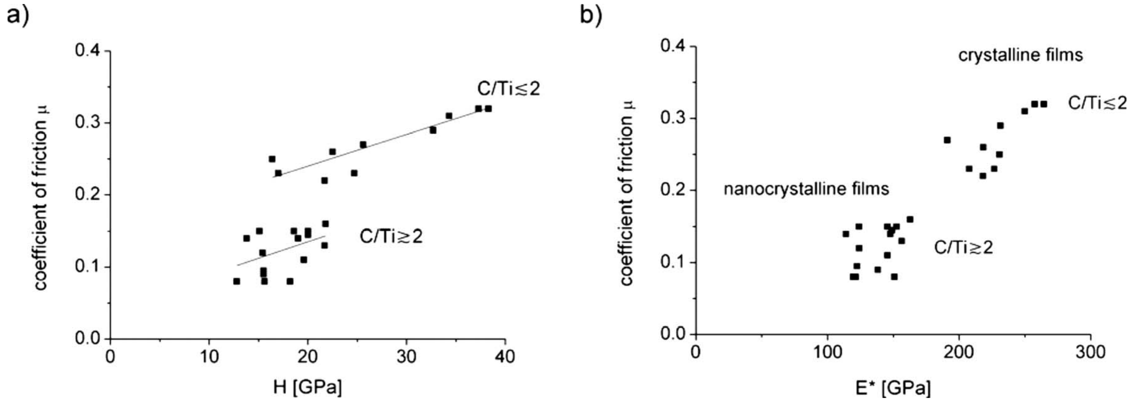

FIG. 2. Coefficient of friction μ of TiC/*a*-C film as a function of (a) H and (b) E^*.

1. Interrelationships between film structure, mechanical properties, friction, and wear

The structure of film is well indicated by the C/Ti ratio, as shown in Fig. 1. The TiC/*a*-C films with $C/Ti \leq 2$ are polycrystalline composite films. On the contrary, the TiC/*a*-C films with $x \geq 2$ are nanocrystalline composite films, which gradually transform to amorphous films at $C/Ti > 10$. Therefore, it is interesting to compare the values of μ and k of TiC/*a*-C films with $C/Ti \leq 2$ and $C/Ti \geq 2$.

Dependences of μ and k as function of H and E^* are displayed in Figs. 2 and 3. These figures show that the value of E^* is of key importance because (1) μ and k can exhibit different values at the same value of H, (2) the lowest values of μ exhibit nc-TiC/*a*-C films with H ranging from ~12 to ~19 GPa and E^* ranging from ~110 to ~150 GPa, and (3) the lowest values of k exhibit nc-TiC/*a*-C films with lowest values of H and E^*. The nc-TiC/*a*-C films with H ranging from ~12 to ~19 GPa and E^* ranging from ~110 to ~150 GPa, exhibit low values of μ (~0.07–~0.15) and low values of k $[(\sim 0.9-\sim 3) \times 10^{-7}\ \mathrm{mm^3/N\ m}]$. This range of values of E^* and H also shows that there is an optimum range of the ratio H^3/E^{*2} ranging from ~0.15 to ~0.30 and H/E^* ranging from ~0.11 to ~0.13.

Very recently, Lindquist *et al.*[45] showed that also the TiAlC nanocomposite coatings with $\mu \approx 0.1$ exhibit $H^3/E^{*2} = 0.23$ (lying just in the range we found for the nc-TiC/*a*-C film) while the TiC coating with higher μ (0.22) exhibits a higher ratio $H^3/E^{*2} = 0.54$. This result is in a good agreement with our finding, i.e., with the fact that (i) there is an optimum range of the H^3/E^{*2} ratio in which the lowest values of μ and k can be achieved and (ii) the ratio H^3/E^{*2} cannot be increased unlimited. Also, it is worthwhile to note that the wear-resistant coatings with values of the ratio H^3/E^{*2} lying in the optimum interval exhibit also a minimum erosion resistance. This fact is confirmed by experiments of Wei[57] who found that the erosion resistance of Ti–Si–C–N coatings decreases with increasing H^3/E^{*2} ratio and the lowest erosion resistance was achieved when the ratio $H^3/E^{*2} = 0.216$.

Usually, the wear-resistant coatings reported in literature are characterized by a low ratio $H/E^* \leq 0.1$. It means that these coatings can be optimized as to achievement of the lowest values of μ and k if the value of E^* is reduced and the ratio H^3/E^{*2} increased to a value of ≥ 0.1. The ratio $H/E^* \geq 0.1$ seems to be a good indicator for the coatings with lowest values of μ and k. However, the ratio H^3/E^{*2} is a more sensitive parameter controlling changes in μ and k, see

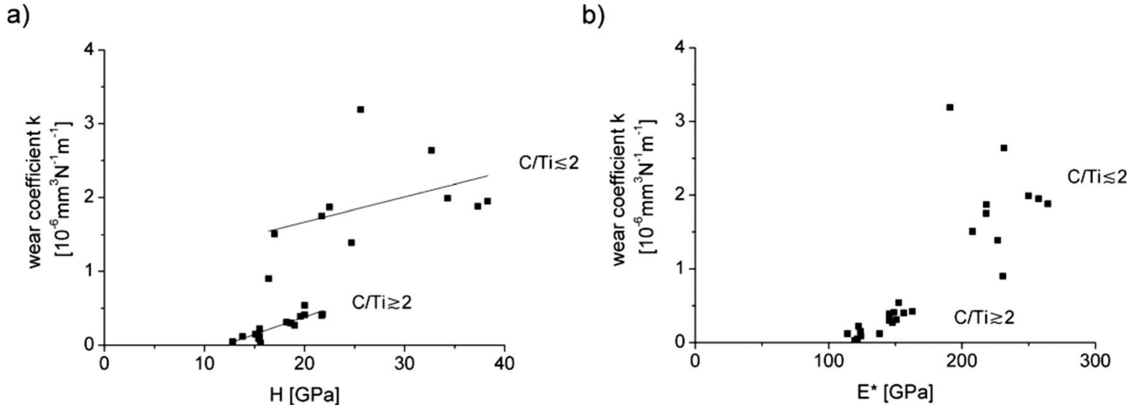

FIG. 3. Wear coefficient k of TiC/*a*-C film as a function of (a) H and (b) E^*.

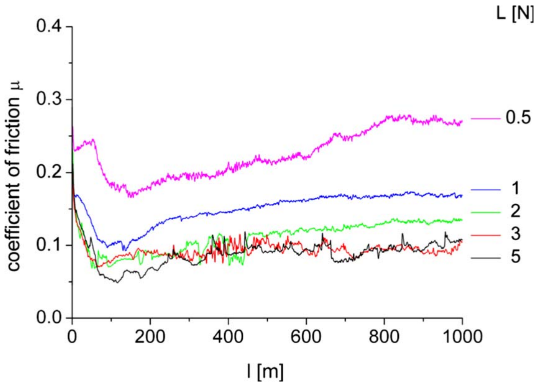

FIG. 4. (Color online) Coefficient of friction μ of *a*-C film with 0.3 at. % Ti and hardness $H=14$ GPa as a function of sliding distance l at different loads L of testing WC ball.

Table I. The increase in the ratio H^3/E^{*2} above ~0.3 already results in no further decrease of μ and k due to strong changes in the film structure.

The effect of ratios H/E^* and H^3/E^{*2} on μ and k is illustrated in Table I. Two films with approximately the same hardness $H=15.4$ GPa (x-ray amorphous with $H/E^*>0.1$) and $H=16.4$ GPa (well crystalline with $H/E^*<0.1$) are compared The nc-TiC/*a*-C film with $H/E^*>0.1$ exhibits compared to the TiC/*a*-C film with $H/E^*<0.1$ (1) much lower values of μ and k, (2) considerably lower (0.54×) value of E^*, and (3) strong increase (2.9×) in the resistance of film to plastic deformation characterized by increase in (i) the H^3/E^{*2} ratio and (ii) the elastic recovery W_e of film. The low value $E^*=124$ GPa of nc-TiC/*a*-C film with $H/E^*>0.1$ results in its improved resilient behavior which is characterized by a relatively high value of the ratio $H^3/E^{*2}=0.24$. We believe that the improved resilient behavior of film is the right way in the development of new advanced well lubricating, wear-resistant, and erosion-resistant coatings. Again, it is necessary to underline that so far the lowest values of μ and k exhibit nc-TiC/*a*-C films with hardness H ranging from ~12 to ~20 GPa only.

Also, it is worthwhile to note that ~3000 nm thick nc-TiC/*a*-C films exhibit relatively low (<1.5 GPa) compressive macostress σ. It is favorable for the film adhesion and is a good indicator that the measured hardness H of film is (i) the inherent property of film material not influenced by σ and (ii) the values of H and E^* measured by indentation are correct values.

2. Effect of load of testing ball on measured value of coefficient of friction

It is well known that the friction coefficient μ of the film depends not only on its structure and mechanical properties but also on the material and the load L of the sliding partner (testing ball). For instance, μ of the TiC/*a*-C film strongly decreases with increasing L, see Fig. 4. From this figure it is clearly seen that the measured values of μ of the same TiC/*a*-C film can differ more than two times according to the value of load L used in measurement. Therefore, μ of different films can be compared only in the case if the films are measured under the same load L of the testing ball.

Similar decrease in μ with increasing L is reported, e.g., for MoS_x films[58] or Mo–Se–C films.[59] This decrease in μ with increasing L was explained using the Hertzian contact model (smooth balls and flat substrates loaded below the elastic limit) and is well predicted by the formula in which $\mu \propto L^{-1/3}$.[58] Using this proportionality, the coefficient of friction μ of the film measured under different load L of testing ball can be compared.

Also, it is worthwhile to note that the measurement of μ depends not only on the material of testing ball, the velocity of its movement, its load L, and the atmosphere selected in the test but also on the mechanical properties of the substrate (H_s, E_s); the index s denotes the substrate. Therefore, in our study only one Si(100) substrate was used to avoid the effect of substrate on the measured values of μ and k. At high loads L the cracking of the film occurs.[56] It was found that the ratio $E^*/E_s^* \geq 1.3$ is the necessary condition to avoid the film cracking.[56]

At present, it is relatively difficult and sometimes even impossible to compare μ and k of different tribological coatings because not all parameters of the tribological tests are reported in published papers. Therefore, the comparison of the measured μ of different solid lubricating films may be often incorrect and confusing.

IV. CONCLUSIONS

Detailed investigation of the correlations between the x-ray structure, elemental, and phase composition of ~3000 nm thick TiC/*a*-C composite films, their mechanical properties (H, E^*, and W_e), μ, and k give a new insight on the design of well lubricating and wear-resistant coatings. The *a*-C/nc-TiC nanocomposite films with (i) the low effective Young's modulus E^* and the microhardness $H<20$ GPa satisfying the condition that the ratio $H/E^*>0.1$ and (ii) the ratio H^3/E^{*2} ranging from ~0.15 to ~0.30 exhibit lowest values of μ (≤ 0.1) and k ($\leq 2\times 10^{-7}$ $\mathrm{mm}^3/\mathrm{N\,m}$).

The finding that the amorphous/nanocrystalline composite film composed of the nc grains embedded in the amorphous matrix exhibit low values of E^* satisfying condition $H/E^*>0.1$ is of great scientific and practical importance. This finding opens a new way in the formation of advanced functional coatings with unique properties, and particularly in the development of new well lubricating and well wear-resistant protective coatings exhibiting simultaneously high hardness and high toughness.

ACKNOWLEDGMENTS

This work was supported in part by the Ministry of Education of the Czech Republic under Project No. MSM 4977751302 and the Grant Agency of the Academy of Sciences of the Czech Republic under Project No. KAN 400480701.

[1]A. A. Voevodin, R. Bantle, and A. Matthews, Wear **185**, 151 (1995).
[2]J. M. Schneider, A. A. Voevodin, C. Rebholz, and A. Matthews, J. Vac. Sci. Technol. A **13**, 2189 (1995).
[3]A. A. Voevodin, S. V. Prasad, and J. S. Zabinski, J. Appl. Phys. **82**, 855 (1997).
[4]A. A. Voevodin and J. S. Zabinski, J. Mater. Sci. **33**, 319 (1998).
[5]A. A. Voevodin, J. P. O. Neill, and J. S. Zabinski, Thin Solid Films **342**, 194 (1999).
[6]A. A. Voevodin and J. S. Zabinski, Thin Solid Films **370**, 223 (2000).
[7]A. Erdemir, O. L. Eryilmaz, and G. Fenske, J. Vac. Sci. Technol. A **18**, 1987 (2000).
[8]K. Bewilogua, C. V. Cooper, C. Specht, J. Schroder, R. Wittorf, and M. Grischke, Surf. Coat. Technol. **127**, 223 (2000).
[9]J. C. Damasceno, S. S. Camaro, Jr., F. L. Freire, Jr., and R. Carius, Surf. Coat. Technol. **133–134**, 247 (2000).
[10]T. Zehnder and J. Pascheider, Surf. Coat. Technol. **133–134**, 138 (2000).
[11]B. K. Tay, Y. H. Cheng, X. Z. Ding, S. P. Lau, X. Shi, G. F. You, and D. Sheeja, Diamond Relat. Mater. **10**, 1082 (2001).
[12]J. L. Endrino, J. J. Nainaparampil, and J. E. Krzanowski, Scr. Mater. **47**, 613 (2002).
[13]M. Ban and T. Hasegawa, Surf. Coat. Technol. **162**, 1 (2003).
[14]D. Nilsson, F. Svahn, U. Wiklund, and S. Hogmark, Wear **254**, 1084 (2003).
[15]A. A. Voevodin and J. S. Zabinski, in *Nanostructured Thin Films and Nanodispersion Strengthened Coatings*, edited by A. A. Voevodin, D. V. Shtansky, E. A. Levashov, and J. J. Moore (Kluwer Academic, Dordrecht, 2004), Chap. 1, pp.1–8.
[16]S. Zhang, X. L. Bui, and Y. Fu, Thin Solid Films **467**, 261 (2004).
[17]Y. Pauleau and F. Thiery, Surf. Coat. Technol. **180–181**, 313 (2004).
[18]C. Corbella, E. Pascual, G. Oncins, C. Canal, J. L. Andujar, and E. Bertran, Thin Solid Films **482**, 293 (2005).
[19]C. Corbella, G. Oncins, M. A. Gomez, M. C. Polo, E. Pascual, J. Garcia-Cespedes, J. L. Andujar, and E. Bertran, Diamond Relat. Mater. **14**, 1103 (2005).
[20]A. A. Voevodin and J. S. Zabinski, Compos. Sci. Technol. **65**, 741 (2005).
[21]R. J. Narayan and D. Scholvin, J. Vac. Sci. Technol. B **23**, 1041 (2005).
[22]Y. T. Pei, D. Galvan, J. Th. M. De Hosson, and A. Cavaleiro, Surf. Coat. Technol. **198**, 44 (2005).
[23]Y. T. Pei, P. Huizenga, D. Galvan, and J. Th. M. De Hosson, J. Appl. Phys. **100**, 114309 (2006).
[24]C. Donnet and A. Erdemir, in *Materials Surface Processing by Directed Energy Techniques*, edited by Y. Pauleau (Elsevier, Oxford, 2006), Chap. 17, pp. 573–594.
[25]J. M. Anton, B. Mishra, J. J. Moore, J. A. Rees, and W. D. Sproul, Surf. Coat. Technol. **201**, 4131 (2006).
[26]K. Baba, R. Hatada, and Y. Tanaka, Surf. Coat. Technol. **201**, 8362 (2007).
[27]X. Wu, M. Suzuki, T. Ohana, and A. Tanaka, Diamond Relat. Mater. **17**, 7 (2008).
[28]W. J. Meng and B. A. Gilispie, J. Appl. Phys. **84**, 4314 (1998).
[29]W. J. Meng, R. C. Tittsworth, and L. E. Rehn, Thin Solid Films **377–378**, 222 (2000).
[30]H. Dimigen, H. Hubsch, and R. Memming, Appl. Phys. Lett. **50**, 1056 (1987).
[31]Y. T. Pei, D. Galvan, and J. Th. M. De Hosson, Acta Mater. **53**, 4505 (2005).
[32]Y. T. Pei, D. Galvan, J. Th. M. De Hosson, and C. Strondl, J. Eur. Ceram. Soc. **26**, 565 (2006).
[33]U. Wiklund, M. Nordin, O. Wanstrand, and M. Larsson, Surf. Coat. Technol. **124**, 154 (2000).
[34]M. Stüber, H. Leiste, S. Ulrich, H. Holleck, and D. Schild, Surf. Coat. Technol. **150**, 218 (2002).
[35]S. Zhang, X. L. Bui, and D. Sun, in *Nanocomposite Thin Films and Coatings*, edited by S. Zhang and N. Ali (Imperial College Press, London, 2007), Chap. 2, pp.111–164; S. Zhang, X. L. Bui, J. Jiang, and X. Li, Surf. Coat. Technol. **198**, 206 (2004).
[36]J. L. Lin, B. Mishra, M. Pinkas, and J. J. Moore, Mater. Sci. Forum **561–565**, 1177 (2007).
[37]N. G. Chechenin, P. N. Chernych, V. S. Kulikaukas, Y. Pei, D. Vainstein, and J. Th. M. de Hosson, Journal of Surface Investigation-X-ray Synchrotron and Neutron Techniques, **1**, 674 (2007).
[38]K. Polychronopoulou, C. Rebholz, M. A. Baker, L. Theodorou, N. G. Demas, S. J. Hinder, A. A. Polycarpou, C. C. Doumanidis, K. Böbel, Diamond Relat. Mater. **17**, 2054 (2008).
[39]D. Martinez-Martinez, C. Lopez-Cartes, A. Fernandez, and J. C. Sanchez-Lopez, Surf. Coat. Technol. **203**, 756 (2008).
[40]V. J. Benavides, C. D. Salazar, M. E. Espitia, D. M. Devia, and A. Devia, Phys. Scr. **T131**, 014021 (2008).
[41]Y. H. Wang, X. Zhang, X. Y. Wu, H. Zhang, and X. Zhang, Appl. Surf. Sci. **254**, 5085 (2008).
[42]E. Lewin *et al.*, Surf. Coat. Technol. **202**, 3563 (2008).
[43]N. G. Chechenin, P. N. Chernych, V. S. Kulikauskas, Y. T. Pei, D. Vainshtein, and J. Th. M. De Hosson, J. Phys. D: Appl. Phys. **41**, 085402 (2008).
[44]Y. T. Pei, C. Q. Chen, K. P. Shaha, J. Th. M. De Hosson, J. W. Bradley, S. A. Voronin, and M. Cada, Acta Mater. **56**, 696 (2008).
[45]M. Lindquist, O. Wilhelmsson, U. Jansson, and U. Wiklund, Wear **266**, 379 (2009).
[46]C. Corbella, E. Bertran, M. C. Polo, E. Pascual, and J. L. Andujar, Diamond Relat. Mater. **16**, 1828 (2007).
[47]D. Martinez-Martinez, C. Lopez-Cartes, A. Fernandez, and J. C. Sanchez-Lopez, Thin Solid Films **517**, 1662 (2009).
[48]J. Musil, M. Louda, Z. Soukup, and M. Kubasek, Diamond Relat. Mater. **17**, 1905 (2008).
[49]T. Y. Tsui, G. M. Pharr, W. C. Oliver, C. S. Bhatia, R. L. White, S. Anders, A. Anders, and I. G. Brown, Mater. Res. Soc. Symp. **383**, 447 (1995).
[50]A. Leyland and A. Matthews, Wear **246**, 1 (2000).
[51]A. Leyland and A. Matthews, Surf. Coat. Technol. **177–178**, 317 (2004).
[52]A. Leyland and A. Matthews, in *Nanostructured Coatings*, edited by A. Cavaleiro and J. Th. M. De Hosson (Springer, New York, 2006), Chap. 11, pp.511–538.
[53]S. Neuville and A. Matthews, Thin Solid Films **515**, 6619 (2007).
[54]A. Matthews and A. Leyland, Materials related aspects of nanostructured tribological coatings, SVC Bulletin, Spring, 2009, pp. 40–44.
[55]J. Musil, F. Kunc, H. Zeman, and H. Polakova, Surf. Coat. Technol. **154**, 304 (2002).
[56]J. Musil and M. Jirout, Surf. Coat. Technol. **201**, 5148 (2007).
[57]R. Wei, Surf. Coat. Technol. **203**, 538 (2008).
[58]J. L. Grosseau-Poussard, P. Moine, and M. Brendle, Thin Solid Films **307**, 163 (1997).
[59]T. Polcar, M. Evarsto, R. Colaco, and C. Silviu Sandu, Acta Mater. **56**, 5101 (2008).

3.2.2 B-II: Coefficient of friction and wear of sputtered a-C thin coatings containing Mo

Surface & Coatings Technology 205 (2010) 1486–1490

Contents lists available at ScienceDirect

Surface & Coatings Technology

journal homepage: www.elsevier.com/locate/surfcoat

Coefficient of friction and wear of sputtered a-C thin coatings containing Mo

P. Novák [a], J. Musil [a,b,*], R. Čerstvý [a], A. Jäger [b]

[a] Department of Physics, Faculty of Applied Sciences, University of West Bohemia, Univerzitní 22, CZ-30614 Plzeň, Czech Republic
[b] Institute of Physics, Academy of Sciences of the Czech Republic, Na Slovance 2, CZ-182 21 Praha 8, Czech Republic

ARTICLE INFO

Available online 18 July 2010

Keywords:
Mo–C coating
Mechanical properties
Friction
Wear
Magnetron sputtering

ABSTRACT

The paper reports on preparation of ~3000 nm thick a-C coatings containing Mo, interrelationships between their mechanical properties, a coefficient of friction μ and wear rate k and the effect of Mo content in the a-C coating on these interrelationships. The Mo–C coatings were prepared by sputtering using an unbalanced magnetron (UM) equipped with a graphite targets ($\varnothing = 100$ mm, 99.9% purity) fixed to the UM cathode with Mo ring of different inner diameter $\varnothing_i$. The content of Mo in the a-C coating was controlled by $\varnothing_i$. It is shown that μ and k of the coating strongly depend not only on its hardness H but also on its effective Young's modulus $E^* = E/(1-\nu^2)$, the ratios H/E^*, H^3/E^{*2} and the elastic recovery W_e; here E is the Young's modulus and ν is the Poisson ratio. The ratio H^3/E^{*2} characterizes the resistance of coating to plastic deformation. Coatings with a low amount of Mo composed of nanograins of carbides dispersed in a-C matrix exhibit low values of $\mu \approx 0.07$ and $k \approx 10^{-7}$ mm^3/Nm measured with WC ball at the rotation speed $v = 0.05$ m/s, total sliding length $l = 1000$ m and the load $L = 2$ N.

1. Introduction

In recent years, a great attention was devoted to the investigation of tribological properties of amorphous carbon (a-C) coatings containing selected elements. For instance, the following systems were investigated in details: a-C/Ti [1–13], a-C/W [14–17], a-C/Nb [16,18,19], a-C/Mo [18,19], etc. These studies contain many important relations between the physical and the tribological properties. However the present knowledge in this field is still insufficient to define correctly the conditions under which a-C/Me composite coatings exhibit the lowest values of the coefficient of friction μ and the wear rate k.

Very recently, it has been shown that μ and k of a-C coatings containing a small amount of Cu [20] or Ti [21] correlates well with mechanical properties of the composite. Particularly, correlations of μ and k with the hardness, H, the effective Young's modulus, E^*, the ratios H^3/E^{*2} and H/E^* and the elastic recovery W_e are interesting. It was found that a high hardness H alone is not a sufficient condition to achieve a minimum value of μ and k. The coatings with the ratio H^3/E^{*2} ranging from ~0.15 to ~0.3, $H/E^* \geq 0.1$ and $W_e \geq 70\%$ exhibit low values of μ (≤ 0.1) and low values of k ($\leq 0.5 \times 10^{-6}$ mm^3/Nm) [21,22]. Besides it, there was shown that two-phase, amorphous coatings composed of a small amount of nanograins (one phase) dispersed in the amorphous matrix (second phase) and called the Dispersed Nanograins/Amorphous Matrix (DNG/AM) nanocomposite coatings, are very elastic due to a low value of E^* at $H/E^* \geq 0.1$. The key advantage of the DNG/AM nanocomposite coatings is their resilient behaviour which allow the development of hard and tough coatings with strongly suppressed brittleness [22].

The aim of this article is to show that the conclusions given above are valid also for other elements incorporated into a-C matrix. This article reports on the mechanical and tribological properties of a-(C,Mo) composite coatings.

2. Experimental

The Mo–C thin coatings were non-reactively sputtered from a composed C/Mo target composed of C (99.99 at.%) round plate ($\varnothing = 100$ mm) covered by Mo ring ($\varnothing 100$ mm/$\varnothing_{in}$) fixed to the cathode of DC unbalanced magnetron (UM) by a stainless steel fixing ring. The content of Mo in Mo–C coatings was controlled by the inner diameter $\varnothing_{in}$ of Mo ring, see Fig. 1. The Mo–C coatings were sputtered in a pure argon onto unheated Si(100) substrates with two dimensions: (1) $20 \times 20 \times 0.381$ mm^3 for mechanical and tribological tests and (2) $35 \times 5 \times 0.381$ mm^3 for measurement of the coating macrostress σ evaluated from the substrate bending. For sputtering of Mo–C coatings the following process parameters were used: discharge current $I_d = 0.5$ A and 1 A, substrate at a floating potential $U_s = U_{fl}$, argon pressure $p = 1$ Pa, substrate-to-target distance $d_{s-t} = 60$ mm with the coating deposition rate a_D ranging from 25 to 150 nm/min.

The structure of coatings was determined by X-ray diffraction (XRD) using a Dron 4.07 diffractometer in the Bragg–Brentano configuration with CuKα ($\lambda = 0.1541874$ nm) radiation. To avoid a strong reflection from Si substrate the asymmetrical diffraction geometry was used. Surface morphology was determined by the high resolution scanning

---

* Corresponding author. Institute of Physics, Academy of Sciences of the Czech Republic, Na Slovance 2, CZ-182 21 Praha 8, Czech Republic.
E-mail address: musil@kfy.zcu.cz (J. Musil).

0257-8972/$ – see front matter © 2010 Elsevier B.V. All rights reserved.
doi:10.1016/j.surfcoat.2010.07.038

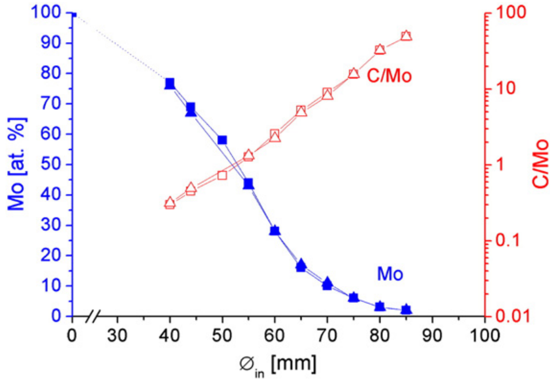

Fig. 1. Content of Mo and ratio C/Mo as a function of inner diameter $\varnothing_{in}$ of Mo ring at two values of discharge current $I_d = 0.5$ (squares) and $I_d = 1$ A (triangles).

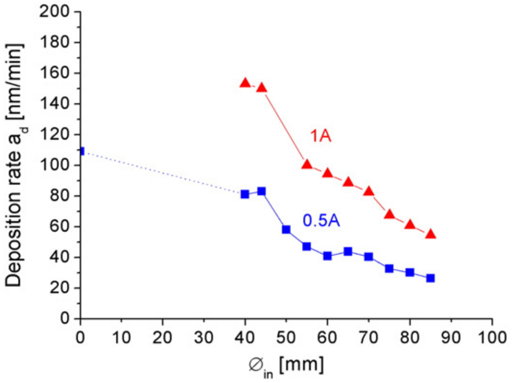

Fig. 2. Deposition rate a_d of Mo–C films as a function of inner diameter $\varnothing_{in}$ of Mo ring at two values of discharge current $I_d = 0.5$ (squares) and $I_d = 1$ A (triangles).

electron microscope (FE SEM) with focused ion beam (FIB) DualBeam FEI Quanta 3D FEG. RMS roughness was meassured by the AFM Bruker Nanos. The mechanical properties of coatings, the microhardness, H, the effective Young's modulus, E^*, and the elastic recovery W_e were evaluated from the load vs. displacement curves determined by a computer controlled microhardness tester Fischerscope H 100 equipped with the Vicker's diamond indenter. The mechanical properties of the coatings were measured at a low value of the indentor load $L = 30$ mN to ensure that the ratio $d/h \leq 0.1$ which is a necessary condition to eliminate the effect of the substrate on indentation measurements; here d is the depth of the diamond tip impression and h is the thickness of coating. The values of H, E^* and we were measured with the accuracy ± 10%. The coating thickness h and the macrostress σ generated in the coating during its growth were determined from the electro-mechanical Dektak 8 Profilometer analysis. The elemental composition of coatings was determined by X-ray fluorescence (XRF) and RBS measurements with the accuracy ± 10%. The coefficient of friction μ of all Mo–C coatings was measured using a ball-on-disk tribometer (CSM) in ambient air with a WC ball ($\varnothing = 6$ mm) rotating at radius $r = 3$ mm under the load $L = 2$ N at the velocity $v = 0.05$ m/s and the sliding distance $l = 1000$ m (53 052 revolutions). The wear rate k of the coatings was measured under the same conditions as those used in the friction tests. The wear loss, defined as the coating volume loss per the sliding distance l, was measured by the Dektak 8 Profilometer.

3. Results and discussion

3.1. Deposition rate, structure, surface morphology, mechanical and tribological properties

The deposition rate a_d depends on the power $P_d = I_d U_d$ delivered to the magnetron and the content of Mo incorporated into Mo–C coating, see Fig. 2. The deposition rate a_D decreases with increasing $\varnothing_{in}$ of Mo ring, i.e. with a decreasing amount of Mo in the coating, due to a lower sputtering yield γ of C compared to Mo ($\gamma_C = 0.2$, $\gamma_{Mo} = 0.9$ [23]). As expected, a_D increases with increasing I_d, i.e. with increasing power P_d delivered to the magnetron.

The structure of Mo–C coating strongly depends on the amount of Mo incorporated in it. The evolution of the XRD patterns from the Mo–C coating, sputtered at $I_d = 0.5$ with an increasing amount of Mo is displayed in Fig. 3. The XRD patterns show that

1. The Mo–C coatings with high (≥40 at.%) content of Mo are crystalline. Their phase composition gradually changes from a pure polycrystalline Mo film containing 100 at.% Mo and characterized with (100), (211) and (220) reflections through (Mo,C) solid solution coatings first to well crystalline γ-Mo_2C/(Mo,C) composite coatings at ~70 at.% Mo and then to nanocrystalline (nc-) δ-$MoC_{0.75}$/a-(Mo,C) composite coatings with <57 at.% Mo content.
2. Mo–C films with Mo content lower than ~28 at.% are X-ray amorphous a-(C,Mo) films.

Both the structure and the phase composition of the coating, which are controlled by the amount of Mo in the coating, strongly influence properties of Mo–C films what is shown below.

Typical evolution of the surface morphology of Mo–C coatings with increasing content of Mo is displayed in Fig. 4. This figure shows that the surface of coating is smoothened when the content of Mo increases. The δ-$MoC_{0.75}$/a-(C,Mo) coating composed of δ-$MoC_{0.75}$ nanograins embedded in a-(C,Mo) matrix exhibits a lower surface roughness compared to that of the a-(C,Mo) coating. It indicates, that not only Mo content but also the microstructure of a-(C,Mo) coating influences its surface roughness.

Basic mechanical properties of thin coatings are the microhardness, H, the effective Young's modulus, $E^* = E/(1-\nu^2)$ and the elastic recovery W_e; here E is the Young's modulus and ν is the Poisson's ratio. All these three quantities – H, E^* and W_e – are displayed as a function of Mo content in the Mo–C coating in Fig. 5a and b, respectively. From Fig. 5 it is seen that the dependence of H and E^* with increasing Mo content in the Mo–C coating is more complicated than that of W_e. The elastic

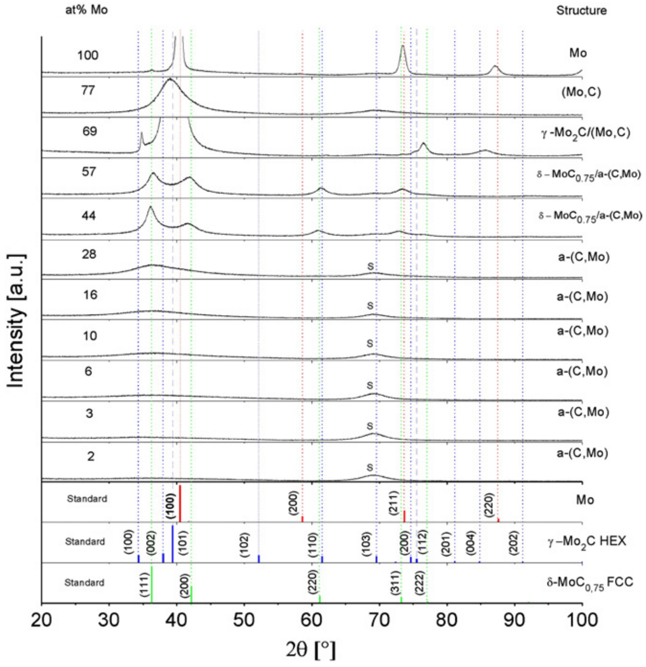

Fig. 3. Evolution of XRD patterns from Mo–C coatings, sputtered $I_d = 0.5$ A, with increasing content of Mo. S denotes reflection from the substrate.

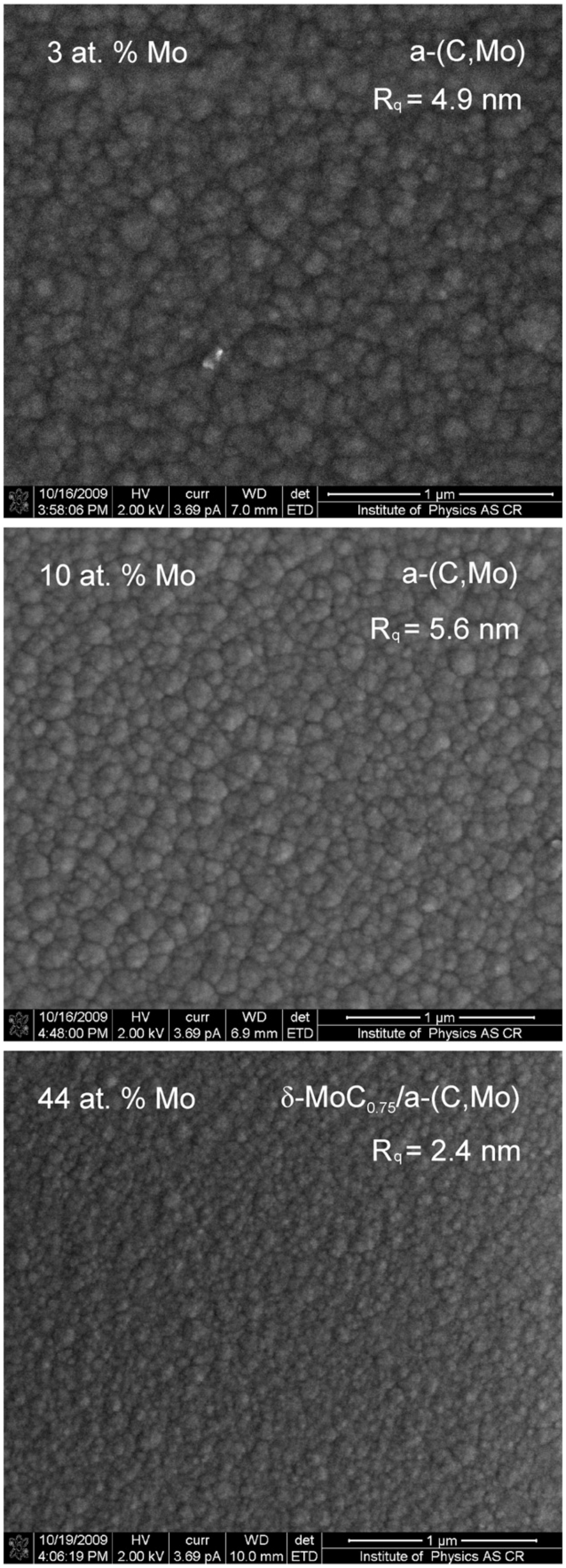

Fig. 4. Evolution of surface morphology of Mo–C coatings with increasing content of Mo.

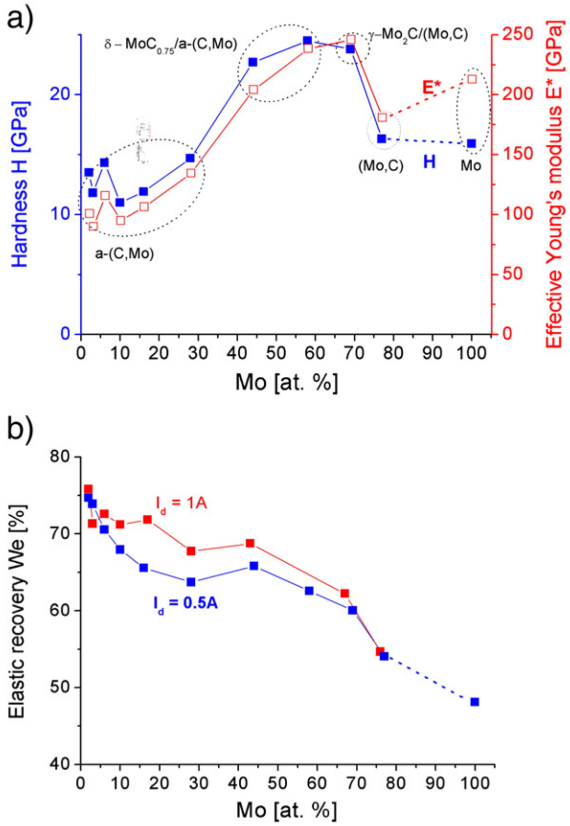

Fig. 5. H and E^* (a) and W_e (b) of Mo–C coatings sputtered at $I_d = 0.5$ A (squares) and $I_d = 1$ A (triangles) as a function of Mo content.

recovery W_e almost continuously decreases with an increasing amount of Mo in the coating. On the contrary, H strongly depends on the coating crystallinity and its phase composition: (i) amorphous a-(C, Mo) coatings exhibit the lowest hardness H ≈ 10 GPa, (ii) nc-δ-$MoC_{0.75}$/a-(C,Mo) are approximately two times harder (~23 GPa) and have almost the same H as well crystallized γ-Mo_2C/(Mo,C) containing ~ 70 at.% Mo and (iii) (Mo,C) solid solution coatings produced at ~77 at.% Mo exhibit much lower (~17 GPa) H approaching to that of pure crystalline Mo coatings.

The following issues are of fundamental importance for tribological behaviour of the coating [21]: (1) C–Mo coatings with Mo content lower than 57 at.% exhibit the ratio $H/E^* > 0.1$ and (2) the amorphous a-(C,Mo) coatings exhibit (i) the lowest value of the effective Young's modulus

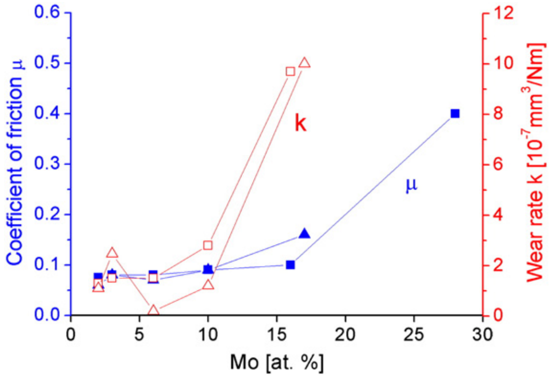

Fig. 6. Coefficient of friction μ (full symbols) and wear rate k (open symbols) as a function of amount of Mo in C–Mo coatings sputtered at two values of discharge current $I_d = 0.5$ A (squares) and $I_d = 1$ A (triangles).

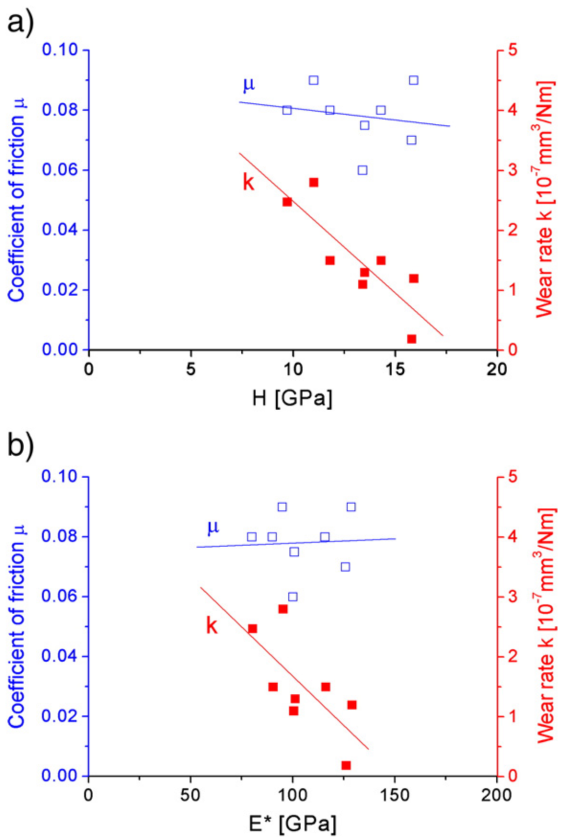

Fig. 7. Coefficient of friction μ and wear rate k of coatings as a function of (a) hardness H and (b) effective Young's modulus E^*.

$E^* < 150$ GPa and (ii) the highest values of the elastic recovery $W_e \geq 70\%$. Moreover, it is worthwhile to note that W_e of coatings with Mo content ranging from 10 to 67 at.% can be slightly increased if higher I_d, i.e. a more intensive magnetron discharge, is used in sputtering of the coating.

The values of μ and k of the a-(C, Mo) coating, measured at load L = 2 N in ambient air with a WC ball (Ø = 6 mm) and sliding distance l = 1000 m, as a function of Mo content is displayed in Fig. 6. This figure shows that both μ and k strongly increase for coatings containing more than 10 at.% Mo. This increase of μ and k is caused by the change of mechanical properties of the coating as shown below. The a-(C,Mo) coatings exhibit a compressive macrostress σ ranging from −0.6 to −1.1 GPa. No relation between the macrostress σ in the a-(C,Mo) coating and its tribological properties was found.

3.2. Interrelationships between mechanical properties, coefficient of friction and wear

Interrelationships between the μ (open symbols) and k (full symbols) and the hardness, H, and the effective Young's modulus, E^*, of the a-(C,Mo) coatings are displayed in Fig. 7 and summarized in Table 1. From this figure it is seen that while μ is almost independent on both H and E^*, k decreases with increasing both H and E^* to a minimum value. It indicates that there is an optimum value of H at which both μ and k are minimal. More information on correlations between μ, k and H, E^*, W_e. H/E and H^3/E^{*2} are given in Table 1.

From Table 1 it is seen that (1) X-ray amorphous (XRA) coatings, probably composed of a low amount of small nanograins of carbides dispersed in a-C matrix, exhibit the lowest values of μ and k, (2) both μ and k decrease with increasing ratio H/E^* and the decrease of k is much stronger than the decrease of μ and (3) the decrease of μ and k correlates well with increasing (i) elastic recovery W_e of coating and (ii) resistance to plastic deformation, i.e. with increasing ratio H^3/E^{*2}, but only if the value of the effective Young's modulus E^* is sufficiently low and the ratio $H/E^* \geq 0.1$. The increase of H and H^3/E^{*2} which results in the decrease of H/E^*, see for instance the coating with C/Mo = 2.5, does not ensure the lowest values of μ and k due to high values of E^*. It means that there is an optimum interval of H, E^*, H^3/E^{*2} which ensures that μ and k of the coating are minimal. A similar result was already found for the a-C/TiC composite coatings [12].

3.3. Loading–unloading curves of a-(C,Mo) coatings

The loading–unloading curves determined during indentation measurements of mechanical properties illustrate well the plastic–elastic properties of Mo alloyed carbon coatings, see Fig. 8. Generally, the elasticity of the coating increases when the area between loaded and unloaded curve decreases. Fig. 8a illustrates the effect of decrease of E^* at the same value of H and Fig. 8b illustrates the effect of the decrease of E^* at different values of H on the plastic–elastic properties of the coating. In both cases the elasticity of the coating increases with decreasing E^* and increasing H/E^* ratio, see Table 1. The coating with the highest value of W_e exhibits the lowest values of μ and k. This experiment clearly shows that the increase of H is not a sufficient condition to reduce μ and k of the coating. Obtained results indicate that the resilience behaviour of the coating is of key importance for the reduction of μ and k.

4. Conclusions

The article presents results of a detailed investigation of the correlations between the mechanical and tribological properties of a-(C,Mo)

Table 1
Mechanical and tribological properties of ~3000 nm thick coatings sputtered at $I_d = 0.5$ A on Si(100) substrate and measured at a load L = 30 mN and 2 N, respectively, as a function of at.% Mo added in a-C and X-ray structure (XRA, crystalline). The coefficient of friction μ and wear k was measured using WC ball and sliding distance l = 1000 m. The XRD patterns from these coatings are displayed in Fig. 3.

C/Mo	Mo[at.%]	a_d [nm/min]	X-ray structure	σ [GPa]	H [GPa]	E* [GPa]	W_e [%]	H^3/E^{*2} [GPa]	H/E^*	μ	k [10^{-7} mm^3/Nm]
49.0	2	26.4	XRA	−0.8	13.5	101	74.7	0.24	0.134	0.075	1.34
32.3	3	30.1	XRA	−0.9	11.8	90	73.9	0.20	0.131	0.077	1.51
15.7	6	32.6	XRA	−0.8	14.3	116	70.5	0.22	0.123	0.079	1.53
9.0	10	40.3	XRA	−0.6	11.0	95	67.9	0.15	0.116	0.090	2.88
5.3	16	43.7	XRA	−0.9	11.9	106	65.6	0.15	0.112	0.100	9.73
2.5	28	40.8	XRA	−1.1	14.7	135	63.7	0.18	0.109	0.440	–
1.3	44	47.0	nc-	−0.8	22.7	204	65.8	0.28	0.111	–	–
0.7	57	58.0	nc-	−0.6	24.5	238	62.6	0.26	0.102	–	–
0.4	69	82.5	Crystalline	0.1	23.8	246	60.0	0.22	0.097	–	–
0.3	77	80.6	nc-	−0.8	16.2	181	54.1	0.13	0.090	–	–
0	100	108.7	Crystalline	0.2	15.9	213	48.1	0.09	0.075	–	–

The mark — denotes that μ and k could not be evaluated due to partial cracking of testing coating.

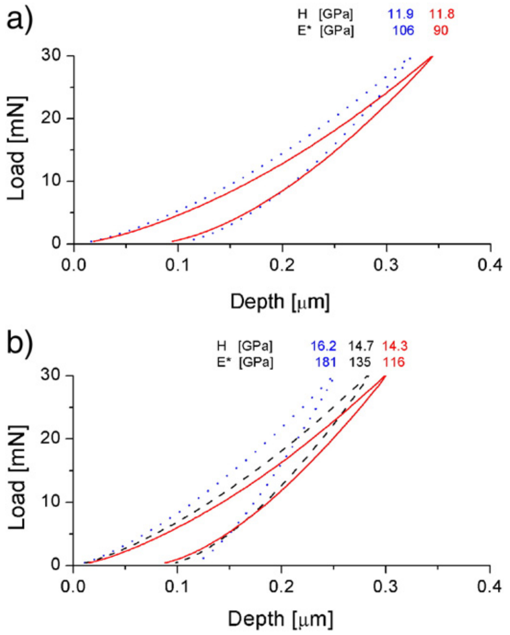

Fig. 8. Loading–unloading curves of selected a-(C,Mo) coatings: a) coatings with the same H and b) coatings with different H. Mechanical parameters of coatings are given in Table 1.

thin coatings non-reactively sputtered from the composite C/Mo target. Obtained results can be summarized as follows.

1. The sputtered C coatings containing less than 28 at.% Mo are 220 X-ray amorphous a-(C,Mo) coatings.
2. The a-(C,Mo) with Mo content lower than 10 at.% coatings exhibit low (≤ 0.1) values of the coefficient of friction μ and low ($\leq 5 \times 10^{-7}$ mm^3/Nm) values of the wear rate k.
3. The values of μ and k decrease with increasing H/E^* and H^3/E^{*2} ratio. However, the H^3/E^{*2} ratio cannot be increased unlimitedly. There is an optimum interval of the ratio H^3/E^{*2} which ensures that μ and k of the coating are minimum.
4. The a-(C,Mo) coatings with low value of E^* satisfying condition $H/E^* \geq 0.12$ exhibit high values of the elastic recovery $W_e \geq 70\%$.

Acknowledgements

This work was supported in part by the Ministry of Education of the Czech Republic under Project No. MSM 4977751302 and Grant of the Academy of Sciences of the Czech Republic KAN300100801.

References

[1] A.A. Voevodin, R. Bantle, A. Matthews, Wear 185 (1995) 151.
[2] M. Schneider, A.A. Voevodin, C. Rebholz, A. Matthews, J. Vac. Sci. Technol., A 13 (4) (1995) 2189.
[3] A.A. Voevodin, S.V. Prasad, J.S. Zabinski, J. Appl. Phys. 82 (2) (1997) 855.
[4] A.A. Voevodin, J.S. Zabinskites, J. Mater. Sci. 33 (1998) 319.
[5] A.A. Voevodin, J.S. Zabinski, Thin Solid Films 370 (2000) 223.
[6] J.M. Anton, B. Mishra, J.J. Moore, J.A. Rees, W.D. Sproul, Surf. Coat. Technol. 201 (2006) 4131.
[7] K. Baba, R. Hatada, Y. Tanaka, Surf. Coat. Technol. 201 (2007) 8362.
[8] H. Dimigen, H. Hubsch, R. Memming, Appl. Phys. Lett. 50 (16) (1987) 1056.
[9] Y.T. Pei, D. Galvan, J.Th.M. De Hosson, Acta Mater. 53 (2005) 4565.
[10] Y.T. Pei, D. Galvan, J.Th.M. De Hosson, C., J. Eur. Ceram. Soc. 26 (2006) 565.
[11] S. Zhang, X.L. Bui, J. Jiang, X. Li, Surf. Coat. Technol. 198 (2004) 206.
[12] N.G. Chechenin, P.N. Chernych, V.S. Kulikauskas, Y.T. Pei, D. Vainshtein, J.Th.M. De Hosson, J. Phys. D Appl. Phys. 41 (8) (2008) 085402.
[13] Y.T. Pei, C.Q. Chen, K.P. Shaha, J.Th.M. De Hosson, J.W. Bradley, S.A. Voronin, M. Cada, Acta Mater. 56 (4) (2008) 696.
[14] W.J. Meng, B.A. Gillispie, J. Appl. Phys. 84 (8) (1998) 4314.
[15] A.A. Voevodin, J.P. O Neill, J.S. Zabinski, Thin Solid Films 342 (1999) 194.
[16] K. Bewilogua, C.V. Cooper, C. Specht, J. Schroder, R. Wittorf, M. Grischke, Surf. Coat. Technol. 127 (2000) 223.
[17] D. Nilsson, F. Svahn, U. Wiklund, S. Hogmark, Wear 254 (2003) 1084.
[18] C. Corbella, E. Pascual, G. Oncins, C. Canal, J.L. Andujar, E. Bertran, Thin Solid Films 455–456 (2005) 293.
[19] C. Corbella, G. Oncins, M.A. Gomez, M.C. Polo, E. Pascual, J. Garcia-Cespedes, J.L. Andujar, E. Bertran, Diamond Relat. Mater. 14 (2005) 1103.
[20] J. Musil, M. Louda, Z. Soukup, M. Kubásek, Diamond Relat. Mater. 17 (2008) 1905.
[21] J. Musil, P. Novák, R. Čerstvý, Z. Soukup, J. Vac. Sci. Technol., A 28 (2) (2010) 244.
[22] J. Musil, Galvanotechnik 101 (Part 1, No. 8) (Part 2, No. 9) (in press).
[23] http://www.angstromsciences.com/reference/sputtering-yields/.

3.3 Část C

Multifunkční vrstvy Al-Cu-O, Zr-Al-O, Al-O-N se zvýšenou odolností proti vzniku trhlin při namáhání

3.3.1 C-I: Properties of nanocrystalline Al–Cu–O films reactively sputtered by DC pulse dual magnetron

Applied Surface Science 258 (2011) 1762–1767

Contents lists available at SciVerse ScienceDirect

Applied Surface Science

journal homepage: www.elsevier.com/locate/apsusc

Properties of nanocrystalline Al–Cu–O films reactively sputtered by DC pulse dual magnetron

J. Blažek, J. Musil*, P. Stupka, R. Čerstvý, J. Houška

Department of Physics, Faculty of Applied Sciences, University of West Bohemia, Univerzitní 22, CZ-306 14 Plzeň, Czech Republic

ARTICLE INFO

Article history:
Received 23 September 2011
Received in revised form 7 October 2011
Accepted 8 October 2011
Available online 14 October 2011

Keywords:
Al_2O_3-based films
Cu addition
Mechanical properties
Elasticity
Resistance to cracking
Pulse reactive sputtering

ABSTRACT

The article reports on the effect of the addition of copper in the Al_2O_3 film on its mechanical and optical properties. The Al–Cu–O films were reactively co-sputtered using DC pulse dual magnetron in a mixture of $Ar + O_2$. One magnetron was equipped with a pure Al target and the second magnetron with a composed Al/Cu target. The amount of Al and Cu in the Al–Cu–O film was controlled by the length of pulse at the Al/Cu target. The Al–Cu–O films with ≤16 at.% Cu were investigated in detail. The addition of Cu in Al_2O_3 film strongly influences its structure and mechanical properties. It is shown that (1) the structure of Al–Cu–O film gradually varies with increasing Cu content from γ-Al_2O_3 at 0 at.% Cu through $(Al_{8-2x},Cu_{3x})O_{12}$ nanocrystalline solid solution to $CuAl_2O_4$ spinel structure, (2) the Al–Cu–O films with ≥3 at.% Cu exhibit (i) relatively high hardness H increasing from ~15 GPa to ~20 GPa, (ii) enhanced elastic recovery W_e increasing from ~67% to ~76% with increasing Cu content from ~5 to ~16 at.% Cu and (iii) low values of Young's modulus E^* satisfying the ratio $H/E^* > 0.1$ at ≥5 at.% Cu, and (3) highly elastic Al–Cu–O films with $H/E^* > 0.1$ exhibit enhanced resistance to cracking during indentation under high load.

1. Introduction

The Al–Cu–O thin films represent a huge potential for many new industrial applications such as p-type $CuAlO_2$ transparent conductive oxides (TCO) [1], buffer layers for growth of films on incompatible substrates [2], nanocomposites with enhanced mechanical properties [3] or selective solar absorbers in solar collectors [4]. Also, photocatalytic activity of spinel $CuAl_2O_4$ nanoparticles was demonstrated [5]. Using different methods and preparation conditions either single phase $CuAl_2O_4$ [6] and $CuAlO_2$ [7,8] compounds or Cu/Al_2O_3 [3] and $Cu/CuAl_2O_4$ [4] nanocomposites were prepared.

Very often Al–Cu–O films are prepared by sputtering. Lan et al. used RF sputtering of a ceramic $CuAlO_2$ target to investigate the influence of the partial pressure of oxygen on electrical resistivity and transparency of Cu–Al–O TCO films [9]. Ong et al. used the reactive co-sputtering of Al and Cu targets to prepare p-type Cu–Al–O TCO films and investigated the effect of the Cu/Al ratio on their properties [10]. Alkoy et al. deposited the copper oxide and copper aluminum oxide thin films by pulsed magnetron sputtering of powder targets [7]. Shy et al. prepared $CuAlO_2$ thin film by rapid thermal annealing (RTA) of the reactively sputtered Al_2O_3/Cu_2O/sapphire structure [8]. Tsuboi et al. investigated the effect of Cu/Al ratio on composition and structure of reactively sputtered Cu–Al–O films [11]. No investigation of mechanical properties of reactively sputtered Al–Cu–O films was, however, carried out so far. This investigation is a subject of this article.

The aim of our study is to reactively sputter Al–Cu–O films with different content Cu and to investigate the effect of the addition of Cu in the Al_2O_3 film on its structure, mechanical properties and resistance to cracking during indentation under high load. The main task of this investigation is to find out if Cu added in the Al_2O_3 can reduce the brittleness of Al_2O_3 film and enhance its resistance to cracking.

2. Experimental details

The Al–Cu–O films were reactively sputtered by a dual magnetron in an $Ar + O_2$ sputtering gas mixture. The dual magnetron consists of two magnetically closed magnetrons with targets of 50 mm in diameter and tilted with respect to the vertical axis at an angle of 20°. One magnetron is equipped with target made of pure Al, the second magnetron with a composed Al/Cu target, see Fig. 1. The Cu content in the film is controlled by the length of negative voltage pulse $\tau_{Al/Cu}$ at the Al/Cu target in the range from 8 to 32 μs; the content of Cu in the film increases with increasing length of $\tau_{Al/Cu}$ pulse. The dual magnetron was supplied by a floating DC pulse power supply RMP-10 (Hüttinger Electronic, Inc.) operated

---

* Corresponding author. Tel.: +420 377632200; fax: +420 377632202.
E-mail address: musil@kfy.zcu.cz (J. Musil).

0169-4332/$ – see front matter © 2011 Elsevier B.V. All rights reserved.
doi:10.1016/j.apsusc.2011.10.039

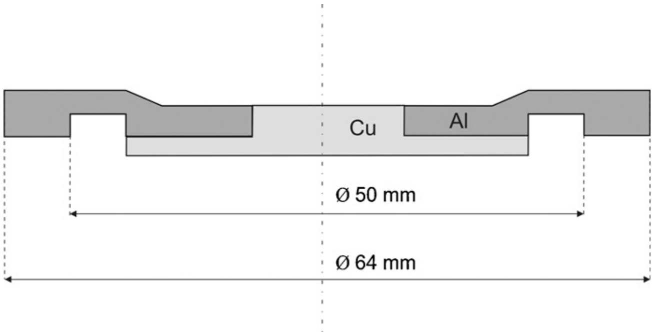

Fig. 1. Geometry and dimensions of composed Al/Cu target used in dual magnetron.

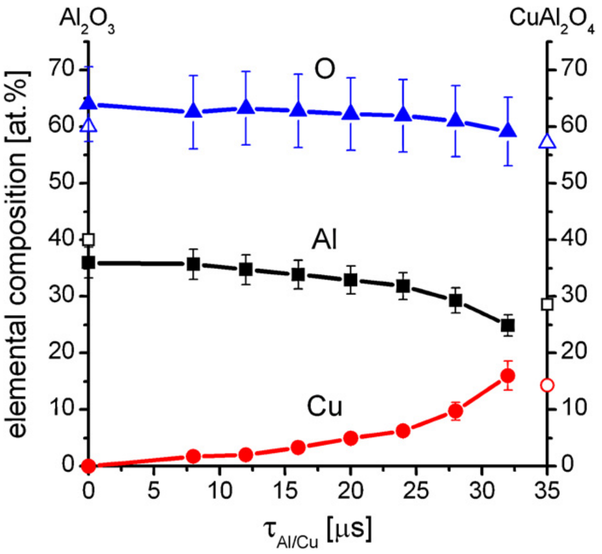

Fig. 3. Elemental composition of Al–Cu–O film sputtered at f_r = 25 kHz as a function of $\tau_{Al/Cu}$. Open symbols indicate elemental composition of stoichiometric Al_2O_3 and $CuAl_2O_4$ compounds.

in bipolar mode at a repetition frequency f_r = 25 kHz. Typical time dependence of the discharge voltage $U_d = f(t)$ and current $I_d = f(t)$ waveforms for $\tau_{Al/Cu}$ = 24 µs are given in Fig. 2.

The Al–Cu–O films were deposited on Si (1 0 0) substrates (20 mm × 20 mm × 0.38 mm and 35 mm × 5 mm × 0.38 mm) in the oxide mode of sputtering. The following deposition conditions were used: the discharge power averaged over pulse period P_{da} = 1.2 kW, the substrate temperature T_s = 500 °C, the substrate bias $U_s = U_{fl}$, the substrate-to-target distance d_{s-t} = 110 mm, the oxygen partial pressure $p_{O_2} = 0.2$ Pa and the total pressure $p_T = p_{Ar} + p_{O_2} = 0.5$ Pa; here U_{fl} is the floating potential.

The thickness of the film and the macrostress σ generated in it during its growth were measured by a stylus profilometer Dektak 8. The macrostress σ was evaluated from the bending of a thin Si plate (35 mm × 5 mm × 0.38 mm) using the Stoney's formula. The structure of films was characterized by glancing incidence X-ray diffraction (GIXRD) at angle of 0.75° using a PANalytical X'Pert PRO diffractometer. The elemental composition of the films was measured by a PANalytical X-ray fluorescence (XRF) spectrometer MagiX PRO calibrated using results obtained from the Rutherford Backscattering Spectroscopy (RBS) of selected samples. The accuracy of the measurement of the elemental composition is denoted by error bars in Fig. 3. The surface morphology of films was investigated using scanning electron microscope FEI QUANTA 200 in the ESEM regime enabling to study nonconducting films. Mechanical properties of Al–Cu–O films were determined from the load vs. displacement curves measured by a Fischerscope H-100 microhardness tester with the Vicker's diamond indenter at the load L = 20 mN. The resistance of the film to cracking was determined by generation of cracks during penetration of the diamond indenter into the film under high load L = 1 N [12]. The optical properties of films, i.e. the film transparency T, index of refraction n and the extinction coefficient k, were investigated in the visible (VIS) and near infrared (NIR) regions between 300 and 2000 nm, using a variable angle spectroscopic ellipsometry (VASE) using the J.A. Woollam Co. Inc. instrument. The optical properties were evaluated from reflections at incident angles 65°, 70° and 75°. The measured data were fitted using the VASE software and the optical model of the system composed of the c-Si substrate and the Al–Cu–O layer described by a Cauchy dispersion formula and surface roughness layer [13].

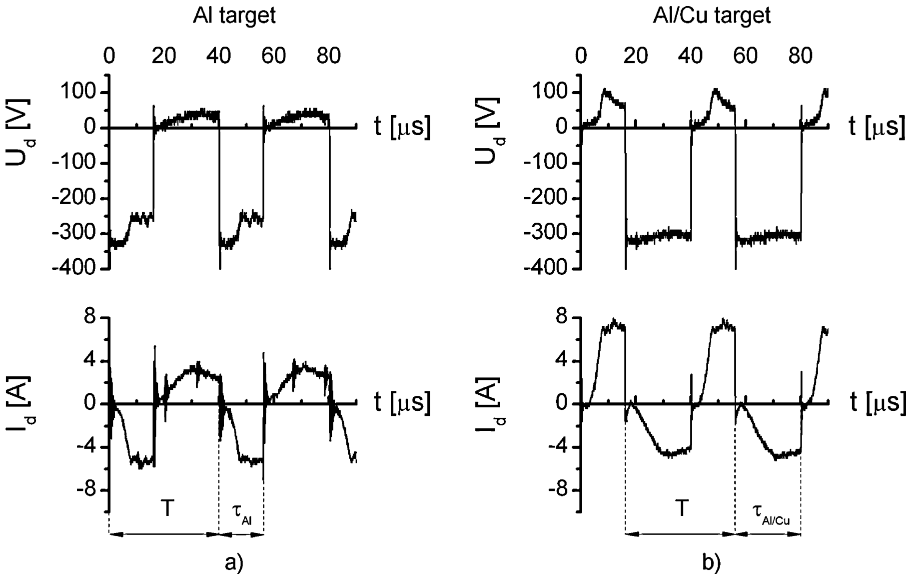

Fig. 2. Current $I_d(t)$ and voltage $U_d(t)$ waveforms measured with respect to ground potential at (a) Al target and (b) Al/Cu target of dual magnetron operated at the repetition frequency f_r = 25 kHz, pulse period $T = 1/f_r$ = 40 µs, τ_{Al} = 16 µs and $\tau_{Al/Cu}$ = 24 µs.

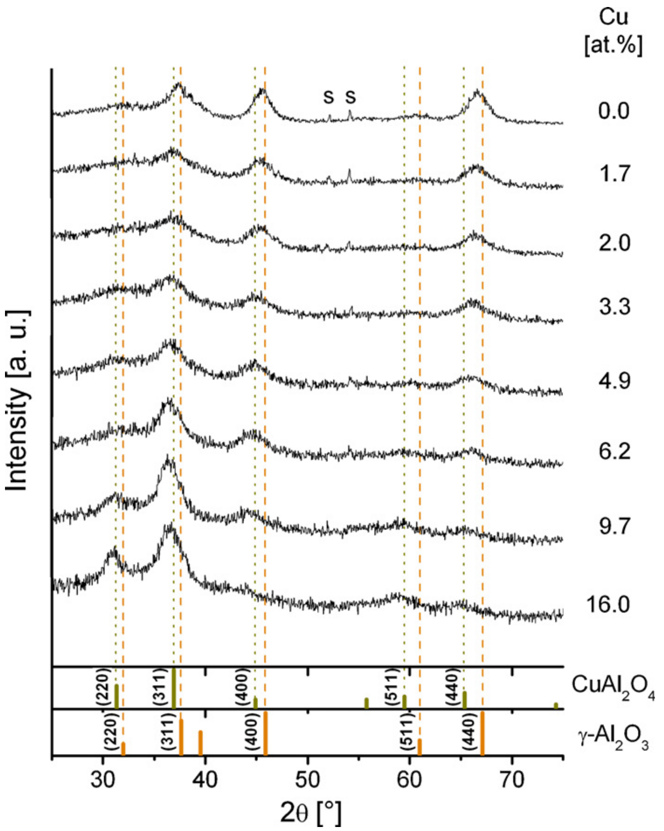

Fig. 4. Evolution of GIXRD patterns from the Al–Cu–O film on Si (1 0 0) substrate with increasing Cu content. Reflections from $CuAl_2O_4$ and γ-Al_2O_3 powder standards are also given for better structure evaluation. The letter s denotes the reflection from the substrate.

3. Results and discussion

3.1. Elemental composition

The elemental composition of Al–Cu–O film is controlled by the length of negative voltage pulse $\tau_{Al/Cu}$ at the Al/Cu target. The Cu content in the Al–Cu–O film increases with increasing $\tau_{Al/Cu}$ and reaches ~16 at.% at $\tau_{Al/Cu} = 32$ μs, see Fig. 3. On the contrary, the content of Al in the Al–Cu–O film decreases with increasing $\tau_{Al/Cu}$. The accuracy of measurement of the elemental composition is (i) marked by error bars and (ii) slightly less than ±10%. Insufficient accuracy of our measurements is very probably a reason why the elemental composition of the pure Al_2O_3 film prepared in our experiment differs from the theoretical one.

The addition of Cu in the Al_2O_3 film, however, strongly influences its structure and thus also its properties as shown below.

3.2. Structure and phase composition

The structure of Al–Cu–O films was characterized by GIXRD technique at the incident angle 0.75°, see Fig. 4. From this figure it is seen that all sputtered films are nanocomposite films composed of nanograins embedded in amorphous (a-) matrix. Pure Al_2O_3 films are nc-γ-Al_2O_3/a-Al_2O_3 composites characterized by broad, low-intensity (3 1 1), (4 0 0) and (4 4 0) reflections from γ-Al_2O_3 nanograins superposed on a broad amorphous peak; more details are given in the paper [14]. The addition of Cu in the Al_2O_3 film results in a gradual shift of (3 1 1), (4 0 0) and (4 4 0) reflections of γ-Al_2O_3 phase to lower angles 2θ up to positions corresponding to (2 2 0), (3 1 1), (5 1 1) and (4 4 0) reflections of $CuAl_2O_4$ phase. As the macrostress σ in the films does not change with increasing Cu content (see Table 1) this shift indicates that Cu atoms are dissolved in γ-Al_2O_3 grains and the $(Al_{8-2x},Cu_{3x})O_{12}$ nanocrystalline solid solution is formed; the formula for the solid solution describes correctly changes in the Al–Cu–O film but does not show which Cu atoms substitute for Al and which atoms are in vacant interstitial sites. However, there are also other facts. The intensity of γ-Al_2O_3 (4 0 0) reflection decreases with increasing Cu content in the film and almost disappears at ≥16 at.% Cu. A new $CuAl_2O_4$ (2 2 0) reflection rises at ~6 at.% Cu and increases with increasing Cu content. Also, the asymmetry of the $CuAl_2O_4$ (3 1 1) peak to higher 2θ angles indicates the co-existence of $CuAl_2O_4$ (3 1 1) and $(Al_{8-2x},Cu_{3x})O_{12}$ nanograins. All these facts indicate that the structure of Al–Cu–O films with ≤10 at.% Cu is very complex and probably nc-$(Al_{8-2x},Cu_{3x})O_{12}$/a-(Al–Cu–O) nanocomposite is formed. The confirmation of this statement needs further and more detailed investigation, which is not, however, the subject of this article. More details on the formation of γ-alumina films can be found in the following papers [15–20]. The Al–Cu–O films containing ≥16 at.% Cu are nc-$CuAl_2O_4$/a-(Al–Cu–O) nanocomposites.

Also, it is worthwhile to note that all ~2000 nm thick Al–Cu–O films exhibit almost the same value of the compressive macrostress $\sigma \approx -2$ GPa. It indicates that changes of properties of Al–Cu–O films with different Cu content, particularly their mechanical properties (H, E^*) can be explained by changes of their structure.

3.3. Mechanical properties

Mechanical properties of the coating are the hardness H and the effective Young's modulus E^*. Mechanical behavior of the coating is characterized by the elastic recovery W_e, the ratio H/E^* [21] and the ratio H^3/E^{*2} which is proportional to a resistance of the material to plastic deformation [22]. The plastic deformation is reduced in materials with high hardness H and low modulus E^*. Therefore, a low modulus E^* is desirable as it allows the given load to be distributed over a wider area and this way increases the resistance of the coating against cracking.

The addition of Cu in Al_2O_3 film strongly influences its structure, elemental and phase composition and so also its mechanical properties. Therefore, it is possible to investigate the mechanical properties as a function of Cu content in the Al_2O_3 film. The measured dependences of H, E^*, W_e and the ratio H/E^* of sputtered Al–Cu–O films as a function of the Cu content are given in Table 1 and displayed in Fig. 5. All values increase with increasing Cu content. However, there is a great difference in a gradient of the increase of H and E^*, W_e and H/E^* ratio at Cu content ≥2 at.%. The Al–Cu–O films with Cu content ≤2 at.% exhibit low values of $H \approx 8$ GPa and $E^* \approx 100$ GPa what corresponds well to their almost X-ray amorphous structure [18]. The hardness H strongly increases with increasing Cu content at ≥2 at.% Cu. On the contrary, the increase of $E^*$is slower. It results in the increase of (i) the ratio $H/E^* > 0.1$ and (ii) the elastic recovery $W_e \geq 70\%$ what plays a decisive role in enhancement of the resistance of the Al–Cu–O film to its cracking as shown below.

3.4. Resistance of film to cracking

The resistance of the Al–Cu–O film to cracking can be enhanced in the case when the effective Young's modulus E^* at a given hardness H is reduced and thus the applied load L is distributed over lager area. It is achieved in the case when the ratio $H/E^* > 0.1$, the film exhibits a high elastic recovery W_e and the plastic deformation of film is reduced. This statement can be confirmed by the generation of cracks in the film during a penetration of the diamond indenter into it under a high load L.

Table 1
Hardness H, effective Young's modulus E^*, elastic recovery W_e, H/E^* and H^3/E^{*2} ratio of the Al–Cu–O films with different Cu content and macrostress σ generated in them during sputtering. All values were measured at the diamond indenter load L = 20 mN.

Film	Cu (at.%)	h (nm)	H (GPa)	E^* (GPa)	W_e (%)	H/E^*	H^3/E^{*2} (GPa)	σ (GPa)
1	16.0	3080	20.1	151	76.0	0.133	0.36	−1.79
2	9.7	2070	18.5	143	74.8	0.129	0.31	−2.20
3	6.2	2020	16.7	135	71.0	0.124	0.26	−2.24
4	4.9	1990	16.2	134	70.1	0.121	0.24	−2.15
5	3.3	1900	14.5	130	66.6	0.112	0.18	−2.32
6	2.0	1930	10.0	111	57.5	0.090	0.08	−2.23
7	1.7	2080	8.3	98	53.6	0.085	0.06	−1.80
8	0.0	2520	7.3	100	49.4	0.073	0.04	−0.40

h is the thickness of film.

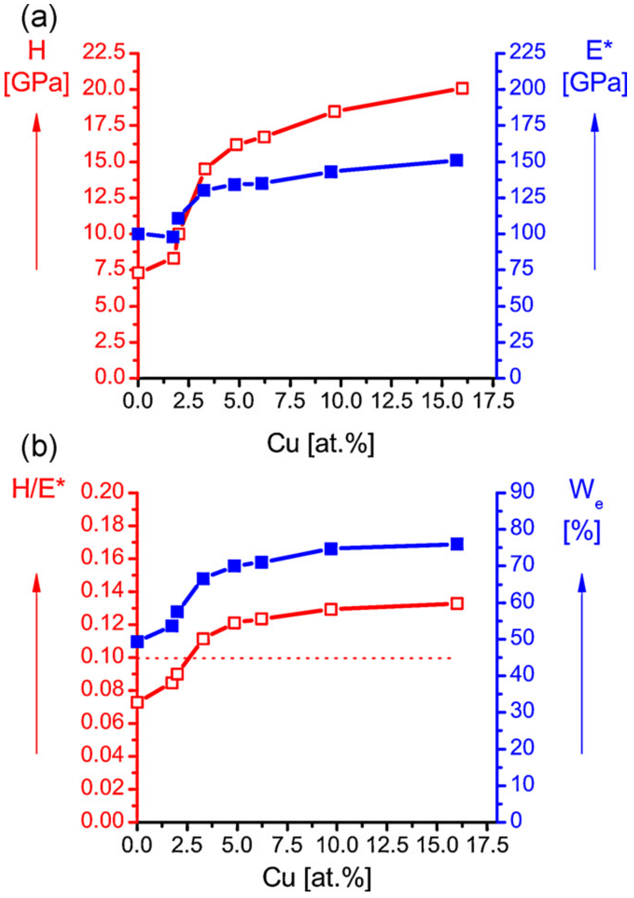

Fig. 5. (a) Hardness H and effective Young's modulus E^* and (b) elastic recovery W_e and H/E^* ratio of Al–Cu–O film as a function of Cu content.

The film cracking induced by the diamond impression under high load L was investigated in detail in [12]. It was shown that the resistance of the film to cracking depends on many parameters, particularly on the hardness H, effective Young's modulus E^* of both the film and the substrate, the $H_f/E_f{}^*$ and $H_s/E_s{}^*$ ratio, the thickness h of film and the macrostress σ in it; here the index f and s denotes the film and the substrate, respectively. This way it is possible to find correlations between the mechanical properties of the film and its resistance to cracking. The resistance of the Al–Cu–O film to cracking was tested by indentation at high load L = 1 N. The results of this test are summarized in Fig. 6.

Fig. 6 illustrates the effect of the amount of Cu added in the Al_2O_3 film on its cracking during loading by the diamond indenter. It is seen that only the pure Al_2O_3 film and the Al–Cu–O film with 2 at.% Cu exhibit clear radial cracks. No cracks are formed in the films with a higher (>2 at.%) Cu content. It indicates that the incorporation of Cu in Al_2O_3 enhances the resistance of Al–Cu–O to cracking. However, the amount of Cu incorporated in the film has to overpass a critical value what ensures that the film is (i) highly elastic (high $W_e \geq 60\%$) and (ii) well resistant to plastic deformation ($H/E^* \geq 0.1$, $H^3/E^{*2} > 0.1$). As seen in Table 1 high values of W_e and H/E^* are main parameters characterizing films with enhanced resistance to cracking. These requirements meet the nc-(Al_{8-2x},Cu_{3x})O_{12}/a-(Al–Cu–O) composite films with >2 at.% Cu.

Besides high values of $H/E^* \geq 0.1$ and $W_e \geq 60\%$ an important role in the resistance of the film to cracking plays also the macrostress σ generated in it during its growth [12]. The effect of σ on the resistance of Al–Cu–O films to cracking is illustrated in Fig. 7. The macrostress σ was controlled by the total pressure $p_T = p_{Ar} + p_{O_2}$ of sputtering Ar + O_2 gas mixture. As expected, the film sputtered at lower value of p_T exhibits a higher σ. The nc-(Al_{8-2x},Cu_{3x})O_{12}/a-(Al–Cu–O) composite films with higher compressive stress σ exhibits no cracks. On the contrary, nc-(Al_{8-2x},Cu_{3x})O_{12}/a-(Al–Cu–O) composite films with the same content of Cu and lower macrostress σ exhibit clear radial cracks. This fact indicates that a higher compressive macrostress

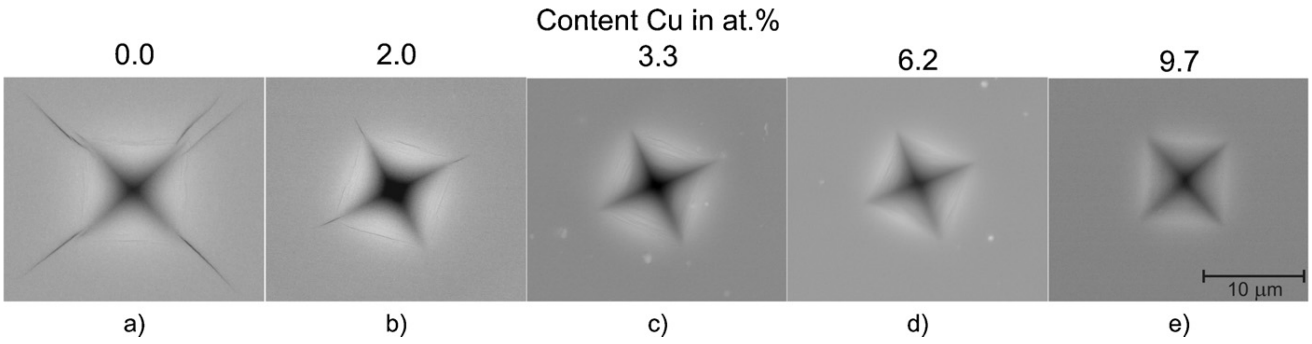

Fig. 6. SEM images of diamond indenter impression into (a) nc-(γ-Al_2O_3)/a-Al_2O_3 and (b)–(d) nc-(Al_{8-2x},Cu_{3x})O_{12}/a-(Al–Cu–O) composite films created under load L = 1 N. Mechanical properties of these films are given in Table 1.

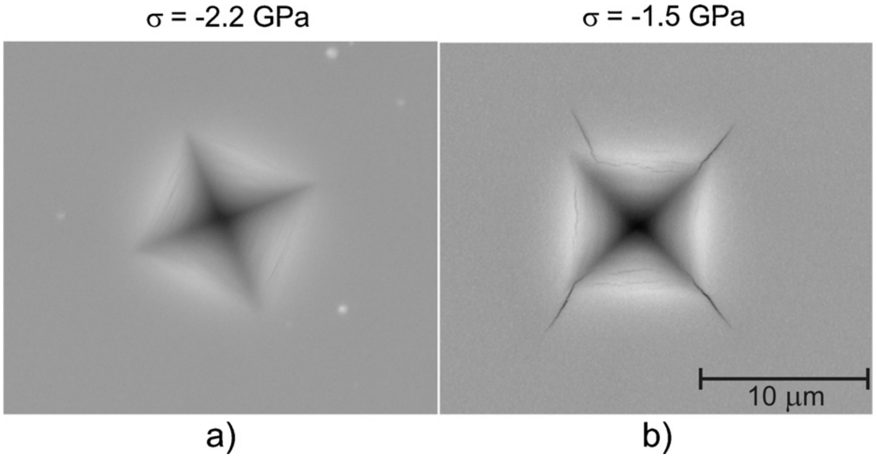

Fig. 7. SEM images of diamond indenter impression into nc-(Al_{8-2x},Cu_{3x})O_{12}/a-(Al–Cu–O) composite films with almost the same (≈6.4 at.%) Cu content but with (a) high $\sigma = -2.2$ GPa and (b) low $\sigma = -1.5$ GPa compressive macrostress formed under load $L = 1$ N. Mechanical properties of these films are given in Table 2.

Table 2
Hardness H, effective Young's modulus E^*, elastic recovery W_e, H/E^* and H^3/E^{*2} ratio of nc-(Al_{8-2x},Cu_{3x})O_{12}/a-(Al–Cu–O) composite films with different macrostress σ generated in them during sputtering. All values were measured at the diamond indenter load $L = 20$ mN.

Film	p_T (Pa)	Cu (at.%)	h (nm)	H (GPa)	E^* (GPa)	W_e (%)	H/E^*	H^3/E^{*2} (GPa)	σ (GPa)
3	0.5	6.2	2020	16.7	135	71.0	0.124	0.26	–2.24
9	1.5	6.5	1850	19.4	170	70.0	0.114	0.25	–1.50

helps to close cracks in the film after de-loading of diamond indenter. Table 2 shows that both films exhibit almost the same values of W_e and H^3/E^{*2} (resistance to plastic deformation) but very different values of E^* and H/E^*. It indicates that a greater role of the H/E^* ratio compared to the H^3/E^{*2} ratio in determination of resistance of film to cracking. The nc-(Al_{8-2x},Cu_{3x})O_{12}/a-(Al–Cu–O) composite film with higher H/E^* and lower E^* exhibits no cracks. It is very probable that the lowest absolute value of E^* is a key parameter which decides about resistance of the film to cracking. This question needs a special investigation which is not, however, the target of this paper.

3.5. Optical properties

The transmittance T, index of refraction n and extinction coefficient k of the Al–Cu–O films with different Cu content were measured in detail, see Figs. 8 and 9. Fig. 8 displays T as a function of the wavelength λ. This experiment clearly shows that the transparency T of the Al–Cu–O films strongly decreases with increasing Cu content and the films with ≥16 at.% Cu are opaque. Fig. 9 displays the evolution of the index of refraction n and the extinction coefficient k measured at λ = 550 nm as a function of Cu content; to see correlations with mechanical properties the hardness H of Al–Cu–O films is also displayed. All three quantities n and k and H increase with increasing at.% Cu. Increase of H is due to the change of the structure of nanocrystals from γ-Al_2O_3 through (Al_{8-2x},Cu_{3x})O_{12} to $CuAl_2O_4$, see Fig. 4.

The index of refraction $n = 1.53$ of pure Al_2O_3 film corresponds to that already reported for the Al_2O_3 film by Vitanov [23]. The $n = 1.96$ of the film with the highest Cu content can be considered as the refractive index of the nanocrystalline $CuAl_2O_4$ phase

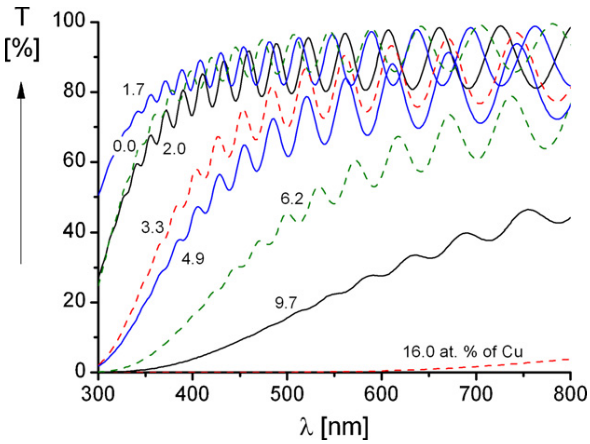

Fig. 8. Transmittance T of Al–Cu–O films containing different amount of Cu deposited on microscopic glass substrates vs. wavelength λ of the incident electromagnetic wave.

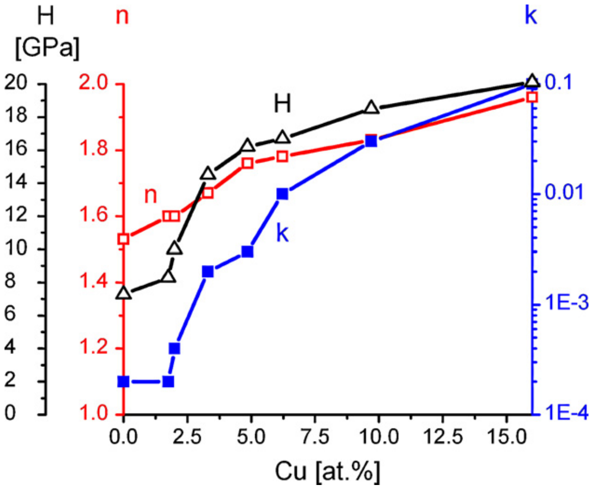

Fig. 9. Index of refraction n and extinction coefficient k measured at λ = 550 nm and hardness H of Al–Cu–O film as a function of Cu content.

(see the elemental composition in Fig. 3). The extinction coefficient k increasing with increasing Cu content can be explained by increasing number of electronic states (localized on Cu atoms) around the Fermi level: note the γ-Al_2O_3 band gap >6 eV [23] and the $CuAl_2O_4$ band gap of ≈2.1 eV [24]. Also, it is worthwhile to note that a loss of the Al–Cu–O film transparency T at ≥10 at.% Cu content in the film is compensated by the increase of its hardness H up to 18–20 GPa and increased resistance to cracking as shown in section 3.4 due to increase of (i) elastic recovery W_e, (ii) ratio H/E^* and (iii) the H^3/E^{*2} characterizing the film resistance to plastic deformation. Therefore, we can conclude that the amount of Cu added in Al_2O_3 film is very efficient tool for the control of structure, physical and functional properties of the Al–Cu–O films.

4. Conclusions

Main results of our study of the effect of Cu addition in the Al_2O_3 film reactively sputtered by the DC pulse dual magnetron sputtering on its structure and properties can be summarized as follows:

1. The Al–Cu–O films with ≤16 at.% Cu are nanocomposite films composed of nanograins embedded in a-(Al–Cu–O) matrix. The structure of nanograins continuously varies from γ-Al_2O_3 through $(Al_{8-2x}, Cu_{3x})O_{12}$ to $CuAl_2O_4$. Changes in the film structure strongly influence its properties.
2. The addition of Cu in the Al_2O_3 film strongly increases its hardness H. However, the effective Young's modulus E^* strongly increases for ≤3.5 at.% only and thus these Al–Cu–O films exhibit the ratio $H/E^* \leq 0.1$. The increase of $E^*$is strongly slowed down in the Al–Cu–O films with >3.5 at.% and it results in increase of (i) the ratio $H/E^* > 0.1$, (ii) the elastic recovery $W_e \geq 70\%$ and (iii) resistance of the film to cracking.
3. The Al–Cu–O films containing ~16 at.% Cu have high hardness $H \approx 20$ GPa, low Young's modulus $E^* \approx 150$ GPa, very high elastic recovery $W_e = 77\%$ and exhibit the enhanced resistance to cracking due to high ratio $H/E^* > 0.1$.
4. The film resistance to cracking was determined using the indentation test, i.e. it was assessed from (i) cracks created by the diamond indenter at a high load $L = 1$ N and (ii) correlations between cracking and H, E^*, W_e and H/E^* of the Al–Cu–O film.
5. The amount of Cu added in the Al_2O_3 film is an efficient tool for controlling of the structure, mechanical and optical properties of the Al–Cu–O film.

Acknowledgements

This work was supported in part by the Ministry of Education of the Czech Republic under Projects MSM 4977751302 and COST OC10045 and the Grant Agency of the Czech Republic GACR under Project No. P108/12/0393.

References

[1] H. Kawazoe, M. Yasukawa, H. Hyodo, M. Kurita, H. Yanagi, H. Hosono, P-type electrical conduction in transparent thin films of $CuAlO_2$, Nature 389 (1997) 939–942.
[2] K. Lee, I. Song, Park S G., Preparation of $Bi_2Sr_2CaCu_2O_y$ films on alumina substrates with a $CuAl_2O_4$ buffer layer, J. Appl. Phys. 74 (1993) 1459–1461.
[3] M. Kim, F. Sun, J. Lee, Y.K. Hyun, D. Lee, Influence of ultrasonication on the mechanical properties of Cu/Al_2O_3 nanocomposite thin films during electrocodeposition, Surf. Coat. Technol. 205 (2010) 2362–2368.
[4] D. Ding, W. Cai, M. Long, H. Wu, Y. Wu, Optical, structural and thermal characteristics of Cu–$CuAl_2O_4$ hybrids deposited in anodic aluminum oxide as selective solar absorber, Sol. Energy Mater. Sol. Cells 94 (2010) 1578–1581.
[5] W.Z. Lv, B. Liu, Q. Qiu, F. Wang, Z. Luo, P. Zhang, S. Wei, Synthesis, characterization and photocatalytic properties of spinel $CuAl_2O_4$ nanoparticles by a sonochemical method, J. Alloys Compd. 479 (2009) 480–483.
[6] L.C. Leu, D.P. Norton, G.E. Jellison Jr., V. Selvamanickam, X. Xiong, Optical and dielectric properties of $CuAl_2O_4$ films synthesized by solid-phase epitaxy, Thin Solid Films 515 (2007) 6938–6942.
[7] E.M. Alkoy, P.J. Kelly, The structure and properties of copper oxide and copper aluminium oxide coatings prepared by pulsed magnetron sputtering of powder targets, Vacuum 79 (2005) 221–230.
[8] J.H. Shy, B.H. Tseng, Characterization of $CuAlO_2$ thin film prepared by rapid thermal annealing of an Al_2O_3/Cu_2O/sapphire structure, J. Phys. Chem. Solids 66 (2005) 2123–2126.
[9] W. Lan, M. Zhang, G. Dong, P. Dong, Y. Wang, H. Yan, The effect of oxygen on the properties of transparent conducting Cu–Al–O thin films deposited by rf magnetron sputtering, Mater. Sci. Eng. B 139 (2007) 155–159.
[10] C.H. Ong, H. Gong, Effects of aluminum on the properties of p-type Cu–Al–O transparent oxide semiconductor prepared by reactive co-sputtering, Thin Solid Films 445 (2003) 299–303.
[11] N. Tsuboi, Y. Itoh, J. Ogata, S. Kobayashi, H. Shimizu, K. Kato, F. Kaneko, Composition and structure control of Cu–Al–O films prepared by reactive sputtering and annealing, Jpn. J. Appl. Phys. 46 (2007) 351–355.
[12] J. Musil, J. Jirout, Toughness of hard nanostructured ceramic thin films, Surf. Coat. Technol. 201 (2007) 5148–5152.
[13] J.A. Woollam Co., Inc., WVASE32 Software Manual, J.A. Woollam Co., Inc., Lincoln, NE, 2008.
[14] J. Musil, J. Blažek, P. Zeman, Š. Prokšová, M. Šašek, R. Čerstvý, Thermal stability of alumina thin films containing γ-Al_2O_3 phase prepared by reactive magnetron sputtering, Appl. Surf. Sci. 257 (2010) 1058–1062.
[15] D.H. Trinh, K. Back, G. Pozina, T. Blomqvist, T. Selinder, M. Collin, I. Reineck, L. Hultman, H. Högberg, Phase transformation in κ- and γ-Al_2O_3 coatings on cutting tool inserts, Surf. Coat. Technol. 203 (2009) 1682–1688.
[16] V. Edlmayr, M. Moser, C. Walter, C. Mitterer, Stability of sputtered Al_2O_3 coatings, Surf. Coat. Technol. 204 (2010) 1576–1581.
[17] P. Eklund, M. Sridharan, G. Singh, J. Bottiger, Thermal stability and phase transformation of γ-/amorphous-Al_2O_3 thin films, Plasma Process. Polym. 6 (2009) S907–S911.
[18] O. Zywitzki, G. Hoetzsch, Effect of plasma activation on the phase transformations of aluminium oxide, Surf. Coat. Technol. 76-77 (1995) 754–762.
[19] O. Kyrylov, R. Cremer, D. Neuschütz, Deposition of alumina hard coatings by bipolar pulsed PECVD, Surf. Coat. Technol. 163–164 (2003) 203–207.
[20] M. Sridharan, M. Sillassen, J. Bottiger, J. Chevallier, H. Birkedal, Pulsed DC magnetron sputtered Al_2O_3 and their hardness, Surf. Coat. Technol. 202 (2007) 920–924.
[21] A. Leyland, A. Mathews, On the significance of the H/E ratio in wear control: a nanocomposite coating approach to optimized tribological behavior, Wear 246 (2000) 1–11.
[22] T.Y. Tsui, G.M. Pharr, W.C. Oliver, C.S. Bhatia, R.L. White, S. Anders, A. Anders, I.G. Brown, Nano indentation and nanoscratching of hard carbon coatings for magnetic disks, Mater. Res. Soc. Symp. Proc. 383 (1995) 447–451.
[23] P. Vitanov, Tz. Babeva, Z. Alexieva, A. Harizanova, Z. Nenova, Optical properties of $(Al_2O_3)_x(TiO_2)_{1-x}$ films deposited by the sol–gel method, Vacuum 76 (2004) 219–222.
[24] M. Salavati-Niasari, F. Davar, M. Farhadi, Synthesis and characterization of spinel-type $CuAl_2O_4$ nanocrystalline by modified sol–gel method, J. Sol–Gel Sci. Technol. 51 (2009) 48–52.

3.3.2 C-II: Transparent Zr-Al-O oxide coatings with enhanced resistance to cracking

Surface & Coatings Technology 206 (2012) 2105–2109

Contents lists available at SciVerse ScienceDirect

Surface & Coatings Technology

journal homepage: www.elsevier.com/locate/surfcoat

Transparent Zr–Al–O oxide coatings with enhanced resistance to cracking

J. Musil *, J. Sklenka, R. Cerstvy

Department of Physics, Faculty of Applied Sciences, University of West Bohemia, Univerzitní 22, CZ-306 14 Plzeň, Czech Republic

ARTICLE INFO

Article history:
Received 9 May 2011
Accepted in revised form 15 September 2011
Available online 22 September 2011

Keywords:
Two-phase oxide
Optical properties
Mechanical properties
Resistance to cracking
DC pulsed reactive sputtering
Dual magnetron

ABSTRACT

The article reports on structure, transparency and mechanical properties of Zr–Al–O oxide thin films with Zr/Al>1 produced by reactive DC pulse dual magnetron sputtering. Special attention is devoted to the formation of transparent Zr–Al–O oxide films in the transition mode of sputtering and their unique properties. It is shown that (i) the transparent Zr–Al–O films can be deposited in the transition mode of sputtering with a high deposition rate a_D achieving up to 80 nm/min at relatively low value of the magnetron target power density $W_t \approx 45$ W/cm^2, (ii) the Zr–Al–O films sputtered in the transition and oxides mode of sputtering are highly elastic and exhibit relatively high hardness (typically $H \approx 18$ to 19 GPa), low effective Young's modulus E^* satisfying the ratio $H/E^* > 0.1$ and high elastic recovery W_e up to 78%, and highly elastic Zr–Al–O oxide films with $H/E^* > 0.1$ exhibit an enhanced resistance to cracking.

1. Introduction

It is well known that oxide films can be easily prepared in the oxide mode (OM) of sputtering [1–5]. However, the main problem of this preparation is an extremely low deposition rate $a_D = a_{D\ in\ OM}$. Therefore, a huge effort is concentrated on the deposition of stoichiometric, highly transparent oxide films in the transition mode (TM) of sputtering where these films can be prepared at much higher deposition rate $a_{D\ in\ TM} > a_{D\ in\ OM}$ [6–14]. This article demonstrates not only a possibility of a high-rate deposition of the transparent Zr–Al–O oxide films in the transition mode of sputtering but also their unique properties characterized by a relatively high hardness H ranging from ~18 to ~19 GPa, high hardness H to the effective Young's modulus E^* ratio $H/E^* > 0.1$ and high value of the elastic recovery $W_e > 70\%$; here $E^* = E/(1-\nu^2)$, E is the Young's modulus and ν is the Poisson's ratio. The Zr–Al–O films with $H/E^* > 0.1$ and $W_e \geq 70\%$ exhibit enhanced resistance to cracking.

2. Experimental

The Zr–Al–O thin films were reactively sputtered in an $Ar + O_2$ mixture using a dual magnetron equipped with a composed ZrAl targets ($\varnothing = 50$ mm) consisting of Al circular plate (99.99 at.%) fixed with a Zr (99.9) ring of inner diameter $\varnothing_{in\ Zr} = 20$ mm and closed magnetic field B. This geometrical arrangement of composite target made possible to form Zr–Al–O films with the ratio Zr/Al>1. The magnetron was operated in ac pulse mode generated by a pulse power supply DORA MSS-10 with an output power 10 kW (made by DORA Electronics in Poland). The repetition frequency f_r of pulses was 2 kHz and the ac frequency inside pulses was 56 kHz. The magnetron discharge current I_d was controlled by the duty cycle τ/T; here τ is the length of pulse and $T = 1/f_r$ is the repetition frequency of pulses. The Zr–Al–O films were sputtered under the following conditions: discharge current $I_{da} = 2$ A averaged over the pulse period T, substrate bias voltage $U_s = U_{fl}$, substrate temperature $T_s = 500°C$, substrate-to-target distance $d_{s-t} = 80$ mm, variable values of the partial pressure of oxygen p_{O_2} and constant value of the total pressure $p_T = p_{Ar} + p_{O_2} = 1$ Pa; here U_{fl} is the floating potential.

The film thickness h was measured using a stylus profilometer DEKTAK 8. The film structure was characterized using an XRD spectrometer PANalytical X Pert PRO in Bragg–Brentano configuration with CuKα radiation. The elemental composition was determined by X-ray Fluorescence (XRF) spectroscopy with PANalytical XRF Spectrometer MagiX PRO. Mechanical properties were determined from load vs. displacement curves measured by a microhardness tester Fischerscope H100 with a Vicker's diamond indenter at a load L = 10 mN. For all sputtered films the ratio d/h of diamond depth impression d to the film thickness h was less than 0.1. The ratio d/h for the most soft film was 0.1. It indicates that the measured hardness H of our films is not influenced by the substrate. The transparency of Zr–Al–O films was measured in the range from 300 to 800 nm using a spectrometer Specord M400. The resistance of the film to cracking was investigated in a bending test. The principle of the bending test is shown in Fig. 1. The film was deposited on a Mo strip ($80 \times 15 \times 0.1$ mm^3) and the coated strip was bended up to its cracking in a bending apparatus.

---

* Corresponding author.
E-mail address: musil@kfy.zcu.cz (J. Musil).

0257-8972/$ – see front matter © 2011 Elsevier B.V. All rights reserved.
doi:10.1016/j.surfcoat.2011.09.035

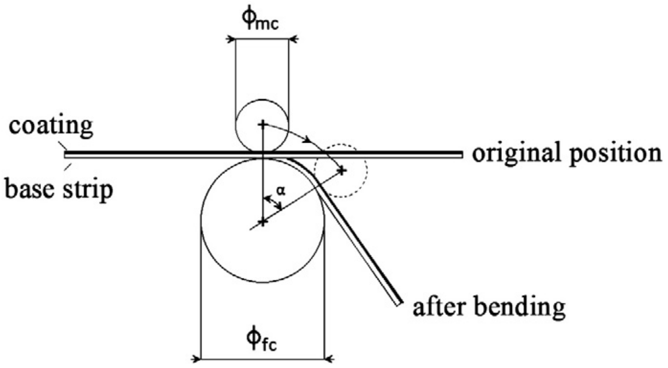

Fig. 1. (a) Schematic illustration of bending test used to induce cracks in film deposited on metallic strip. $\varnothing_{mc}$ and $\varnothing_{fc}$ are the diameters of moving and fixed cylinder, respectively.

3. Results and discussion

3.1. Reactive sputtering of transparent oxide film in transition mode

The evolution of the partial pressure of oxygen p_{O_2} and the film deposition rate a_D, measured in the reactive magnetron sputtering of Zr–Al–O films from composed AlZr targets, with increasing flow rate of oxygen ϕ_{O_2} are displayed in Fig. 2. As expected, in the metallic mode (MM) of sputtering p_{O_2} is zero = O because all oxygen is sorbed by sputtered Zr and Al atoms. In the transition mode p_{O_2} gradually increases with increasing ϕ_{O_2} because (1) the surface of metallic targets are rapidly covered by an oxide, (2) the sputtering of atoms from targets is reduced due to the decrease of sputtering yield ($\gamma_{Al} > \gamma_{Zr} > \gamma_{Zr–Al–O}$) and (3) all surfaces in the deposition chamber made of stainless steel are already oxidized and the excess of oxygen occurs. Despite the last fact, a sufficient amount of the atomic oxygen N_O has not been available to form with sputtered Zr and Al atoms stoichiometric fully transparent oxide films in the whole region of TM. The amount of N_O generated in the magnetron discharge depends on (i) the degree of ionization of the oxygen gas, i.e. on the intensity of the magnetron discharge, and (ii) on the amount of oxygen, i.e. on the oxygen flow rate ϕ_{O_2}, introduced in the deposition chamber. In our case fully transparent Zr–Al–O films sputtered in the TM of sputtering are formed at $\phi_{O_2} \leq 5.5$ sccm, see Table 1 and Fig. 3. The transparency of the Zr–Al–O films sputtered in the OM of sputtering is very similar to that of films sputtered in the TM of sputtering; transparency curves of films sputtered in TM and OM of sputtering are overlapping. It indicates that in our case the deposition rate a_D of transparent films almost does not influence their transparency.

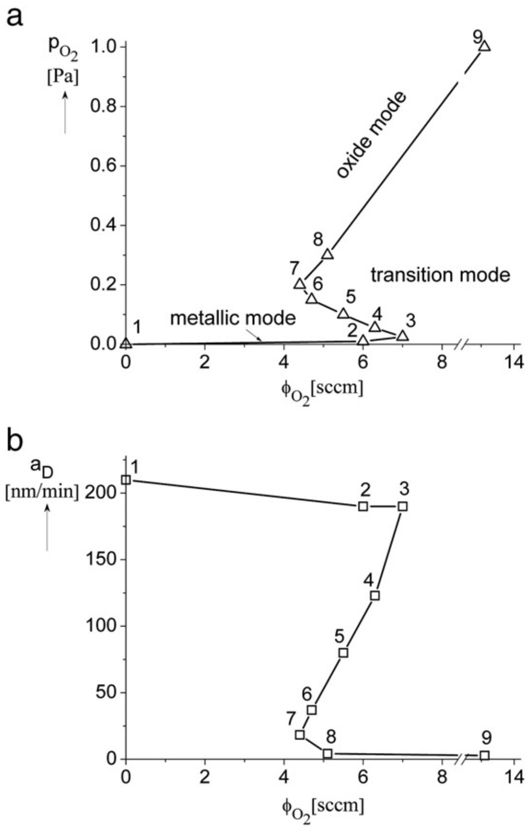

Fig. 2. Evolution of (a) p_{O_2} in deposition chamber and (b) a_D of Zr–Al–O films sputtered at $T_s = 500°C$, $I_{da} = 2$ A, $U_s = U_{fl}$, $d_{s-t} = 80$ mm and $p_T = p_{Ar} + p_{O_2} = 1$ Pa as a function of flow rate of oxygen ϕ_{O_2}.

3.2. Transparency of Zr–Al–O films

The measured transparency T of the Zr–Al–O films sputtered on a glass substrate is displayed in Fig. 3. From this figure it is seen that the film transparency decreases when p_{O_2} decreases and the operating point on the curve $p_{O_2} = f(\phi_{O_2})$ approaches to the MM of sputtering — compare the transparency T of the film no. 5 with that of the film no. 4. It is due to the excess of (Al + Zr) metal atoms and the deficiency O atoms needed to form stoichiometric Al_2O_3 and ZrO_2 oxides. At first, the Al_2O_3 oxide is formed because of a higher negative enthalpy $\Delta H_{Al_2O3} = -1678.2$ kJ/mol of the Al_2O_3 oxide compared to the enthalpy $\Delta H_{ZrO_2} = -1101.3$ kJ/mol of the ZrO_2 oxide.

3.3. Structure of Zr–Al–O films

The structure of sputtered Zr–Al–O films strongly depends on the partial pressure of oxygen p_{O_2} and the film deposition rate a_D, see Fig. 4. The films deposited in the metallic mode (MM) of sputtering at very low (≤0.01 Pa) value of p_{O_2} are two-phase nc-/a- composites: nc-h-Zr(101)/a-Al_2O_3 composite films; here nc- and a- are the nanocrystalline and amorphous phases, respectively, and h is hexagonal phase. All available atomic oxygen O is bonded to Al and as the result a-Al_2O_3 phase is formed. Films produced at p_{O_2} ranging from ~0.02 to ~0.06 Pa are two-phase a-/a- composites, i.e. a-ZrO_2/a-Al_2O_3 amorphous composite films, because the energy W_f delivered to the growing film in this region of p_{O_2} is insufficient to form a crystalline ZrO_2 phase. The energy W_f delivered to the growing films held on a floating potential is very roughly proportional to the energy W_d delivered to the magnetron discharge. Under this assumption however, the energy W_f gradually increases with increasing p_{O_2} and at $p_{O_2} \geq 0.1$ Pa when the energy W_f is already sufficient for the crystallization of the ZrO_2 phase, nc-/a- composites, i.e. nc-t-ZrO_2(101)/a-Al_2O_3 composite films, composed of one crystalline and one amorphous phase are formed; here t- is the tetragonal phase. We believe that the nc-t-ZrO_2/a-Al_2O_3 composite films are composed of ZrO_2 grains surrounded by the amorphous Al_2O_3 phase. These composite films are highly elastic and exhibit a high resistance to cracking.

3.4. Mechanical properties of Zr–Al–O films

The measured mechanical properties of the coating are its hardness H and the effective the effective Young's modulus $E^* = E/(1-\nu^2)$; here E is the Young's modulus and ν is the Poisson's ratio. Mechanical behavior of the coating is characterized by the elastic recovery W_e, the ratio H/E^* [15] and the ratio H^3/E^{*2} [16] which is proportional to a resistance of the material to plastic deformation [17]. The plastic deformation is significantly reduced in materials with high hardness H and low modulus E^*. This means that a low modulus E^* is very desirable as it allows the given load to be distributed over a wider area and to increase the resistance of coating against cracking.

Table 1
Deposition conditions used in formation of Zr–Al–O films, their (i) deposition rate a_D at the substrate-to-target distance $d_{s-t} = 80$ mm, (ii) optical transparency, and the power P and the energy W_d delivered to the magnetron discharge. Constant deposition conditions: $I_{da} = 2$ A, $T_s = 500°C$, $p_T = p_{Ar} + p_{O_2} = 1$ Pa.

Film no.	ϕ_{O_2} [sccm]	p_{O_2} [Pa]	Mode	P_{av} [kW]	a_D [nm/min]	a_D/P_{av} [nm/min kW]	t_D [min]	W_d [J]	h [nm]	Transparency
1	0.0	0.00	MM	2.22	208	94	6	13.3	1250	Opaque
2	6.0	0.01	MM	2.06	190	92	10	20.6	1900	Opaque
3	7.0	0.03	MM	2.02	190	94	10	20.2	1900	Opaque
4	6.3	0.06	TM	1.90	123	65	13	24.7	1600	Semi-transparent
5	5.5	0.10	TM	1.80	80	44	20	36.0	1600	Transparent
6	4.7	0.15	TM	1.62	37	23	30	48.6	1100	Transparent
7	4.4	0.20	TM	1.46	18	12	60	87.6	1100	Transparent
8	5.1	0.30	OM	1.35	4	3	120	162.0	1000	Transparent
9	13.1	1.00	OM	1.80	3	2	480	864.0	1350	Transparent

MM, TM and OM denote the metallic, transition and oxide mode of sputtering, respectively. P_{av} is the power averaged over pulse period $T = 1/f_r$.

The measured dependences of H, E^* and W_e as a function of partial pressure of oxygen p_{O_2} are displayed in Fig. 5. In this figure also the ratio H/E^*, calculated from measured values of H and E^*, is given and intervals p_{O_2} corresponding to MM, TM and OM of sputtering are clearly denoted. From Fig. 5 it is seen that all quantities (H, E^*, W_e) including the ratio H/E^* increase with increasing p_{O_2} and reach a maximum in the TM of sputtering. This increase of H and E^* is connected with (i) the reduction of the amount of free Zr_1 atoms in the coating, (ii) the gradual conversion of the three-phase a-Al_2O_3 + a-Zr_1O_2/Zr_2 composite first to the two-phase a-ZrO_2/a-Al_2O_3 composite composed of two amorphous phases and later to the c-ZrO_2/a-Al_2O_3 composite composed of one crystalline and one amorphous phase at $p_{O_2} \approx 0.1$ Pa and (iii) the formation of harder c-ZrO_2 phase substituting the softer a-ZrO_2 phase; here $Zr = Zr_1 + Zr_2$ is the total amount of Zr in the film, Zr_1 are atoms forming Zr_1O_2 oxide and Zr_2 are free atoms.

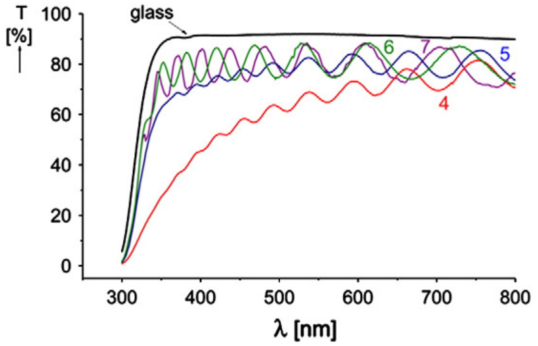

Fig. 3. Transmittance T of Zr–Al–O films deposited at different values of ϕ_{O_2} on microscopic glass substrates vs. wavelength λ of the incident electromagnetic wave. Numbers of individual curves correspond to the films defined in Table 1.

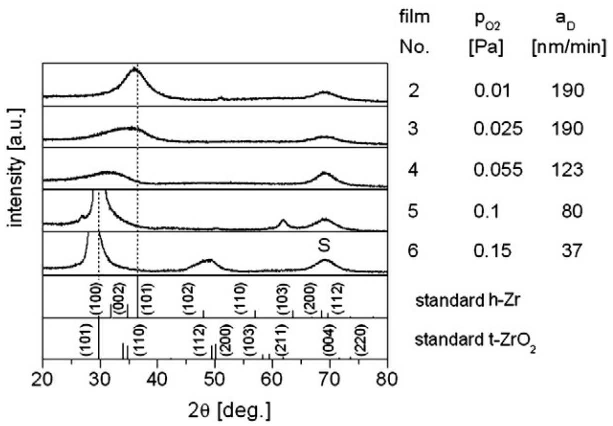

Fig. 4. Evolution of the structure of Zr–Al–O films with increasing partial pressure of oxygen p_{O_2} and decreasing deposition rate a_D of film.

The most important finding is, however, the fact that the ratio H/E^*, which increases with increasing p_{O_2}, exceeds the value 0.1 approximately at $p_{O_2} \approx 0.1$ Pa and is greater than 0.1 at $p_{O_2} > 0.1$. The films with $H/E^* > 0.1$ exhibit unique property — in our case the high elasticity characterized by a high value of elastic recovery W_e. Fig. 5 clearly shows a step increase of the elastic recovery W_e of films, produced already in a high-pressure part of the TM and the whole OM of sputtering, from ~55 to ~77% with the ratio H/E^* increasing above 0.1; the film elasticity increases by ~40%, see Table 2. This increase of W_e is due to a low value of E^* and results in a dramatic increase of the resistance of films with $H/E^* > 0.1$ against cracking, see Fig. 5.

3.5. Resistance against cracking of Zr–Al–O film during its bending

The resistance of the film to cracking was investigated by its bending along a cylinder (∅ = 25 mm). For this test the Zr–Al–O film was deposited on Mo strip ($80 \times 15 \times 0.1$ mm^3). The formation of cracks in film during bending the film/substrate couple is illustrated in Fig. 6. In this figure the surface morphology of (i) Mo strip prior to film deposition, (ii) as-deposited 3300 nm thick Zr–Al–O film with low hardness H = 7.1 GPa, low ratio $H/E^* = 0.06$ and low $W_e = 44\%$ and (iii) film morphology after bending the film/substrate couple to angle α = 30° are compared. Cracks created in the film during bending are clearly seen. It means that bending test can be used to assess the resistance of the film against cracking.

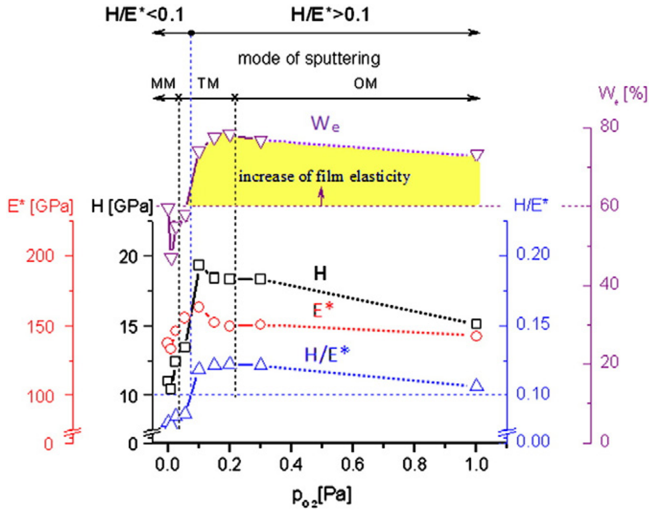

Fig. 5. Evolution of H, E^*, W_e, H/E^* of Zr–Al–O films with increasing partial pressure of oxygen p_{O_2} used in their sputtering at $T_s = 500°C$, $I_{da} = 2$ A, $U_s = U_{fl}$, $d_{s-t} = 80$ mm and $p_T = p_{Ar} + p_{O_2} = 1$ Pa.

Table 2
Deposition conditions, thickness h, deposition rate a_D, elemental composition, mechanical properties (H, E^*, H/E^*, W_e) of Zr–Al–O films with Zr/Al > 1 sputtered in different modes of sputtering at the substrate-to-target distance $d_{s-t} = 80$ mm and formation of cracks in bending as a function of ϕ_{O_2} and p_{O_2}. Constant deposition conditions: $I_{da} = 2$ A, $T_s = 500°C$, $p_T = p_{Ar} + p_{O_2} = 1$ Pa.

Filmno.	ϕ_{O_2} [sccm]	p_{O_2} [Pa]	Mode	h [nm]	a_D [nm/min]	Zr [at.%]	Al [at.%]	O [at.%]	H [GPa]	E* [GPa]	H/E*	W_e [%]	Cracks at α
1	0	0	MM	1250	208	51	37	12	11	137	0.08	60	35°
2	6	0.01	MM	1900	190	46	30	24	10.4	133	0.08	47	35°
3	7	0.025	MM	1900	190	32	18	50	12.4	146	0.085	55	40°
4	6.3	0.055	TM	1600	123	19	11	70	13.4	155	0.086	58	40°
5	5.5	0.1	TM	1600	80	19	10	71	19.3	163	0.118	74	No[a]
6	4.7	0.15	TM	1100	37	19	8	73	18.4	152	0.121	77	No[a]
7	4.4	0.2	TM	1100	18.3	20	7	73	18.3	150	0.122	78	No[a]
8	5.1	0.3	OM	1000	4.2	20	7	73	18.3	151	0.121	77	No[a]
9	13.1	1.0	OM	1350	2.8	24	1	75	15.1	142	0.106	73	No[a]

MM, TM and OM denote the metallic, transition and oxide mode of sputtering, respectively.

[a] Means no cracks up to bending angle α = 180°.

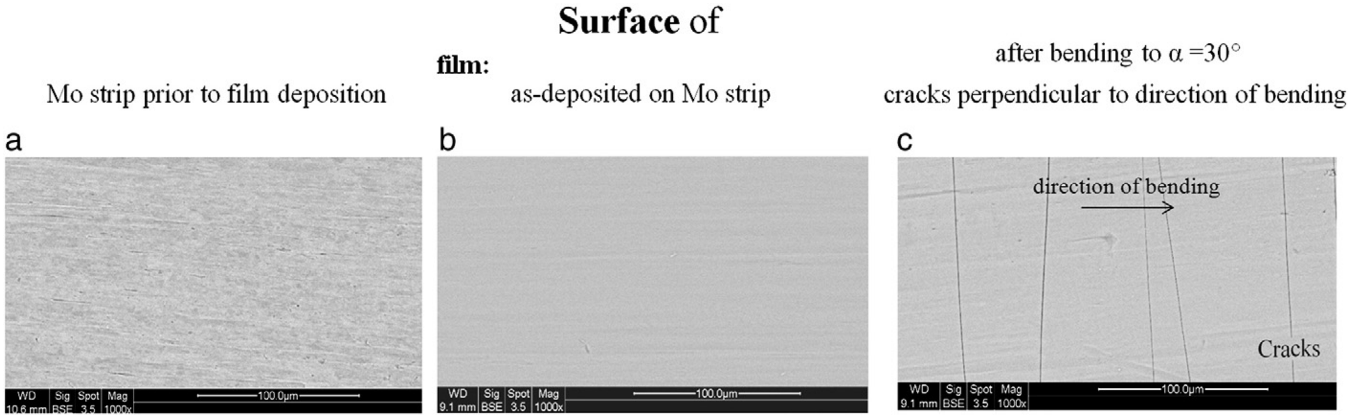

Fig. 6. Surface morphology of (a) Mo strip prior to film deposition, (ii) as-deposited 3300 nm thick Zr–Al–O film with low hardness H = 7.1 GPa, low ratio $H/E^* = 0.06$ and low $W_e = 44\%$ and (iii) film morphology after bending the film/substrate couple along steel cylinder of diameter ∅ = 25 mm to angle α = 30°. Photos were in back scattering electrons (BSE) mode.

Results of bending tests are summarized in Table 2. From Table 2 it is seen that the resistance of film to cracking depends on the ratio H/E^* and the elastic recovery W_e. It was found that highly elastic films with high ratio $H/E^* \geq 0.1$ and high $W_e \geq 70\%$ are more resistant to cracking compared to films with low ratio $H/E^* < 0.1$ and low $W_e \leq 70\%$. It is due to the fact that the material with $H/E^* > 0.1$, which exhibits a lower value of E^* at a given hardness H, is much more elastic compared to the film with $H/E^* \leq 0.1$, distributes the applied load over a wider area and this way strongly increases the resistance of the coating against cracking. The films with low E^*, high ratio $H/E^* > 0.1$ and high $W_e \geq 70\%$ exhibit no cracks even after bending at α = 180°. This finding is of great importance for many applications.

4. Conclusions

Main results of our study of reactive sputtering of the Zr–Al–O composite films with Zr/Al > 1 by DC pulse dual magnetron equipped with composed Al/Zr targets in a mixture of $Ar + O_2$ and their properties can be summarized as follows.

1. Transparent Zr–Al–O films can be deposited in the TM of sputtering with up to more than one order of magnitude higher deposition rate compared with that of transparent Zr–Al–O films deposited in the OM of sputtering, i.e. $a_{D\ in\ TM} > a_{D\ in\ OM}$. Transparent Zr–Al–O films sputtered in the TM of sputtering are crystalline with a strong t-ZrO_2(101) preferred crystallographic orientation.
2. Transparent Zr–Al–O films sputtered in TM of sputtering exhibit relatively high hardness H = 18–19 GPa, low effective Young's modulus E^* satisfying the ratio $H/E^* > 0.1$ and high value of elastic recovery $W_e > 70\%$.
3. Transparent Zr–Al–O films with H = 18–19 GPa, $H/E^* > 0.1$ and $W_e \geq 70\%$ exhibit strongly enhanced resistance to cracking in bending. No cracks occur in ~1600 nm thick Zr–Al–O film deposited on Mo strip after bending along a SS cylinder of diameter 25 mm even at angle α = 180°.
4. Hard coatings with low E^* can be based not only on oxides as shown in this article but also on nitrides [18], carbides [19] and other compounds.

Acknowledgments

This work was supported in part by the Ministry of Education of the Czech Republic under Project Nos. MSM 4977751302 and COST OC10045, and by the Grant Agency of the Czech Republic GACR under Project No. P108/12/0393.

References

[1] S. Schiller, U. Heisig, Chr. Korndorfer, G. Beister, J. Reschke, K. Steinfelder, J. Strumpfel, Surf. Coat.Technol. 49 (1987) 405.
[2] W.D. Westwood (Ed.), Handbook of Thin Solid Film Process Technology, IOP, Bristol, 1998.
[3] I. Safi, Surf. Coat.Technol. 127 (2000) 203.
[4] J. Musil, P. Baroch, J. Vlček, K.H. Nam, J.G. Han, Thin Solid Films 475 (2005) 208.
[5] W.D. Sproul, D.J. Christie, D.C. Carter, Thin Solid Films 491 (2005) 1.
[6] M.A. Scobey et al.: U.S. Patent No. 4 851 095, July 25, 1989.
[7] J.P. Lehan, R.B. Sargent, R.E. Klinger, J. Vac. Sci. Technol. A 10 (6) (1992) 3401.
[8] B.P. Hichwa, Proc. of the 2nd International Symposium on ISSP, 93, The Chair of ISSP 2011 Committee, Kanazawa Institute of Technology, Japan, 1993, p. 61, Tokyo.
[9] J.M. Schneider, W.D. Sproul, R.W.J. Chia, M.S. Wong, A. Matthews, Surf. Coat.Technol. 96 (1997) 262.

[10] M.K. Olsson, K. Macak, U. Helmersson, B. Hjorvarsson, J. Vac. Sci. Technol. A 16 (2) (1998) 639.
[11] S.J. Nadel, P. Greene, Thin Solid Films 392 (2001) 174.
[12] N. Boling, B. Wood, P. Morand, Deposition Sciences Inc., Santa Rosa, CA, 2002, p. 1.
[13] J. Sicha, D. Herman, J. Musil, Z. Stryhal, J. Pavlik, Nanoscale Res. Lett. 2 (2007) 123, doi:10.1007/s11671-007-9042-z.
[14] J. Musil, V. Satava, P. Baroch, Thin Solid Films 519 (2010) 775.
[15] A. Leyland, A. Mathews, Wear 246 (2000) 1.
[16] J. Musil, J. Jirout, Surf. Coat.Technol. 201 (2007) 5148.
[17] T.Y. Tsui, G.M. Pharr, W.C. Oliver, C.S. Bhatia, R.L. White, S. Anders, A. Anders, I.G. Brown, Mater. Res. Soc. Symp. Proc. 383 (1995) 447.
[18] J. Musil, J. Vlček, Surf. Coat.Technol. 142–144 (2001) 557.
[19] J. Musil, P. Novák, R. Čerstvý, Z. Soukup, J. Vac. Sci. Technol. A28 (2) (2010) 244.

3.3.3 C-III: Two-phase single layer Al-O-N nanocomposite films with enhanced resistance to cracking

Surface & Coatings Technology 206 (2012) 4230–4234

Contents lists available at SciVerse ScienceDirect

Surface & Coatings Technology

journal homepage: www.elsevier.com/locate/surfcoat

Two-phase single layer Al-O-N nanocomposite films with enhanced resistance to cracking

J. Musil *, R. Jílek, M. Meissner, T. Tölg, R. Čerstvý

Department of Physics, Faculty of Applied Sciences, University of West Bohemia, Univerzitní 22, CZ-306 14 Plzeň, Czech Republic

ARTICLE INFO

Article history:
Received 20 December 2011
Accepted in revised form 10 April 2012
Available online 20 April 2012

Keywords:
Two-phase nanocomposites
Oxynitride
Al-based composites
Mechanical properties
Reactive sputtering
Pulsed inlet of oxygen

ABSTRACT

The article reports on dc pulsed reactive sputtering of *two-phase single layer* Al-O-N nanocomposite films using dual magnetron in a mixture of N_2+O_2 with pulsed inlet of oxygen. Two kinds of nanocomposite films were sputtered: (1) nc-AlN/a-(Al-O-N) film and (2) nc-(γ-Al_2O_3)/a-(Al-O-N) nanocomposite film; here nc- and a- denotes the nanocrystalline and amorphous phase, respectively. The transition from the nc-AlN/a-(Al-O-N) nanocomposite to the nc-(γ-Al_2O_3)/a-(Al-O-N) nanocomposite was controlled by the length of the period of oxygen pulses T_{O2}. It was found that both nanocomposites are highly elastic films with relatively high hardness $H = 15$ to 20 GPa, low effective Young's modulus E^* satisfying the condition that the ratio $H/E^* > 0.1$, high elastic recovery $W_e > 60\%$ and high resistance to cracking in bending. Correlations between the film structure and its mechanical properties are discussed in detail.

1. Introduction

AlON is the aluminium oxynitride spinel ceramic material which exhibits technologically interesting physical properties, particularly optical, mechanical and thermal properties [1–7]. These properties of the Al-O-N material such as thermal, chemical and mechanical stability, refractive index, band-gap, transparency can be controlled and optimized by its elemental composition. Therefore, the Al-O-N material is successfully used in many applications, for instance, as transparent armor, military aircraft and missile domes, IR and laser windows, etc. The Al-O-N is produced not only as a bulk material [1,2] but also as thin films and coatings [3–7]. The Al-O-N thin films are used for optical applications, optoelectronic and microelectronic devices, the Al-O-N coatings as protective coatings against wear, diffusion and corrosion [3].

The Al-O-N material is a very complex system and not all correlations between the mechanical and optical properties and its elemental and phase composition were found. Our study is concentrated on a systematic investigation of the mechanical properties of the Al-O-N coatings only. For enhancement of the mechanical properties of the Al-O-N coating is very important in the relation between its hardness H and the effective Young's modulus E^* because the ratio H/E^* makes it possible to assess a toughness of the coating by measurement of a resistance of the coating to cracking; here $E^* = E/(1-\nu^2)$, E is the Young's modulus and ν is the Poisson's ratio. A formation of hard coatings with enhanced toughness is now a new task in the development of new generation of hard coatings [8–12]. No such investigation was performed so far. Up to now, an attention was devoted mainly to the increase of H of the AlON material by its incorporation in nanomultilayers, e.g. ZrN/AlON [5], VN/AlON [6].

A simple way on how to increase the hardness H of the Al-O-N coating is to control its structure. Therefore, a main attention in our study was concentrated on the structure, hardness H, effective Young's modulus E^*, elastic recovery W_e of the Al-O-N coating and the relation between the ratio H/E^* and the cracking of the coating during bending. The Al-O-N coating is a two-phase nc-grains/a-matrix nanocomposite composed of nanocrystalline grains embedded in the amorphous matrix. H and E^* of the Al-O-N coating is determined by its structure which is controlled by the relative content of the nanocrystalline and amorphous phase.

This article reports on new single-layer nc-AlN/a-(Al-O-N) and nc-(γ-Al_2O_3)/a-(Al-O-N) two-phase composite thin films composed of either AlN or Al_2O_3 nanograins embedded in an X-ray amorphous (Al-O-N) matrix which were reactively sputtered by DC pulsed dual magnetron in a mixture of N_2+O_2 gases. The main aim of this investigation is to determine the mechanical properties (the hardness H and the effective Young's modulus E^*) and mechanical behavior (the elastic recovery W_e and the ratio H/E^*) of these nitride/oxide and oxide/oxide nanocomposite films and to find conditions under which the hard Al-O-N nanocomposite films resistant to cracking in bending can be formed.

2. Experimental

The Al-O-N films were reactively sputtered using a DC pulsed dual magnetron, operated in a bipolar mode and equipped with Al targets

---

* Corresponding author.
E-mail address: musil@kfy.zcu.cz (J. Musil).

0257-8972/$ – see front matter © 2012 Elsevier B.V. All rights reserved.
doi:10.1016/j.surfcoat.2012.04.028

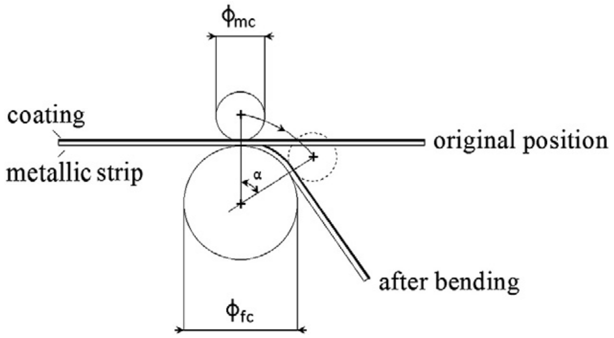

Fig. 1. (a) Schematic illustration of bending test used to create cracks in the film deposited on a metallic strip. $\varnothing_{mc}$ and $\varnothing_{fc}$ is the diameter of moving and fixed cylinder, respectively.

($\varnothing = 50$ mm), in a mixture $N_2 + O_2$ gases. During the film deposition the nitrogen N_2 gas was introduced continuously and the O_2 gas in pulses into the deposition chamber. The pulsing of oxygen enabled to form AlN nanocrystals due to lower affinity of N to Al (the formation enthalpy of the AlN nitride $\Delta H_{AlN} = -318.6$ kJ/mol [13]) compared to that of O to Al ($\Delta H_{Al2O3} = -1678.2$ kJ/mol [13]). The AlN nanocrystals were embedded in the amorphous Al_2O_3 matrix and the nc-AlN/a-Al_2O_3 nitride/oxide nanocomposite film was formed.

The dual magnetron was supplied by an Advanced Energy pulsed power supply at a repetition frequency $f_r = 100$ kHz, the magnetron current $I_{da} = 3$ A averaged over the pulse period $T = 1/f_r$ and the duty cycle $\tau/T = 0.5$ in bipolar mode; here τ is the length of the magnetron pulse. The pumping speed v of the deposition chamber is approximately 33 l/s. The sputtering process was carried out as follows. At first, prior to the magnetron discharge ignition Ar gas was introduced in the deposition chamber at a flow rate $\phi_{Ar} = 20$ sccm. Then, the discharge was started and held at the argon pressure $p_{Ar} = 1$ Pa. Then the argon was fully replaced with nitrogen and held at the pressure $p_{N2} = 1$ Pa with a flow rate $\phi_{N2} = 27$ sccm. The oxygen was introduced in pulses with the oxygen pulse-on time $\tau_{O2} = 2$ s and the repetition frequency $f_{r\ O2} = 1/T_{O2}$ increasing with increasing oxygen flow rate ϕ_{O2} from 0 (pure nitride film) to 5 sccm (pure oxide film); here T_{O2} is the period of oxygen pulses. The oxygen pulse-on time $\tau_{O2} = 2$ s was kept constant. Films were deposited on a floating substrate, i.e. at the substrate bias $U_s = U_{fl}$, two values of the substrate temperature $T_s = RT$ (unheated substrates) and $T_s = 500$ °C, the substrate-to-target distance $d_{s\text{-}t} = 100$ mm and the partial pressure of nitrogen $p_{N2} = 1$ Pa; here U_{fl} is the floating potential and RT is the room temperature. The Si(100) plates ($20 \times 20 \times 0.3$ mm^3 for XRD measurements and $30 \times 5 \times 0.3$ mm^3 for the measurement of a macrostress σ in the film), microscopic glass ($25 \times 25 \times 1$ mm^3 for the measurement of an optical transparency) and Mo strips ($80 \times 15 \times 0.1$ mm^3 for the measurement of a resistance of the film to cracking) were used as substrates.

The film thickness h was measured using a stylus profilometer DEKTAK 8. The film structure was characterized using an XRD spectrometer PANalytical X Pert PRO in Bragg–Brentano configuration with CuKα radiation. The elemental composition was determined by X-ray Fluorescence (XRF) spectroscopy with PANalytical XRF Spectrometer MagiX PRO. Mechanical properties were determined from load vs. displacement curves measured by a microhardness tester Fischerscope H100 with a Vicker's diamond indenter at a load $L = 30$ mN. The transparency of Al-O-N films was measured using a spectrometer Specord M400. The resistance of the film to cracking was investigated in a bending test. The principle of the bending test is shown in Fig. 1. The film was deposited on a Mo strip ($80 \times 15 \times 0.1$ mm^3) and the coated strip was bended along a fixed cylinder of diameter $\varnothing_{fc}$ up to angle α at which cracks in the film occurred. The bending of the coated strip was performed in a bending apparatus developed in our labs.

3. Results and discussion

3.1. Structure of sputtered films

3.1.1. Effect of substrate temperature

The structure of the Al-O-N film depends on the period T_{O2} of oxygen pulses and the substrate temperature T_s used in the film sputtering, see Figs. 2 and 3. Fig. 2 compares the structure of Al-O-N films sputtered on unheated substrates ($U_s = RT$) and the substrates heated at $T_s = 500$ °C. The films deposited on heated substrates exhibit a lower crystallinity (lower intensities of X-ray reflections) compared to those deposited on the unheated substrate. It is due to a release of oxygen from the chamber walls heated by a hot substrate holder, enhanced dissociation of O_2 on the surface of heated substrates, incorporation of more O into the film and by the formation of a higher amount of the a-Al_2O_3 phase in the film at $T_s = 500$ °C. Moreover, it is worthwhile to note that already a small amount of oxygen contained in a residual atmosphere of the deposition chamber after its evacuation to a base pressure p_0 and/or evolved from the chamber walls at $T_s = 500$ °C is sufficient to react with sputtered Al. Therefore, a good reproducibility of properties of the Al-O-N films sputtered under the same conditions is difficult problem; the film properties are strongly influenced by the value of residual pressure p_0, i.e. by the efficiency and time of the evacuation of the deposition chamber, and the state of chamber walls prior to the film deposition. Therefore, a longer series with finer steps in T_{O2} was prepared to see better the evolution of the film structure, see Fig. 3.

3.1.2. Effect of duty cycle of oxygen pulses

The structure of the Al-O-N film strongly depends on a duty cycle of the oxygen pulses τ_{O2}/T_{O2}, i.e. on the amount of oxygen incorporated in the film. The films produced at $\tau_{O2}/T_{O2} = 1$ (the deposition at continuous inlet of oxygen) are nc-(γ-Al_2O_3)/a-(Al-O-N) composites.

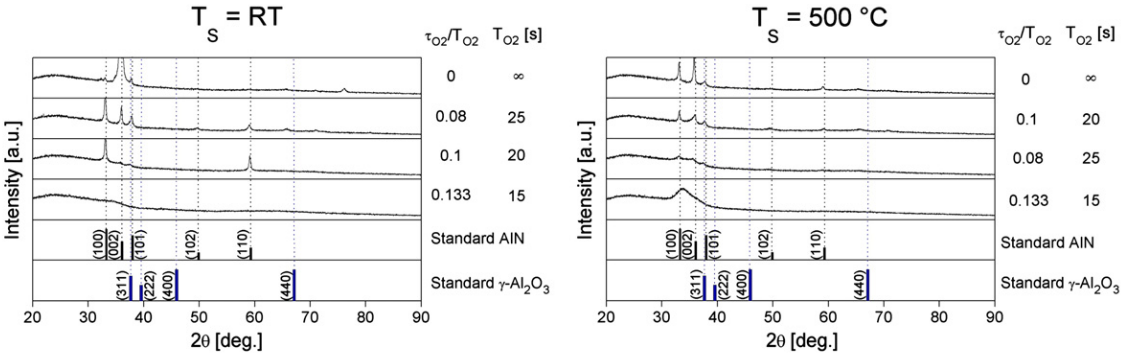

Fig. 2. XRD patterns of Al-O-N films sputtered on glass substrate as a function of repetition frequency of oxygen pulses $f_{r\ O2}$ at $\tau_{O2} = 2$ s and two values of the substrate temperature $T_s = RT$ (unheated substrate) and $T_s = 500$ °C.

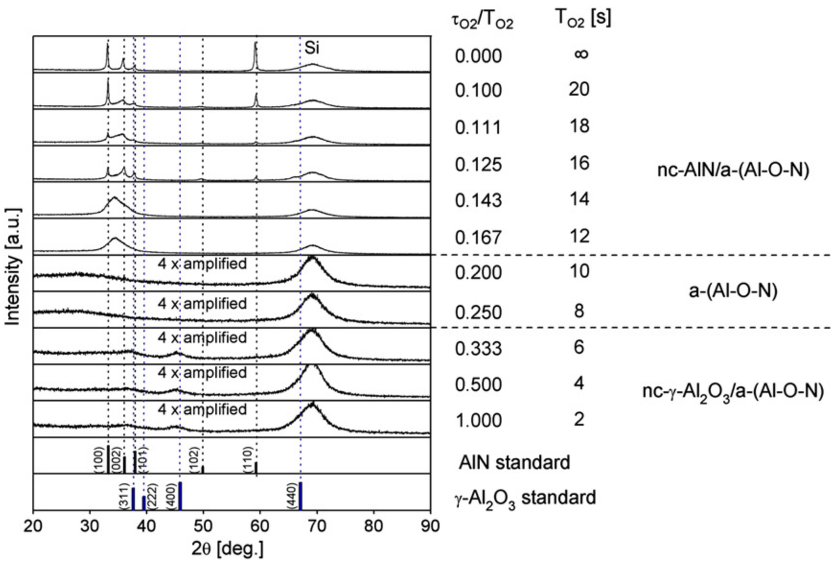

Fig. 3. Evolution of XRD patterns of Al-O-N films, sputtered at $U_s = U_{fl}$ and $T_s = 500$ °C, with increasing repetition frequency of oxygen pulses $f_{r\ O2}$.

The films produced at $\tau_{O2}/T_{O2} = 0$ (deposition in pure nitrogen) are crystalline c-AlN films. The addition of oxygen O in the c-AlN film ($0 < \tau_{O2}/T_{O2} < 1$) results in the formation of nc-AlN/a-(Al-O-N) composite films which gradually change first to fully amorphous a-(Al-O-N) films at $\tau_{O2}/T_{O2} \approx 0.2$–0.25 and then to nc-(γ-$Al_2O_3$)/a-(Al-O-N) composite films when the ratio τ_{O2}/T_{O2} increases to 1, see Fig. 3. These changes of the structure of the Al-O-N film result in strong changes of its mechanical properties.

3.2. Mechanical properties of Al-O-N films

Mechanical properties of the film are the hardness H and the effective Young s modulus E^*. Mechanical behavior of the film is characterized by the elastic recovery W_e, the ratio H/E^* [14–16] and the ratio H^3/E^{*2} [17]. The ratio H/E^* is proportional to a fracture toughness of the film [10,11]. The ratio H^3/E^{*2} is proportional to a resistance of the material to plastic deformation. It means that the films with enhanced resistance to cracking and plastic deformation should have low values of E^*. This statement was already confirmed for the Al-Cu-O films [10] and for the Zr-Al-O films [11]. It was found that the films with $H/E^* > 0.1$ are highly elastic ($W_e \geq 60\%$) and exhibit an enhanced resistance to cracking. The main aim of the present investigation is to find if also the Al-O-N films can be highly elastic and can exhibit an enhanced resistance to cracking.

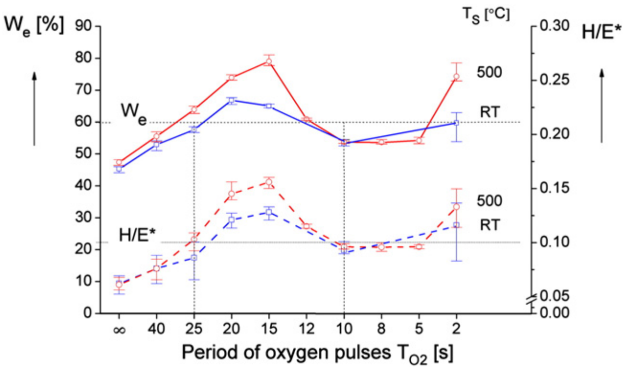

Fig. 4. W_e and H/E^* of the Al-O-N films sputtered at $T_s = RT$ and 500 °C as a function of period of oxygen pulses T_{O2}.

The hardness H, effective Young's modulus E^* and elastic recovery W_e of Al-O-N films sputtered on unheated substrates ($T_s = RT$) and heated ($T_s = 500$ °C) substrates were measured in detail. The evolution of the H/E^* ratio and W_e of the Al-O-N films sputtered at $T_s = RT$ with increasing frequency of oxygen pulses $f_{r\ O2} = 1/T_{O2}$ is displayed in Fig. 4; the thickness h and values of H and E^* of these films are given in Table 1. From this figure it is seen that the Al-O-N films sputtered at T_{O2} ranging from ~12 to ~25 s exhibit (1) high ratio $H/E^* > 0.1$ and (2) high value of the elastic recovery $W_e \geq 60\%$, i.e. the properties we wanted to find. The values of the ratio H/E^* and W_e of the Al-O-N films grow with increasing substrate temperature T_s.

The formation of the Al-O-N films with high values of H/E^* and W_e is a result of the change of their structure with increasing amount of oxygen added in $N_2 + O_2$ sputtering gas mixture, see Fig. 2. To obtain the Al-O-N films with maximum hardness H, $H/E^* > 0.1$ and $W_e > 60\%$ the relative amount of the nc-AlN phase and the a-(Al-O-N) phase in the nc-AlN/a-(Al-O-N) composite film needs to be optimized. It can be achieved by the control of the amount of oxygen added into $N_2 + O_2$ mixture, see Fig. 5. The hardness H of the Al-O-N films sputtered on the substrate held on a floating potential ($U_s = U_{fl}$) increases with increasing substrate temperature T_s; compare the values of H of the Al-O-N films sputtered on the unheated ($T_s = RT$, Table 1) and heated ($T_s = 500$ °C, Table 2) substrate.

Fig. 5. shows correlations between the mechanical properties (H, E^*) and H/E^* ratio of the Al-O-N films sputtered at $T_s = 500$ °C and their structure. From this figure the following important issues can be drawn: (1) the nc-AlN/a-(Al-O-N) and nc-(γ-Al_2O_3)/a-(Al-O-N)

Table 1
Thickness h, hardness H, effective Young's modulus E^*, H/E^* and H^3/E^{*2} of the Al-O-N films reactively sputtered in $N_2 + O_2$ mixture on unheated substrate ($T_s = RT$) as a function of the period between oxygen pulses T_{O2} at a constant length of the oxygen pulse $\tau_{O2} = 2$ s.

T_{O2} [s]	h [nm]	H [GPa]	E^* [GPa]	W_e [%]	H/E^*	H^3/E^{*2} [GPa]
∞	3100	6.7	108.7	45.3	0.062	0.025
40	2600	8.9	117.2	52.9	0.076	0.051
25	2900	10.5	121.4	57.6	0.086	0.079
20	3100	15.5	127.9	66.8	0.121	0.228
15	2900	13.8	118.0	65.0	0.128	0.225
10	2500	9.7	104.0	53.2	0.093	0.084
2	1200	10.8	83.4	59.7	0.116	0.144

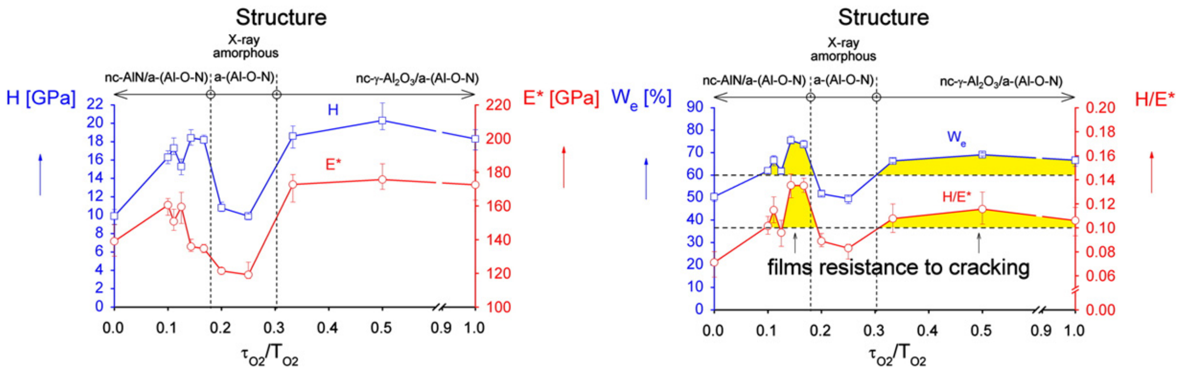

Fig. 5. H, E^*, W_e and H/E^* of the Al-O-N films sputtered at $T_s = 500$ °C as a function of oxygen duty cycle τ_{O2}/T_{O2}.

nanocomposite films have a higher hardness H compared with that of the c-AlN (sputtered at $\tau_{O2}/T_{O2} = 0$) and amorphous a-(Al-O-N) films (sputtered at τ_{O2}/T_{O2} ranging from ~0.18 to ~0.3), (2) two kinds of the nanocomposite films with $H/E^* > 0.1$ are formed: (a) the nc-AlN/a-(Al-O-N) nanocomposite films in the interval τ_{O2}/T_{O2} ranging from ~0.1 to ~0.18 in which the hardness H is almost constant and the effective Young's modulus E^* decreases and (b) the nc-(γ-Al_2O_3)/a-(Al-O-N) nanocomposite films at $\tau_{O2}/T_{O2} \geq 0.3$, and (3) the Al-O-N films with $H/E^* > 0.1$ exhibit a high elastic recovery $W_e \geq 60\%$.

Correlations between values of H, E^*, W_e, H/E^*, H^3/E^{*2}, macrostress σ of the Al-O-N films sputtered at Si(100) substrate and cracks generated in the Al-O-N sputtered on Mo strip during bending are given in Table 2. The following facts should be underlined: (1) nc-AlN/a-(Al-O-N) and nc-(γ-Al_2O_3)/a-(Al-O-N) composite films with $H/E^* > 0.1$ exhibit relatively high hardness H = ~15 to ~18 GPa, (2) the hardness H of the nc-AlN/a-(Al-O-N) composite increases with increasing ratio τ_{O2}/T_{O2}, i.e. with decreasing content of the nc-AlN phase, and the hardness H of the nc-(γ-Al_2O_3)/a-(Al-O-N) composite increases with the ratio τ_{O2}/T_{O2} increasing above 0.3, i.e. with increasing content of nc-(γ-Al_2O_3) phase, and (3) the hardness H of the a-(Al-O-N) films is low of about 10 GPa only; these films exhibit low elastic recovery $W_e \leq 50\%$, $H/E^* < 0.1$, low resistance to plastic deformation ($H^3/E^{*2} < 0.1$) and low compressive macrostress σ. The incorporation of the nanocrystalline phase in the amorphous a-(Al-O-N) matrix strongly increases H, W_e, H/E^* and H^3/E^{*2}, i.e. increases the resistance of the film to plastic deformation and its resistance to cracking in bending. It is of great importance for many applications.

3.3. Resistance of Al-O-N films to cracking in bending

The resistance of the Al-O-N film to cracking was investigated by the bending of Mo strip ($80 \times 15 \times 0.1$ mm^3) coated with sputtered Al-O-N film along the fixed cylinder of diameter $\varnothing = 25$ mm. The resistance of the film to cracking is assessed from the angle α_c at which macrocracks in the film occurred. The higher angle α_c the higher is the resistance of the film to cracking. This method is based on the assumption that the adhesion of the film to Mo strip is good. It was found that (i) the resistance of the film to cracking depends on the ratio H/E^* and the elastic recovery W_e and (ii) all Al-O-N films with $H/E^* > 0.1$ and high $W_e \geq 60\%$ resist well to cracking in bending. This fact is illustrated in Fig. 6 where the Al-O-N films with $H/E^* < 0.1$ and $H/E^* > 0.1$ are compared. Cracks perpendicular to the direction of bending of the coated strip are produced in the X-ray amorphous a-(Al-O-N) film with $H/E^* < 0.1$. No cracking of the nc-nitride/a-oxide composite film with $H/E^* > 0.1$ takes place when the Mo strip covered by this film is bended along a fixed SS cylinder of diameter 25 mm up to angle $\alpha = 180° < \alpha_c$. Recently, similar results were obtained also for the sputtered Zr-Al-O films with $H/E^* < 0.1$ and $H/E^* > 0.1$ [11].

In some cases, however, also the Al-O-N films with $H/E^* < 0.1$ exhibit no cracking in bending, see Table 2. The reason why no cracks occur in the film with $H/E^* < 1$ is not clear. Typical example is the film sputtered at $T_s = 500$ °C without inlet of oxygen ($T_{O2} = \infty$ in Table 2). This film despite low H = 9.6 GPa, low $E^* = 138$ GPa, i.e. $H/E^* = 0.07$, and relatively low $W_e = 50\%$ does not crack on the Mo strip in bending up to 180 °C. As shown in Fig. 2 this film is nitride/oxide composite. It indicates that the resistance of the film to cracking is controlled also

Table 2
Thickness h, hardness H, effective Young's modulus E^*, H/E^* and H^3/E^{*2} of Al-O-N films reactively sputtered in $N_2 + O_2$ mixture on heated substrate ($T_s = 500$ °C) as a function of the period between oxygen pulses T_{O2} at a constant length of the oxygen pulse $\tau_{O2} = 2$ s. The Mo strip coated with Al-O-N film was bended along cylinder $\varnothing_{fc} = 25$ mm up to angle $\alpha = 180°$ if no cracks occurred.

T_{O2} [s]	h [nm]	H [GPa]	E^* [GPa]	W_e [%]	H/E^*	H^3/E^{*2} [GPa]	σ [GPa]	Cracks	α [deg]	Structure
∞	2900	9.6	138	50	0.070	0.047	−0.47	No		c-AlN/(a-Al_2O_3)[a]
20	2900	16.1	160	62	0.101	0.164	−0.50		40	nc-(AlN)/a-(Al-O-N)
18	2900	17.3	150	67	0.115	0.229	−0.55	No		″
16	2700	15.3	160	62	0.096	0.141	−0.43		40	″
14	2700	18.4	136	75	0.135	0.335	−0.58	No		″
12	3300	18.2	135	74	0.135	0.332	n.m.	No		″
10	2900	10.8	122	52	0.089	0.086	−0.18		40	a-(Al-O-N)
8	2800	9.9	119	50	0.083	0.068	−0.14	No		″
6	1700	18.6	173	66	0.108	0.217	−1.60	No		nc-(γ-Al_2O_3)/a-(Al-O-N)
4	1500	20.3	176	69	0.115	0.268	−2.20	No		″
2	1700	18.3	172	67	0.106	0.206	−2.10	n.m.[b]		″

n.m. = not measured.

[a] a-Al_2O_3 phase is formed in reaction of Al atoms with oxygen contained in a residual atmosphere.

[b] The film was delaminated from the Mo strip.

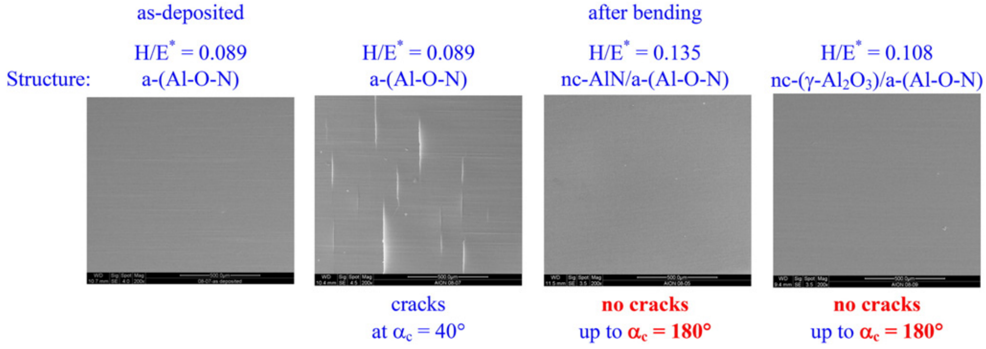

Fig. 6. Typical photos of surface morphology of the Al-O-N films with $H/E^* < 0.1$ and $H/E^* > 0.1$ deposited on Mo strip in the as-deposited state and after bending.

by the amount of individual phases in the composite material. Therefore, further investigation is needed to confirm this hypothesis.

4. Conclusions

Main results of our study of mechanical properties of the Al-O-N nanocomposite films reactively sputtered in a mixture of $N_2 + O_2$ using a pulse injection of oxygen can be summarized as follows.

1. The pulsed injection of oxygen into nitrogen gas during the reactive sputtering of pure Al target enables to form two kinds of single layer nanocomposites: (1) nc-nitride/a-oxide nanocomposite with a low O content and (2) nc-oxide/a-oxide nanocomposite with a high O content composed of the nc-AlN phase or the nc-(γ-Al_2O_3) phase embedded in the amorphous (Al-O-N) phase, respectively. In the transition between the nc-nitride/a-oxide and the nc-oxide/a-oxide nanocomposite films the X-ray amorphous a-(Al-O-N) films are formed. Relative content of individual phases in the nanocomposite was controlled by the period T_{O2} between pulses at constant length of oxygen pulse $\tau_{O2} = 2$ s.
2. The addition of the nanocrystalline phase in an amorphous matrix strongly increases the hardness of the nanocomposite material compared with the amorphous material. Both the nc-nitride/a-oxide and the nc-oxide/a-oxide nanocomposite films exhibit relatively high hardness $H = 15$ to 20 GPa, low Young's modulus E^* satisfying the ratio $H/E^* > 0.1$ and high elastic recovery $W_e > 60\%$. On the contrary, the X-ray amorphous a-(Al-O-N) films exhibit much lower hardness $H \approx 10$ GPa, low ratio $H/E^* < 0.1$ and low $W \approx 50\%$.
3. Hard nanocomposite films with $H/E^* > 0.1$ deposited on the Mo strip resist well to cracking in bending.
4. The hard Al-O-N nanocomposite films with hardness H ranging from ~15 to ~20 GPa, $H/E^* > 0.1$ and $W_e > 60\%$ deposited on the 0.1 mm thick Mo strip which did not crack during bending along the fixed cylinder of diameter 25 mm up to angle 180° were successfully prepared.

Acknowledgements

This work was supported in part by the Grant Agency of the Czech Republic GACR under Project No. P108/12/0393.

References

[1] J.W. McCauley, P. Patel, M. Chen, G. Gilde, E. Strassburger, B. Paliwl, K.T. Ramesh, D.P. Dandekar, J. Eur. Ceram. Soc. 29 (2009) 223.
[2] Z. Zhang, X. Wang, W. Li, J. Alloys Compd. 387 (2005) 74.
[3] S. Dreer, R. Krismer, P. Wilhartitz, Thin Solid Films 354 (1999) 43.
[4] S. Dreer, R. Krismer, P. Wilhartitz, Surf. Coat. Technol. 114 (1999) 29.
[5] Y. Dong, J. Yue, Y. Liu, G. Li, J. Phys. D: Appl. Phys. 39 (2006) 4838.
[6] J. Yue, Y. Liu, W. Zhao, G. Li, Scr. Mater. 55 (2006) 895.
[7] H.C. Barshilia, N. Selvakumar, K.S. Rajan, A. Biswas, Sol. Energy Mater. Sol. Cells 92 (2008) 1425.
[8] S. Zhang, D. Sun, Y. Fu, H. Du, Surf. Coat. Technol. 198 (2005) 2.
[9] J. Musil, P. Novak, R. Cerstvy, Z. Soukup, J. Vac. Sci. Technol. A28 (2) (2010) 244.
[10] J. Blazek, J. Musil, P. Stupka, R. Cerstvy, J. Houska, Appl. Surf. Sci. 258 (2011) 1762.
[11] J. Musil, J. Sklenka, R. Cerstvy, Surf. Coat. Technol. 206 (2012) 2105.
[12] J. Musil, V. Satava, P. Zeman, R. Cerstvy, Surf. Coat. Technol. 203 (2009) 1502.
[13] Smithells Metals Reference Book, Six Edition, E.A.Brandes (Ed.). London, 1992, p. 8–23 Table 8.8c and p. 8–25 Table 8.8e.
[14] A. Leyland, A. Mathews, Surf. Coat. Technol. 177–178 (2004) 317.
[15] A. Matthews, A. Leyland, Material related aspects of nanostructured tribological coatings, SVS 2008 Fall, Bulletin, 2008, 40–45.
[16] J. Musil, J. Jirout, Surf. Coat. Technol. 201 (2007) 5148.
[17] T.Y. Tsui, G.M. Pharr, W.C. Oliver, C.S. Bhatia, R.L. White, S. Anders, A. Anders, I.G. Brown, Mater. Res. Soc. Symp. Proc. 383 (1995) 447.

3.3.4 C-IV: The effect of addition of Al in ZrO_2 thin film on its resistance to cracking

Surface & Coatings Technology 207 (2012) 355–360

Contents lists available at SciVerse ScienceDirect

Surface & Coatings Technology

journal homepage: www.elsevier.com/locate/surfcoat

The effect of addition of Al in ZrO_2 thin film on its resistance to cracking

J. Musil [a,*], J. Sklenka [a], R. Čerstvý [a], T. Suzuki [b], T. Mori [b], M. Takahashi [b]

[a] Department of Physics, Faculty of Applied Sciences, University of West Bohemia, Univerzitní 22, CZ-306 14 Plzeň, Czech Republic
[b] Center for Science of Environment, Resources and Energy, Keio University, 3-14-1 Hyoshi, Kohoku, Yokohama 223-8522, Japan

ARTICLE INFO

Article history:
Received 4 May 2012
Accepted in revised form 3 July 2012
Available online 10 July 2012

Keywords:
Zr–Al–O film
Structure
Mechanical properties
Resistance to cracking
Optical properties
Reactive magnetron sputtering

ABSTRACT

The paper reports on the structure, mechanical and optical properties of sputtered Zr–Al–O films. The Zr–Al–O films with Zr/Al>1 and Zr/Al<1 were prepared by a reactive sputtering using ac pulse dual magnetrons. The magnetrons were equipped with a target composed of Al plate (∅ = 50 mm) fixed to the magnetron cathode by a Zr fixing ring with inner diameter $\varnothing_{in}$. The content of Al in the Zr–Al–O film was controlled by $\varnothing_{in}$. It makes possible to control effectively the structure of the Zr–Al–O film determined by a mixture of the crystalline ZrO_2 phase and the amorphous Al_2O_3 phase. The effect of Al content on the structure, mechanical and optical properties of the Zr–Al–O film is investigated in detail. It was found that (i) the Zr–Al–O films with Zr/Al<1 are X-ray amorphous and exhibit low hardness ($H \leq 13$ GPa), an effective Young's modulus E^* resulting in a low $H/E^* < 0.1$ ratio and low elastic recovery $W_e \leq 60$ and (ii) the Zr–Al–O films with Zr/Al>1 are crystalline and exhibit high hardness (H = 18 to 19 GPa), an E^* satisfying a high $H/E^* \geq 0.1$ ratio, high W_e up to 78% and strongly enhanced resistance to cracking during bending even for thick films up to 5 μm.

1. Introduction

It is well known that the addition of one or several elements in a base material is a very effective method used to influence its structure and phase composition and thereby its properties. There are many papers demonstrating this fact. For illustrating this phenomenon we present several examples. The addition of Al in the HfO_2 film improves the thermal stability of an $(HfO_2)_{1-x}(Al_2O_3)_x$ film due to the increase of its crystallization temperature T_{cr}. On the other hand, the addition of Zr in the HfO_2 film decreases the thermal stability of $(HfO_2)_{1-x}(ZrO_2)_x$ film due to decreasing T_{cr} in consequence of a strong tendency of the ZrO_2 oxide to form a crystalline phase [1]. The addition of a small amount of Si (<10 at.%) in the TiN film can strongly increase the hardness Ti–Si–N film due to its conversion from the one-phase TiN material in a two-phase nc-TiN/a-Si_3N_4 nanocomposite material composed of TiN nanograins surrounded by a tissue amorphous Si_3N_4 phase [2]; here nc- and a- denotes the nanocrystalline and amorphous phase, respectively. On the other hand, the addition of a high amount of Si (≥20 at.%) in the MeN film can considerably increase the resistance of a two-phase nc-TiN/a-Si_3N_4 nanocomposite material to oxidation due to the dominance of the a-Si_3N_4 phase in the nanocomposite over the nc-TiN phase [3]. The addition of several elements in alloys are used to form equiatomic amorphous solid solution films with enhanced mechanical properties and high corrosion and wear resistance [4–6]; these coatings are called as multi-element or high entropy alloys (HEA), nitrides and carbides. Recently, the addition of Cu in Al_2O_3 [7], Al in ZrO_2 [8] and N in Al_2O_3 [9] was used to enhance the resistance of Al–Cu–O, Zr–Al–O and Al–O–N films to cracking.

As to the last application, i.e. the improvement of the film resistance to cracking by the addition of a selected element, many questions remain open so far. For instance, the enhanced resistance of the Zr–Al–O films was demonstrated only for the films with a high ratio Zr/Al>1. However, there is also the question if the Zr–Al–O films with a low ratio Zr/Al<1 can exhibit the enhanced resistance to cracking. Therefore, the investigation of mechanical and optical properties of the Zr–Al–O films with low ratio Zr/Al<1 and their resistance to cracking is the main aim of this paper. The mechanical and optical properties of the Zr–Al–O films with Zr/Al<1 to Zr/Al>1 are compared in detail, and the very different resistance to cracking is explained by their strongly different mechanical properties.

2. Experimental

The Zr–Al–O thin films were reactively sputtered in an $Ar+O_2$ mixture using a dual magnetron equipped with Zr–Al targets (∅ = 50 mm) composed of the Al circular plate (99.99 at.%) fixed with two Zr (99.9 at.%) rings of inner diameter $\varnothing_{in\ Zr} = 20$ and 24 mm and operated in a closed magnetic field B. The Zr–Al–O films with Zr/Al<1 and Zr/Al>1 were sputtered from targets fixed with the Zr fixing ring of inner diameter $\varnothing_{in\ Zr} = 24$ and 20 mm, respectively. The magnetron was operated in an ac pulse mode generated by a

---

[*] Corresponding author.
E-mail address: musil@kfy.zcu.cz (J. Musil).

0257-8972/$ – see front matter © 2012 Elsevier B.V. All rights reserved.
doi:10.1016/j.surfcoat.2012.07.017

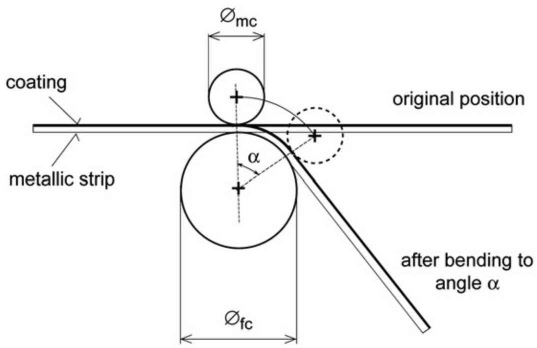

Fig. 1. (a) Schematic illustration of bending test used to induce cracks in the film deposited on metallic strip. $\varnothing_{mc}$ and $\varnothing_{fc}$ is the diameter of the moving and fixed cylinder, respectively.

pulse power supply DORA MSS-10 with an output power 10 kW (made by DORA Electronics in Poland). The repetition frequency f_r of pulses was 2 kHz and the ac frequency inside pulses was 56 kHz. The magnetron discharge current I_d was controlled by the duty cycle τ/T; here τ is the length of pulse and $T = 1/f_r$ is the repetition frequency of pulses. The Zr–Al–O films were sputtered under the following conditions: discharge current $I_{da} = 1$ and 2 A averaged over the pulse period T, substrate bias voltage $U_s = U_{fl}$, substrate temperature $T_s = 500$ °C, substrate-to-target distance $d_{s-t} = 80$ mm, variable values of the partial pressure of oxygen p_{O2} and constant value of the total pressure $p_T = p_{Ar} + p_{O2} = 1$ Pa; here U_{fl} is the floating potential.

The film thickness h was measured using a stylus profilometer DEKTAK 8. The film structure was characterized using an XRD spectrometer PANalytical X Pert PRO in Bragg–Brentano configuration with CuKα radiation. The elemental composition and density was determined by X-ray Fluorescence (XRF) spectroscopy with PANalytical XRF Spectrometer MagiX PRO. The density of the film was determined by weighting. The density of the film was calculated from the measured weight of the substrate with and without the film. Mechanical properties, i.e. the microhardness H, the effective Young's modulus E^* and the elastic recovery W_e, were determined from load vs. displacement curves measured by a microhardness tester Fischerscope H100 with a Vickers diamond indenter at a load L = 10 mN; here $E^* = E/(1-\nu^2)$, E is the Young's modulus, ν is the Poisson's ratio, $W_e = A_1/(A_1 + A_2)$, A_1 and A_2 are the elastic energy and the plastic (dissipated) energy, respectively, applied to the film during the loading of the diamond indenter. For all sputtered films the ratio d/h of the diamond depth impression d in the film surface to the film thickness h was less than 0.1. The ratio d/h for the softest film was 0.1. It indicates that the measured hardness H of our films is not influenced by the substrate. The transparency of Zr–Al–O films was measured in the range from 300 to 800 nm using a spectrometer Specord M400. The resistance of the film to cracking was investigated in a bending test. The principle of the bending test is shown in Fig. 1. The film

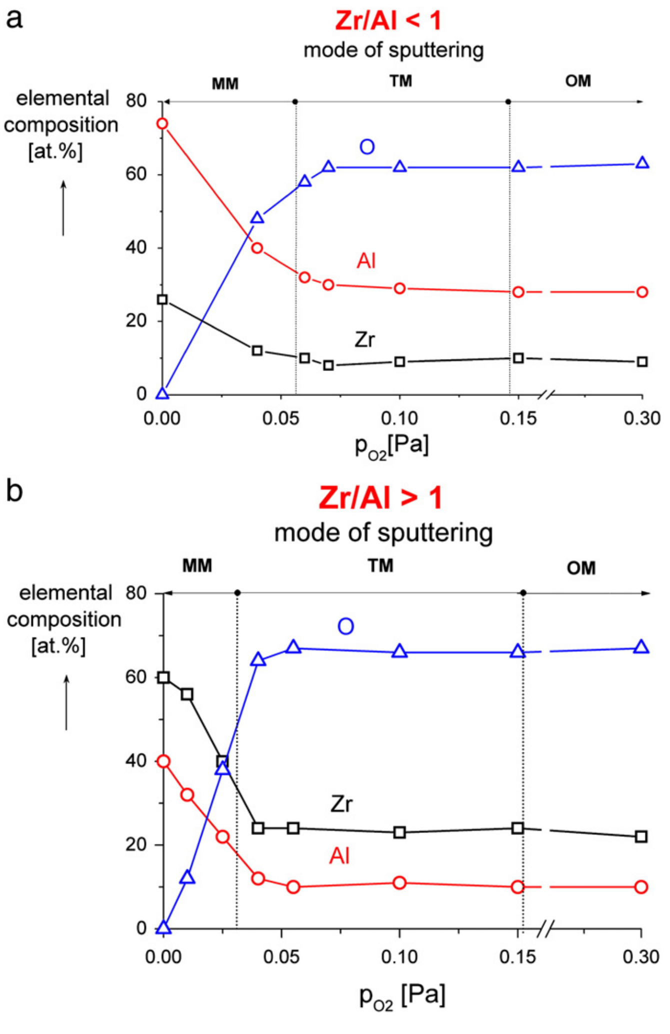

Fig. 2. The elemental composition of the Zr–Al–O films with (a) low ratio Zr/Al<1 and (b) high ratio Zr/Al>1 sputtered on Si(100) substrate at $U_s = U_{fl}$, $T_s = 500$ °C, $p_T = 1$ Pa and $I_{da} = 1$ and 2 A, respectively, as a function of partial pressure of oxygen p_{O2}. MM, TM and OM are the metallic, transition and oxide modes of sputtering, respectively.

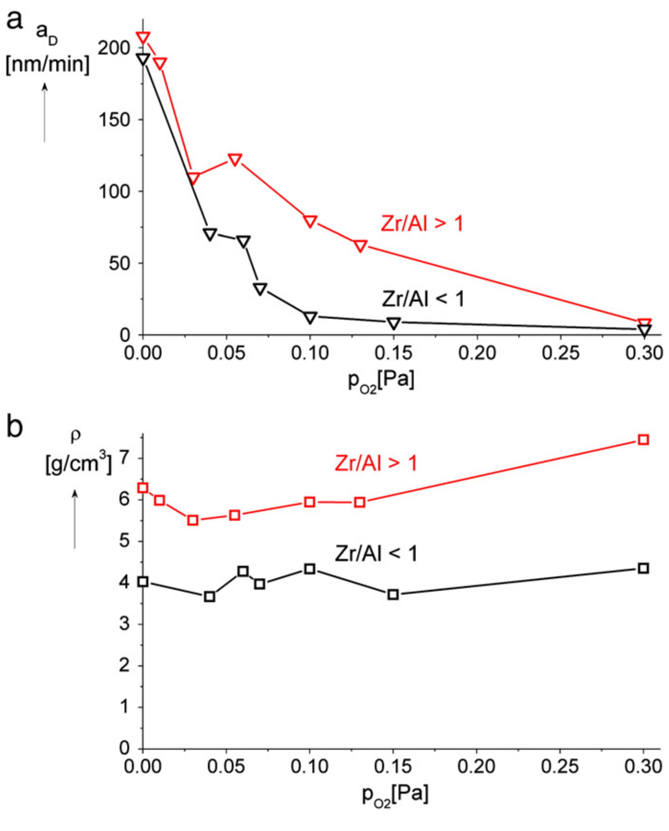

Fig. 3. (a) The deposition rate a_D and (b) density ρ of the Zr–Al–O films with low ratio Zr/Al<1 and high ratio Zr/Al>1 sputtered on Si(100) substrate at $U_s = U_{fl}$, $T_s = 500$ °C, $p_T = 1$ Pa and $I_{da} = 1$ and 2 A, respectively, as a function of partial pressure of oxygen p_{O2}.

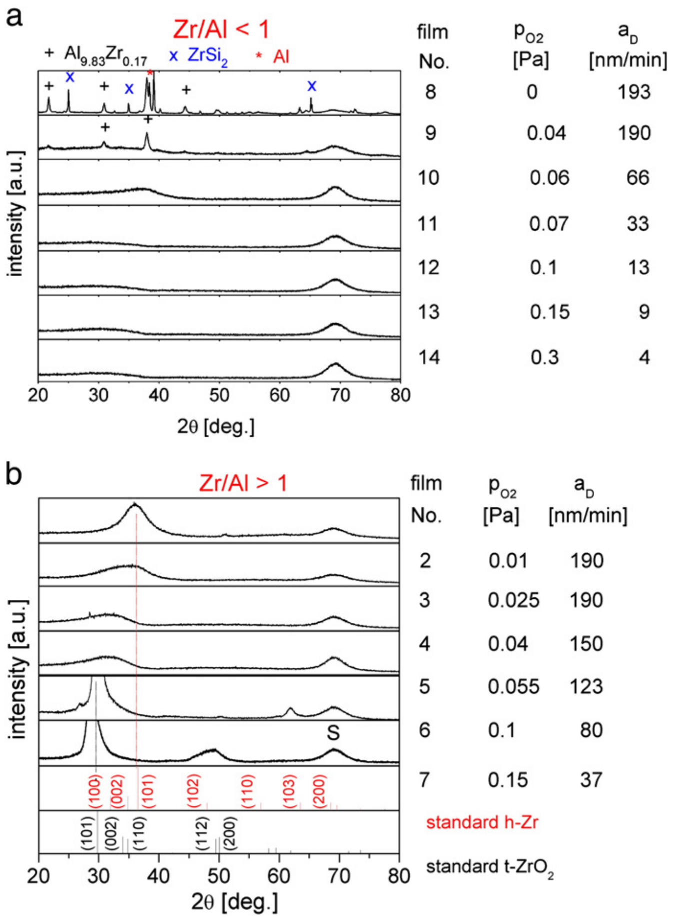

Fig. 4. The structure of the Zr–Al–O films with (a) low ratio Zr/Al<1 and (b) high ratio Zr/Al>1 sputtered on Si(100) substrate at $U_s = U_{fl}$, $T_s = 500$ °C, $p_T = 1$ Pa and $I_{da} = 1$ and 2 A, respectively, as a function of partial pressure of oxygen p_{O2}.

was deposited on a Mo strip ($80 \times 15 \times 0.1$ mm^3) and the coated strip was bent up to its cracking point in the bending apparatus developed in our labs.

3. Results

3.1. Elemental composition

The evolution of the elemental composition in the Zr–Al–O films with low Zr/Al<1 and high Zr/Al>1 reactively sputtered using ac pulsed dual magnetrons is displayed in Fig. 2. In this figure modes of sputtering in which films were prepared are also denoted. It can be seen that most of the films, which were sputtered in the transition mode (TM) of sputtering and the oxide mode (OM) of sputtering, have almost the same elemental composition. The transition mode of sputtering corresponds to a range of the partial pressure of oxygen p_{O2} at which there is a deficiency of atomic oxygen in the discharge necessary to form stoichiometric oxides. The deposition rate a_D of the Zr–Al–O films decreases with increasing p_{O2}, but it is higher for the Zr–Al–O films with high ratio Zr/Al>1, see Fig. 3a. The Zr–Al–O films with high ratio Zr/Al>1 are also denser than the Zr–Al–O films with low ratio Zr/Al<1, see Fig. 3b. It is due to the different structure of the Zr–Al–O films with low Zr/Al<1 and high Zr/Al>1 ratio and a higher Zr content in the Zr–Al–O films with high Zr/Al>1 ratio. The films containing a lower amount of the amorphous Al_2O_3 phase, i.e. the Zr–Al–O films with high ratio Zr/Al>1, are denser.

3.2. Structure

The structure of the sputtered Zr–Al–O film strongly depends on its elemental and phase composition, i.e. on the Zr/Al ratio and the partial pressure of oxygen p_{O2} used in its deposition. The Zr–Al–O films with ratio Zr/Al<1 sputtered in the metallic mode (MM) of sputtering are crystalline. The increase of p_{O2} results in (i) the formation of Zr and Al oxides and (ii) the gradual change of the crystalline film ($p_{O2} = 0$) through the crystalline/amorphous composite ($p_{O2} = 0.04$ Pa) to the X-ray amorphous film ($p_{O2} \geq 0.06$ Pa), see Fig. 4a. The X-ray amorphous film mainly consists of the a-Al_2O_3 phase because (i) the free oxygen is preferentially bounded to Al compared to Zr due to a higher negative formation enthalpy ΔH of the Al_2O_3 oxide compared to that of the ZrO_2 oxide ($|\Delta H_{Al2O3} = -1678.2$ kJ/mol$| > |\Delta H_{ZrO2} = -1101.3$ kJ/mol$|$ [10]) and (ii) a low ratio Zr/Al<1 resulting in a low content of the ZrO_2 oxide phase in the film compared to the content of the a-Al_2O_3 phase; no reflections from the ZrO_2 phase are seen due to a low ratio Zr/Al<1. It is also possible that the amorphous Al_2O_3 acts as a template

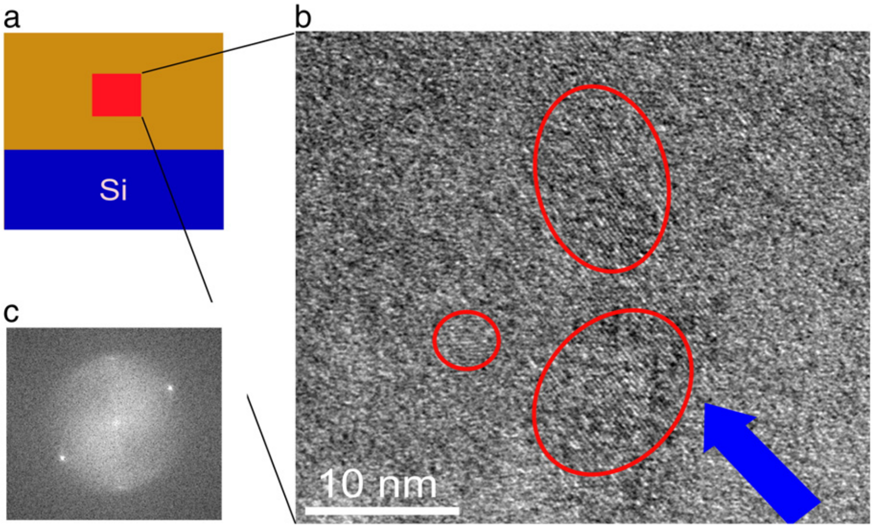

Fig. 5. Photo of the HRTEM image of the cross-section of the 1600 nm thick Zr–Al–O film on Si(100) substrate with Zr/Al>1 taken in the middle between the film surface and the film/substrate interface. The Zr–Al–O film with H = 19.2 GPa, $E^* = 163$ GPa, $W_e = 74\%$ and $H/E^* = 0.118$ is a composite composed of ZrO_2 nanograins embedded in the amorphous matrix. (a) Schematic of the film/substrate couple, (b) the HRTEM image of the cross-section microstructure in the square marked in Fig. 5a and (c) the Fast Fourier Transformation (FFT) image in the place of HRTEM image.

for the formation of the nanoscale ZrO_2 and forces the ZrO_2 into an amorphous state. On the other hand, the Zr–Al–O film with high ratio Zr/Al > 1 is the nc-ZrO_2/a-Al_2O_3 composite film containing ZrO_2 nanograins embedded in the amorphous Al_2O_3 matrix as can be seen in Fig. 4b and Fig. 5 where the photo of a cross-section of this film is given. Fig. 4b also clearly demonstrates that the film crystallinity of the Zr–Al–O film with high ratio Zr/Al > 1 improves with increasing p_{O2} and decreasing deposition rate a_D.

3.3. Microstructure

Typical microstructure of the Zr–Al–O film with Zr/Al > 1 (film no.5 in Fig. 4b) approximately in the middle between the film surface and the film/substrate interface is displayed in Fig. 5. Fig. 5a denotes the place (red square) in which the microstructure was investigated. Fig. 5b displays HRTEM image of the film microstructure in this place. From Fig. 5b it is seen that nanograins in the film are surrounded by an amorphous phase and have different crystallographic orientation. Most of the nanograins would be oriented in one crystallographic direction as it indicates a strong t-ZrO_2 (101) preferred crystallographic orientation shown in Fig. 4b what was not demonstrated by HRTEM so far. The existence of nanocrystalline regions in the film is, however, observed by a Fast Fourier Transformation (FFT) image performed for the crystalline phase, see Fig. 5c. The finding that the Zr–Al–O film with Zr/Al > 1 is the composite composed of nanograins dispersed in amorphous matrix is of fundamental importance because the nanocomposites of this type exhibit enhanced mechanical properties.

3.4. Mechanical properties

The mechanical properties of the coating are its hardness H and the effective Young's modulus $E^* = E/(1-\nu^2)$; here E is the Young's modulus and ν is the Poisson's ratio. The mechanical behavior of the coating is characterized by the elastic recovery W_e, the ratio H/E^* [7–9,11] and the ratio H^3/E^{*2} which is proportional to a resistance of the material to plastic deformation [12,13]. The plastic deformation is significantly reduced in materials with high hardness H and low Young's modulus E^* due to their enhanced elasticity which occurs only in the case when the material or coating exhibits a high ratio $H/E^* \geq 0.1$; more details are given in references [8,9]. Recently, the validity of this statement was confirmed also for the Zr–Si–O coatings [14]. It means that a low modulus E^* is very desirable as it allows the given load to be distributed over a wider area and to increase the resistance of the coating to cracking.

The measured dependences of H, E^* and W_e of the Zr–Al–O film with a low ratio Zr/Al < 1 and a high Zr/Al > 1 as a function of partial pressure of oxygen p_{O2} are displayed in Fig. 6a and b, respectively. In these figures also the ratio H/E^*, calculated from measured values of H and E^*, is given and intervals p_{O2} corresponding to the metallic (MM), transition mode (TM) and oxide mode (OM) of sputtering are clearly denoted. A comparison of Fig. 6a and b clearly shows that the mechanical properties of the Zr–Al–O film with Zr/Al < 1 and Zr/Al > 1 strongly differ. The Zr–Al–O films with Zr/Al < 1 are softer and less elastic and exhibit a low ratio $H/E^* < 1$ compared to the Zr–Al–O film with Zr/Al > 1. This difference is a consequence of different structure of the film with Zr/Al < 1 and Zr/Al > 1, see Fig. 4, which results in different mechanical behaviors of the Zr–Al–O film with low ratio Zr/Al < 1 and high ratio Zr/Al > 1. Key parameters deciding on the mechanical behavior of the Zr–Al–O film are its elastic recovery W_e and the H/E^* ratio. Recently, it was shown that an enhanced mechanical behavior, particularly the enhanced resistance to cracking, exhibits the hard highly elastic ($W_e \geq 60\%$) films with low effective Young's modulus E^* satisfying the ratio $H/E^* \geq 0.1$ only [8,9]. These requirements, however, do not meet relatively soft ($H \approx 12$ GPa), X-ray amorphous Zr–Al–O films with Zr/Al < 1; these films easily crack. On the other hand, the hard Zr–Al–O film with Zr/Al > 1, $H \approx 18$ to 19 GPa, $H/E^* > 0.1$ and $W_e \geq 60\%$, produced in a wide range of p_{O2} marked in yellow in Fig. 6b, exhibit the enhanced resistance to cracking, see next section.

3.4.1. Resistance to cracking

The resistance of the film to cracking was investigated by bending of the metallic strip coated by the film along a fixed cylinder (∅ = 25 mm). For this test the Zr–Al–O film was deposited on a Mo strip ($80 \times 15 \times 0.1$ mm^3). The formation of cracks in the film during the bending of the film/substrate couple is illustrated in Fig. 7. In this figure the surface morphology of two films after bending are compared: (1) the Zr–Al–O film with a low ratio Zr/Al < 1 and (2) Zr–Al–O film with a high ratio Zr/Al > 1. The main parameters of both films are given in Table 1.

As expected the X-ray amorphous Zr–Al–O film with low ratio Zr/Al < 1 and low values of (i) $W_e \approx 44\%$ and (ii) $H/E^* \approx 0.06$ ratio

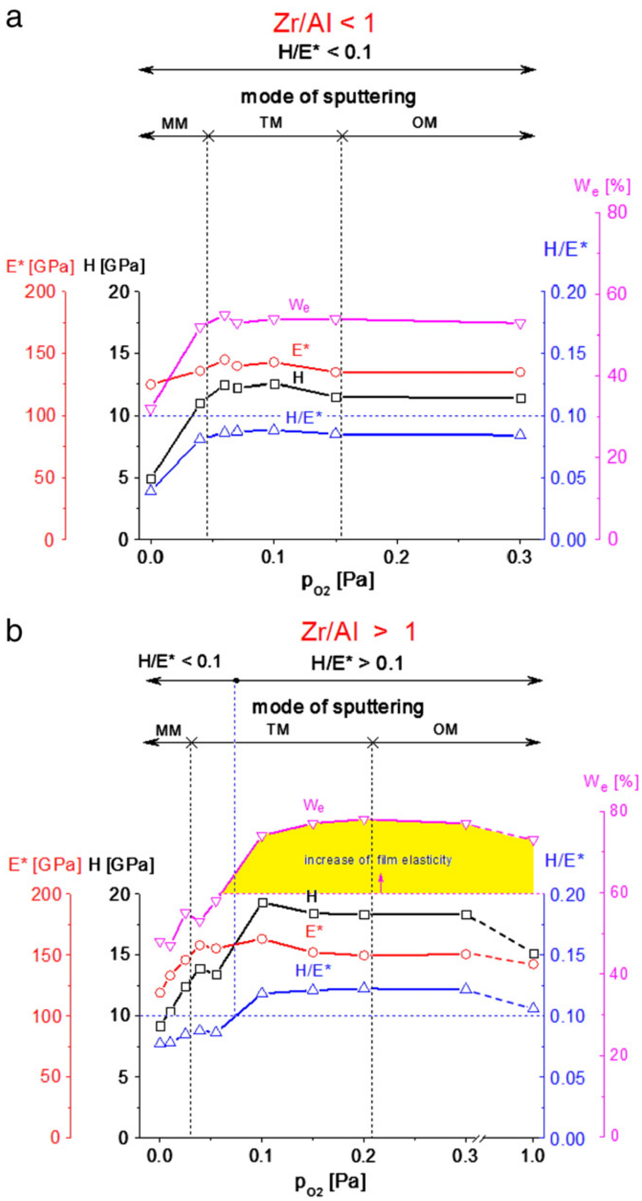

Fig. 6. Hardness H, effective Young's modulus E^*, elastic recovery W_e and H/E^* ratio of the Zr–Al–O films with (a) low Zr/Al < 1 and (b) high Zr/Al > 1 sputtered on Si(100) substrate at $U_s = U_{fl}$, $T_s = 500$ °C, $p_T = 1$ Pa, and $I_{da} = 1$ and 2 A, respectively, as a function of partial pressure of oxygen p_{O2}. MM, TM and OM are the metallic, transition and oxide modes of sputtering, respectively.

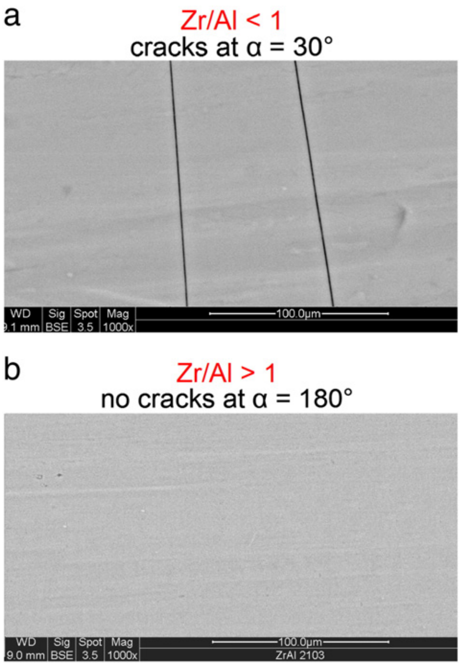

Fig. 7. Surface morphology of (a) the Zr–Al–O film with Zr/Al<1 and (b) the Zr–Al–O film with Zr/Al>1 after bending of the film/substrate couple along the steel cylinder of diameter ∅ = 25 mm to angle α = 30° and 180°, respectively. Photos are images in a back scattering electrons (BSE) mode.

easily cracks already at small bending at $\alpha \approx 30°$. On the other hand, the Zr–Al–O composite film with Zr/Al > 1 and high values of (i) $W_e \approx 75\%$ and (ii) $H/E^* \approx 0.118$ ratio, composed of nanograins embedded in the amorphous matrix, exhibits an enhanced resistance to cracking; no cracks in the film occurred after bending at $\alpha =$ 180° even in thick films up to 5 μm. It is due to the fact that the hard film with $H/E^* > 0.1$, which exhibits a low value of E^* satisfying the high ratio $H/E^* > 0.1$, is highly elastic compared to the film with the low ratio $H/E^* \leq 0.1$, which distributes the applied load over a wider area and thereby strongly increases its resistance to cracking.

The structure of the Zr–Al–O film with a low ratio Zr/Al<1 and a high ratio Zr/Al>1 also strongly differ, see Fig. 8. The structure of the Zr–Al–O film with Zr/Al<1 is X-ray amorphous. On the other hand, the Zr–Al–O film with Zr/Al>1 exhibits a clear t-ZrO_2 (101) preferred crystallographic orientation. It indicates that the mechanical properties of the film and its mechanical behavior, particularly its resistance to cracking, are strongly influenced by the incorporation of nanograins in the amorphous matrix. At present, the optimization of these properties remains, however, an open problem. It is very probable that the optimization of the film properties will depend on the ratio of the amount of the nanocrystalline phase and the amount of the amorphous phase, the separation distance between the nanocrystalline regions, their crystallographic orientations and dimensions. This investigation is now under way in our labs.

Table 1
Thickness h, deposition rate a_D, hardness H, effective Young's modulus E^*, elastic recovery W_e and H/E^* ratio of the Zr–Al–O film with low Zr/Al<1 and high Zr/Al>1 ratio, and the angle α of bending of Mo strip coated with the film used in the assessment of its resistance to cracking.

Zr/Al	h [nm]	a_D [nm/min]	H [GPa]	E^* [GPa]	W_e [%]	H/E^*	α [deg]	Cracks
<1	2200	66	12.3	147	52	0.084	30	Yes
>1	5000	63	17.9	152	75	0.118	up to 180	No

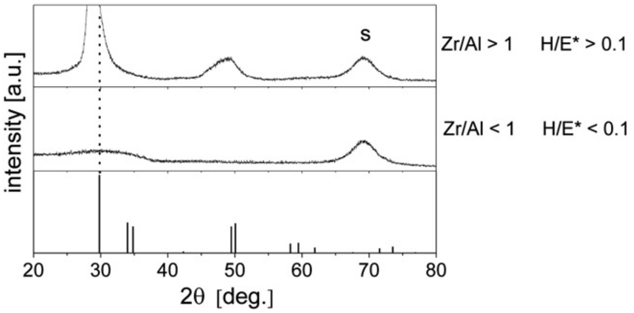

Fig. 8. The XRD patterns of the Zr–Al–O film with (i) Zr/Al<1 and low ratio $H/E^* < 0.1$ and (ii) Zr/Al>1 and high ratio $H/E^* > 0.1$. The surface morphology of these films after bending of the film/Mo strip couple is shown in Fig. 7.

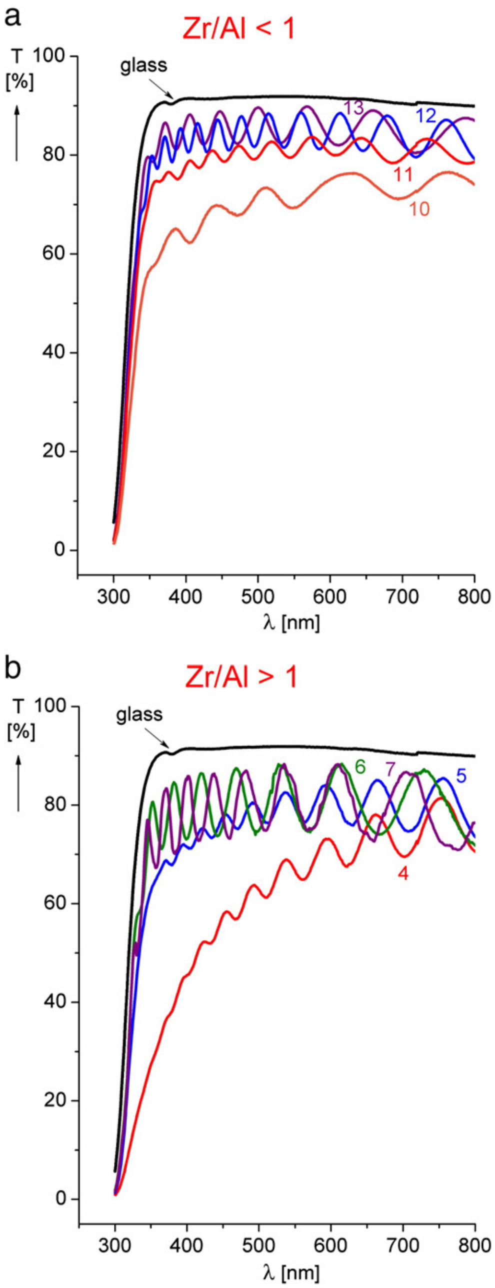

Fig. 9. Transmittance T of the Zr–Al–O films with (a) low Zr/Al<1 and (b) high Zr/Al>1 ratios as a function of wavelength λ of incident electromagnetic wave. Numbers of individual curves correspond to the films with different elemental composition and mechanical properties given in Table 2.

Table 2
Elemental composition, mechanical properties and visual transparency of Zr–Al–O films used for measurements of their transmittance spectra at the wavelength λ of incident electromagnetic waves ranging from 300 to 800 nm.

Film no.	h [nm]	Zr [at.%]	Al [at.%]	O [at.%]	Free Zr* [at.%]	H [GPa]	E* [GPa]	W_e [%]	H/E*	Visual transparency
Zr/Al>1										
4	1600	24	12	64	1	13.4	155	58	0.086	Semi-transparent
5	1600	23	11	66	No	19.3	163	74	0.118	Transparent
6	1100	24	10	66	No	18.4	152	77	0.121	Transparent
7	1100	23	10	67	No	18.3	150	78	0.122	Transparent
Zr/Al<1										
10	3100	10	30	60	2	12.5	145	55	0.086	Semi-transparent
11	1600	8	30	62	No	12.2	140	53	0.087	Transparent
12	1600	9	29	62	No	12.6	143	54	0.088	Transparent
13	2200	10	28	62	no	11.5	135	54	0.085	Transparent

3.5. Optical properties

The transparency T was measured for both kinds of Zr–Al–O films with a low Zr/Al<1 and a high Zr/Al>1 ratio, see Fig. 9. The transparency T of the Zr–Al–O film is determined by the amount of free Zr and Al atoms in the film. It means that the transparency T of the film strongly depends on the partial pressure of oxygen p_{O2} and the discharge current I_{da} used in its sputtering. Both parameters p_{O2} and I_{da} determine the mode of sputtering and the excess amounts of free Zr and Al atoms that occur in the transition mode (TM) of sputtering close to the metallic mode (MM) of sputtering where there is a deficiency of the atomic oxygen to form both stoichiometric Al_2O_3 and ZrO_2 oxides. Free Zr atoms will be present in the film in the case when the amount of atomic oxygen will be higher than that necessary to form the stoichiometric Al_2O_3 oxide with all Al atoms and insufficient to form the stoichiometric ZrO_2 oxide with all Zr atoms, see Table 2. It is the case of the Zr–Al–O films denoted as the film no.4 and the film no.10. The accuracy of the determination of the free Zr atoms is limited by the accuracy of measurement of the elemental composition in the film and values of the free Zr atoms in the film given in Table 2 are therefore of informative value only. The mechanical properties and the ratio H/E* of tested Zr–Al–O films with low Zr/Al<1 and high Zr/Al>1 ratio and the information about their visual transparency are also given in Table 2.

The visual transparency of the Zr–Al–O film decreases with increasing number of free Zr atoms. The films no. 4 and 10 are semi-transparent. A lower transparency of the film no.4 and slower increase of T with increasing λ compared with the film no.10 is probably due to a scattering of the light at nanocystalline regions incorporated in the amorphous Al_2O_3 matrix.

4. Conclusions

The main results of the investigation of the Zr–Al–O films reactively sputtered using dual magnetrons which are reported in this paper can be summarized as follows:

1. The addition of Al in ZrO_2 strongly influences the structure and properties of Zr–Al–O films.
2. The content of Al in the Zr–Al–O film is a crucial parameter which decides on its properties. The Zr–Al–O films with Zr/Al<1 are soft films with X-ray amorphous structure, low elastic recovery (W_e<60%) and H/E*<0.1. On the other hand, the Zr–Al–O films with Zr/Al>1 are highly elastic, crystalline hard films with H/E*>0.1.
3. The hard Zr–Al–O films with Zr/Al>1, low effective Young's modulus E* satisfying the ratio H/E*>0.1 and W_e>60% exhibit strongly enhanced resistance to cracking. The enhanced resistance to cracking was found also in thick films with the thickness, h = 5000 nm, which was the maximum thickness of sputtered films.
4. The Zr–Al–O nanocomposite films with enhanced resistance to cracking are composed of nanograins incorporated in the amorphous Al_2O_3 matrix.
5. The X-ray amorphous Zr–Al–O films are very brittle and easily crack.

Acknowledgments

This work was supported in part by the Grant Agency of the Czech Republic under project no. P 108/12/0393 and by the European Regional Development Fund under project NTIS, CZ.1.05/1.1.00/02.0090.

References

[1] Y.E. Hong, Y.S. Kim, K. Do, D. Lee, D.H. Ko, J. Vac. Sci. Technol. A23 (5) (2005) 1413.
[2] S. Veprek, S. Reiprich, Thin Solid Films 265 (1995) 64.
[3] J. Musil, J. Vlček, P. Zeman, Adv. Appl. Ceram. 107 (3) (2008) 148.
[4] J.W. Yeh, S.K. Chen, S.J. Lin, J.Y. Gan, T.S. Chin, T.T. Shun, C.H. Tsau, S.Y. Chang, Adv. Eng. Mater. 6 (2004) 299.
[5] C.W. Tsai, S.W. Lai, K.H. Cheng, M.H. Tsai, A. Davidson, J.W. Yeh, C.H. Tsau, Thin Solid Films 520 (2012) 2613.
[6] K.H. Cheng, C.H. Weng, C.H. Lai, S.J. Lin, Thin Solid Films 517 (2009) 4989.
[7] J. Blazek, J. Musil, P. Stupka, R. Cerstvy, J. Houska, Appl. Surf. Sci. 258 (2011) 1762.
[8] J. Musil, J. Sklenka, R. Cerstvy, Surf. Coat. Technol. 206 (2012) 2105.
[9] J. Musil, M. Meissner, R. Jilek, T. Tolg, R. Cerstvy, Surf. Coat. Technol. 206 (2012) 4230.
[10] Smithells Metal Reference Book, E.A. Brandes (Ed.), in association with Fulmer Research Institute, 6th edition Butterworth, Heinemann, 1992, Table 8.8c, pp. 8-25.
[11] A. Leyland, A. Mathews, Wear 246 (2000) 1.
[12] T.Y. Tsui, G.M. Pharr, W.C. Oliver, C.S. Bhatia, R.L. White, S. Anders, A. Anders, I.G. Brown, Mater. Res. Soc. Symp. Proc. 383 (1995) 447.
[13] J. Musil, J. Jirout, Surf. Coat. Technol. 201 (2007) 5148.
[14] J. Musil, J. Sklenka, R. Cerstvy, Highly elastic Zr–Si–O nanocomposite films with enhanced resistance to cracking, (2012) unpublished results.

3.4 Část D

Fotokatalytické vrstvy TiO_2

3.4.1 D-I: Nanostructure of photocatalytic TiO_2 films sputtered at temperatures below 200 °C

Available online at www.sciencedirect.com

ScienceDirect

Applied Surface Science 254 (2008) 3793–3800

applied surface science

www.elsevier.com/locate/apsusc

Nanostructure of photocatalytic TiO_2 films sputtered at temperatures below 200 °C

J. Šícha, J. Musil *, M. Meissner, R. Čerstvý

Department of Physics, Faculty of Applied Sciences, University of West Bohemia, Univerzitní 22, 306 14 Plzeň, Czech Republic

Received 19 October 2007; received in revised form 30 November 2007; accepted 1 December 2007
Available online 15 December 2007

Abstract

The article reports on correlations between the process parameters of reactive pulsed dc magnetron sputtering, physical properties and the photocatalytic activity (PCA) of TiO_2 films sputtered at substrate surface temperature $T_{surf} \leq 180$ °C. Films were deposited using a dual magnetron system equipped with Ti (Ø50 mm) targets in Ar + O_2 atmosphere in oxide mode of sputtering. The TiO_2 films with highly photoactive anatase phase were prepared without a post-deposition thermal annealing. The decomposition rate of the acid orange 7 (AO7) solution during the photoactivation of the TiO_2 film with UV light was used for characterization of the film PCA. It was found that (i) the partial pressure of oxygen p_{O_2} and the total sputtering gas pressure p_T are the key deposition parameters influencing the TiO_2 film phase composition that directly affects its PCA, (ii) the structure of sputtered TiO_2 films varies along the growth direction from the film/substrate interface to the film surface, (iii) ~500 nm thick anatase TiO_2 films with high PCA were prepared and (iv) the structure of sputtered TiO_2 films is not affected by the substrate surface temperature T_{surf} when $T_{surf} < 180$ °C. The interruption of the sputtering process and deposition in long (tens of minutes) pulses alternating with cooling pauses has no effect on the structure and the PCA of TiO_2 films and results in a decrease of maximum value of T_{surf} necessary for the creation of nanocrystalline nc-TiO_2 film. It was demonstrated that crystalline TiO_2 films with high PCA can be sputtered at $T_{surf} \leq 130$ °C. Based on obtained results a phase zone model of TiO_2 films was developed.

Keywords: TiO_2 film; Structure; Anatase; UV induced photocatalysis; Low-temperature sputtering; Dual magnetron

1. Introduction

In recent years, a great attention has been devoted to the titanium dioxide (TiO_2) due to its excellent chemical stability, high refractive index, nontoxicity, and good mechanical hardness. Besides, the TiO_2 films can exhibit excellent photocatalytic and superhydrophilic properties [1,2] after UV light irradiation. The TiO_2 exists in three different crystalline forms (anatase, rutile and brookit) [3], among which the anatase phase is referred to be the most photoactive phase [4]. The photoactivation of TiO_2 by the UV light irradiation results in the formation of electron-hole pair that diffuses to the surface. A favorable chemical potential of the electron-hole pair enables to form highly reactive hydroxyl radicals ($^{\bullet}OH$) on the surface of TiO_2 material in reactions with the water molecules, see Fig. 1. Here, a comparison of the potential of e-h pair versus standard hydrogen electrode (SHE) and basic reactions are given. The hydroxyl radicals ($^{\bullet}OH$) very quickly oxidize and decompose a wide range of organic pollutants. Therefore, the photoactivity of TiO_2 films can be utilized in many applications, such as self-cleaning, antifogging, antibacterial and self-sterilization processes and in removal of organic pollutants from surfaces, dissociation of water, and in production of hydrogen [5].

There are several drawbacks that limit a wider utilization of the TiO_2 photocatalyst. One of very difficult problems is the formation of photoactive TiO_2 coatings on thermally sensitive substrates, e.g., polymer foils or polycarbonate, at $T_{surf} < 200$ °C. Among many deposition methods [7–14], the magnetron sputtering is very promising one for the large-area deposition of thin, high quality, photoactive, crystalline anatase TiO_2 films at low values of $T_{surf} \leq 200$ °C [4,7,13–16]. However, the deposition of crystalline photoactive TiO_2 films without the substrate heating or a post-deposition thermal annealing has not been fully mastered yet [12–18].

---

* Corresponding author. Tel.: +420 37763 2200; fax: +420 37763 2202.
E-mail address: musil@kfy.zcu.cz (J. Musil).

0169-4332/$ – see front matter © 2007 Elsevier B.V. All rights reserved.
doi:10.1016/j.apsusc.2007.12.003

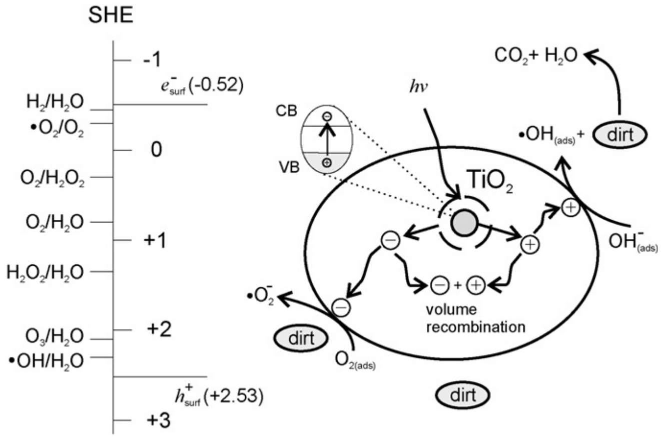

Fig. 1. The principle of photocatalytic processes and formation of highly reactive radicals on the surface of TiO_2 film and electron-hole potential related to standard hydrogen electrode (SHE) [5,6].

Recently, it has been shown, that the magnetron sputtering of crystalline TiO_2 films with anatase structure at low values of T_{surf} and without the high temperature post-deposition annealing is possible only in the oxide mode of sputtering [13,14,19]. In the transition mode of sputtering, when significantly higher deposition rates a_D of films compared to those of films produced in the oxide mode can be achieved [20,21], (i) a strong suppression of highly photoactive anatase phase in the film takes place and (ii) amorphous films or films with rutile phase exhibiting a weak PCA are formed. The formation of TiO_2 films with anatase phase and high PCA in the transition mode of sputtering is possible only at $T_s > 200$ °C or in the case when TiO_2 film sputtered at $T_s < 200$ °C is after sputtering thermally annealed at $T_a > 200$ °C, i.e. the two-step process is used [13–15,18].

The main aim of this study is (i) to find optimum conditions of sputtering of TiO_2 films in oxide mode, which ensures that TiO_2 films with anatase phase and high PCA will be formed at $T_{surf} \leq 180$ °C and (ii) to produce thin (<1000 nm) crystalline TiO_2 films with high PCA. Correlations between the deposition parameters and the structure of TiO_2 films sputtered at high repetition frequency $f_r = 350$ kHz [22] are discussed in detail.

2. Experimental

A pulsed dual magnetron in a closed magnetic field configuration equipped with Ti (99.5) targets (Ø50 mm) was used for a reactive sputtering of transparent TiO_2 films in the $Ar + O_2$ mixture [23]. The magnetrons were supplied by a pulsed Advanced Energy Pinnacle Plus + 5 kW power supply unit operating in asymmetric bipolar mode at the repetition frequency $f_r = 350$ kHz with duty cycle $\tau/T = 0.5$ and the average pulse magnetron current I_{da} kept at 3A and pulse power densities W_{da} ranging from 60 to 70 W cm^{-2} according to deposition conditions used; W_{da} was averaged over the whole target area. The high repetition frequency of pulses $f_r = 350$ kHz ensured a strong improvement of (i) the efficiency of deposition process and (ii) the PCA of sputtered TiO_2 films [22]. Films were sputtered in the oxide mode on unheated glass (25 mm × 25 mm × 1 mm) substrates located at the substrate to target distance $d_{s-t} = 100$ mm with the deposition rate $a_D \approx 10$ nm/min. The substrate surface temperature T_{surf} was measured by thermostrips (Kager GmbH, Germany). T_{surf} was lower than $T_{surf} \leq 180$ °C in all experiments. More details on the measurement of T_{surf} are given in Ref. [13]. A contamination of TiO_2 films by the Na^+ ions diffusing from the soda-lime glass and deteriorating their PCA recently observed in [24] can be neglected in our case, due to the low process temperature. This fact was verified on TiO_2 films deposited on Na^+ free Si substrates.

The phase composition of films was determined by the X-ray diffraction (XRD) analysis using a PANalytical X'Pert PRO diffractometer working in Bragg-Brentano geometry with Cu Kα (40 kV, 40 mA) radiation. The structure development along the growth direction was characterized by irradiation of film at the glancing incidence angles α ranging from 0.5° to 1.5°. The thickness of films was measured by a stylus profilometer DEKTAK 8 with the resolution of 1 nm. The surface roughness R_a was measured by an atomic force microscopy (AFM) in non-contact mode using an AFM-Metris-2000. The measurements were performed in ambient atmosphere at room temperature.

The PCA of TiO_2 film was determined from a decomposition of acid orange 7 (AO7) organic dye solution (Fluka Chemie GmbH). This dye exhibits a very good stability against UV light irradiation [25]. The TiO_2 films were (i) immersed in the AO7 solution with initial concentration $c_0 = 0.01$ mmol/l in the distilled water (volume $V = 10$ ml) and (ii) irradiated by the UV light (PHILIPS TL-DK 30 W/05, $W_{ir} = 0.9$ mW/cm^{-2} at $\lambda = 365$ nm) for 5 h. The changes in the dye concentration were determined every hour by measuring of the magnitude of the dye absorption at $\lambda = 485$ nm (absorption maximum for AO7) calibrated on the dye concentration by spectrometer SPECORD M400 (Carl Zeis Jena). The decomposition rate constant k_r, that characterize the PCA, is defined by the following equation [26]:

$$c(t_{ir}) = c_0 e^{-k_r t_{ir}},$$

where c_0 and $c(t_{ir})$ are the initial concentration of the dye and its concentration after UV light irradiation for a given time t_{ir}, respectively. A plot of $\ln(c_0/c)$ as a function of time t_{ir} represents a straight line with slope of k_r. More details on the decomposition of AO7 solution and the measurement of the PCA of TiO_2 films are given in Refs. [25–27].

3. Results and discussion

Recently, it was reported that TiO_2 films with dominant anatase phase and high PCA can be created at $T_{surf} \leq 180$ °C but only in the oxide mode of sputtering [13,14,19]. However, conditions under which such films can be created are not mastered yet. Therefore, this article is devoted to an investigation of the correlations between the deposition parameters and the structure and the PCA of TiO_2 films created in the oxide mode. There are three main parameters which strongly influences the structure and the PCA of TiO_2 films: (i) total pressure of sputtering gas p_T which controls the

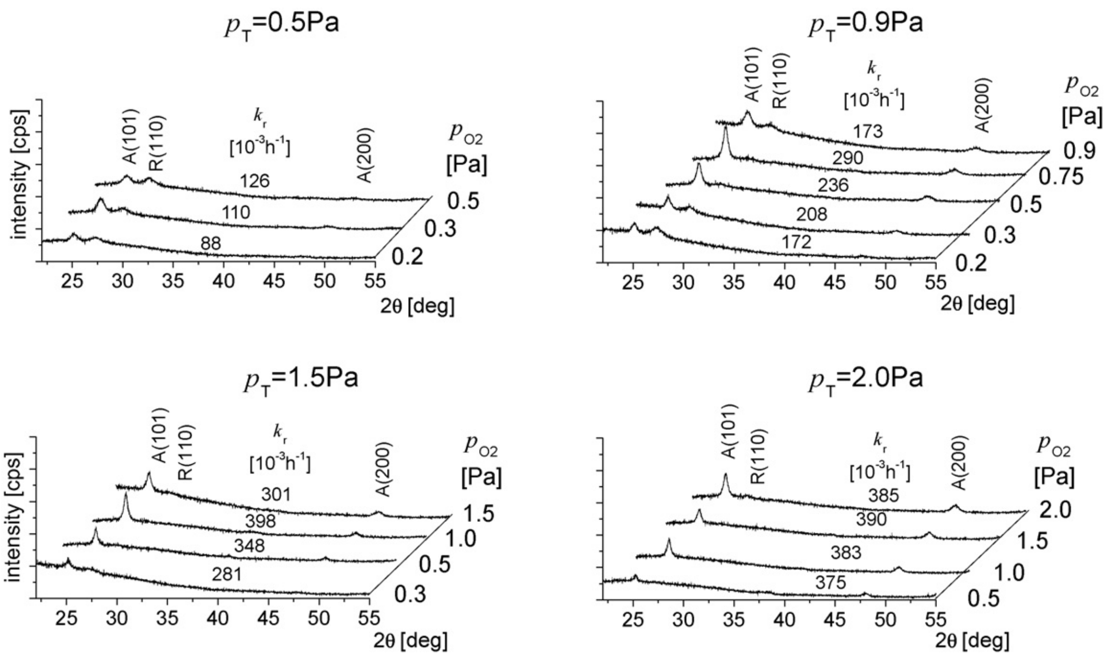

Fig. 2. Evolution of XRD patterns from 500 nm thick TiO_2 films sputtered with $a_D \approx 10$ nm/min in the oxide mode of sputtering at $T_{surf} \leq 180$ °C, with increasing p_{O_2} at four values of $p_T = 0.5$, 0.9, 1.5 and 2 Pa.

energy of particles incident on the growing film through control of their mean free path [18], (ii) partial pressure of oxygen p_{O_2} which influences plasmo-chemical processes and (iii) the film thickness h which determines the total energy delivered to the film during its growth. The production of TiO_2 films with anatase phase and high PCA at different combinations of p_T, p_{O_2} and h is discussed in detail.

3.1. Effect of p_T and p_{O_2}

3.1.1. Structure

The structure of sputtered 500 nm thick TiO_2 films strongly depends on both p_{O_2} and p_T, see Fig. 2. From this figure it is seen that (i) TiO_2 films are composed of a mixture of R(1 1 0) + A(1 0 1) phases and the crystallinity of anatase phase improves with increasing p_{O_2} if they are sputtered at $p_T \geq 0.5$ Pa, (ii) the content of rutile phase in film decreases with increasing p_T and (iii) TiO_2 films sputtered at high total pressures $p_T \geq 1.5$ Pa exhibit already a pure anatase phase. The rutile is a high temperature TiO_2 phase and therefore higher activation energy is needed for its formation in comparison with the anatase phase. The deterioration of the crystallinity of the rutile phase with increasing p_T is thus caused by higher losses of particles energy in collisions.

3.1.2. Photocatalytic activity (PCA)

The PCA of TiO_2 film is characterized by the decomposition rate constant k_r of a solution of the AO7. The partial pressure of oxygen p_{O_2} and the total working pressure p_T also strongly influence the PCA of sputtered TiO_2 films. The typical evolution of the PCA for 500 nm TiO_2 films with increasing p_{O_2}/p_T ratio is displayed in Fig. 3. The PCA of TiO_2 films improves with increasing p_T. The improvement of the PCA correlates well with the decrease of (1 1 0) rutile XRD peak intensity and the increase of (1 0 1) anatase XRD peak, see Fig. 4. The effect of a surface morphology of TiO_2 film on the PCA can be neglected because all films sputtered at $p_T = 0.9$ and different p_{O_2} exhibited similar surface roughness $R_a = 6$ nm. Slight increase of surface roughness was observed with increasing p_T. The highest PCA is observed for pure anatase films and rutile phase should be suppressed in the films in order to obtain high photoactivity.

Obtained results are summarized in a schematic diagram, see Fig. 5. This diagram illustrates the evolution of structure of TiO_2 films sputtered in oxide mode and their PCA as function of p_T and the ratio p_{O_2}/p_T. The diagram is valid for thick (≥500 nm) TiO_2 films sputtered at low temperatures $T_{surf} \leq 180$ °C. Here, it is necessary to note that properties

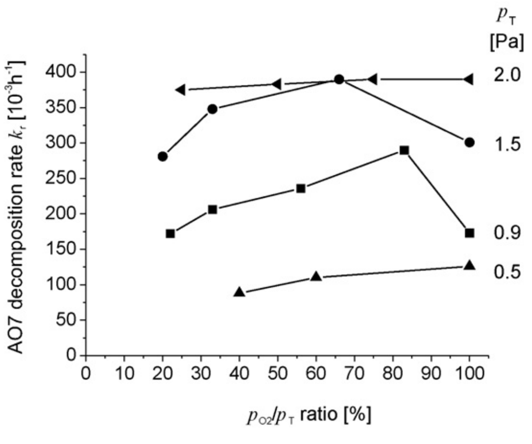

Fig. 3. The PCA of 500 nm thick TiO_2 films sputtered in the oxide mode of sputtering at $T_{surf} \leq 180$ °C as a function of ratio p_{O_2}/p_T for four values of $p_T = 0.5$, 0.9, 1.5 and 2 Pa.

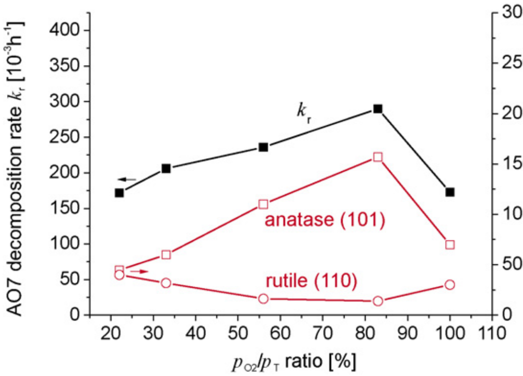

Fig. 4. Evolution of anatase and rutile phase and PCA characterized by the acid orange 7 decomposition rate constant k_r for 500 nm thick TiO_2 films sputtered at $p_T = 0.9$ Pa with increasing p_{O_2}/p_T ratio.

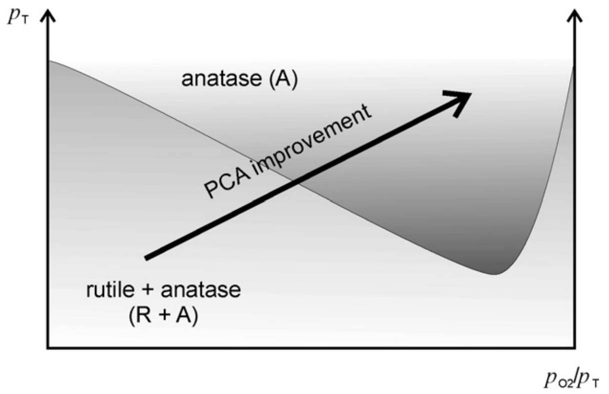

Fig. 5. Schematic illustration of evolution of phase composition and PCA of ~500 nm thick TiO_2 films sputtered on glass substrates at $T_{surf} \approx 180$ °C in (p_{O_2}/p_T, p_T) coordinate system.

of thin (<500 nm) TiO_2 films strongly differ from those of thick (≥500 nm) TiO_2 films.

3.2. *Effect of film thickness*

The structure of TiO_2 film strongly depends on its thickness *h* [19]. To investigate the effect of film thickness *h* on the structure and the PCA in detail, the TiO_2 films with *h* ranging from 100 to 3000 nm were prepared. The development of structure of TiO_2 films, sputtered in the oxide mode at four combinations of p_{O_2} and p_T (i) $p_{O_2} = 0.3$ Pa and three values of $p_T = 0.75$, 0.9 and 1.5 Pa and (ii) $p_{O_2} = 1$ Pa and $p_T = 2.0$ Pa, with increasing *h* is shown in Fig. 6.

The same trend in development of film structure with increasing *h* is observed for all sputtered TiO_2 films. The increase of *h* leads to the improvement of film crystallinity and to a gradual conversion of amorphous films ($h < h_{min} \approx 100$ nm) at first, to films with a mixture of rutile and anatase phase and then to films ($h > 200$ nm) with dominant anatase phase. Further increase in *h* leads to next improvement of crystallinity of anatase phase in films with $h > 500$ nm. Here, the h_{min} denotes the thickness of amorphous interlayer on the substrate/film interface and the pure anatase phase is observed at $h > h_{R+A} \geq h_{min}$. No rutile phase was detected even in very thin films sputtered at $p_T = 2.0$ Pa and $p_{O_2} = 1.0$ Pa.

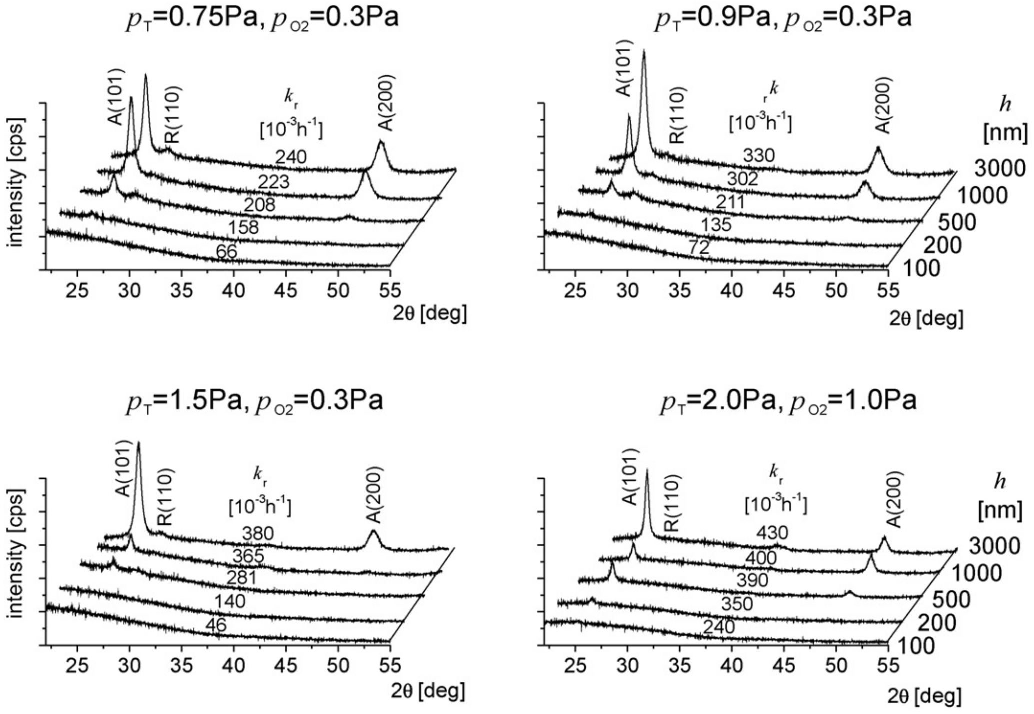

Fig. 6. Development of XRD patterns from TiO_2 films, sputtered in the oxide mode at $a_D \approx 10$ nm/min and $T_{surf} \approx 180$ °C, with increasing thickness *h* for different combinations of p_T and p_{O_2}.

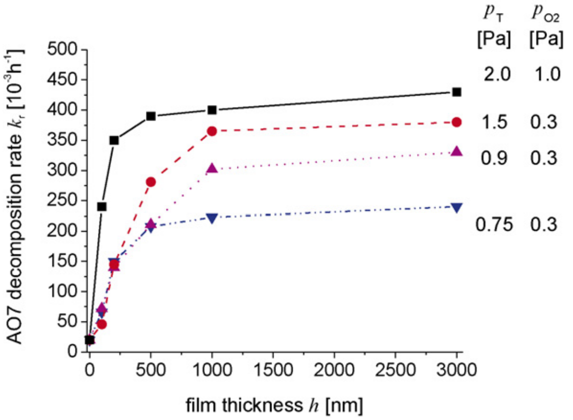

Fig. 7. PCA of TiO_2 films sputtered in the oxide mode of sputtering at $T_{surf} \approx 180\ ^\circ C$ and different conditions of p_T and p_{O_2} as a function of h.

The effect of film thickness h on the PCA of TiO_2 films is summarized in Fig. 7. From this figure is seen that the PCA improves with increasing h and p_T. The improvement of the PCA with increasing h is due to (i) improvement of crystallinity of anatase phase, (ii) increase of the volume of surface layer with anatase phase and (iii) increase of film surface roughness that positively influences the PCA due to the increase of area of the film surface [19]. The saturation of the PCA with increasing h takes place for all TiO_2 films, but at different h according to a combination of deposition conditions. The films sputtered at $p_T = 2.0$ Pa exhibit very fast saturation of the PCA at $h \approx 500$ nm and also the highest values of k_r. These TiO_2 films with $h > 500$ nm exhibit only a slight improvement of the PCA with increasing h. This result indicates that the formation of charge carriers and their transport to the film surface, that influences the PCA, goes on in ~500 nm layer under the film surface only. This means that thickness of several hundreds nm is sufficient to achieve high values of the PCA for TiO_2 films sputtered at $T_{surf} = 180\ ^\circ C$. This finding agrees well with results obtained by Eufinger et al. [16], who reported that the saturation of the PCA exhibit the films with $h = 300$–350 nm. The shift of the saturation of the PCA to higher h in our study can be explained by changes in phase composition of the film during its low-temperature growth.

3.2.1. Structure development along growth direction

For thick (≥ 1000 nm) TiO_2 films it is important to know the structure distribution along the film thickness, i.e. along direction of the film growth. This information can give XRD measurement performed at small glancing angles. The XRD at different glancing angles α makes it possible to determine phases in the TiO_2 film in different distances from the film surface. The angle α was varied in the interval from 0.5° to 1.5°. Using this method structure of 1000 nm thick TiO_2 film was investigated in detail. Results of measurements are given in Fig. 8. The measurement performed at $\alpha = 0.5^\circ$ gives information on the film structure in the subsurface layer (to the depth ~400 nm from the surface). On the contrary, XRD patterns measured at $\alpha = 1.5^\circ$ gives information from the whole volume of 1000 nm thick film; amorphous background from the glass substrate is also detected at $\alpha = 1.5^\circ$. The intensity of rutile peak increases with increasing α. It means that the rutile phase is in a region near to the film/substrate interface and its amount in the film surface region decreases with increasing h depending on the p_T. The anatase phase dominates all the analyzed films.

3.2.2. Phase zone model for TiO_2 films

The results displayed in Fig. 8 clearly show that the growth of TiO_2 films on glass substrate can be divided into four zones, see Fig. 9. Here, a schematic illustration of the structure evolution in the TiO_2 films sputtered at $T_{surf} \approx 180\ ^\circ C$ is shown. The structure evolution is represented by four zones.

1. Zone 1 represents the amorphous a-TiO_2 films. Thin a-TiO_2 films with $h \leq h_{min}(T_{surf}) \leq 500$ nm are formed at $p_T \leq p_1$. Thicker a-TiO_2 films are created at $p_T > p_1$ and the thickness h of these films increases with increasing p because the energy E delivered to the growing film decreases due to the particles collisions and is insufficient to stimulate the film crystallization [7].

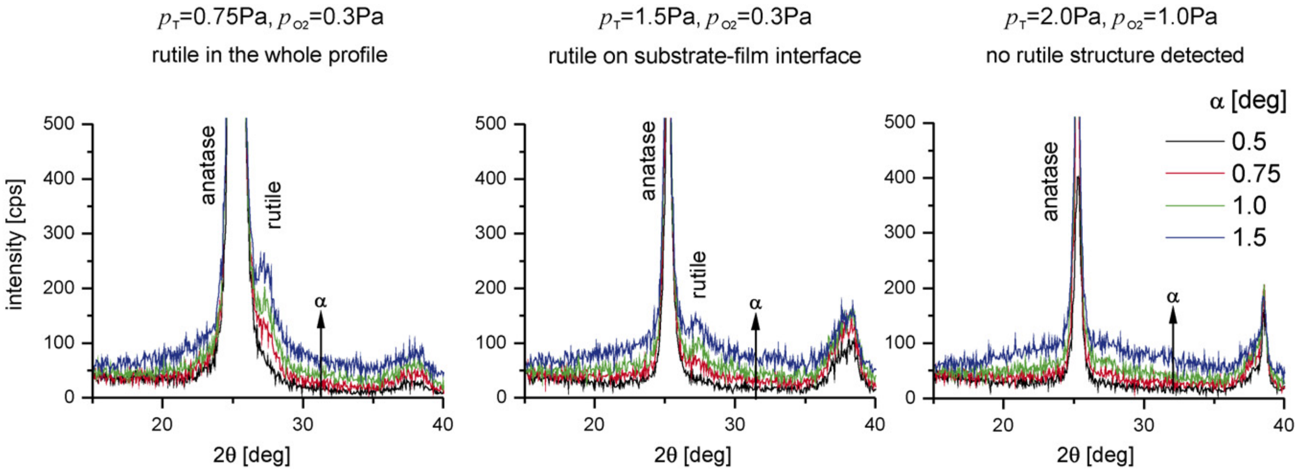

Fig. 8. XRD patterns from 1000 nm thick TiO_2 films measured at glancing angle α ranging from 0.5° to 1.5°.

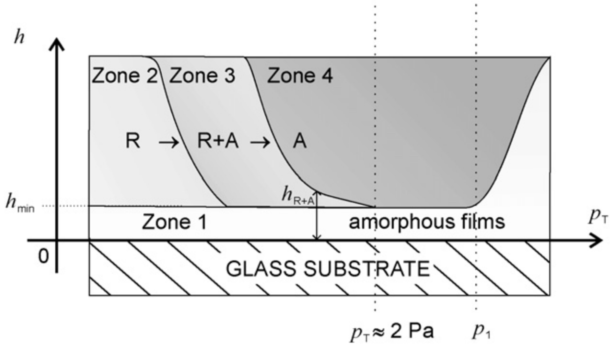

Fig. 9. Schematic illustration of phase zone mode of TiO_2 films sputtered in oxide mode at low substrate surface temperature $T_{surf} \approx 180$ °C on glass substrate.

2. Zone 2 represents the crystalline c-TiO_2 film with rutile phase [7,19]. These films are formed at low values of p_T and p_{O_2} when the energy E delivered to growing film by incident and condensing atoms increases and is sufficient for the crystallization of the film. The energy E increases with decreasing p_T in consequence of a decrease of collisions between particles with decreasing p_T. Also changes of the chemical processes at low p_{O_2} contribute to the formation of the rutile phase.
3. Zone 3 represents the crystalline c-TiO_2 R + A films. The crystalline phase gradually changes from R phase through a mixture R + A phases to A phase with increasing p_T; here R and A denote the rutile and anatase phase, respectively. The amount of A phase in the mixture R + A increases with increasing h at p_T = const and thus the thickness of film region composed of R + A phases h_{R+A} decreases with increasing p_T up to ~2 Pa.
4. Zone 4 represents the crystalline c-TiO_2 films with pure A phase. The thickness h of these films decreases if sputtered at $p_T \geq p_1$ because the energy of condensing particles decreases with increasing p_T and more time (greater h) is needed to deliver to the growing film sufficient amount of energy necessary to stimulate the crystallization of A phase, i.e. h_{min} increases; p_1 is defined as the pressure at which the energy of particles decreases due to the collisions to a value insufficient for the film crystallization. c-TiO_2 films with pure A phase produced in the zone 4 at $p_T \geq 2$ Pa grow directly from amorphous phase.

From Fig. 9 it is clearly seen that there is a certain interval of pressures ranging from ~2 Pa to p_1 in which c-TiO_2 films with pure A phase and minimum thickness h to be produced. ~500 nm thin TiO_2 films with high PCA are produced in this interval. Moreover, the complete suppression of the rutile phase in films sputtered at $p_T \geq 2.0$ Pa and the growth of anatase phase from the amorphous film/substrate interface enables the formation of very thin ~100 nm TiO_2 films with a good PCA, see Fig. 6.

3.3. Effect of substrate surface temperature

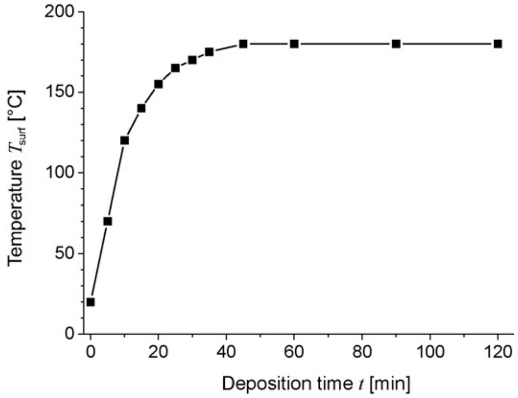

Fig. 10. The evolution of substrate surface temperature T_{surf} during sputtering of TiO_2 film at $p_T = 0.9$ Pa and $p_{O_2} = 0.3$ Pa with increasing deposition time t.

The evolution of substrate surface temperature T_{surf} during the deposition of TiO_2 film with mixed anatase + rutile phase sputtered at $p_T = 0.9$ and $p_{O_2} = 0.3$ Pa is displayed in Fig. 10. This figure shows that T_{surf} increases with increasing t and a maximum value $T_{surf} = 180$ °C is achieved only 40 min after beginning of a continuous deposition of the film. In this case, in spite of no intentional heating, the T_{surf} rises significantly from the room temperature due to the substrate heating during the deposition process. For more details see Ref. [13].

3.3.1. Structure evolution along film thickness

To understand the effect of increase of T_{surf} during deposition on film structure three TiO_2 films with the same thickness $h = 1000$ nm were prepared under the following conditions:

1. TiO_2 film was sputtered *continuously* without interruption; T_{surf} increases with t up to $T_{surf} = 180$ °C as shown in Fig. 10.
2. TiO_2 film was sputtered *with an interruption* every $t = 33$ min (it corresponds to 330 nm thick film) followed by pause 60 min (cooling) at a lower final temperature $T_{surf} = 170$ °C.
3. TiO_2 film was sputtered *with an interruption* every $t = 14$ min (it corresponds to 140 nm thick film) followed by a pause 60 min (cooling) at still lower final temperature $T_{surf} = 130$ °C.

The XRD structure of 1000 nm thick TiO_2 films and those after first interruption is displayed in Fig. 11. From this figure it is clearly seen that (i) all three 1000 nm thick films exhibit almost the same, well developed A(1 0 1) structure independently on the value of T_{surf}, (ii) 330 nm thick film deposited for 33 min is poorly crystalline and exhibits a mixture of A + R phases with very low intensity of R phase and (iii) 140 nm thick film deposited for 14 min is almost X-ray amorphous.

This experiment indicates that the crystallization of film is induced mainly by the energy E delivered to it during its growth by bombarding and condensing particles, not by T_{surf} which is too low to stimulate the crystallization. Therefore, the structure of 1000 nm thick TiO_2 film is the same for all three films and does not depend on the evolution of T_{surf} during the deposition process and even on its final value ranging from ~130 to ~180 °C. This means that c-TiO_2 films with anatase phase can

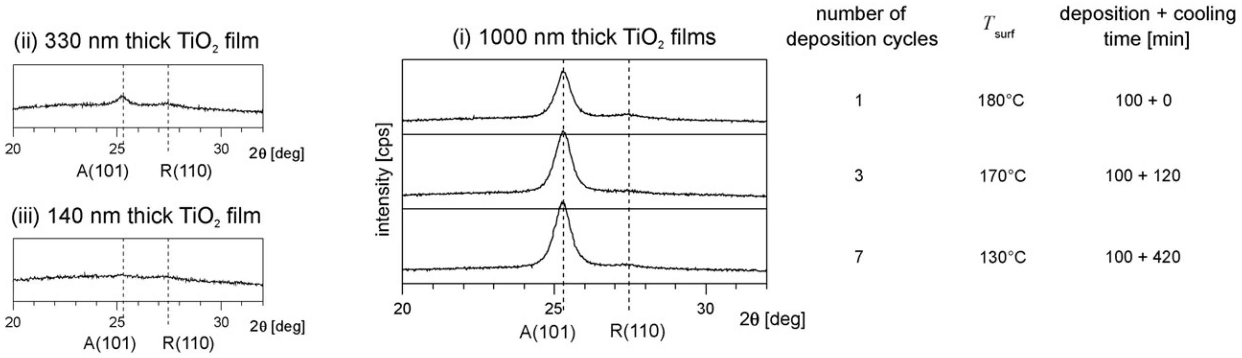

Fig. 11. The effect of deposition interruption on XRD structure of 1000 nm thick TiO_2 films sputtered (1) continuously without interruption and T_{surf} = 180 °C, (2) with interruption every t = 33 min (three cycles × 330 nm) and T_{surf} = 170 °C and (3) with interruption every t = 14 min (seven cycles × 140 nm) and T_{surf} = 130 °C and under the same conditions at p_T = 0.9 Pa and p_{O_2} = 0.3 Pa.

be created if sufficient amount of E is delivered to the growing film independently on the T_{surf} (for $T_{surf} \leq 180$ °C).

Since the maximum substrate surface temperature T_{surf} does not affect the TiO_2 film properties up to ~180 °C crystalline c-TiO_2 films with anatase phase and high PCA can be sputtered at T_{surf} less than 130 °C by a simple interruption of the deposition process.

3.4. Comparison of PCA of TiO_2 films prepared by different methods

As shown above, ~500 nm thick, photoactive TiO_2 films with anatase phase and high PCA can be sputtered at p_T = 2.0 Pa, p_{O_2} = 1.0 Pa and $T_{surf} \approx 180$ °C. The PCA of these films is compared with that of (i) Pilkington Active^{TM} and (ii) Saint-Gobain Bioclean^{TM} ~15–25 nm thin TiO_2 coatings produced at $T > 600$ °C by a CVD process for self-cleaning applications [28–30], see Fig. 12. The PCA of all films was measured in our labs using the same analyzing system. This comparison shows that the reactive pulsed dc dual magnetron sputtering process is suitable for the low-T deposition of TiO_2 films with high PCA on thermally sensitive substrates.

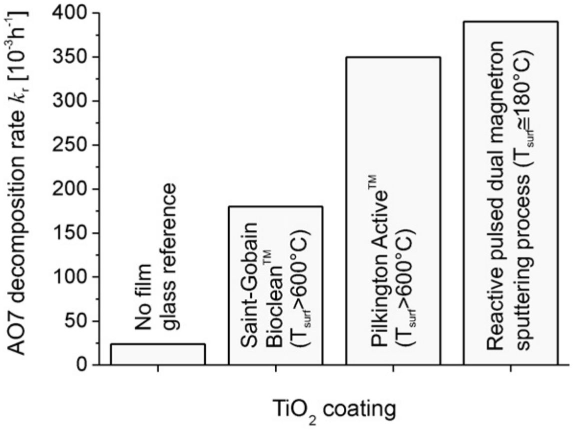

Fig. 12. Comparison of the PCA characterized by the AO7 photodegradation rate constant k_r of (i) 500 nm thick TiO_2 film reactively sputtered using pulsed dc dual magnetron at p_T = 2.0 Pa, p_{O_2} = 1.0 Pa and T_{surf} = 180 °C, (ii) Pilkington Active^{TM} [28] and (iii) SGG Bioclean^{TM} [29] thin (15–25 nm) TiO_2 coatings prepared at $T > 600$ °C by a CVD process.

4. Conclusions

Experiments described in this article show that TiO_2 films with high PCA can be created by a low-temperature reactive sputtering using pulsed dc dual magnetron at the substrate surface temperature $T_{surf} \leq 180$ °C. Main issues of our investigation can be summarized as follows.

1. The partial pressure of oxygen p_{O_2} and the total pressure of sputtering gas $p_T = p_{Ar} + p_{O_2}$ are key deposition parameters influencing the structure and the PCA of the TiO_2 film. The presence of rutile phase in the films deteriorates its PCA and highly photoactive TiO_2 films with pure anatase phase and high PCA can be sputtered in the oxide mode at high values of p_T and p_{O_2}.
2. The substrate surface temperatures $T_{surf} < 180$ °C do not influence the structure of growing TiO_2 film. Only the energy E delivered to the growing film by bombarding and condensing particles is important.
3. The structure of sputtered TiO_2 films varies along the growth direction from film/substrate interface to film surface and its evolution strongly affects the PCA of the film.
4. Thin (~100 nm) TiO_2 films with anatase phase exhibit a good PCA. The PCA improves with increasing h up to 500 nm. The increase of h above 500 nm results in no further increase of the PCA. ~500 nm thick TiO_2 film with anatase phase and high PCA can be sputtered at T_{surf} = 180 °C and $a_D \approx 10$ nm/min.
5. The interruption of sputtering process with cooling pauses allows (i) to keep the substrate surface temperature T_{surf} at the end of deposition low, less than ≤130 °C, and (ii) does not influence the structure and the PCA of TiO_2 film if the delivered energy E is sufficient to stimulate its crystallization. Thinner (<500 nm) TiO_2 film with anatase phase can be also sputtered at $T_{surf} < 180$ °C only in the case that a_D is sufficiently low.
6. Based on obtained results the phase zone model of sputtered TiO_2 films was developed.

Acknowledgements

This work was supported in part by the Ministry of Education of the Czech Republic under Project No. MSM # 4977751302 and the Grant Agency of the Czech Republic under Project No. 106/06/0327.

References

[1] A. Fujishima, K. Honda, Nature 238 (1972) 37.

[2] N. Sakai, A. Fujishima, T. Watanable, K. Hashimoto, J. Phys. Chem. B 107 (2003) 1028.

[3] U. Diebold, Surf. Sci. Rep. 48 (2003) 53.

[4] A. Fukushima, K. Hashimoto, T. Watanabe, TiO_2 Photocatalysis—Fundamentals and Applications, BKC, Inc., Tokyo, 1999.

[5] J.O. Carneiro, V. Teixeira, A. Portinha, L. Dupák, A. Magalhaes, P. Coutinho, Vacuum 78 (2003) 37.

[6] A. Fujishima, X. Zhang, C. R. Chim. 9 (2006) 750.

[7] P. Zeman, S. Takabayashi, J. Vac. Sci. Technol. A20 (2) (2002) 1.

[8] G. Zhao, Q. Tian, Q. Liu, G. Han, Surf. Coat. Technol. 198 (2005) 55.

[9] T. Modes, B. Scheffel, Chr. Meetzner, O. Zywitzki, E. Reinhold, Surf. Coat. Technol. 200 (2005) 306.

[10] Q. Ye, P.Y. Liu, Z.F. Tang, L. Zhai, Vacuum 81 (2007) 627.

[11] S. Konstantinidis, J.P. Dauchot, M. Hecq, Thin Solid Films 515 (2006) 1182.

[12] S. Mathur, P. Kuhn, Surf. Coat. Technol. 201 (2006) 807.

[13] J. Musil, D. Heřman, J. Šícha, J. Vac. Sci. Technol. A 24 (3) (2006) 521.

[14] D. Gloss, P. Frach, O. Zywitzki, T. Modes, S. Klinkenberg, C. Gottfried, Surf. Coat. Technol. 200 (2005) 967.

[15] S. Ohno, D. Sato, M. Kon, Y. Sato, M. Yoshikawa, P. Frach, Jpn. J. Appl. Phys. 43 (2004) 8234.

[16] K. Eufinger, D. Poelman, H. Poelman, R. De Gryse, G.B. Martin, Appl. Surf. Sci. 254 (2007) 148.

[17] A. Mills, J. Wang, M. Crow, G. Taglioni, L. Novela, J. Photochem. Photobiol. A: Chem. 187 (2007) 370.

[18] J. Musil, J. Šícha, D. Heřman, R. Čerstvý, J. Vac. Sci. Technol. 25 (2007) 666.

[19] J. Šícha, J. Musil, D. Heřman, Z. Strýhal, J. Pavlík, Plasma Process. Polym. 4 (2007) 345.

[20] I. Safi, Surf. Coat. Technol. 127 (2000) 203.

[21] P. Baroch, J. Musil, J. Vlček, K.H. Nam, J.G. Han, Surf. Coat. Technol. 193 (2005) 107.

[22] J. Šícha, D. Heřman, J. Musil, Z. Strýhal, J. Pavlík, Nanoscale Res. Lett. 2 (2007) 123.

[23] J. Musil, P. Baroch, IEEE Trans. Plasma Sci. 33 (2) (2005) 338.

[24] H.-J. Nam, T. Amemiya, M. Murabayashi, K. Itoh, J. Phys. Chem. B 108 (2004) 8254.

[25] J. Šícha, J. Musil, Proceedings of the 28th ICPIG Conference, Prague, Czech Republic, July 15–20, 2007, p. 671, ISBN 978-80-87026-01-4.

[26] I.K. Konstantinou, T.A. Albanis, Appl. Catal. B: Environ. 49 (2004) 1.

[27] M. Stylidi, D.I. Kondarides, X.E. Verykios, Appl. Catal. B: Environ. 47 (2004) 189.

[28] http://www.pilkington.com/.

[29] http://saint-gobain-glass.com/.

[30] P. Evans, S. Mantke, A. Mills, A. Robinson, D.W. Steel, J. Photochem. Photobiol. A: Chem. 188 (2007) 387.

4. Závěr

Tato dizertační práce je zaměřena na analýzu prvkového složení (pomocí metody rentgenové fluorescence) a struktury (pomocí metody rentgenové difrakce) čtyř typů nových tenkovrstvých materiálů vytvářených různými metodami magnetronové depozice. Jejím cílem je přispět k objasnění složitých vzájemných vztahů mezi parametry depozičních procesů, prvkovým složením a strukturou vytvořených tenkovrstvých materiálů a jejich vlastnostmi. Všechny cíle dizertační práce, uvedené v kapitole 3, byly splněny.

Hlavní výsledky dosažené v rámci této dizertační práce jsou shrnuty v následujících bodech:

Část A – Ochranné povlaky Al-Si-N, Al-Ti-O, Si-Zr-O, Si-B-C-N a Al_2O_3 s dostatečnou tvrdostí a vysokou teplotní stabilitou ve vzduchu za velmi vysokých teplot

A-I: Properties of magnetron sputtered Al-Si-N thin films with a low and high Si content.

Prvkové složení Al-Si-N vrstev je silně ovlivněno parciálním tlakem dusíku p_{N_2} a vnitřním průměrem (Φ_i) Al upevňovacího kroužku z hliníku (Al), který zasahuje do erozivní zóny rozprašovaného složeného magnetronového terče o průměru 50 mm. Je-li použit Al kroužek o vnitřním průměru Φ_i = 15 mm, je množství Si v deponovaných vrstvách nízké (~ 5 at.%) a množství Al v nich převládá nad množstvím Si při všech hodnotách p_{N_2}. Při p_{N_2}= 0 Pa deponovaná vrstva obsahuje ~ 98 at.% Al a ~ 2 at.% Si. S rostoucím p_{N_2} pak množství Al v deponovaných vrstvách klesá a množství Si a N naopak roste. Pro $p_{N_2} \geq 0{,}1$ Pa však již mají deponované Al-Si-N vrstvy téměř neměnné prvkové složení ~ 52 at.% Al, ~ 4 at.% Si a ~ 44 at.% N. V případě použití Al kroužku o vnitřním průměru Φ_i = 26 mm, je množství Si v deponovaných vrstvách vysoké (~ 40 at.%) a pro $p_{N_2} > 0{,}1$ Pa je množství N v deponovaných vrstvách vždy vyšší než množství Si a Al. Při p_{N_2} = 0 Pa deponovaná vrstva obsahuje ~ 80 at.% Al a ~ 20 at.% Si. S rostoucím p_{N_2} množství Al v deponovaných vrstvách spojitě klesá až na hodnotu ~ 7 at.% při p_{N_2} = 0,2 Pa, přičemž se s dalším růstem p_{N_2} dále nemění. Množství Si naopak vzroste na hodnotu ~ 45 at.% při p_{N_2} = 0,05 Pa, a s dalším nárůstem p_{N_2} kolísá mezi 36 – 43 at.%. Množství N nejprve spojitě roste na hodnotu 55 at.% při p_{N_2} = 0,15 Pa a s dalším růstem p_{N_2} již roste jen mírně. Nejvyšší hodnoty, 60 at.% N, dosahuje při p_{N_2} = 0,4 Pa. Všechny Al-Si-N vrstvy s nízkým (< 10 at.%) obsahem Si jsou krystalické. Vrstva deponovaná při p_{N_2}= 0 Pa je tvořena směsí 2 fází, Al a Si. Při $p_{N_2} \geq 0{,}1$ Pa se objevují difrakční linie odpovídající polykrystalickému AlN s hexagonální strukturou, jehož přednostní orientace se s rostoucím p_{N_2} mění z AlN(101) na AlN(002). Naopak, Al-Si-N vrstvy s vysokým (≥ 20 at%.) obsahem Si jsou od $p_{N_2} \geq 0{,}05$ Pa amorfní, i když jsou deponované při relativně vysoké teplotě substrátu T_s = 500 °C. Pouze pro p_{N_2}= 0 Pa je vrstva polykrystalická tvořená opět směsí 2 fází, Al a Si. Z hlediska mechanických vlastností jsou amorfní vrstvy a-(Al-Si-N), v porovnání s polykrystalickými c-(Al-Si-N) vrstvami, tvrdší ($H \approx 25$ GPa), lépe odolávají plastické deformaci a jejich teplotní stabilita tvrdosti je vysoká a s teplotou žíhání se nemění až do 1100 °C, a to dokonce ani po 4 hodinách. Odolnost proti oxidaci jak polykrystalických c-(Al-Si-N) vrstev s nízkým (< 10 at.%) obsahem Si, tak amorfních a-(Al-Si-N) vrstev s vysokým (≥ 20 at%.) obsahem Si je rovněž vysoká. Polykrystalická c-(Al-Si-N) vrstva vykazuje vysokou odolnost proti oxidaci do ~ 1000 °C a amorfní a-(Al-Si-N) vrstva až do ~ 1150 °C.

A-II: Formation of crystalline Al-Ti-O thin films and their properties.

Prvkové složení Al-Ti-O vrstev primárně závisí na vnitřním průměru ($\Phi_{\mathrm{in\ Ti}}$) upevňovacího kroužku z titanu (Ti), který zasahuje do erozivní zóny rozprašovaného složeného magnetronového terče o průměru 116 mm, a je prakticky nezávislé na teplotě substrátu T_s. Je-li použit Ti kroužek o vnitřním průměru $\Phi_{\mathrm{in\ Ti}}$ = 35 mm je poměr Al/(Al + Ti) = 0,58 a Al-Ti-O vrstvy obsahují ~ 19 at.% Al, ~ 14 at.% Ti a ~ 67 at.% O. Pro Ti kroužek o vnitřním průměru $\Phi_{\mathrm{in\ Ti}}$ = 50 mm je poměr Al/(Al + Ti) = 0,61 a Al-Ti-O vrstvy obsahují ~ 20 at.% Al, ~ 13 at.% Ti a ~ 67 at.% O. V případě Ti kroužku o vnitřním průměru $\Phi_{\mathrm{in\ Ti}}$ = 60 mm je poměr Al/(Al + Ti) = 0,80 a Al-Ti-O vrstvy obsahují ~ 31 at.% Al, ~ 7 at.% Ti a ~ 62 at.% O. Struktura Al-Ti-O vrstev závisí jak na teplotě substrátu T_S, tak na množství Ti ve vrstvě. Vrstvy Al-Ti-O s poměrem Al/(Al + Ti) = 0,58, resp. 0,61, připravené při teplotách substrátu $T_s \lesssim 700$ °C jsou charakteristické amorfně/nanokrystalickou strukturou tvořenou nanokrystaly metastabilního kubického γ-Al_2O_3 v amorfní fázi Al_2O_3, kdežto při $T_s \gtrsim 700$ °C vzniká ortorombická fáze sloučeniny Al_2TiO_5. Vrstvy Al-Ti-O s poměrem Al/(Al + Ti) = 0,80 deponované při teplotách substrátu $T_s < 600$ °C jsou charakteristické amorfní fází Al_2O_3, kdežto při $T_s \geq 600$ °C mají strukturu amorfně/nanokrystalickou tvořenou nanokrystaly metastabilního kubického γ-Al_2O_3 v amorfní fázi Al_2O_3. Krystalizační teplota Al-Ti-O vrstev tedy klesá s rostoucím obsahem Ti v těchto vrstvách. Se strukturou Al-Ti-O vrstev velice silně souvisí jejich mechanické vlastnosti, reprezentované tvrdostí H. Al-Ti-O vrstvy s amorfně/nanokrystalickou strukturou tvořenou nanokrystaly metastabilního kubického γ-Al_2O_3 v amorfní fázi Al_2O_3 mají více než 2x vyšší tvrdost (H = 25–27 GPa) v porovnání se strukturou vrstev tvořenou Al_2TiO_5 (H = 10–14 GPa). Při vyžíhání vrstev $Al_{31}Ti_7O_{62}$ na teplotu 1000 °C ve vzduchu dochází k rozpadu původní struktury γ-Al_2O_3 na směs rutilu (fáze TiO_2) a korundu (fáze α-Al_2O_3), přičemž tato teplota transformace definuje teplotní stabilitu Al-Ti-O vrstev deponovaných na Si.

A-III: Protective Zr-containing SiO_2 coatings resistant to thermal cycling in air up to 1400 °C.

Prvkové složení všech deponovaných Si-Zr-O vrstev bylo v rámci přesnosti použité techniky WDXRF stanoveno na ~ 31 at.% Si, 5 at.% Zr a ~ 64 at.% O. Za účelem stanovení teplotní stability deponovaných vrstev byla studována změna struktury deponovaných $Si_{31}Zr_5O_{64}$ vrstev s teplotou žíhání $T_{\mathrm{a\ max}}$ v rozmezí 900 °C až 1700 °C. Deponované Si-Zr-O vrstvy jsou amorfní a krystalizace u nich začíná při $T_{\mathrm{a\ max}} > 900$ °C, kdy se objevují první slabé difrakční linie t-ZrO_2 superponované na širokém píku původní amorfní fáze. Jejich intenzita s rostoucí teplotou $T_{\mathrm{a\ max}}$ postupně roste a jejich FWHM naopak postupně klesá, což ukazuje na růst velikosti a množství krystalitů t-ZrO_2, tedy na zvýšení krystalinity materiálu Si-Zr-O vrstev. Kromě zmíněné fáze t-ZrO_2, je v teplotním rozsahu 1000 °C až 1400 °C navíc detekováno i malé množství fáze $ZrSi_2$. Bylo zjištěno, že jakmile jednou dojde ve vrstvách $Si_{31}Zr_5O_{64}$ ke krystalizaci fáze t-ZrO_2, struktura vrstev $Si_{31}Zr_5O_{64}$ se teplotně stabilizuje, tj. nedochází zde při ochlazování k transformaci t-ZrO_2 na m-ZrO_2, a to v širokém teplotním rozsahu od pokojové teploty až do 1500 °C. V případě vrstev $Si_{31}Zr_5O_{64}$ deponovaných na safírový substrát dochází při $T_{\mathrm{a\ max}} > 1500$ °C ke krystalizaci fáze SiO_2 a její následné interakci se safírem za vzniku krystalické fáze $Al_5Si_2O_{13}$. Struktura $Si_{31}Zr_5O_{64}$ vrstev po ohřátí na $T_{\mathrm{a\ max}} > 1500$ °C a následném ochlazení na pokojovou teplotu je pak tvořena směsí fází t-ZrO_2, m-ZrO_2, SiO_2 a $Al_5Si_2O_{13}$. Struktura deponovaných $Al_5Si_2O_{13}$ vrstev také závisí na době žíhání t_a a byla studována v průběhu tepelného cyklování do $T_{\mathrm{a\ max}}$ = 1400 °C. Při tomto procesu dochází k rychlé krystalizaci deponovaných vrstev $Al_5Si_2O_{13}$. Jako první se objevuje fáze t-ZrO_2 a pak, pro $t_a \geq 133$ min nad teplotou $T_a \geq 1000$ °C dochází k postupné krystalizaci fáze SiO_2, jejíž množství roste s rostoucím t_a. Po teplotní stabilizaci struktury $Si_{31}Zr_5O_{64}$ vrstev již nedochází ani ke změnám jejich mechanických vlastností a vrstvy si zachovávají tvrdost $H \sim 10{,}5$ GPa, efektivní Youngův modul pružnosti $E^* \sim 80$ GPa a poměr $H^3/E^{*2} \sim 0{,}18$ GPa. Vrstvy rovněž vykazují vysokou odolnost proti tepelnému namáhání ve vzduchu do 1400 °C.

A-IV: Thermal stability of magnetron sputtered Si-B-C-N materials at temperatures up to 1700 °C.

Byla provedena strukturní analýza 3 typů Si-B-C-N vrstev, označených I, II a III, jak v deponovaném stavu, tak po vyžíhání na různé teploty při DSC a TG analýzách. Vrstvy I a II byly připraveny v plynné směsi 50% Ar + 50% N_2 při předpětí substrátu $V_b = -100$ V, resp. $V_b = V_f = -34$ V a jeho teplotě $T_s = 350$ °C, resp. $T_s = 190 – 250$ °C. Jejich složení (v at.%) bylo $Si_{32\text{-}34}B_{10}C_2N_{50\text{-}51}$ při nízké příměsi (≤ 5 at.%) vodíku a kyslíku. Vrstva III byly připravena v plynné směsi 75% Ar + 25% N_2 při předpětí substrátu $V_b = -100$ V a jeho teplotě $T_s = 350$ °C. Její složení bylo $Si_{40}B_{11}C_2N_{43}$ při nízké příměsi (≤ 5 at.%) vodíku, kyslíku a argonu. Všechny 3 deponované Si-B-C-N vrstvy jsou charakterizované velmi širokým píkem, nacházejícím se v úhlovém rozsahu $2\theta = 20 - 40°$, který svědčí o jejich amorfní struktuře. Kromě toho lze ještě detekovat dvě velice slabé difrakční linie na pozicích $2\theta = 26{,}65°$ a $2\theta = 28{,}41°$, které patří nečistotám SiO_2 a Si, jež se do vzorků dostaly při jejich nadrcení v achátové třecí misce. Po vyžíhání na teplotu 1600 °C v argonu při DSC analýze se struktura Si-B-C-N vrstev I a II nezměnila a zůstala amorfní, na rozdíl od Si-B-C-N vrstvy III, u které došlo k velmi výrazné změně struktury. Si-B-C-N vrstva III totiž zkrystalizovala a její fázové složení odpovídá směsi 4 různých fází, α-Si_3N_4, β-Si_3N_4, t-B(C)N a Si. Dále bylo zjištěno, že změna struktury této vrstvy začíná již při teplotě vyšší než 1230 °C. Při teplotě 1270 °C se objevují první difrakční linie nanokrystalické fáze α-Si_3N_4, jejichž intenzita s rostoucí teplotou roste. Při teplotě 1300 °C k nim přibývají difrakční linie Si a při teplotě 1430 °C difrakční linie β-Si_3N_4 a t-B(C)N. V případě TG analýzy byly vzorky vyhřáty v heliu až na teplotu 1600 °C a 1700 °C. Při vyhřátí na teplotu 1600 °C se struktura Si-B-C-N vrstev I a II nezměnila a zůstala amorfní, přičemž Si-B-C-N vrstva III opět zkrystalizovala na směs 4 různých fází, α-Si_3N_4, β-Si_3N_4, t-B(C)N a Si. Po vyhřátí na teplotu 1700 °C se již změnila struktura i Si-B-C-N vrstev I a II, když u nich došlo ke krystalizaci malého množství α-Si_3N_4, přičemž většina objemu vrstvy zůstala i nadále amorfní. Struktura Si-B-C-N vrstvy III se při vyhřátí na teplotu 1700 °C příliš nezměnila. Její fázové složení zůstalo stejné, pouze se zvětšily intenzity difrakčních linií Si a naopak klesly intenzity difrakčních linií α-Si_3N_4, což svědčí o poklesu množství α-Si_3N_4 ve vrstvě a naopak nárůstu množství Si. Rovněž vymizela široká difrakční linie na $2\theta = 25°$ připisovaná neuspořádané turbostratické fázi t-B(C)N a naopak se zvýšila intenzita difrakční linie na $2\theta = 26{,}71°$ patřící hexagonálnímu h-BN. Ze strukturní analýzy vyplynulo, že kritickým depozičním parametrem pro přípravu Si-B-C-N vrstev s vysokou teplotní stabilitou je složení argon-dusíkové pracovní atmosféry, která určuje prvkové složení vrstev. Nejvyšší teplotní stabilitu, až do1600 °C, vykazovaly amorfní Si-B-C-N vrstvy I a II, připravené v plynné směsi 50% Ar + 50% N_2, zatímco amorfní struktura Si-B-C-N vrstvy III, připravené v plynné směsi 75% Ar + 25% N_2, byla stabilní pouze do teploty 1230 °C.

A-V: Thermal stability of alumina thin films containing γ-Al_2O_3 phase prepared by reactive magnetron sputtering.

Prvkové složení všech deponovaných Al_2O_3 vrstev bylo v rámci přesnosti použité techniky WDXRF stanoveno na ~ 40 at.% Al a ~ 60 at.% O, což odpovídá stechiometrickému složení sloučeniny Al_2O_3. Z hlediska struktury jsou všechny deponované vrstvy Al_2O_3 charakterizované 3 širokými difrakčními liniemi (311), (400) a (440) nanokrystalického γ-Al_2O_3 s nízkou intenzitou. Nelze však vyloučit i přítomnost malého množství amorfní fáze Al_2O_3. Za účelem stanovení teplotní stability deponovaných vrstev byla studována změna struktury těchto vrstev s teplotou žíhání T_a, dobou žíhání t_a a jejich tloušťkou. Deponované vrstvy Al_2O_3 o tloušťce ~ 1200 nm byly žíhány v rozmezí teplot 700 °C až 1150 °C po dobu 5 hodin. Bylo zjištěno, že s rostoucí teplotou žíhání T_a se zlepšuje krystalinita vrstev, neboť intenzita difrakčních linií (311), (400) a (440) γ-Al_2O_3 se zvětšuje a navíc se objevují i další difrakční linie (220) a (222) této fáze. Při teplotě žíhání $T_a \approx 1050$ °C se společně s metastabilní fází θ-Al_2O_3 objevují i první difrakční linie fáze α-Al_2O_3 ukazující na počátek krystalizace této termodynamicky stabilní fáze. Vrstvy vyžíhané při teplotě $T_a \approx 1100$ °C jsou pak tvořeny směsí větších zrn α-Al_2O_3 a malých zrn θ-Al_2O_3 a při $T_a = 1150$ °C se vytváří již jen vrstvy krystalického α-Al_2O_3. Změna struktury deponovaných Al_2O_3 vrstev s dobou žíhání t_a a jejich tloušťkou byla studována pouze při $T_a = 1100$ °C, což je teplota blízko transformace $\gamma \rightarrow \alpha$. Ohřátí vrstvy na 1100 °C následované okamžitým ochlazením na pokojovou teplotu nemá prakticky žádný vliv na strukturu vrstvy, a to bez ohledu na její tloušťku. Naopak, výdrž na této teplotě po dobu $t_a \geq 1$ h vede ke vzniku termodynamicky stabilní fáze α-Al_2O_3, přičemž tato změna je tím výraznější, čím je vrstva tlustší.

Část B – Otěruvzdorné ochranné povlaky nc-TiC/*a*-C a Mo-C s dostatečnou tvrdostí a nízkým koeficientem tření

B-I: Tribological and mechanical properties of nanocrystalline-TiC/*a*-C nanocomposite thin films.

Prvkové složení TiC/*a*-C vrstev závisí na vnitřním průměru (Φ_{in}) upevňovacího kroužku z titanu (Ti), který zasahuje do erozivní zóny rozprašovaného složeného magnetronového terče o průměru 100 mm, takže změnou (Φ_{in}) lze řídit množství Ti v TiC/*a*-C vrstvách v rozsahu 2,6 – 53,8 at.%. Struktura TiC/*a*-C vrstev pak silně závisí právě na obsahu Ti v těchto vrstvách, respektive na poměru C/Ti. Pro poměr C/Ti $\leq$ 1,54 jsou TiC/*a*-C vrstvy charakterizované krystalickou fází TiC a pravděpodobně i malým množstvím amorfní fáze uhlíku *a*-C. S rostoucím poměrem C/Ti se však struktura TiC/*a*-C vrstev značně mění. Nejprve na vrstvy nanokrystalické, kdy se intenzity difrakčních linií TiC snižují a jejich FWHM se zvětšuje v důsledku postupného zmenšování „velikosti zrn“ TiC z ~ 35 nm na ~ 1 – 2 nm, až zcela zanikají v širokém píku amorfní fáze uhlíku *a*-C při C/Ti $\geq$ 9,1. Jelikož se se změnou poměru C/Ti nemění mřížkový parametr TiC, neboť nedochází k posunu jeho difrakčních linií, znamená to, že se jedná o vrstvy kompozitní, tvořené nanokrystaly TiC v amorfní uhlíkové matrici *a*-C. „Velikost zrn“ krystalické fáze TiC a poměr C/Ti, tj. množství krystalické a amorfní fáze ve vrstvě, jinak též struktura a prvkové složení, určují jak mechanické vlastnosti (jako je tvrdost H a efektivní Youngův modul pružnosti E^*), tak tribologické vlastnosti (jako koeficient tření μ a rychlost otěru k) kompozitní TiC/*a*-C vrstvy. Nanokompozitní vrstvy nc-TiC/*a*-C s poměrem

C/Ti > 1,5 a poměrem H^3/E^{*2} v rozsahu ~ 0,2 až ~ 0,3 vykazují nejnižší hodnoty koeficientu tření ($\mu \leq 0{,}1$) a rychlosti otěru ($k \leq 2\text{x}10^{-7}$ mm^3/Nm) při dostatečné tvrdosti H ~ 15 – 20 GPa.

B-II: Coefficient of friction and wear of sputtered a-C thin coatings containing Mo.

Prvkové složení připravených Mo-C vrstev závisí na vnitřním průměru (Φ_{in}) kroužku z molybdenu (Mo), který zasahuje do erozivní zóny rozprašovaného složeného magnetronového terče o průměru 100 mm, takže změnou (Φ_{in}) lze řídit množství Mo v Mo-C vrstvách v širokém rozmezí 2 - 100 at.%. Struktura Mo-C vrstev pak silně závisí právě na obsahu Mo v těchto vrstvách. Mo-C vrstvy s vysokým (≥ 40 at.%) obsahem Mo jsou krystalické a jejich fázové složení se postupně mění od čistého Mo přes tuhý roztok uhlíku v molybdenu (Mo,C) na kompozit γ-Mo_2C/(Mo,C) při ~ 70 at.% Mo a dále pak na nanokrystalický kompozit (nc-) δ-$MoC_{0,75}$/a-(C,Mo) při < 57 at.% Mo. Pokud však množství Mo v Mo-C vrstvě poklesne pod ~ 28 at.%, vytváří se amorfní a-(C,Mo) materiál. Jak prvkové složení, tak struktura, resp. fázové složení, výrazně ovlivňují jak mechanické (tvrdost, elastická vratnost), tak tribologické (koeficient tření, rychlost otěru) vlastnosti Mo-C vrstev. Zatímco elastická vratnost Mo-C vrstev téměř spojitě klesá s rostoucím obsahem Mo, tvrdost Mo-C vrstev závisí na jejich struktuře mnohem komplexněji. Amorfní a-(C,Mo) mají nejnižší tvrdost (H ~ 10 GPa), avšak nanokrystalický kompozit (nc-) δ-$MoC_{0,75}$/a-(C,Mo) je přibližně 2x tvrdší (~ 23 GPa) a má téměř stejnou tvrdost jako krystalický kompozit γ-Mo_2C/(Mo,C). Tvrdost tuhého roztoku uhlíku v Mo (Mo,C) pak opět klesá na ~ 17GPa a je srovnatelná s tvrdostí čistě molybdenové vrstvy. Amorfní a-(C,Mo) vrstvy obsahující méně než 10 at.% Mo vykazují nízké (≤ 0,1) hodnoty koeficientu tření a nízké (≤ $5\text{x}10^{-7}$ mm^3/Nm) hodnoty rychlosti otěru. S rostoucím obsahem Mo v a-(C,Mo) vrstvách však hodnoty koeficientu tření a rychlosti otěru rychle rostou.

Část C – Multifunkční vrstvy Al-Cu-O, Zr-Al-O, Al-O-N se zvýšenou odolností proti vzniku trhlin při namáhání

C-I: Properties of nanocrystalline Al–Cu–O films reactively sputtered by DC pulse dual magnetron.

Prvkové složení Al-Cu-O vrstev závisí na době trvání negativního napěťového pulzu $\tau_{Al/Cu}$ na složeném Al/Cu terči, a to tak, že obsah Cu v Al-Cu-O vrstvách s dobou trvání negativního napěťového pulzu $\tau_{Al/Cu}$ roste, přičemž dosahuje nejvyšší hodnoty ~ 16 at.% při $\tau_{Al/Cu}$ = 32 µs. Naopak, obsah Al v Al-Cu-O s dobou trvání negativního napěťového pulzu $\tau_{Al/Cu}$ klesá z hodnoty ~ 37 at.% na hodnotu ~ 25 at.% při $\tau_{Al/Cu}$ = 32 µs. Obsah O v Al-Cu-O vrstvách se v rámci chyby měření nemění a má průměrnou hodnotu ~ 62 at.%. Přidání Cu do vrstvy Al_2O_3 silně ovlivňuje její strukturu. Obecně lze všechny deponované Al-Cu-O vrstvy charakterizovat jako nanokrystalický kompozitní materiál tvořený velice malými zrny krystalické fáze v amorfní matrici. Čistě Al_2O_3 vrstvy jsou charakterizovány širokými difrakčními liniemi (311), (400) a (440) nanokrystalického γ-Al_2O_3 s nízkou intenzitou superponovanými na širokém píku amorfního Al_2O_3 a představují tedy nanokrystalický nc-γ-Al_2O_3/a-Al_2O_3 kompozit. Přidávání Cu do Al_2O_3 vrstvy vede k postupné posouvání difrakčních linií (311), (400) a (440) nanokrystalického γ-Al_2O_3 k nižším difrakčním úhlům 2θ, a to až na pozice odpovídající difrakčním liniím (220), (311), (511) a (440) sloučeniny $CuAl_2O_4$. Jelikož se pnutí s rostoucím obsahem Cu v Al-Cu-O vrstvách nemění, tak toto posouvání difrakčních linií ukazuje na fakt, že se atomy Cu rozpouštějí v zrnech nanokrystalického γ-Al_2O_3 a že se tak vytváří nanokrystalický tuhý roztok $(Al_{8-2x}Cu_{3x})O_{12}$. Intenzita difrakční linie γ-Al_2O_3(400) s rostoucím obsahem Cu ve vrstvě klesá, přičemž při obsahu ≥ 16 at.% Cu takřka vymizí. Zároveň se při ~ 6 at.% Cu objevuje difrakční linie $CuAl_2O_4$(220), jejíž intenzita s rostoucím obsahem Cu ve vrstvě roste. Zřetelná asymetrie difrakční linie $CuAl_2O_4$(311) ve směru k vyšším difrakčním úhlům 2θ naznačuje koexistenci $CuAl_2O_4$(311) a nanokrystalického tuhé roztoku $(Al_{8-2x}Cu_{3x})O_{12}$. Všechna tato zjištění tak ukazují na fakt, že struktura Al-Cu-O vrstev s obsahem Cu ≤ 10 at.% je velmi složitá. Jak mechanické vlastnosti (tvrdost a efektivní Youngův modul pružnosti), včetně odolnosti Al-Cu-O vrstev proti vzniku trhlin při namáhání, tak i optické vlastnosti (propustnost, index lomu a extinkční koeficient) Al-Cu-O vrstev silně korelují s obsahem Cu v těchto vrstvách. Až na optickou propustnost, která s obsahem Cu ve vrstvě klesá a při obsahu ≥ 16 at.% Cu se vrstva stává neprůhlednou, všechny ostatní sledované veličiny s obsahem Cu v Al-Cu-O vrstvách rostou.

C-II: Transparent Zr-Al-O oxide coatings with enhanced resistance to cracking.

Prvkové složení Zr-Al-O vrstev silně závisí na parciálním tlaku kyslíku p_{O_2}, respektive depoziční rychlosti a_D. Obsah Al ve vrstvách s rostoucím p_{O_2} spojitě klesá z 37 at.% na ~ 1 at.%. Rovněž obsah Zr s rostoucím p_{O_2} nejprve klesá z 51 at.% na 19 at.% (pro p_{O_2} ~ 0,06 Pa), však s dalším růstem p_{O_2} se již dále nemění a pohybuje se kolem ~ 20 at.%. Pokud jde o O, tak jeho obsah s růstem p_{O_2} nejprve roste z 12 at.% na ~ 73 at.% (pro p_{O_2} ~ 0,15 Pa), ale s dalším růstem p_{O_2} se již také nemění. Rovněž struktura deponovaných Zr-Al-O vrstev silně závisí na parciálním tlaku kyslíku p_{O_2}, respektive depoziční rychlosti a_D. Vrstvy Zr-Al-O deponované v kovovém módu naprašování při velice nízkých (≤ 0,01 Pa) hodnotách parciálního tlaku kyslíku p_{O_2} jsou dvoufázové, tvořené nanokrystalickou fází h-Zr s hexagonální strukturou a amorfní fází a-Al_2O_3. Lze je tedy považovat za kompozitní materiál. Vrstvy Zr-Al-O připravené při p_{O_2} v rozsahu ~ 0,02 až ~ 0,06 Pa jsou amorfní, neboť energie dodávaná do rostoucích vrstev není dostatečná pro krystalizaci ZrO_2. K té dochází až při $p_{O_2} \geq$ 0,1 Pa, kdy vzniká nanokrystalická fáze t-ZrO_2 s tetragonální strukturou a vrstvy pak tvoří kompozit nanokrystalických t-ZrO_2 zrn v amorfní matrici a-Al_2O_3, nc-t-ZrO_2/a-Al_2O_3. Se strukturou Zr-Al-O vrstev velice úzce souvisí jejich mechanické vlastnosti (tvrdost, efektivní Youngův modul pružnosti a elastická vratnost), které s rostoucím p_{O_2} rostou, přičemž nejvyšších hodnot dosahují u vrstev deponovaných v přechodovém módu, kdy vrstvy tvoří nanokompozit nc-t-ZrO_2/a-Al_2O_3. Tyto vrstvy jsou průhledné, dosahují tvrdosti $H \approx 18$ GPa, poměru $H/E^* > 0{,}1$ a jejich elastická vratnost $W_e > 70\%$. Rovněž vykazují vysokou odolnost proti vzniku prasklin při ohybu, neboť nepraskají ani při ohnutí o 180°.

C-III: Two-phase single layer Al-O-N nanocomposite films with enhanced resistance to cracking.

Struktura Al-O-N vrstev silně závisí na periodě T_{O_2} kyslíkových pulzů a na činiteli využití kyslíkových pulzů τ_{O_2}/T_{O_2}, tj. na množství kyslíku v deponované vrstvě. Částečně závisí též na teplotě substrátu T_s. Teplotní závislost struktury Al-O-N vrstev je poněkud překvapivá, neboť vrstvy připravené při teplotě substrátu T_s = 500 °C vykazují horší krystalinitu než vrstvy připravené na nevyhřívaném substrátu při pokojové teplotě (T_s = RT). Toto chování však lze snadno vysvětlit vyšší desorpcí kyslíku ze stěn komory při vyšší depoziční teplotě, což je do určité míry v podstatě ekvivalentní zvětšování činitele využití kyslíkových pulzů τ_{O_2}/T_{O_2}. Vrstvy připravené při τ_{O_2}/T_{O_2}= 1, což odpovídá kontinuálnímu napouštění kyslíku ke stávajícímu dusíku, obsahují 2 fáze. Fázi nanokrystalického γ-Al_2O_3 a amorfní fázi a-(Al-O-N), a lze je tedy považovat za kompozitní materiál. Vrstvy připravené při τ_{O_2}/T_{O_2}= 0, což odpovídá depozici v čistém dusíku, obsahují pouze krystalickou fázi AlN. Při přidávání kyslíku do AlN vrstvy, tj. pro $0 < \tau_{O_2}/T_{O_2} < 1$, dochází nejprve k tvorbě nanokompozitních nc-AlN/a-(Al-O-N) vrstev, které se postupně mění v amorfní a-(Al-O-N) vrstvy při $\tau_{O_2}/T_{O_2} \approx 0{,}20 - 0{,}25$ a následně v nanokrystalický kompozit nc-γ-Al_2O_3/a-(Al-O-N) při $\tau_{O_2}/T_{O_2} \geq 0{,}33$. Popsané změny ve struktuře deponovaných vrstev samozřejmě významně mění jejich mechanické vlastnosti. Je zjevné, že vytvoření nanokrystalické fáze nc-AlN nebo nc-γ-Al_2O_3 v amorfní matrici a-(Al-O-N) výrazně zvyšuje tvrdost těchto nanokompozitních materiálů ve srovnání s amorfním materiálem tvořeným pouze a-(Al-O-N). Tyto nanokompozity dosahují tvrdosti H = 15 až 20 GPa, mají nízký efektivní Youngův modul pružnosti E^*, takže poměr $H/E^* > 0{,}1$, vysokou elastickou vratnost $W_e > 60\%$ a nepraskají ani při ohnutí o 180°. Naproti tomu amorfní a-(Al-O-N) materiály vykazují nižší tvrdost $H \approx 10$ GPa, poměr $H/E^* < 0{,}1$, elastickou vratnost $W_e \approx 50\%$ a praskliny se u nich objevují již při ohnutí o 40°.

C-IV: The effect of addition of Al in ZrO_2 thin film on its resistance to cracking.

Prvkové složení Zr-Al-O vrstev silně závisí na parciálním tlaku kyslíku p_{O_2} a vnitřním průměru ($\Phi_{in\ Zr}$) upevňovacího kroužku ze zirkonia (Zr), který zasahuje do erozivní zóny rozprašovaného složeného magnetronového terče o průměru 50 mm. Je-li použit Zr kroužek o vnitřním průměru $\Phi_{in\ Zr}$ = 20 mm, je množství Al ve vrstvách nízké (~ 11 at.%) a množství Zr ve vrstvách převládá nad množstvím Al při všech hodnotách parciálního tlaku kyslíku p_{O_2}, tj. poměr Zr/Al > 1. Kromě toho mají vrstvy Zr-Al-O deponované při $p_{O_2} \geq 0{,}05$ Pa téměř shodné prvkové složení ~ 23 at.% Zr, ~ 11 at.% Al a ~ 66 at.% O. Je-li použit Zr kroužek o vnitřním průměru $\Phi_{in\ Zr}$ = 24 mm, je množství Al ve vrstvách vysoké (~ 29 at.%) a množství Al ve vrstvách převládá nad množstvím Zr při všech hodnotách parciálního tlaku kyslíku p_{O_2}, tj. poměr Zr/Al < 1. Kromě toho mají vrstvy Zr-Al-O deponované při $p_{O_2} \geq 0{,}07$ Pa téměř shodné prvkové složení ~ 9 at.% Zr, ~ 29 at.% Al a ~ 62 at.% O. Struktura naprašovaných Zr-Al-O vrstev silně závisí na jejich prvkovém složení, zejména na poměru Zr/Al, a na parciálním tlaku kyslíku p_{O_2}. Zr-Al-O vrstvy s poměrem Zr/Al < 1 deponované při p_{O_2}= 0 Pa jsou krystalické a tvořené fázemi Al, $Al_{9,83}$ $Zr_{0,17}$ a $ZrSi_2$. S rostoucím parciálním tlakem kyslíku p_{O_2}pak dochází k tvorbě oxidů Zr a Al, k poklesu krystalinity vrstev a postupnému přechodu původně krystalických vrstev na vrstvy krystalicko/amorfní (při p_{O_2}= 0,04 Pa) a nakonec na vrstvy amorfní (při $p_{O_2} \geq 0{,}06$ Pa), tvořené převážně a-Al_2O_3. Na druhou stranu, Zr-Al-O vrstvy s poměrem Zr/Al > 1 jsou zpočátku krystalicko/amorfní, ale jejich krystalinita se s rostoucím p_{O_2} zlepšuje. Při $p_{O_2} \geq 0{,}06$ Pa jsou pak tvořeny nanokompozitem zrn t-ZrO_2 v amorfní a-Al_2O_3 matrici. Přidávání Al do ZrO_2 silně ovlivňuje strukturu, a tím i vlastnosti Zr-Al-O vrstev. Zr-Al-O vrstvy s poměrem Zr/Al < 1 mají převážně amorfní strukturu, jsou měkké, mají nízkou elastickou vratnost, poměr $H/E^* < 0{,}1$ a velice snadno praskají. Naopak, Zr-Al-O vrstvy s poměrem Zr/Al > 1 a kompozitní strukturou nc-ZrO_2/a-Al_2O_3 jsou tvrdé, vysoce elastické s poměrem $H/E^* > 0,1$ a vykazují vysokou odolnost proti praskání.

Část D – Fotokatalytické vrstvy TiO_2

D-I: Nanostructure of photocatalytic TiO_2 films sputtered at temperatures below 200 °C.

Struktura deponovaných vrstev TiO_2 silně závisí na parciálním tlaku reaktivního plynu p_{O_2}, celkovém tlaku plynu p_T a na jejich tloušťce h. Je však relativně nezávislá na depoziční teplotě pro $T_{surf} < 180$ °C. Z hlediska tloušťky vrstvy h byl pro všechny deponované vrstvy TiO_2 pozorován stejný trend ve vývoji jejich struktury. S růstem tloušťky h dochází ke zlepšení krystaličnosti TiO_2 vrstev, tedy k postupnému přechodu od amorfních vrstev (pro $h < 100$ nm) k vrstvám krystalickým (pro $h \geq 100$ nm), tvořených směsí rutilu a anatasu, přičemž poměr anatasu a rutilu s rostoucím h roste. Krystaličnost anatasové fáze se dále zvyšuje s rostoucím parciální tlakem p_{O_2}, jsou-li vrstvy TiO_2 deponované při celkovém tlaku $p_T \geq 0,5$ Pa. Kromě toho se s rostoucím celkovým tlakem p_T snižuje i množství rutilové fáze ve vrstvě, takže vrstvy TiO_2 deponované při celkových tlacích $p_T \geq 1,5$ Pa již obsahují pouze fázi anatasu. Struktura deponovaných vrstev TiO_2 se však také mění ve směru růstu vrstvy, tj. od rozhraní vrstva-substrát k povrchu vrstvy, kdy se u rozhraní vrstva-substrát primárně vytváří rutilová fáze, jejíž množství pak klesá s rostoucí tloušťkou vrstvy h a v závislosti na celkovém tlaku p_T. Na základě získaných výsledků byl sestaven fázový zonální model naprašovaných TiO_2 vrstev. Dále bylo zjištěno, že fotokatalytická aktivita TiO_2 vrstev úzce souvisí právě s jejich strukturou. Fotokatalytická aktivita vrstvy TiO_2 roste s rostoucím množstvím anatasové fáze ve vrstvě a s rostoucí tloušťkou vrstvy, a to až do $h = 500$ nm.

Resumé česky

Tato dizertační práce je zaměřena na analýzu prvkového složení (pomocí metody rentgenové fluorescence) a struktury (pomocí metody rentgenové difrakce) čtyř typů nových tenkovrstvých materiálů vytvářených různými metodami magnetronové depozice. Jde o následující materiály:

A. Ochranné povlaky Al-Si-N, Al-Ti-O, Si-Zr-O, Si-B-C-N a Al_2O_3 s dostatečnou tvrdostí a vysokou teplotní stabilitou ve vzduchu za velmi vysokých teplot.
B. Otěruvzdorné ochranné povlaky nc-TiC/*a*-C a Mo-C s dostatečnou tvrdostí a nízkým koeficientem tření.
C. Multifunkční vrstvy Al-Cu-O, Zr-Al-O, Al-O-N se zvýšenou odolností proti vzniku trhlin při namáhání.
D. Fotokatalytické vrstvy TiO_2.

Práce je rozdělena do 4 kapitol. Kapitola 1 je věnována obecnému úvodu a základním principům použitých metod rentgenové fluorescence a rentgenové difrakce. V kapitole 2 jsou definovány cíle dizertační práce. Ve 3. kapitole, obsahově nejrozsáhlejší, jsou uvedeny dosažené výsledky, a to ve formě 12 vědeckých článků publikovaných v impaktovaných mezinárodních časopisech, tematicky rozdělených do 4 částí (A – D).

Část A zahrnuje 5 studií:

A-I : Properties of magnetron sputtered Al-Si-N thin films with a low and high Si content.
A-II : Formation of crystalline Al-Ti-O thin films and their properties.
A-III: Protective Zr-containing SiO_2 coatings resistant to thermal cycling in air up to 1400 °C.
A-IV: Thermal stability of magnetron sputtered Si-B-C-N materials at temperatures up to 1700 °C.
A-V : Thermal stability of alumina thin films containing γ-Al_2O_3 phase prepared by reactive magnetron sputtering.

Část B zahrnuje 2 studie:

B-I : Tribological and mechanical properties of nanocrystalline-TiC/*a*-C nanocomposite thin films.
B-II: Coefficient of friction and wear of sputtered a-C thin coatings containing Mo.

Část C zahrnuje 4 studie:

C-I : Properties of nanocrystalline Al–Cu–O films reactively sputtered by DC pulse dual magnetron.
C-II : Transparent Zr-Al-O oxide coatings with enhanced resistance to cracking.
C-III: Two-phase single layer Al-O-N nanocomposite films with enhanced resistance to cracking.
C-IV: The effect of addition of Al in ZrO_2 thin film on its resistance to cracking.

Část D zahrnuje 1 studii:

D-I: Nanostructure of photocatalytic TiO_2 films sputtered at temperatures below 200 °C.

Kapitola 4 je věnována závěrům dizertační práce. Lze konstatovat, že dizertační práce přispívá k objasnění složitých vzájemných vztahů mezi parametry depozičních procesů, prvkovým složením a strukturou vytvořených tenkovrstvých materiálů a jejich vlastnostmi.

Abstract

This thesis is focused on the analysis of elemental composition (by X-ray fluorescence method) and the structure (by X-ray diffraction method) of four types of the new thin-film materials prepared by different methods of magnetron deposition. These are the following materials:

A. Al-Si-N, Al-Ti-O, Si-Zr-O, Si-B-C-N and Al_2O_3 protective coatings with a sufficient hardness and high temperature stability in air at very high temperatures.
B. Nc-TiC/*a*-C and Mo-C abrasion resistant coatings with a sufficient hardness and low coefficient of friction.
C. Al-Cu-O, Zr-Al-O, Al-O-N multifunctional layers with an increased resistance to stress cracking.
D. Photocatalytic TiO_2 layers.

The thesis is divided into 4 Chapters. Chapter 1 is devoted to a general introduction and basic principles of X-ray fluorescence and X-ray diffraction methods. In Chapter 2, the aims of thesis are defined. Chapter 3 is the most extensive and it is devoted to the achieved results. The results are presented in a form of 12 scientific papers published in prestigious international journals divided into 4 parts (A – D).

Part A includes 5 papers:

A-I : Properties of magnetron sputtered Al-Si-N thin films with a low and high Si content.
A-II : Formation of crystalline Al-Ti-O thin films and their properties.
A-III: Protective Zr-containing SiO_2 coatings resistant to thermal cycling in air up to 1400 °C.
A-IV: Thermal stability of magnetron sputtered Si-B-C-N materials at temperatures up to 1700 °C.
A-V : Thermal stability of alumina thin films containing γ-Al_2O_3 phase prepared by reactive magnetron sputtering.

Part B includes 2 papers:

B-I : Tribological and mechanical properties of nanocrystalline-TiC/*a*-C nanocomposite thin films.
B-II: Coefficient of friction and wear of sputtered a-C thin coatings containing Mo.

Part C includes 4 papers:

C-I : Properties of nanocrystalline Al–Cu–O films reactively sputtered by DC pulse dual magnetron.
C-II : Transparent Zr-Al-O oxide coatings with enhanced resistance to cracking.
C-III: Two-phase single layer Al-O-N nanocomposite films with enhanced resistance to cracking.
C-IV: The effect of addition of Al in ZrO_2 thin film on its resistance to cracking.

Part D includes 1 paper:

D-I: Nanostructure of photocatalytic TiO_2 films sputtered at temperatures below 200 °C.

Chapter 4 is devoted to the conclusions of the thesis. It can be stated that the thesis contributes to the elucidation of the complex interrelationships between the parameters of the deposition

processes and the elemental composition and the structure of the formed thin-film materials and their properties.